

INFORMATION TO USERS

This manuscript has been reproduced from the microfilm master. UMI films the text directly from the original or copy submitted. Thus, some thesis and dissertation copies are in typewriter face, while others may be from any type of computer printer.

The quality of this reproduction is dependent upon the quality of the copy submitted. Broken or indistinct print, colored or poor quality illustrations and photographs, print bleedthrough, substandard margins, and improper alignment can adversely affect reproduction.

In the unlikely event that the author did not send UMI a complete manuscript and there are missing pages, these will be noted. Also, if unauthorized copyright material had to be removed, a note will indicate the deletion.

Oversize materials (e.g., maps, drawings, charts) are reproduced by sectioning the original, beginning at the upper left-hand corner and continuing from left to right in equal sections with small overlaps.

Photographs included in the original manuscript have been reproduced xerographically in this copy. Higher quality 6" x 9" black and white photographic prints are available for any photographs or illustrations appearing in this copy for an additional charge. Contact UMI directly to order.

Bell & Howell Information and Learning
300 North Zeeb Road, Ann Arbor, MI 48106-1346 USA

UMI[®]
800-521-0600

EXPERIMENTAL STUDIES OF STATIC MIXERS
AND TWIN SCREW EXTRUDERS

By
SHAFFIQ A. JAFFER

A Thesis
Submitted to the School of Graduate Studies
in Partial Fulfillment of the Requirements
for the Degree
Doctor of Philosophy

McMaster University

© Copyright by Shaffiq A. Jaffer, September 1998

EXPERIMENTAL STUDIES OF STATIC MIXERS & TWIN SCREW EXTRUDERS

DOCTOR OF PHILOSOPHY (1998)

McMaster University

(Chemical Engineering)

Hamilton, Ontario

TITLE: Experimental Studies of Static Mixers and Twin Screw Extruders

AUTHOR: Shaffiq A. Jaffer

B.Sc. in Chemical Engineering (University of Alberta)

SUPERVISOR: Dr. Philip E. Wood

Chemical Engineering

NUMBER OF PAGES: xxx, 241

Abstract

The laminar flow field in a Kenics KM[®] static mixer and a Werner and Pfleiderer ZSK-30[®] twin screw extruder (TSE) has been studied using laser induced fluorescence (LIF) coupled with digital image analysis, particle image velocimetry (PIV) and laser Doppler anemometry (LDA). The objective of this study was to observe the flow fields in these two devices, to determine their mixing capabilities qualitatively and quantitatively.

Mixing in the static mixer was quantified by measurement of the number average striation thickness, variance of striation widths and interfacial area for elements with 90 degrees of twist. From flow visualisations and LDA measurements, transitions were observed in the flow where vortices developed above the first and second elements. These vortices did not appreciably enhance mixing after 4 to 5 elements with an aspect ratio (L/D) of 1.0.

The velocity field measured over the first four elements ($L/D = 1.5$), captured the mixing nature of the static mixer, where flow was split at the leading edge and recombined at the trailing edge of the elements. Recirculations in the radial plane were observed where fluid flowed from the high-pressure side of the element forward out along the tube wall to the low-pressure side or suction side. The radial flow field required a development length to allow the flow to build in magnitude. The rate of deformation analysis on the flow field indicated that mixing efficiency would be

increased if the first element had a larger helix angle. The highest rates of deformation were measured at the junctions between elements, and between the element and tube surfaces.

The visualisations coupled with image analysis for the TSE demonstrated clearly that the mixing was enhanced by placing a reverse conveying element directly after the last set of kneading discs in the mixing section. The velocity results for the screw profile with extended first and last discs (geometry A) showed an increase in back flow and recirculations with increasing screw rotation. When a forward conveying element was used before and after the kneading discs (geometry B), higher radial and lower axial velocities were measured. The fluid flowed in the direction of rotation and no back-mixing or recirculations in the flow were measured.

Results of a 3D model for the simulation of flow in the kneading disc region and the PIV measurements were compared. Results for geometry A are in good qualitative agreement for low flow rates. Geometry B showed better agreement at higher flow rates compared to lower flow rates.

The performance of the kneading discs was characterised based on the shear, elongation and the magnitude of the rate of deformation tensor within the measured flow fields. For the various cases of screw rotation speed, the largest rates of deformations (elongation and shear) were seen at the first and last disc of the kneading block where flow transitions occurred.

To the memory of my beloved grandfather.

Acknowledgements

There are no words that can convey my appreciation and admiration of my supervisor Dr. Philip Wood. He has been more than just a supervisor. He has been a friend first and foremost. I will always try to emulate the example he set in these last five years.

There are many people who have had a hand in guiding me and helping me achieve success in my studies. Dr. Andrew Hrymak may not have been a supervisor in title but he was always there to give ideas, support and his endless knowledge. I thank him for his patience, continuous challenges and friendship.

Dr. John Vlachopoulos has been a great friend and supporter. I thank him for his open door policy and always keeping me focused on the big picture rather than losing myself in the minute details.

I would like to thank Dr. Donald Woods for his insightful knowledge and continuous support. The knowledge I gained from helping him teach the final year design course can not be measured. I was just as much a student as the young engineers we were teaching.

Sara Gallo-O'Toole and Barbara Owen are like the glue that holds this department together. Without their efforts, I would hate to think where we would be. I will always be thankful to them for their endless help, support, patience and friendship.

I thank Paul Gatt, without his skilled hands and knowledge, I could not have accomplished this high quality research. I thank Justyna Derkach and Gord Slater for all their help over the last five years.

My sincere thanks go out to the Natural Sciences and Engineering Research Council, Werner & Pfleiderer and Gates Rubber Co. for their financial support of this work.

To all my friends, too many to mention, I thank them all for the laughs and enjoyment we shared over these last five years. I especially would like to thank Victor Bravo who has always been there to lean on and have a laugh with. The time we have worked together will always be special in my memory. I have the highest regards for his abilities and I hope to have the opportunity to work with him again one day.

Countless thanks go out to my father, mother and sister who always pushed me to do the best and to never quit. I thank them for their support and love. I will always be in debt to them.

To my mother in-law, father in-law and aunt who since the day I have met them, have always shown confidence in my abilities and welcomed me into their hearts.

I thank my two very dear friends and family, Gavan Gibson and Margarita Diaz, who have always been there to help and give me endless support.

Lastly, I thank my wife for love and support. She has pushed me everyday to succeed. She rode the ups and downs at my side and has always been there to show me a smile when I needed it. This thesis could never have been accomplished without her. This is hers as much as mine to celebrate.

TABLE OF CONTENTS

ABSTRACT	iii
ACKNOWLEDGEMENTS	v
TABLE OF CONTENTS	viii
LIST OF TABLES	xi
LIST OF FIGURES	xi
LIST OF SYMBOLS	xxv
1.0 INTRODUCTION	i
1.1 STATIC MIXERS	2
1.2 TWIN SCREW EXTRUDERS (TSE)	4
1.3 SCOPE OF PROJECT	7
1.4 THESIS ORGANISATION	9
2.0 LITERATURE REVIEW	11
2.1 DEFINITION OF MIXING	11
2.2 MIXING CLASSIFICATION	12
2.3 LAMINAR MIXING	14
2.4 MICRO MIXING	17
2.5 MEASURES OF MIXING	18
2.6 STATIC MIXERS	23
2.7 SIMULATIONS OF STATIC MIXER VELOCITY FIELDS	24
2.8 TWIN SCREW EXPERIMENTAL RESULTS	31
2.9 TWIN SCREW MIXING SIMULATION	35
2.10 SUMMARY	39
3.0 EXPERIMENTAL PROCEDURE	41
3.1 GEOMETRY AND SPECIFICATIONS	41
3.1.1 Static Mixer	41
3.1.2 Intermeshing Co-Rotating Twin Screw Extruder	44
3.2 EQUIPMENT AND MATERIALS	50

3.3	EXPERIMENTAL TECHNIQUES	51
3.3.1	Flow Visualisation and Laser Induced Fluorescence (LIF).....	51
3.3.2	Image Analysis from LIF Visualisation.....	52
3.3.3	Laser Doppler Anemometry (LDA)	53
3.3.4	Particle Image Velocity (PIV)	58
3.3.5	Cross-Correlation, PIV	60
3.4	EXPERIMENTAL PROCEDURE STATIC MIXER	61
3.4.1	Flow Visualisation	61
3.4.2	LDA.....	62
3.4.3	PIV	63
3.5	EXPERIMENTAL PROCEDURE FOR TWIN SCREW EXTRUDER.....	64
3.5.1	Flow Visualisation.....	64
3.5.2	Image Analysis from LIF Visualisations	65
3.5.3	PIV	65
4.0	VALIDATION OF PIV TECHNIQUE.....	68
4.1	INTRODUCTION	68
4.2	BACKGROUND.....	69
4.2.1	PIV	70
4.2.2	Errors in PIV	71
4.3	EXPERIMENTAL DESIGN.....	73
4.3.1	Experimental Procedure and Set-up	73
4.3.2	PIV Procedure and Set-up	74
4.4	RESULTS	83
4.4.1	Influence of Separation Time Between Pulses	83
4.4.2	Interrogation Size	86
4.4.3	PIV and LDA Comparison	88
4.5	CONCLUSIONS.....	89
5.0	QUANTIFICATION OF LAMINAR MIXING IN THE KENICS KM[®] STATIC MIXER	93
5.1	INTRODUCTION	93
5.2	FLOW VISUALISATION	94
5.3	IMAGE ANALYSIS: MIXING QUANTIFICATION.....	97

5.4	EFFECT OF VISCOSITY ON MIXING	100
5.5	EFFECT OF ASPECT RATIO	105
5.6	SUMMARY.....	108
6.0	VELOCITY MEASUREMENTS IN THE KENICS KM[®] STATIC MIXER.....	110
6.1	INTRODUCTION	110
6.2	LDA MEASUREMENTS.....	110
6.3	PIV MEASUREMENTS	117
6.4	RATE OF DEFORMATION ANALYSIS	138
6.5	SUMMARY.....	146
7.0	FLOW AND MIXING IN THE TWIN SCREW EXTRUDER.....	150
7.1	INTRODUCTION	150
7.2	FLOW VISUALISATION	151
7.2.1	Geometry C	151
7.2.2	Geometry D	159
7.2.3	Colour Photography.....	164
7.3	IMAGE ANALYSIS.....	166
7.3.1	Intensity Measurements	166
7.3.2	Striation Measurements	174
7.4	PIV RESULTS.....	176
7.5	VALIDATION OF FINITE ELEMENT SIMULATION.....	186
7.5.1	Computer Simulation – Governing Equations.....	186
7.5.2	Boundary Conditions.....	187
7.5.3	Velocity Comparison.....	191
7.6	CHARACTERISATION OF DISC MIXING PERFORMANCE.....	204
7.7	SUMMARY.....	223
8.0	CONCLUSION AND RECOMMENDATIONS.....	227
8.1	STATIC MIXER	227
8.2	TWIN SCREW EXTRUDER	229
	REFERENCES	233

LIST OF TABLES

3.1.2.1. Technical data ZSK 30® extruder	45
3.1.2.2. Specifications of Screw Profiles (Figure 3.1.2.1.).	48
3.5.1.1. Flow Visualisation Experimental Conditions.	64
3.5.3.1 PIV Experimental conditions	67

LIST OF FIGURES

1.1.1. Static Mixer Configuration, 90° Twist Per Element.	3
1.1.2. Kenics KM® Static Mixer Configuration. (180° Twist Per Element, L/D=1.5, elements abut at 90°) [Dackson (1986)].	3
1.2.1. Cross Section Geometry of Two-tipped Kneading Discs. Nomenclature is Referenced in Section 2.2 and Table 3.1.2.1. [Bravo (1998)]	5
1.2.2. Classification of Twin Screw Extruders. [Cheremisinoff (1987)]	5
1.2.3. Acrylic Fully Inter-meshing Twin Screw Extruder, WP-ZSK 30®.	6
1.2.4. Acrylic Elements of a WP-ZSK 30® Twin Screw Extruder.	6
2.9.1. Schematic of Intermeshing Zone Highlighting the Axial and Transverse (Radial) Gaps Created Between Passing Discs.	39
3.1.1.1. Static Mixer Elements, Acrylic, Aspect Ratio of 1.5.	43
3.1.1.2. Axial Cross Section of Komax L/H® Series Distributor, $D_A/D_B=4$.	43
3.1.1.3. Flow Field Exiting Komax L/H® Distributor, A (Clear Oil), B (Dyed Oil)	44
3.1.2.1. Screw profiles for flow visualisations – a) Geometry C b) Geometry D.	47

3.1.2.2.	Geometry of the elements for the PIV experimental measurements.	49
a)	Geometry A - From left to right: 40 mm straight element, 20 mm, 45° stagger angle forward kneading block, 40 mm straight element;	
b)	Geometry B - From left to right: 20 mm forward conveying element, 20 mm, 45° stagger angle forward kneading block, 20 mm forward conveying element.	
3.2.1.	Laser Sheet Schematic.	50
3.3.3.1	Schematic of Laser Doppler Anemometry Apparatus [TSI (1998)].	57
3.3.3.2	Schematic of Frequency Shifting Technique for LDA [TSI (1998)].	57
3.3.4.1.	PIV image containing a Doubled Pulsed Image [Dantec (1998)].	59
3.3.4.2.	Principle of particle image velocimetry: cross correlation.	61
3.5.2.1.	Image Analysis, Intensity Measurements Location.	65
3.5.3.1.	Light Sheet Plane at $z=25$ mm.	66
3.5.3.2	View of Interrogation (Data) Mesh.	67
4.1.1.	Recirculation Cavity (units are meters) from Johnson (1995).	69
4.2.1.	Schematic of PIV set-up [Dantec (1998)].	71
4.3.1.1.	Recirculation Pumping Circuit.	74
4.3.2.1.	PIV Set-up Schematic.	75
4.3.2.2.	Interrogation of PIV Images, Interrogation Spot (grey) and Interrogation Mesh.	78
4.3.2.3.	Illustration of Pulse Delay for a Standard CCD Camera.	80
4.3.2.4.	Schematic of Correlation Plane [Dantec (1998)].	82

4.4.1.1. Influence of Time Separation of Laser Pulses, Wall Jet Core at $Y=60\text{mm}$	86
4.4.3.1. PIV and LDA Measurements at a Plane of $Y = 60\text{mm}$.	90
4.4.3.2. PIV and LDA Measurements at a Plane of $Y = 120\text{mm}$.	90
4.4.3.3. PIV and LDA Measurements at a Plane of $Y = 180\text{mm}$.	91
4.4.3.4. PIV and LDA Measurements at a Plane of $Y = 240\text{mm}$.	91
5.2.1. Lamellar Structure Created in the Kenics KM® Static Mixer, (courtesy of Chemineer, Dayton, Ohio.).	95
5.2.2. Flow Visualisation at $Re=43$ for $L/D=1.0$.	95
5.2.3. Flow Visualisation at $Re=97$ for $L/D=1.0$, a) Full Flow Field, b) Close-up of Element 1.	96
5.2.4. Flow Visualisation at $Re=125$ for $L/D=1.0$.	96
5.2.5. Onset of Vortex above Second Element.	97
5.3.1. Normalised Number Average Striation Widths for $L/D=1.0$.	99
5.3.2. Variance of Striation Widths for $L/D=1.0$.	100
5.4.1. Radial Cross Section Image Series for $\mu_{ratio} = 0.1$ and $Q_{ratio} = 0.2$.	102
5.4.2. Radial Cross Section Image Series for $\mu_{ratio} = 1$ and $Q_{ratio} = 0.25$.	103
5.4.3. Normalised Perimeter (Interfacial area) Growth for $L/D=1.5$.	104
5.4.4. Normalised Average Striation Widths for $L/D=1.5$.	104
5.4.5. Variance of Striation Widths for $L/D=1.5$.	105
5.5.1. Effect of Aspect Ratio on Striation Thickness.	107
5.5.1. Effect of Aspect Ratio on Variance of Striation Widths.	107
6.2.1. Definitions of co- ordinates for LDA measurements.	113

6.2.2.	Axial Velocity Profile at $Re=60$ at the End of the Splitter Plate.	114
6.2.3.	Axial Velocity Plot at the End of the Splitter Plate at $Re= 56$ and $z=0mm$	114
6.2.4.	Axial Velocity Profile at $y = 5mm$ at Junction of Splitter Plate and Element 1 at $Re = 57$.	115
6.2.5.	Axial Velocity Vector Plot for Element 1 at $Re = 53$ at $y = 10 mm$ and $x = 16 mm$.	115
6.2.6.	Axial Velocities for Element 1 at $Re = 6$ at $x = 16 mm$.	116
6.2.7.	Axial Velocity Vector Plot for Element 1, at $z = 0 mm$ and $Re = 60$.	116
6.3.1.	Contour Plots of y -component (v) (axial) of Velocity, Axial Cross Sections of Element 1, PIV Measurements at $Re=0.1$.	124
6.3.2.	Contour Plots of y -component (v) (axial) of Velocity, Axial Cross Sections of Element 1, PIV Measurements at $Re=0.1$.	125
6.3.3.	Contour Plots of y -component (v) (axial) of Velocity, Axial Cross Sections of Element 1, PIV Measurements at $Re=0.1$.	126
6.3.4.	Contour Plots of x -component (u) (radial) of Velocity, Axial Cross Sections of Element 1, PIV Measurements at $Re=0.1$.	127
6.3.5.	Contour Plots of x -component (u) (radial) of Velocity, Axial Cross Sections of Element 1, PIV Measurements at $Re=0.1$.	128
6.3.6.	Contour Plots of z -component (w) (radial) of Velocity, Axial Cross Sections of Element 1, PIV Measurements at $Re=0.1$.	129
6.3.7.	Contour Plots of y -component (v) (axial) of Velocity, Axial Cross Sections of Element 2, PIV Measurements at $Re=0.1$.	130

6.3.8.	Contour Plots of z-component (w) (radial) of Velocity, Axial Cross Sections of Element 2, PIV Measurements at $Re=0.1$.	131
6.3.9.	Contour Plots of y-component (v) (axial) of Velocity, Axial Cross Sections of Element 3, PIV Measurements at $Re=0.1$.	132
6.3.10.	Contour Plots of y-component (w) (radial) of Velocity, Axial Cross Sections of Element 3, PIV Measurements at $Re=0.1$.	133
6.3.11.	Contour Plots of y-component (v) (axial) of Velocity, Axial Cross Sections of Element 4, PIV Measurements at $Re=0.1$.	134
6.3.12.	Contour Plots of z-component (w) (radial) of Velocity, Axial Cross Sections of Element 4, PIV Measurements at $Re=0.1$.	135
6.3.13.	Contour Plots of x-component (u) (radial) of Velocity, Axial Cross Sections of Element 4, PIV Measurements at $Re=0.1$.	136
6.3.14.	Fluid Flow Simulation Results from Hobbs et al. (1998) for Aspect Ratio of 1.5, $Re=0.15$ and a twist of 180 degrees per element. (a) - (d): contours of the axial velocity component (v_x); (e) - (h): velocity vectors for radial components ($v_y + v_z$). Velocity Magnitude ($ v_y + v_z $) is colour coded. $X=0$ for (b,f); $X=L/8$ for (c,g); $X=L/2$ for (d,h); L = length of element. (Reprinted from CHEM. Eng. Sci., Vol 53, D.M. Hobbs, P.D. Swanson and F.J. Muzzio, 'Numerical Characterization of low reynolds number flow in the Kenics Static Mixer', pp. 1565-1598, Copyright 1998, with permission from Elsevier Science)	137
6.3.15.	Contour Plots of the Magnitude of the Rate of Strain Tensor, Axial Cross Sections of Element 1, PIV Measurements at $Re=0.1$.	141

6.3.16.	Contour Plots of the Magnitude of the Rate of Strain Tensor, Axial Cross Sections of Element 1, PIV Measurements at $Re=0.1$.	142
6.3.17.	Contour Plots of the Magnitude of the Rate of Strain Tensor, Axial Cross Sections of Element 4, PIV Measurements at $Re=0.1$.	143
6.3.18.	Contour Plots of the Magnitude of the Rate of Strain Tensor, Axial Cross Sections of Element 4, PIV Measurements at $Re=0.1$.	144
6.3.19.	Cross sectional profiles of the magnitude of the rate of strain tensor (ξ) for the mixer cross sections shown in Figure 6.3.14 from Hobbs et al. (1998). [(a): $X=0$; (b) $X=L/8$; (c): $X=L/4$; (d) $X=L/2$, where L = length of element] (Reprinted from CHEM. Eng. Sci., Vol 53, D.M. Hobbs, P.D. Swanson and F.J. Muzzio, 'Numerical Characterization of low reynolds number flow in the Kenics Static Mixer', pp. 1565-1598, Copyright 1998, with permission from Elsevier Science)	145
7.2.1.1.	Location: Right Screw Kneading Disc Section, 1 st and 2 nd set of Discs, ~1 to 2 Rotations (~1s) after Dye Injection, 100 rpm.	154
7.2.1.2.	Location: Right Screw Kneading Disc Section, 1 st set of Discs after ~10 Screw Rotations (~5-6s), 100 rpm.	154
7.2.1.3.	Location: Right Screw Kneading Disc Section, 2 nd set of Discs after ~10 Screw Rotations (~5-6s), 100 rpm.	154
7.2.1.4.	Location: Nip Region Kneading Disc Section, 1 st set of Discs after ~10 Screw Rotations (~5-6s), 100 rpm.	155

7.2.1.5. Location: Nip Region Kneading Disc Section, 2 nd set of Discs after ~10 Screw Rotations (~5-6s), 100 rpm.	155
7.2.1.6. Location: Left Disc Kneading Disc Section, 1 st set of Discs after ~5 Screw Rotations (~3s), 100 rpm.	156
7.2.1.7. Location: Left Disc Kneading Disc Section, 2 nd set of Discs after ~5 Screw Rotations (~3s), 100 rpm.	156
7.2.1.8. Location: Right Screw Kneading Disc Section, 1 st set of Discs after ~5 to 6 Rotations after Dye Injection (~3s), 150 rpm.	156
7.2.1.9. Location: Nip Region Kneading Disc Section, 1 st set of Discs, ~5 to 6 Rotations after Dye Injection (~3s), 150 rpm.	157
7.2.1.10. Location: Left Screw Kneading Disc Section, 1 st set of Discs, ~1 to 2 Rotations after Dye Injection.	157
7.2.1.11. Location: Right Screw Kneading Disc Section, 1 st set of Discs, ~5 to 6 Rotations after Dye Injection (~2s), 200 rpm.	157
7.2.1.12. Location: Right Screw Kneading Disc Section, 1 st and 2 nd set of Discs, ~10 to 12 Rotations after Dye Injection (~3-4s), 200 rpm.	158
7.2.1.13. Location: Left Screw Kneading Disc Section, 2 nd set of Discs, ~5 to 6 Rotations after Dye Injection (~2s), 200 rpm.	158
7.2.1.14. Location: Left Screw Kneading Disc Section, 1 st and 2 nd set of Discs, ~10 to 12 Rotations after Dye Injection (~3-4s), 200 rpm.	158
7.2.2.1. Location: Right Screw Kneading Disc Section, 1 st set of Discs, ~5 Seconds after Dye Injection, 100 rpm.	160

7.2.2.2. Location: Right Screw Kneading Disc Section, 1 st set of Discs, ~10 Seconds after Dye Injection, 100 rpm.	160
7.2.2.3. Location: Right Screw Kneading Disc Section, 1 st set of Discs, ~15 Seconds after Dye Injection, 100 rpm.	160
7.2.2.4. Location: Right Screw Kneading Disc Section, 2 nd set of Discs, ~5 Seconds after Dye Injection, 100 rpm.	161
7.2.2.5. Location: Right Screw Kneading Disc Section, 2 nd set of Discs, ~10 Seconds after Dye Injection, 100 rpm.	161
7.2.2.6. Location: Right Screw Kneading Disc Section, 2 nd set of Discs, ~15 Seconds after Dye Injection, 100 rpm.	161
7.2.2.7. Location: Right Screw Kneading Disc Section, 1 st set of Discs, ~5 Seconds after Dye Injection, 150 rpm.	162
7.2.2.8. Location: Right Screw Kneading Disc Section, 2 nd set of Discs, ~5 Seconds after Dye Injection, 150 rpm.	162
7.2.2.9. Location: Right Screw Kneading Disc Section, 1 st set of Discs, ~5 Seconds after Dye Injection, 200 rpm.	163
7.2.2.10. Location: Right Screw Kneading Disc Section, 2 nd set of Discs, ~5 Seconds after Dye Injection, 200 rpm. A folded striation is outlined by the box.	163
7.2.3.1. Left Screw Visualisation at 30 rpm and 10 mL/s (Clear) and 1 mL/s (Dye).	165
7.2.3.2. Nip Region Visualisation at 30 rpm and 10mL/s (Clear) and 1mL/s (Dye).	165

7.2.3.3. Left Screw Visualisation at 60 rpm and 10mL/s (Clear) and and 1mL/s (Dye).	165
7.3.1.1. Intensity Plots for Right Screw, 150 rpm, 5 mL/s (Clear), 2 Second Pulse of Dye, Configurations C and D, 5 Seconds After Pulse.	168
7.3.1.2. Intensity Plots for Right Screw, 150 rpm, 5 mL/s (Clear), 2 Second Pulse of Dye, Configurations C and D, 10 Seconds After Pulse.	168
7.3.1.3. Intensity Plots for Right Screw, 150 rpm, 5 mL/s (Clear), 2 Second Pulse of Dye, Configurations C and D, 15 Seconds After Pulse.	169
7.3.1.4. Intensity Plots for Right Screw, 150 rpm, 5 mL/s (Clear), 2 Second Pulse of Dye, Configurations C, Progression of Tracer Pulse.	169
7.3.1.5. Intensity Plots for Right Screw, 150 rpm, 5 mL/s (Clear), 2 Second Pulse of Dye, Configuration D, Progression of Tracer Pulse.	170
7.3.1.6. Intensity Plots for Right Screw, 5 mL/s (Clear), 2 Second Pulse of Dye, Configuration D, Influence of rpm 5 Seconds After Pulse.	170
7.3.1.7. Intensity Plots for Right Screw, 5 mL/s (Clear), 2 Second Pulse of Dye, Configuration D, Influence of rpm, 15 Seconds After Pulse.	171
7.3.1.8. Variance of Intensities versus time for Geometry D.	172
7.3.1.9. Variance of Intensities versus Time for 150 rpm for Geometries C and D.	172
7.3.1.10. Average Intensity versus Time, Geometry D.	173
7.3.1.11. Average Intensity versus Time, 150 rpm, 5 mL/s.	173
7.3.2.1. Normalised Striation Thickness versus Axial Distance, 5 Seconds After Pulse, 5 mL/s, 150 rpm.	175

7.3.2.2.	Normalised Striation Thickness versus Axial Distance, 5 Seconds	175
	After Pulse, 5 mL/s, Geometry D.	
7.4.1.	Velocity Vectors, Q=2.5 mL/s, 30 rpm. Geometry A.	178
7.4.2.	Velocity Vectors, Q=5.0 mL/s, 60 rpm. Geometry A.	178
7.4.3.	Velocity Vectors, Q=5.0 mL/s, 60 rpm, z=20mm. Geometry A.	179
7.4.4.	Velocity Vectors, Q=5.0 mL/s, 60 rpm, z=15mm. Geometry A.	179
7.4.5.	Velocity vectors for Q=5.0 mL/s and 100 rpm. Geometry A.	180
7.4.6.	Velocity Vectors for Q=5.0 mL/s and 150 rpm. Geometry A	182
7.4.7.	Velocity vectors, Q=8.5 mL/s, 60 rpm. Geometry A.	183
7.4.8.	Velocity vectors, Q=2.5 mL/s, 60 rpm. Geometry B.	183
7.4.9	Velocity vectors, Q=5.0 mL/s, 60 rpm, z=15 mm. Geometry B.	184
7.4.10	Velocity vectors, Q=8.5 mL/s, 60 rpm. Geometry B.	184
7.4.11	Velocity vectors, Q=5.0 mL/s, 100 rpm. Geometry B.	185
7.4.12	Velocity vectors, Q=8.5 mL/s, 100 rpm. Geometry B.	185
7.5.2.1.	Kneading disc configuration and location of inlet/outlet boundary conditions. a) Inlet and outlet boundary condition at the ends of the kneading blocks; b) Inlet and outlet boundary condition at the ends of long elements. [Bravo (1998)]	190
7.5.3.1.	Contours of the x-component of velocity. Left screw, 60 rpm, 5 mL/s. Long straight elements are deployed before and after the kneading blocks. a) Experimental b) Simulation	192

- 7.5.3.2. Contours of the x -component of velocity. Right screw, 60 rpm, 5 mL/s. 193
Long straight elements are deployed before and after the kneading blocks. a) Experimental b) Simulation
- 7.5.3.3. Contours of the y -component of velocity. Left screw, 60 rpm, 5 mL/s. 195
Long straight elements are deployed before and after the kneading blocks. a) Experimental b) Simulation
- 7.5.3.4. Contours of the y -component of velocity. Right screw, 60 rpm, 5 mL/s. 196
Long straight elements are deployed before and after the kneading blocks. a) Experimental b) Simulation
- 7.5.3.5. Comparison between simulation and experimental u and v components 199
of velocity at $x = 2.836$ mm. Left screw, 60 rpm, 5 mL/s. Long straight elements are deployed before and after the kneading blocks.
- 7.5.3.6. Comparison between simulation and experimental u and v components 199
of velocity at $x = 2.836$ mm. Left screw, 60 rpm, 5 mL/s. Conveying elements are deployed before and after the kneading blocks.
- 7.5.3.7. Contours of the x -component of velocity. Left screw, 60 rpm, 200
8.5 mL/s. Conveying elements deployed before and after the kneading blocks. a) Experimental b) Simulation.
- 7.5.3.8. Contours of the x -component of velocity. Right screw, 60 rpm, 201
8.5 mL/s. Conveying elements deployed before and after the kneading blocks. a) Experimental b) Simulation.

7.5.3.9.	Contours of the y -component of velocity. Left screw, 60 rpm, 8.5 mL/s. Conveying elements deployed before and after the kneading blocks. a) Experimental b) Simulation.	202
7.5.3.10.	Contours of the y -component of velocity. Right screw, 60 rpm, 8.5 mL/s. Conveying elements are deployed before and after the kneading blocks. a) Experimental b) Simulation.	203
7.5.3.11.	Comparison between simulation and experimental u and v components of velocity at $x = 2.836$ mm. Left screw, 60 rpm, 8.5 mL/s. Conveying elements are deployed before and after the kneading blocks for the experimental runs.	204
7.6.1.	Contour Plots at 60 rpm and 5 mL/s, Extended First and Last Discs (Geometry A), a) Total Absolute Shear, b) Total Elongation and c) Second Invariant.	208
7.6.2.	Contour Plots at 100 rpm and 5 mL/s, Extended First and Last Discs (Geometry A), a) Total Absolute Shear, b) Total Elongation and c) Second Invariant.	208
7.6.3.	Contour Plots at 150 rpm and 5 mL/s, Extended First and Last Discs (Geometry A), a) Total Absolute Shear, b) Total Elongation and c) Second Invariant.	209
7.6.4.	Contour Plots at 60 rpm and 5 mL/s, Conveying Elements Before and After (Geometry B), a) Total Absolute Shear, b) Total Elongation and c) Second Invariant.	209

7.6.5.	Contour Plots at 100 rpm and 5 mL/s, Conveying Elements Before and After (Geometry B), a) Total Absolute Shear, b) Total Elongation and c) Second Invariant.	210
7.6.6.	Contour Plots at 100 rpm and 8.5 mL/s, Conveying Elements Before and After (Geometry B), a) Total Absolute Shear, b) Total Elongation and c) Second Invariant.	210
7.6.7.	a) Total Elongation b) Second Invariant as a Function of y Co-ordinate at Different Axial Positions (x) on the Left Screw for the KB/45/20 Kneading Discs at 60 rpm and 5 mL/s (Geometry A).	215
7.6.8.	a) Total Elongation b) Second Invariant as a Function of y Co-ordinate at Different Axial Positions (x) on the Left Screw for the KB/45/20 Kneading Discs at 100 rpm and 5 mL/s (Geometry A).	216
7.6.9.	a) Total Elongation b) Second Invariant as a Function of y Co-ordinate at Different Axial Positions (x) on the Left Screw for the KB/45/20 Kneading Discs at 150 rpm and 5 mL/s (Geometry A).	217
7.6.10.	a) Total Elongation b) Second Invariant as a Function of y Co-ordinate at Different Axial Positions (x) on the Left Screw for the KB/45/20 Kneading Discs at 150 rpm and 5 mL/s (Geometry A).	218
7.6.11.	a) Total Elongation b) Second Invariant as a Function of y Co-ordinate Varying Flow Rate at the 1 st Disc on the Right Screw for the KB/45/20 Kneading Discs at 150 rpm and 5 mL/s (Geometry A).	219

- 7.6.12. a) Total Elongation b) Second Invariant as a Function of y Co-ordinate 220
Varying Rotation Speed (rpm) at the 1st Disc on the Right Screw for the
KB/45/20 Kneading Discs at 150 rpm and 5 mL/s (Geometry A).
- 7.6.13. a) Total Elongation b) Second Invariant as a Function of y Co-ordinate 221
at Different Axial Positions (x) on the Left Screw for the KB/45/20
Kneading Discs at 60 rpm and 5 mL/s (Geometry B).
- 7.6.14. a) Total Elongation b) Second Invariant as a Function of y Co-ordinate 222
at Different Axial Positions (x) on the Left Screw for the KB/45/20
Kneading Discs at 100 rpm and 5 mL/s (Geometry B).

LIST OF SYMBOLS

B	Clearance disc-barrel, mm
C	Mean number of particles per cell
C_i	Number of particles per cell
C_L	Centre to centre distance of screws, mm
D	Diameter, mm
D_A/D_B	Ratio of diameters (clear A to dyed B fluid entrance diameters)
D_b	Barrel bore diameter, mm
D_i	Screw root diameter, mm
D_o	Screw outside diameter, mm
D	Rate of deformation tensor, s ⁻¹
<i>e</i>	Efficiency of mixing
E_o	Mixing efficiency
<i>f_d</i>	Frequency obtained at light detector, Hz
G	Clearance between discs, mm
l/l_o	Material line stretch
L_B	laser beam separation distance, mm
L/D	Aspect ratio: length of element/ diameter of tube
M	Magnification, m

n	Number of striations
n_d	Refraction index
P	Pressure, Pa
Q	Volumetric flow rate, mL/s
r	Cylindrical co-ordinates, mm
Re	Reynolds number
Re_{crit}	Critical Reynolds number
s^2	Variance of striation widths, pixels
s^2/w_{avg}	Normalised variance of striation widths
S_{number}	Number of striations
t	time, s
u	Axial velocity, m/s
\mathbf{u}	Velocity vector, m/s
U	Total average superficial velocity, m/s
v	Velocity component in the y- co-ordinate direction, m/s
w	Velocity component in the z- co-ordinate direction, m/s
w_{avg}	Average striation thickness, m
w_i	Striation width of striation i, m
\mathbf{W}	Vorticity tensor
x	Cartesian Co-ordinate, mm
y	Cartesian Co-ordinate, mm

z Cartesian Co-ordinate, mm

Greek characters

α Angle between laser beams

ε Viscous dissipation per unit volume per unit time, W/m³

$\dot{\gamma}, \xi$ Magnitude of the rate of deformation tensor (second invariant), s⁻¹

η Area stretch, m²; Generalised Newtonian viscosity, Pa·s

λ Length stretch, m

λ_M Degree of elongational flow

μ Newtonian fluid viscosity, Pa·s

μ_0 Zero –shear viscosity, Pa·s

μ_{ratio} Ratio of dyed to clear fluid viscosities

ρ Fluid density, kg/m³

σ Variation coefficient across radial cross sections

σ_{xx} Normal stress difference, Pa

τ Stress tensor, Pa

ω Magnitude of vorticity tensor, s⁻¹

θ Cylindrical co-ordinate, radians

Δp Pressure drop, Pa

Δp_{cp} Pressure drop for circular empty tube, Pa

Δt Pulse Separation Time, s

Δx Displacement, m

Superscripts.

i Counter

int Interrogation

j Counter

T Transpose

' Dimensional variable (x' , τ' , μ' , u' , P')

Subscripts.

b Barrel bore

w Wall value

Abbreviations

CFD Computational fluid dynamics

CFM Computational fluid mixing

FFT Fast Fourier transform

ICRTSE Intermeshing co-rotating twin screw extruder

KB Kneading Block

LDA Laser Doppler anemometry

LH	Left handed (reverse conveying elements)
LIF	Laser induced fluorescence
LS	Left side screw
NICNRTSE	Non intermeshing counter-rotating twin screw extruder
PE	Polyethylene
PIV	Particle image velocimetry
PMT	Photomultiplier
PS	Polystyrene
RIM	Reaction injection moulding
rms	Root mean square
RS	Right Side Screw
RTD	Residence time distribution
TE	Total elongation
TS	Total absolute shear
TSE	Twin screw extruder; ICRTSE
SDF	Strain distribution functions
WATS	Weighted average total strain

Units of measurement

Hz	Hertz
L	Litre

m	Meter
P	Poises
Pa·s	Pascal seconds
rpm, RPM	Revolutions per minute, 1/min
s, S	Second
Wt%	Percent by weight
W	Watts

1.0. Introduction

Mixing is an operation in industry that has proven to be an extremely formidable task, since in North America alone, an estimated 1 to 20 billion dollars in losses is directly associated to poor mixing every year [Tatterson et al. (1991)]. Even though mixing operations are widely used in the process industries, the fundamentals are not fully understood. As a consequence, mixing quality is dependent on the experience of engineers and operators rather than being soundly based on the physical sciences. Research on mixing in the past focused on the correlation of operating parameters, such as pressure drop or power consumption, to final mix quality. The solution to mixing problems has usually been to increase the energy input to the mixer but this has resulted in higher costs and little change in quality of mixing. Therefore, research on mixing and its relation to the underlying fluid mechanics is required to further our understanding of this daily process operation. With a better understanding of the mixing mechanisms and flow field, energy consumption could be reduced and mixing efficiency increased.

In order to assess the performance of a mixer, some measure of the degree of mixing or mix quality is required. That is, what do we mean when we say that something is well mixed or poorly mixed? This has been one of the stumbling blocks in mixing research. As a result, determining the effect of a parameter, such as geometry, is difficult to quantify in terms of mixing. The difficulty with mixing theory is that it is complex and

numerically challenging to solve and implement. There are a number of research groups that are using computational fluid dynamics (CFD) and computational fluid mixing (CFM) to try and obtain information on mixing. However, there are very few experimental results to verify CFD simulations against, let alone mixing experiments for CFM results to compare with. In this thesis, experimental measurements of the velocity fields and the mixing in models of the Kenics KM[®] static mixer and the Werner & Pfleiderer ZSK-30[®] fully intermeshing co-rotating twin screw extruder have been conducted.

1.1. Static Mixers

Static (also known as motionless or in-line) mixers have found a large range of applications, including blending, reaction, dispersion, heat transfer and mass transfer and are used for both laminar and turbulent mixing. They create a higher degree of turbulence compared to an empty pipe, resulting in a higher degree of mixing. Laminar mixing is achieved by a combination of flow division, flow re-orientation and shear fields. The main trade-off for obtaining more efficient mixing is the pressure loss across the mixer. The greatest asset of motionless mixers is that if a process requires mixing, static mixers are easily integrated into the process at a very low cost.

Although the design of in-line mixers is very sophisticated today, these mixers are simply a series of stationary, flow directing elements or baffles in a pipeline. There are thousands of different elements that can be placed in pipelines but for the purpose of keeping this research focused on the fundamentals of mixing, the elements or inserts

chosen for study are twisted tape inserts as these are by far the most common in North America. They are similar to those used by Chemineer in the Kenics KM[®] mixer with aspect ratios (Length of element/ Diameter of tube, L/D) of 0.8, 1.0 and 1.5 and a twist of 90 degrees per element (Figure 1.1.1) compared to L/D of 1.5 and 180 degrees twist for the Kenics KM[®] elements (Figure 1.1.2).

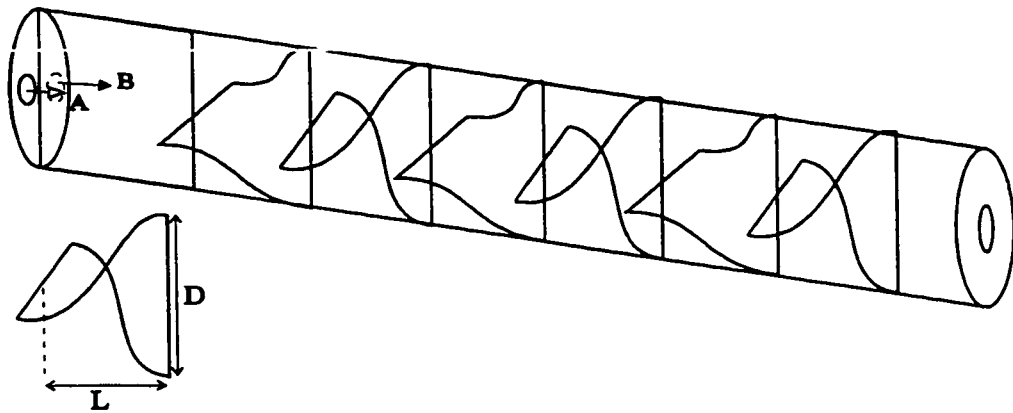


Figure 1.1.1. - Static Mixer Configuration, 90° Twist Per Element.

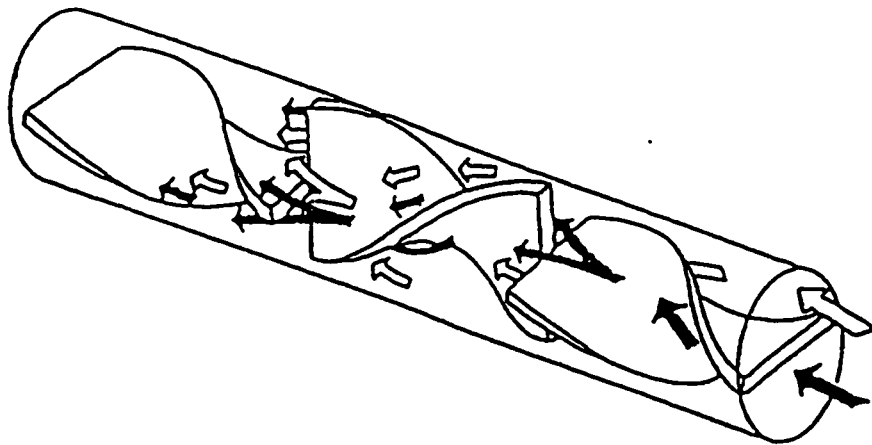


Figure 1.1.2. - Kenics KM[®] Static Mixer Configuration, (180° Twist Per Element, $L/D=1.5$, elements abut at 90°) [Dackson (1986)].

1.2. Twin Screw Extruders (TSE)

A twin screw extruder is simply two extruders side by side forming a figure eight cross-sectional view (Figure 1.2.1). However, there are numerous twin screw extruder configurations, each having their own mixing behaviour. These devices are used to melt and convey material, mix materials and create high pressures for extrusion. The TSE may be classified according to two criteria: firstly, whether the two screws are co-rotating or counter-rotating, and secondly, by the degree of intermeshing of the screw flights. They can be fully or partially intermeshing or non-intermeshing. Examples of different types of twin screw extruders are shown in Figure 1.2.2.

This thesis will focus on the fully intermeshed co-rotating TSE (ICRTSE), primarily studying the kneading discs. A fully acrylic TSE was fabricated to facilitate these studies (Figure 1.2.3). The acrylic elements placed on the shafts of the extruder are shown in Figure 1.2.4. From left to right, the first set of conveying elements is used to build up pressure and the degree of fill in the kneading disc section. In the melting zone of an extruder, the conveying elements would drag the solid pellets of polymer forward to the kneading discs. In the melt mixing zone, these elements convey melted polymer to the kneading discs. The kneading discs are used to create high shear and deformation for the purposes of compounding, melting, dispersion and convective mixing. Typically this section has many more sets of kneading discs than shown. The reverse conveying elements placed on the end of the kneading discs create backpressure, back mixing and maintain a fully filled kneading or mixing zone.

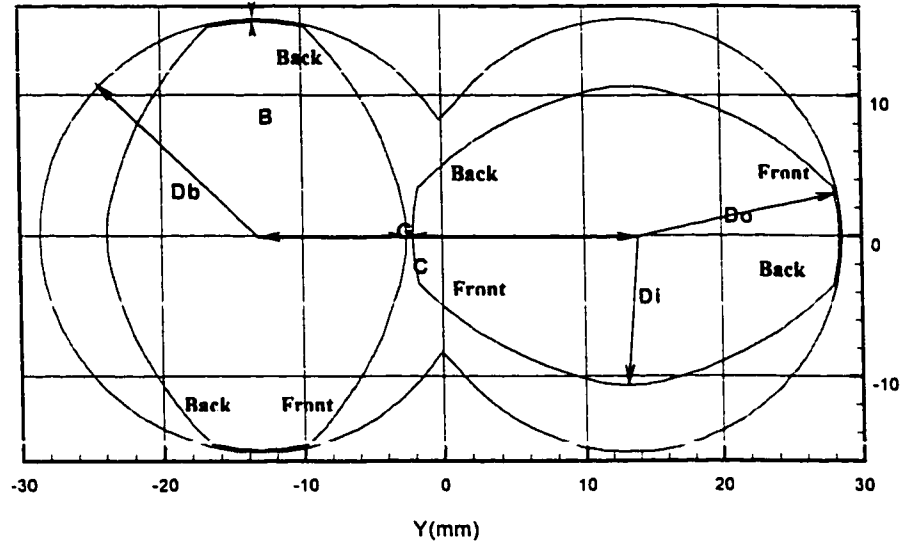


Figure 1.2.1. - Cross section geometry of two-tipped kneading discs. Nomenclature is referenced in Section 2.2 and Table 3.1.2.1. [Bravo (1998)].

SCREW ENGAGEMENT		SYSTEM	COUNTER-ROTATING	CO-ROTATING
INTERMESHING	FULLY INTERMESHING	LENGTHWISE AND CROSSWISE CLOSED	1	2 THEORETICALLY NOT POSSIBLE
		LENGTHWISE OPEN AND CROSSWISE CLOSED	3 THEORETICALLY NOT POSSIBLE	4
		LENGTHWISE AND CROSSWISE OPEN	5 THEORETICALLY POSSIBLE BUT PRACTICALLY NOT REALIZED	6
	PARTIALLY INTERMESHING	LENGTHWISE OPEN AND CROSSWISE CLOSED	7	8 THEORETICALLY NOT POSSIBLE
		LENGTHWISE AND CROSSWISE OPEN	9A	10A
			9B	10B
	NOT INTERMESHING	NOT INTERMESHING	11	12

Figure 1.2.2. - Classification of Twin Screw Extruders [Cheremisinoff (1987)].

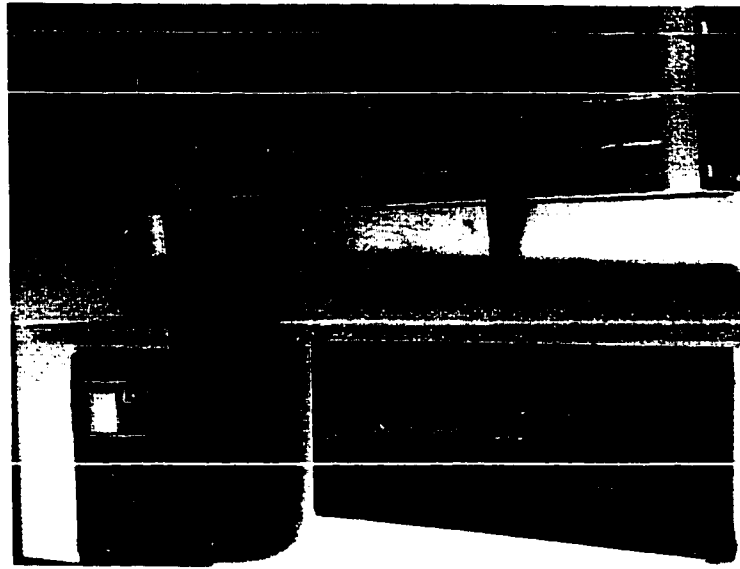


Figure 1.2.3. - Acrylic Fully Inter-meshing Twin Screw Extruder, WP-ZSK 30®.

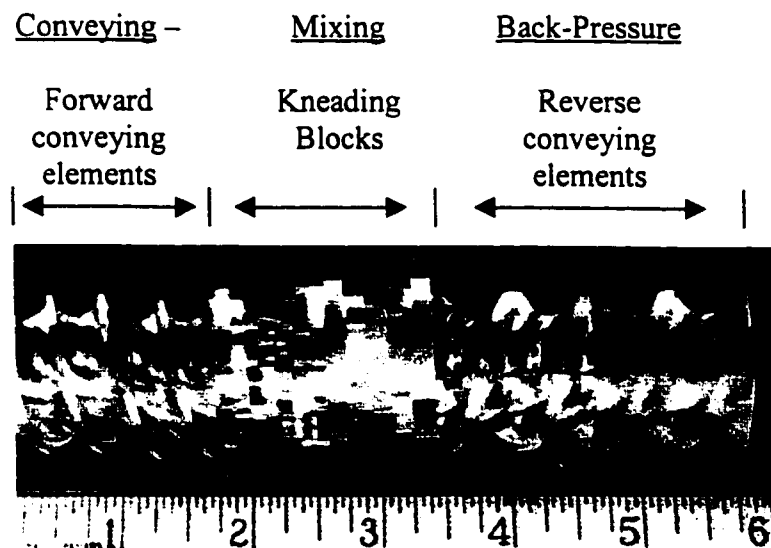


Figure 1.2.4. - Acrylic Elements of a WP-ZSK 30® Twin Screw Extruder.

A detailed discussion of previous studies of the ICRTSE will be presented in chapter 2. Generally, these studies have focused on residence time distributions (RTD) as a measure of mixing quality or strain histories. Recent studies have identified that mixing seems to be of a two dimensional nature in the conveying elements and three dimensional where there are kneading elements present.

1.3. Scope of Project

This project studied single phase, liquid-liquid mixing in static mixers and intermeshing co-rotating twin screw extruders (ICRTSE), specifically oriented towards the polymer processing industry (viscous mixing).

Static mixers are heavily used in the chemical processing industry since they can mix viscous liquids at a low energy cost. However, these mixers are not fully understood fundamentally and as a result, their designs have been almost an art rather than a science. Furthermore, the selection of the proper mixer for a specific application has also been a process of trial and error. The simplicity of the design of motionless mixers makes them ideal for studying the fundamentals of convective mixing.

Twin screw extruders (TSE) are used extensively in the plastics industry for conveying as well as mixing solids and very viscous materials (e.g. polymeric liquids). The mixing in these extruders has been studied via numerical simulations and some preliminary visualisation studies. However, a detailed experimental study of the flow patterns and the nature of the mixing present in an ICRTSE, has not been published. The TSE is similar in many respects to a static mixer when one looks at the kneading section

of these extruders. The difference is that in static mixers the elements are stationary and the mixing energy is obtained from the flowing liquid where as in the TSE, energy is delivered to the liquid through the rotating screws of the extruder which creates the pumping and mixing action. Hence, the fundamental mixing mechanisms in both these mixing devices are still the 'baker's transformation' that is, the stretching, folding and division of fluid elements. In laminar convective mixing, this transformation creates lamella or what are also called striations. These striations help characterise and quantify the degree of mixing. Typically, the objective of the mixer is to stretch and thin the striations as well as to divide and increase the number of striations.

The objectives of this research were to study viscous mixing in static mixers and the ICRTSE with a view to:

- 1) examine fundamentals of convective mixing via the laser induced fluorescence (LIF) flow visualisation technique,
- 2) quantify mixing with existing mixing measures using image analysis coupled with flow visualisation;
- 3) measure fluid velocities via laser Doppler anemometry (LDA) and particle image velocimetry (PIV).

LIF allows flow visualisation in real time using video and still photographs. Mixing fundamentals such as flow division, flow reorientation, shear and elongation can be observed qualitatively and then quantified with the aid of image analysis software. Striation thickness and interfacial area are measurable from the resulting digitized images allowing for the comparison of the various mixing measures. Laser Doppler anemometry

and particle image velocimetry permit measurement of the entire velocity field, and hence, rates of deformation (and consequently, local viscous dissipation rate as a mixing measure). The above velocity fields can give invaluable insight to mathematical models.

The final and most important goal is to relate the fluid mechanics and physics of mixing with the mixing measures to obtain design criteria for mixers and identify parameters that govern the efficiency of mixing. These parameters are geometry, Reynolds number, helix angle, aspect ratio, rpm, flow rate, viscosity ratio, flow rate ratio, interface orientation, etc.

1.4. Thesis Organisation

Chapter 2 covers the background and previous work from the areas of mixing fundamentals, laminar mixing, mixing measures, static mixers and twin screw extruders. The chapter briefly covers the areas of computational simulations of twin screw extruders and static mixers. There has been numerous works in these areas but very little published experimental validation of these results. This has proven to be the largest obstacle for mathematical models and for confidence in their results.

Chapter 3 discusses the experimental techniques of laser Doppler anemometry (LDA), laser induced fluorescence (LIF) and particle image velocimetry (PIV). The experimental procedure, equipment details and geometry specifications are also given. Further discussion of PIV in greater depth is covered in chapter 4. The difficulty with the implementation of PIV was to learn its strengths and limitations before it was applied for use on the static mixer and TSE flow studies and mixing characterisation.

Chapter 5 presents results from laser induced fluorescence and image analysis applied to the static mixer. The effect of aspect ratio, viscosity ratio and Reynolds number on mixing, based on the measures of number average striation thickness, variance of striation thickness and interfacial area, is discussed.

Chapter 6 shows the LDA and PIV results for the static mixer. The analysis of these results for the magnitude of the rate of deformation, shear rate and elongation rates is also presented.

Chapter 7 presents the results from flow visualisation studies and PIV measurements on the fully intermeshing co-rotating twin screw extruder kneading disc section. This chapter briefly discusses the simulation of the kneading disc section of a co-worker [Bravo (1998)] and compares his simulation results with the experimental velocity measurements obtained in the present study.

Chapter 8 summarises the conclusions.

2.0. Literature Review

2.1. Definition of Mixing

Mixing of two or more species is achieved through the physical movement of fluid elements to form a mixture. These fluids are mixed until a criterion for the 'mixedness' of the mixture is satisfied. These criteria, or measures of mixing, are discussed in section 2.5. The physical process of mixing fluid elements can be accomplished by three means as described by Brodkey (1966): bulk diffusion (convective flow), eddy diffusion and molecular diffusion.

Molecular diffusion is a spontaneous process that occurs due to a concentration gradient. This motion is the predominant mechanism by which gases are mixed. Molecular diffusion is present continuously while fluids are being mixed but may occur over time scales much larger than the mixing times of processes driven by bulk or eddy diffusion. Therefore, mixing requires bulk and eddy diffusion for systems where molecular diffusion is slow.

Turbulent mixing is created by fluid elements being convected by random eddy motion, termed eddy diffusion by Brodkey (1966). This motion may occur within a large scale convective flow and will have molecular diffusion super-imposed on it. Turbulent mixing is prevalent in gas and low viscosity liquid flows.

Three mechanisms form the basis of laminar and turbulent mixing of fluid elements. A material volume can be stretched, folded and divided. In laminar convective

mixing, with negligible diffusion and interfacial tensions, these three processes create a well-defined lamellar structure or striations within mixtures. Diffusion causes these interfaces to become blurred resulting in 'grey area'¹.

Convective mixing can be classified as either laminar or distributive mixing. Laminar convective mixing occurs in a variety of flow fields: shear, elongation and squeezing (kneading). Distributive mixing or repetitive mixing is the continuous rearrangement of fluid elements through flow division and re-orientation either random or ordered. Many convective mixers, such as motionless mixers, have both laminar and distributive mixing. Laminar mixing is prevalent in liquid-liquid and solid-liquid systems, and is usually associated with high viscosities and non-Newtonian fluids.

2.2. Mixing Classification

In order to determine the mixing mechanisms and the characteristics of mixing, the physical process needs to be classified. Firstly, mixing is classified according to the phases present (solid, liquid and gas) that are to be mixed. Many combinations of phases for two or more components are possible such as solid-liquid, liquid-liquid, etc.

The second classification is based on the nature of the mixing device, and hence the mixing mechanisms present. There are two general types of mixer: static or dynamic. Dynamic mixers have moving parts and require energy input to mix fluids while static mixers use the energy of the entering fluids to generate mixing since there are no moving

¹ 'Grey area' refers to a mixture created between two species which are identified by the color black and white. Note with no diffusion there would be only black and white species in a lamellar structure.

parts. Even though both of these mixer types are governed by the same principles, they behave very differently and have been researched independently.

The third classification for mixing is based on the flow field in the mixer. This can usually be characterised as either laminar or turbulent. The main difference between laminar and turbulent mixing is the method by which fluid elements are rearranged and convected. Therefore, these two divisions must be considered separately and researched with different experimental techniques.

The nature of the flow in the mixer is typically classified by the ratio of the fluids inertia forces to the viscous forces. This quantity is the Reynolds number, Re , where

$$Re = \frac{\rho u d}{\mu}$$

The average velocity of the flow is typically used for u , the fluid density, ρ , the fluid viscosity, μ , and the characteristic length of the mixer, d . The characteristic length for static mixers is usually the diameter of the tube. For the twin screw, it is difficult to state a characteristic length. From Figure 1.2.1., the barrel diameter, D_b , the channel depth, $(D_b - D_i)$ or even the flight clearance, $(D_b - D_o)$ may be used, depending on the area of interest. Therefore, the notion of trying to state a single Reynolds number for the TSE may not be very useful.

2.3. Laminar Mixing

In the polymer processing field, the predominant mixing mechanism is convection. Since polymeric flows are typically laminar (because of the very high viscosity), convective mixing is achieved by imposing deformation on the system. This occurs in a variety of flow fields: shear, elongation (stretching) or squeezing.

A paper by Spencer and Wiley (1951) is one of the earliest works on identifying mixing mechanisms. The first major result was the identification of stretching, division and folding as the primary mixing mechanisms for convective flow fields. The concept of distributive mixing was described as a necessity for efficient mixing. Secondly, they presented the idea of representing these mixing mechanisms in terms of matrix transformations. Their most important result was the idea of using interfacial area, which is defined as the surface area generated between mixing species at their interface, as a measure to quantify mixing. More importantly they identified that initial orientation of the material to be blended was crucial to the final mix quality. For very small increases in surface area, the optimum angle of the surface for minimum shear is 45° to the displacement vectors. Large surface area increases require the undeformed surface to cut perpendicularly across the displacement vectors for minimum shear. They concluded from their results that mixing was achieved when interfacial area between the fluids was increased and subsequently distributed throughout the volume at the same time. This description of mixing introduced the concepts of elongation, division and folding of flow as mixing mechanisms in addition to shear.

The work by Mohr et al. (1957), attempted to calculate the final striation thickness based on the initial thickness and total strain experienced by the fluid elements. They derived mathematical models based on a viscosity ratio of one and negligible surface tension for the two streams being mixed. Their results assumed that the initial orientation of the surface was not significant in determining final striation thickness. This condition can be assumed for very few flow fields where the effect of initial surface orientation becomes negligible very quickly, but for many geometries such as an extruder it has been shown that the initial orientation is very important [Ottino and Chella (1983)]. Even though their results were incorrect, their initial proposal of relating striation thickness to total strain caused future research to quantify mixing based on striation thickness, average strain, strain distribution functions (SDF) and weighted average total strain (WATS).

An important paper by Cooper (1966) addressed many mixing fundamentals continuing on the work by Mohr et al. (1957) and Spencer and Wiley (1951). He focused on the attenuation of heterogeneities that had directionality, and this became fundamental to understanding how various deformation fields would affect orientation of a surface or interface. The discussion focused primarily on lamellar structures or striations and their attenuation due to shear, streamlines (elongation), and rotation. These results determined the optimum orientation of a surface to be mixed for the various deformations. Critical results to fundamentals of mixing were:

- 1) orientation of striations or lamella structure is very important and can result in a decrease, increase or no change in striation thickness or interfacial area;

- 2) striations and interfaces should be aligned with streamlines when the primary mixing mechanism is elongation;
- 3) rotational fields require that the orientation of the striations to be aligned with streamlines, whereas shear fields require striations to be orthogonal to the stream lines for maximum attenuation; this implies a trade off for the orientation of the interface when rotation and shear are present,
- 4) the efficiency of the shear and rotation field diminish rapidly as striations progress through the flow field; as a result, fluid elements require rearrangement (folding, division of flow) to increase the attenuation of heterogeneities.

The three papers discussed above developed the fundamentals of laminar mixing. However, not many advances in the application of these fundamentals followed. Primarily, work centred on the use of strain measures to quantify mixing [Pinto and Tadmor (1970), McKelvey (1962), Lidor and Tadmor (1976)].

Ranz (1979) applied laminar mixing fundamentals in an attempt to describe and predict mixing using the concept of lamella or material surfaces. This work was followed up by Ottino et al. (1979) who applied these ideas to liquid-liquid mixing. These papers were very critical in refocusing the mixing theories to be related to fluid mechanics rather than statistical theory. Both Ranz (1979) and Ottino et al. (1979) focused on using the rate of deformation tensor to predict the stretching of lamellar structures and the effect of this stretching on mixing. These papers led to definitions of mixing parameters or measures of mixing efficiency derived from fluid mechanics. A description of these measures follows.

2.4. Micro Mixing

Danckwerts' (1957) work was one of the earliest papers to quantify mixing on a molecular (micro-mixing) scale, and became the foundation for many researchers thereafter. His idea of utilising controlled reactions to attain information on mixing was a breakthrough. However, the practical realisation of this technique was difficult and it was mainly used for experiments where mixing was rapid. Primarily, this method became dominant in quantifying turbulent mixing especially used by Bourne and co-workers in the early 1980s to quantify turbulent mixing of aqueous systems within agitated vessels [Baldyga and Bourne (1984a,b,c)].

Work within the laminar mixing regime using the idea of micro mixing has been rare. Kusch et al. (1989) used the azo dye coupling reaction as described by Bourne et al. (1981) to obtain mixing information for reaction injection moulding (RIM). This process impinges jets of reacting monomers to form polymeric products, where the impingement mixing is within the laminar regime. This study was inconclusive, as far as obtaining quantitative results was concerned.

Meyer et al. (1988) used the azo dye coupled reactions to compare the mixing time for an empty tube to that of a static mixer (Sulzer SMX[®]). Even though the mixer geometry is different than the Kenics KM[®] mixer the use of the azo dye coupled reactions to obtain mixing information is important. The main results pertinent to this study were: firstly, as Re increased the scale and intensity of segregation of the mixture decreased. Secondly, the static mixer reduced the degree of segregation in the radial direction as a result of the better radial mixing created by the mixing elements compared

to an empty pipe. These results indicate that the experimental technique of using azo dye coupled reactions can give quantitative mixing results.

Baldyga et al. (1997) studied the micro-, and meso-mixing in the Kenics KM[®] and Sulzer SMXL[®] static mixers using the azo dye coupled reactions. Their studies were under conditions where macro-mixing and turbulent dispersion were not limiting. The main result from this was a mathematical model for fast chemical reactions in a plug flow static mixer. The results of Baldyga et al. (1997) and Meyer et al. (1988) are only useful for rapid mixing, in the turbulent regime where macro mixing is of no concern.

2.5. Measures of Mixing

The experimental techniques used to quantify mixing can be divided into two categories: statistical or dynamical. Statistical methods attempt to quantify the mixture in terms of parameters that are statistical in nature. Dynamical methods seek to quantify mixing in terms of reproducible experiments. Both of these methods are difficult to correlate with the fluid mechanics within the mixer.

Spencer and Wiley (1951) and Mohr et al. (1957) described mixing in terms of striation thickness and interfacial area. This measure of mixing is dynamical in nature and requires fast reliable methods for image capturing or 'frame grabbing' and image analysis techniques. This measure results in a very good qualitative understanding of the mixing process and is useful when the main concern is to reduce large heterogeneities in mixtures.

Mixing may also be quantified in terms of parameters that characterise the mixture on gross uniformity, texture and local structure. Two parameters to quantify mixing proposed by Danckwerts (1957) were: scale of segregation and intensity of segregation. Scale of segregation is a measure of the lengths of the unmixed regions (i.e. dark and light regions in a flow visualisation). Intensity of segregation is a measure of the difference in intensities of mixed and unmixed fluids. Therefore, this measure correlates with concentration of the minor species and the homogeneity of the mixture. Both these measures are statistical measures but for continuous laminar mixing systems, scale of segregation is very similar to measuring striation thickness. Intensity of segregation is useful in laminar mixing systems only when diffusion has a time scale comparable to that of the physical mixing mechanisms (folding, stretching, etc.). Polymer mixing is predominantly laminar with very slow diffusion times; hence, the relevant mixing measure is striation thickness or scale of segregation.

Bigio and Stry (1990) used a normalised variance of striation widths to compare mixing in a Kenics KM[®] static mixer and twin screw extruders. Their definition for this measure was:

$$\frac{s^2}{w_{avg}} = \frac{1}{w_{avg}} \sum_{i=1}^n \frac{(w_i - w_{avg})^2}{(n-1)}$$

where w_i is the striation width of striation i , w_{avg} is the average striation thickness and n is the number of striations. The variance, s^2 , indicates how evenly or unevenly the widths of striations are distributed throughout the flow. A low variance indicates that the

striation widths are the same width, where a high variance indicates there is a distribution of widths in the mixture. Their results showed an increase in the normalised variance, s^2/w_{avg} , with the number of elements passed.

Even though all of these measures are useful they are not directly related to the fluid mechanics. Realistic measures should be able to be measured and predicted so that mixing machinery can be designed based on physical principles, rather than the empirical design rules used presently. Therefore, these measures should be derived using fluid mechanics and the physics of the problem.

Mixing measures or efficiencies were derived by Ottino (1989b), based on the fundamentals of fluid mechanics. These are termed kinematic mixing measures for this discussion. He derived these measures based on the rate of strain or deformation field. Therefore, the only knowledge required to predict the mixing would be the velocity field. Velocity fields can be measured by various techniques (laser Doppler anemometry and particle image velocimetry) or can be simulated by many commercial software packages (Fluent, FIDAP). There are two measures or efficiencies based on either length stretches or area stretches. These measures are respectively:

$$e_{\lambda} = \frac{(D \ln \lambda / Dt)}{(\mathbf{D} : \mathbf{D})^{1/2}}$$

$$e_{\eta} = \frac{(D \ln \eta / Dt)}{2^{1/2} (\mathbf{D} : \mathbf{D})^{1/2}}$$

where λ is the length stretch and η is the area stretch. \mathbf{D} is the rate of deformation tensor. The definitions of the rate of deformation tensor and its counter part, \mathbf{W} , the vorticity tensor are:

$$\mathbf{D} = \frac{1}{2} \left(\left(\frac{\partial \underline{u}}{\partial x_i} \right) + \left(\frac{\partial \underline{u}}{\partial x_i} \right)^T \right) \quad \mathbf{W} = \frac{1}{2} \left(\left(\frac{\partial \underline{u}}{\partial x_i} \right) - \left(\frac{\partial \underline{u}}{\partial x_i} \right)^T \right)$$

The physical meaning of these efficiencies is made clearer if it is recalled that for a Newtonian fluid:

$$\varepsilon = 2\mu(\mathbf{D} : \mathbf{D})$$

where ε is the viscous dissipation per unit volume per unit time. Therefore, these efficiencies are related to the viscous dissipation for viscous fluids and can be interpreted as the local energy dissipated to stretch fluid elements or the ratio of the energy used to create inter-material area to the energy dissipated at a particular point.

These efficiencies typically decay with time of order t^{-1} resulting in strong mixing usually at the entrance of a mixer and poor mixing at the end of the mixer. With flow re-orientation these efficiencies can be kept high resulting in better mixing [Ottino (1989)]. This demonstrates that interfaces should be continuously reoriented to obtain the best mixing and should be oriented such that the deformation field present provides the maximum attenuation on the heterogeneities.

Ottino (1989b) proposed a lamellar model that described mixing as the location and size of interfaces as a function of time and space. This model incorporates diffusion and reaction with the fluid mechanics to describe mixing and requires knowledge of the

entire velocity field. However, the application of this model has been limited since most mixing devices have very complex velocity fields that have not been quantified. A further hindrance is that the numerical tracking of interfaces is difficult and a small error in the location of the interface grows exponentially within most mixer flow fields.

Recently, discussion has centred on the idea of the deformation history as a mixing measure. This requires a detailed knowledge of the deformation field in the mixer. This is a formidable task for complicated mixers but does lend itself well to the principles of fluid mechanics. This approach has many possibilities for simulations but must be verified experimentally. Kwon et al. (1994) have studied the flow field in an extruder and found that the right Cauchy Green tensor's largest eigenvalue is a quantitative measure for this flow field. This value corresponds closely to the strain experienced in the extruder. However, this is an isolated case and further work in this area is required.

A point wise mixing measure or parameter has been developed by Manas-Zloczower (1989,1992) which characterises the degree of elongational flow in a flow field. The parameter, λ_M , is defined as

$$\lambda_M = \frac{\dot{\gamma}}{\dot{\gamma} + \omega}$$

where $\dot{\gamma}$ and ω are the magnitude of the rate of deformation tensor, \mathbf{D} , and the vorticity tensor, \mathbf{W} , respectively. The values of λ_M range from 0, pure rotational flow to 1, pure elongational flow. A value of 0.5 represents the case of simple shear. As mentioned earlier, laminar convective mixing requires shear and elongation for the stretching of

fluid elements. Therefore, efficient mixing would be expected to occur in the range of λ_M between 0.5 to 1 with possibly some point of maximum efficiency.

2.6. Static Mixers

Static mixers, as the name implies, have no moving parts and no external power is provided to the device except for the power loss due to the pressure drop of the fluids that pass through the mixer. The Kenics KM[®] static mixer chosen for study consists of elements cut from right and left hand helixes that are joined in an alternating order of left and right twists. These elements are placed in a pipe as shown in Figures 1.1.1. and 1.1.2.

The streams are mixed by two characteristic actions: flow division and radial mixing. Flow division is accomplished by having element edges abut ninety degrees to one another. The fluid is split into two at the front edge of an element and follows the path created by the geometry of the element until it is split into two again at the front edge of the following element. This causes a lamellar structure to be produced (striations). Ideally, the growth of the number of striations proceeds according to

$$S_{number} = 2^n$$

where n is the number of elements in the unit [Devellian (1972)]. Radial mixing is the result of velocity components of the flow being shifted as a result of the helical elements causing fluid at the centre of the tube to be forced towards the outer tube wall. This

creates recirculation of the fluid from the centre towards the edge of the tube and gives the mixer a plug flow residence time distribution.

Most studies of static mixers have focused on determining correlations for the on-line parameters required for the mixer's operation. These parameters, such as pressure drop, temperature homogeneity and residence time distribution (RTD) have been correlated to the number of elements, the amount of twist per element and aspect ratio (L/D) of an element. Pressure drop data correlations have been attained for Newtonian and generalised Newtonian fluids [Chen and MacDonald (1973), Chandra and Kale (1992), and Shah and Kale (1990)]. Nauman (1979) studied the enhancement of heat transfer and thermal homogeneity using static mixers. This study focused on laminar flow reactors where enhancing the heat transfer and mixing of the reactants would reduce temperature gradients in the mixer. The gradients along the radial co-ordinate were reduced with the addition of the twisted tape inserts almost creating isotherms in the radial direction. Nauman (1991, 1982) and Tung (1976) studied the residence time distributions in motionless mixers, and determined that the number of elements had a strong effect on the RTD. As the number of elements increases the behaviour of the RTD asymptotically approached that of a plug flow RTD.

2.7. Simulations of Static Mixer Velocity Fields

Tung (1976), Arimond (1984), Dackson (1986), Ling and Zang (1995), Bryde and Sawley (1996), Hobbs and Muzzio (1997a,b) and Hobbs et al. (1998) have generated simulations of the velocity field in a static mixer.

Currently, there is a great deal of resources and time being spent in the area of computational fluid mixing (CFM). CFM uses high numbers of particles trajectories ($\sim 10^4$ - 10^6) in a simulated flow field to model species and the lamellar structure created by the flow field. Hobbs and Muzzio (1997a,b) and Hobbs et al. (1998) simulated the flow field for the Kenics KM[®] static mixer at a Re of 0.15. They tracked 10^4 particles and presented the lamellar cross sections. These looked very similar to those presented in Grace (1971). The residence time distributions of the particles compared well with those measured by Tung (1976), Petera (1986) and Pustelnik and Petera (1985). Hobbs and Muzzio (1997a) measured the variation coefficient over a mesh of 64 by 64 cells laid over the radial cross-sections to determine the number of particles per cell (C_i) and mean number of particles per cell (C) ($n=2600$ as only cells entirely in the radial cross-section are used).

$$\sigma^2 = \frac{\sum_{i=1}^n (C_i - \bar{C})^2}{n-1}$$

Their results compared well with those presented by Pahl and Muschelknautz (1982) and Allocca (1982). However, the measurement of the variation coefficient levelled out after 10 mixing elements. This was due to the fact that the characteristic length for the mixture had fallen below the scale of the grid size used for the calculation. Refinement of the grid was not pursued due to the significant increase in computation time required to track the increased number of particles required to resolve smaller mixture scales.

Hobbs et al. (1998) presented a simulated fluid flow field at $Re=0.15$. They used the simulated flow field to calculate the rate of deformation tensor and then calculated the tensors second invariant, $\dot{\gamma} = [1/2(\mathbf{D}:\mathbf{D})]^{0.5}$, at each point. The magnitude of $\dot{\gamma}$ is related to the degree of deformation in the flow field. They found that the highest regions of deformation resulted from the shear created along the element surfaces, tube wall and the junctions between elements. The maximum value they calculated for $\dot{\gamma}$ was approximately 0.6 s^{-1} for a $Re=0.15$.

Hobbs and Muzzio (1997b) measured the performance of the Kenics mixer for mixing small streams of passive tracer into the bulk flow. They investigated the effect on performance for changes in dye injection location and flow rate ratio. They found that given enough elements, the dye injection location had little effect on final mix quality but some dye injection locations would render the first few elements useless to contribute to the mixing. Their analysis showed that mixing elements with 120 degrees of twist per element gave similar mixing (based on the variables of flow rate and dye injection location) as the standard 180 degree kenics elements. However, these elements were more energy efficient than the standard configuration.

Byrde and Sawley (1996a,b,c) simulated the velocity field for the Kenics KM[®] mixer at Re of 25 and 100. They tracked 7×10^4 particles and found that the flow was globally chaotic. However, at low Re , they found that the particles introduced at the centre of the pipe hardly were re-distributed. Islands of material would flow down the centre of the mixer with very little mixing. Their results differ from Hobbs and Muzzio's (1997) quite significantly. This may be attributed to the large convective terms present at

the higher Re. Byrde and Sawley (1996a, 1996b) showed that a mixer consisting of only right handed twisting elements produced significantly poorer mixing than the standard design of successive opposite rotating elements. [This was also found by Hobbs and Muzzio (1997b).] Byrde and Sawley (1996b) quantified mixing based on a similar parameter to the scale of segregation called the global structure radius. This mixing parameter measures the distance between particles of different colour to determine the smallest distance between each particle and its opposite coloured particle. The resulting value that is finally used to characterise the mixture is the smallest distance out of all measured, below which 99% of the measured distances fall. They tracked from 10^3 to 10^6 particles and found that they could discern very small structures. They showed that for a randomly generated mixture of 10^6 particles they were not faced with the problem of resolving distances between particles. The results showed that the largest structure size found at Re of 25 and 100 for a 6 element mixer was 0.1 and 0.03 respectively. These values were also found to be independent of the number of particles tracked above 10^5 . They found that the fluid rotated in the opposite direction to the helix twist of each element, leading to a vortical structure. At Re of 100, secondary vortices formed at the suction or low-pressure side of the elements in the radial plane creating a total of four recirculations. If one visualises the element and tube, there are two semi-circles formed. As the element rotates, each hemisphere has a leading and trailing edge of the element. The trailing edge is the low suction side. Byrde and Sawley's (1996) analysis showed that these vortices helped fluid mixing by reducing the global radius from 0.1 for Re of 25 to 0.03 for Re of 100.

Ling and Zhang (1994) published their results on simulating a Kenics KM[®] mixer with their mixing analysis based on Poincaré sections and the concept of mixing windows [Ling and Schmidt (1992)]. Their simulation consisted of solving the case of infinitely long twisted tapes in a pipe with either clockwise or counter-clockwise helices. They then cut parts of the solution corresponding to a single element and combined a series of left and right handed elements. Their final velocity profile is the combination of the fully developed flows over each element. The underlying assumption to this analysis is that the influence of the junctions between elements is small. This is incorrect but they used their solutions to identify mixing windows or conditions where efficient mixing would result. These windows do not optimise mixing but are more like guidelines of operating regimes that may provide highly efficient mixing. Ling and Zhang (1994) showed that by reducing the aspect ratio to 0.6 and keeping the twist per element 180 degrees, that they were able to achieve the same mixing as a standard Kenics KM[®] element ($L/D = 1$ or 1.5) with 43 percent less pressure drop.

The first generation of simulations of the Kenics KM[®] static mixer transformed the Navier-Stokes equations into a helical co-ordinate [Tung and Laurence (1975)] system and then solved the equations. Tung (1976) numerically solved the transformed momentum equations to obtain the static mixer flow field. His simulation predicted the axial velocity and the pressure drop across the mixer. Tung's (1976) assumption that the radial velocity could be neglected, justified initially on the basis of a small magnitude of the radial pressure gradient, led to an incorrect simulation. He concluded that mixing in

the mixer resulted from entrance effects which was incorrect since the radial velocity component is the key to the mixing in the Kenics KM[®] configuration.

The transformed equations of Arimond and Erwin (1985), were different from those of Tung and Laurence (1975). Dackson (1986) and Wang (1981) had confirmed the transformed equations of Tung (1976). However, the approach that Arimond (1984) used to solve the governing equations was correct. An important result of this work was the attempt to follow the mixing pattern in the static mixer. Arimond used tracer particles together with the solved fluid flow field to obtain the numerical particle trajectories or traces through the mixer. The second significant result was the optimisation of the twist per element to obtain better mixing. This optimisation was based on the ratio of a reference interface rotation to the rotation of the element over a set axial distance. Therefore, a large ratio implies a significant change in the orientation of the interface and therefore, most probably a high degree of mixing [Ottino (1991)].

Shortly after Arimond's work, Dackson and Nauman (1986) solved the equations of motion in the helical co-ordinate system. They defined mixing efficiency in terms of the ratio of deformation of the initial interface to the pressure drop across the element. This measure takes into account the fact that for mixing in a static mixer area needs to be generated but with minimal pressure drop across the element. The mixing parameter is defined as

$$E_o = \frac{\left[\frac{l}{l_o} - 1\right]}{\frac{2L}{D} \left(\frac{\Delta p}{\Delta p_{cp}}\right)}$$

where E_o is the mixing efficiency, l/l_o is the interfacial stretch, $(\Delta p/\Delta p_{cp})$ is the reduced pressure ratio (pressure drop with elements/ pressure drop of empty tube) and $2L/D$ is the aspect ratio based on the radius of the tube. They varied the aspect ratio (L/D) between 0.1 and 6.4 and the amount of twist per element from 0 to 270 degrees. The mixing efficiency had a maximum when the aspect ratio was 0.5 and the twist per element was approximately 90 degrees. The efficiency at this configuration was approximately double that of the Kenics standard configuration of L/D of 1.5 and 180 degrees twist per element [Chemineer (1998)].

Dackson's (1987) simulation was stable for very low Reynolds Number, ($0 < Re \leq 7.5$). Dackson and Nauman (1985) studied the motion of tracer particles in the solved flow field by rerunning the simulation many times with additional particles. They used the particle tracking to simulate two species mixing. They determined the lamellar structure produced for the two mixed species for three elements for L/D of 0.8 and a Re of 0. Profiles presented by Grace (1971) appear to confirm the validity of Dakson's simulation at $Re \sim 0$. Grace (1971) solidified two hot polymer streams mixing within a static mixer by quenching the entire mixer in cold water and then cutting cross sections of the mixer along the axial co-ordinate. These polymers had sufficiently high viscosities such that the Re was close to 0. However, Dackson found that the orientation of the

interfaces was highly dependent on Re . Consequently, the results of Dackson (1986) are not easily applicable since many mixing applications have $Re > 7.5$.

Dackson (1986) studied the effect of finite thickness of the elements and found that there was a negligible effect on the flow field. Since the cross sectional area for flow through the mixer was reduced there was a corresponding increase in the axial velocities and pressure drop across the mixer.

2.8. Twin Screw Experimental Results

Rauwendaal (1981) made an experimental evaluation of twin screw extruders and came to the conclusion that the overall extruder performance appeared to be dominated by the effect of the intermeshing region. Results demonstrated that the flow in the intermeshing zone was highly three-dimensional. This conclusion has been the main motivation for moving from two-dimensional models into more rigorous three-dimensional models for twin screw extruders.

One of the major challenges in the study of twin screw extruders is the experimental validation of the results obtained by numerical models. In the area of flow visualisation, Kalyon et al. (1991) studied the degree of fill and melt densification in fully intermeshing co-rotating twin screw extruders (ICRTSE), with an analysis of the effects of the various reverse and forward stagger angles for a configuration of kneading discs. More recently, Kalyon et al. (1997) presented a work that combined simulation and experiments in the mixing section of ICRTSE for the processing of filled polymers. Measurements of pressure and temperature were taken, but more significant is the

analysis of the degree of distributive mixing of the filler in the extruded polymer with the aid of wide angle X-ray diffractometry. The distributive degree of mixing was measured for the filler in the polymer at the die exit.

Flow visualisation studies have had to use small windows in the side of a metal barrel of a TSE. These methods have given some useful results but it has been difficult to see the entire mixing mechanism. Sastrohartono et al. (1990) observed that in the nip region (the area where the two screws intermesh) of a partially intermeshing co-rotating TSE, the flow is three dimensional.

Flow visualisation studies have been done using transparent barrels to analyse mixing and the flow behaviour in the TSE. Bigio and Stry (1990) have visualised the mixing of a black dye within co-rotating and counter-rotating twin screw extruders fabricated with transparent barrels. They used silicone oils for the working fluid in the TSE, and measured striation counts and variance along the TSE.

Mixing has also been studied by analysing the polymer at various positions in the extruder. Christiano (1993) analysed the mixing of carbon black in the TSE. Christiano (1993) used a feed of polypropylene and five percent carbon black. Samples of the melt exiting the extruder were taken and pressed into plaques, which were then analysed using image analysis. The samples were analysed to measure the mixing index (intensity of segregation) [Tadmor and Gogos (1979)]. Christiano's results showed that the greatest change in the mixing index occurred in the melt and convection zones of the TSE. This indicated that in a very small length of the extruder ($L/D = 5$) about 90 percent of the mixing occurs.

One of the most recent investigations in the area of flow visualisation was presented by Kim and White (1994) who utilised the screw and kneading disc elements from a Werner and Pfleiderer ZSK-30[®], and barrel sections with windows. The visualisation experiments included qualitative observations of aluminium flakes and platelets used to visualise the flow through the Pyrex[®] glass windows. Measurements of residence time were also carried out by taking samples of the aluminium tracers from the die exit and from intermediate positions. They found that kneading discs and reverse conveying elements increase the residence time and broaden the residence time distribution.

There have also been a number of experiments in the ICRTSE using the residence time distribution (RTD) as a measure of mixing [Oberlehner et al. (1994)]. However, these results do not contribute significantly to this study as the RTD is most useful for scaling and designing the TSE, but is very poor for determining the details of the flow field.

Todd (1989) and McCullough and Hilton (1993) have measured experimental pressure profiles on ICRTSE. Todd (1989) studied the complex flow phenomena in a TSE by measuring the pressure flow term for different configurations of kneading discs in a vertically mounted barrel, by pumping a viscous Newtonian fluid upwards to ensure 100% fill. McCullough and Hilton (1993) presented an experimental investigation of the performance of co-rotating twin screw extruders. The data provided by McCullough is not limited to measurements of pressure and temperature at the die, but also include measurements along the barrel at different axial and radial positions.

Christiano and Lindenfelzer (1997) have extended the experimental determination of the dynamic pressure profiles of McCullough and Hilton (1993). In their work, Christiano and Lindenfelzer, made time dependent pressure measurements by recording eight radial data values at every axial position along each mixing element. The eight radial pressures from the transducers are read simultaneously at each axial location. Software was developed to re-map the pressure data files into one file so the entire pressure distribution over the full length of the mixing element for a given screw position could be analysed. These results have the potential of being readily usable for the purpose of validation of mathematical models. In addition, the analysis of the dynamic pressure gradients contributes to the understanding of the flow patterns and gives an indication of the type of mixing occurring in the system.

Karwe and Sernas (1995) and Chandrasekaran and Karwe (1997) investigated the velocity profile in the nip region of a ICRTSE. They used laser Doppler anemometry (LDA) through a small acrylic window in the side of a Werner-Pfleiderer ZSK-30[®] ICRTSE using clear corn syrup as the working fluid. They were only able to measure a single velocity component at each instant in time over a limited region. The largest limitation with LDA for implementation in the TSE is the optical accessibility to the small clearances within the kneading disc region.

A detailed study of polymer blend mixing and dispersion in the kneading disc section of the TSE has been investigated by Huneault et al. (1996). They looked at a 45mm co-rotating TSE for blending 5 to 15 wt% polyethylene (PE) into polystyrene (PS). They found that the minor phase right after the melting section was in a fibrillar form and

that the droplet diameters and fibre widths sizes had already reduced to the micron and sub-micron range. Therefore, a large degree of mixing was accomplished in the melting region and subsequent mixing would require focus on the reduction of the fibre structures to droplets. A theoretical model was developed to predict the size of the droplets and fibres after they had passed through the mixing region (kneading blocks). The model predicted that the shear created in the mixing region would not reduce the fibre form significantly. This prediction was confirmed by morphological observations made at the mixing section exit, where there was little change in the size of the fibres and droplets.

2.9. Twin Screw Mixing Simulation

Conner and Bigio (1992) have used the concept of deformation history or line stretches as a quantitative technique of obtaining a mixing efficiency. They apply this idea to a non-intermeshing counter rotating twin screw extruder, (NICNRTSE), in the nip area. This is the connecting region between the two screws. In previous experimental studies, Bigio et al. (1991) determined that there was a potential for the nip region to benefit the mixing in the TSE. Conner and Bigio (1992) have simulated a two dimensional approximation to the flow behaviour in the nip region and numerically have analysed the mixing. The main result was that the mixing is a function of the pressure gradients created in the nip region.

Ji and Kalyon (1992) and Lawal et al. (1993) have performed a two dimensional computational study of the mixing in the two-tipped or two lobe kneading section of a ICRTSE. They have shown that there is chaotic mixing present in this region and hence,

the initial conditions are important for the mixing quality. In the two dimensional study, fingerprints of chaotic mixing were revealed essentially through positive Lyapunov exponents. This indicated that the fully three dimensional kneading disc may possibly create chaotic mixing. With the real time scales that the fluid remains in the kneading disc section, the number of periods required to see chaotic motion would not be realistic. More importantly, it would be more beneficial to see if there are unmixed regions created by the kneading disc (termed as eyes by Ottino (1989)).

Van Der Wal et al. (1996) mathematically modelled the flow in the kneading disc section of a TSE using a Newtonian fluid. They looked at the back flow created in the kneading disc section as a quantity with which to characterise the mixing. They found that as the flow rate through the kneading disc section increased, the percent of back flow decreased. The average shear rate and elongation rate across the entire element was calculated for varying screw speed (rpm) and flow rate. They found that higher shear rates are created at low flow rates whereas higher elongation rates are created at higher flow rates. Also both shear rate and elongation rate increased with increasing screw speed.

Lawal and Kalyon (1995) solved the fluid flow field for the kneading block section of the TSE. They used 17,000 tracer particles with their solved flow field to simulate a pocket of dyed fluid being mixed. They determined from the particle trajectories the intensity of segregation as a function of the stagger angle of the kneading discs. They found that the intensity of segregation decreased as the stagger angle

between the discs was increased indicating that larger stagger angles created better distributive mixing.

Bravo (1998) used a 3D quasi-steady state simulation of the kneading disc section of the WP ZSK-30[®] extruder. He simulated various geometries of the discs and compared the pressure profiles against those of McCullough and Hilton (1993). The simulation consistently predicted higher pressures at the smallest clearances between discs and the barrel wall compared to those measured by McCullough and Hilton (1993). The possible discrepancies between the simulation and experiments could be attributed to a number of aspects. There may have been experimental error where the pressure transducers did not have a rapid enough response or that the elements were a bit worn down and the clearances may have been slightly larger than the standard WP ZSK-30[®] specifications. The other source of error may have been that in the experiments the kneading discs were placed one after another and the effect of the upstream and downstream may not be captured by simulations of just one set of discs. However, with this in mind, the profiles of simulation and experiments are fairly good qualitatively and for some cases quantitatively.

Bravo (1998) tracked particles in the kneading discs and showed that they undergo a periodic behaviour in strain or deformation. This was attributed to the particles passing through the gaps between the discs. He found that as the length of an element to the barrel diameter increased the periodicity decreased and that a higher number of particles experienced larger strains or deformations. One of the main results of this analysis was that the gap between passing discs had the largest shears and strain.

In the disc – disc gaps there are two gaps formed: axial or transverse gaps. Axial gaps are those created as opposing discs pass each other whereas transverse gaps are those created by discs off centre of one another passing each other in the intermeshing zone. This is shown in Figure 2.9.1. Interestingly, Bravo showed that the largest shear rates are created in the transverse gaps.

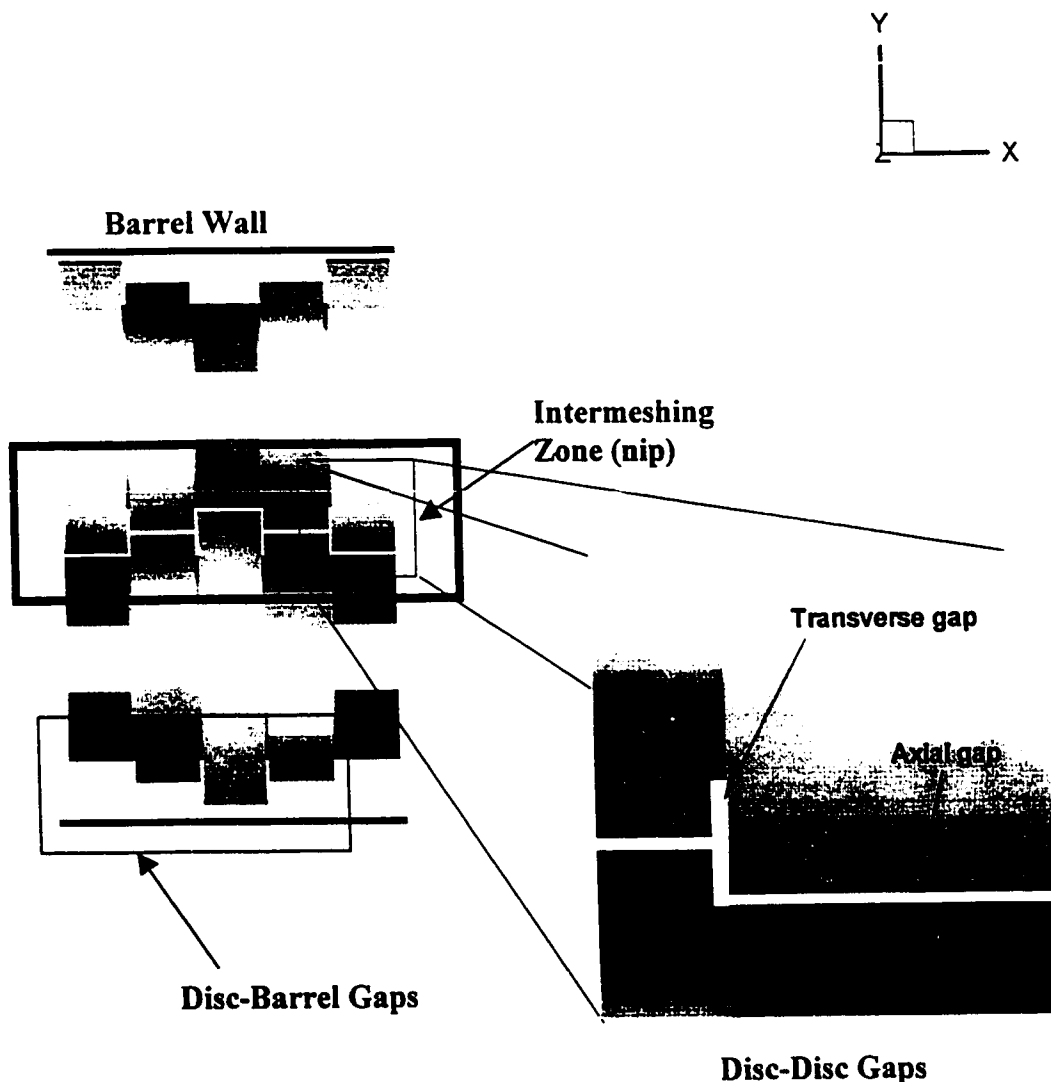


Figure 2.9.1. – Schematic of Intermeshing Zone Highlighting the Axial and Transverse (Radial) Gaps Created Between Passing Discs.

2.10. Summary

From the literature survey conducted, the largest source of data missing in the static mixing area are velocity measurements in the public domain. With the number of works conducted on CFD simulation of the Kenics KM[®] static mixer, the question that can not be resolved is whether the solutions are correct. With the fast advancement in computers the need for these measurements has become extremely critical for advancement of the CFD simulations.

The experimental research on the Kenics[®] static mixer has focused on correlation of pressure drop, heat transfer and residence time distributions. The work in turbulent mixing has centred on micro-mixing and meso-mixing where macro-mixing was not an issue. The data in the laminar regime for mixing has centred on statistical measures such as coefficient of variance. The one lacking source of data has been measurement of mixing using dynamic mixing measures. As a result, the computational research has reached a point where experimental data for comparison has become crucial for the advancement of the mathematical modelling. As a result, Byrde and Sawley (1996a,b,c), Hobbs and Muzzio (1997) and Hobbs et al. (1998) results may look correct but without substantial validation, industry hesitates to implement their recommendations.

For the twin screw extruder, there are quite a few research groups simulating the mixing in the kneading disc section. All the simulation in the public domain have lacked validation with velocity profiles. Some groups have validated against pressure and temperature data but for the mixing community the goal is to have validation with experimental velocity measurement. Karwe and co-workers (1995) have published laser

Doppler velocimetry measurements within the twin screw conveying section. However, they have measured a limited region due to the restrictive optical access.

This thesis will attempt to address the difficulties mentioned above for the TSE and static mixer. From the results of Dackson and Nauman (1985) and Arimond and Erwin (1985a,b), the static elements chosen for study have a twist of ninety degrees, which was predicted to be the optimum or close to it. The dynamic mixing measures of striation thickness, variance of striation thickness and interfacial area will be used to experimentally quantify the mixing in the static mixer. The mixing will be quantified for different aspect ratios, viscosity ratios and flow rates.

The velocity profile in the static mixer and the kneading section of an intermeshing co-rotating twin screw extruder (ICRTSE) will be measured using the experimental techniques of laser Doppler anemometry and particle image velocimetry. The magnitude of the rate of deformation tensor, $\dot{\gamma}$ (second invariant), will be used to determine regions of high deformation. This mixing measure is related to those of Ottino (1989) and has been used by CFD researchers as a basis for quantifying mixing based on simulation.

The following chapter discusses the experimental techniques and methods that will enable the measurements of velocities in the ICRTSE, and static mixer and the quantification of mixing in these two mixers.

3.0. Experimental Procedure

3.1. Geometry and Specifications

3.1.1. *Static Mixer*

The commercial Kenics KM[®] static mixer consists of twisted tape or short helical inserts. These inserts twist 180° with the leading edge and trailing edge of two elements perpendicular to one another. The aspect ratio, length of element to diameter of tube (L/D), of each helical element is 1.5. For the purpose of keeping this research focused on the fundamentals of mixing and reducing experimental difficulty, some modifications were made the basic Kenics KM[®] design. These modifications will be described below.

The housing of the mixer is a rectangular block of acrylic, 38mm x 38 mm x 400 mm, with a 38 mm hole bored lengthwise along the centre of the block. The entire block is highly polished inside and out to improve optical quality. The acrylic is polished with wet sandpaper of 1000 grit and jeweller's rouge.

The helical inserts are fabricated out of acrylic plates and are made by heating the acrylic close to the melting point and then twisting the acrylic 90° into short helixes (left and right hand elements). A jig was designed that allowed the acrylic to be twisted gently without causing severe thinning of the element at any point or causing the acrylic to tear

or crack. The elements are 38 mm in width with aspect ratios of 0.8, 1.0 and 1.5 and a twist of 90° per element. The elements have thickness to diameter ratios of 0.09, 0.17 and 0.04 respectively. The elements had blunt squared off leading and trailing edges. Figure 3.1.1.1. shows elements with an aspect ratio of 1.5.

Three different entrance conditions were used for the static mixer. Figure 1.2. depicts the first case where a divider plate separated the incoming two streams. The divider plate had an L/D ratio of 3.0 with a blunt, squared off trailing edge. This condition was primarily used for flow visualisation studies in which the main concern was to keep the two streams separate. The second inlet condition was a long section of pipe (400 mm) attached at the top of the mixer to ensure that fully developed flow (Poiseuille flow), entered the mixing section. This was used as the entrance condition for PIV measurements to ensure that a well defined boundary condition existed. The third method of input of the fluid into the mixer section was a Komax L/H[®] series distributor. The claimed benefits of this distributor are that high mass flow rate ratios can be successfully mixed. This also makes it ideal for studying high viscosity ratios where typically injecting the lower viscosity material into a large amount of higher viscosity material is usually a formidable task. The bulk of the fluid (higher viscosity) to be mixed enters through the two larger inlets shown in Figure 3.1.1.2., while an additive or dye (less viscous) enters through the much smaller hole. The ratio of the diameters, D_A/D_B , is 4. The dye is pulled and sheared by the bulk stream as it expands, creating a sheet of dyed fluid in the centre as shown in Figure 3.1.1.3. This entrance condition was used for flow visualisation studies.

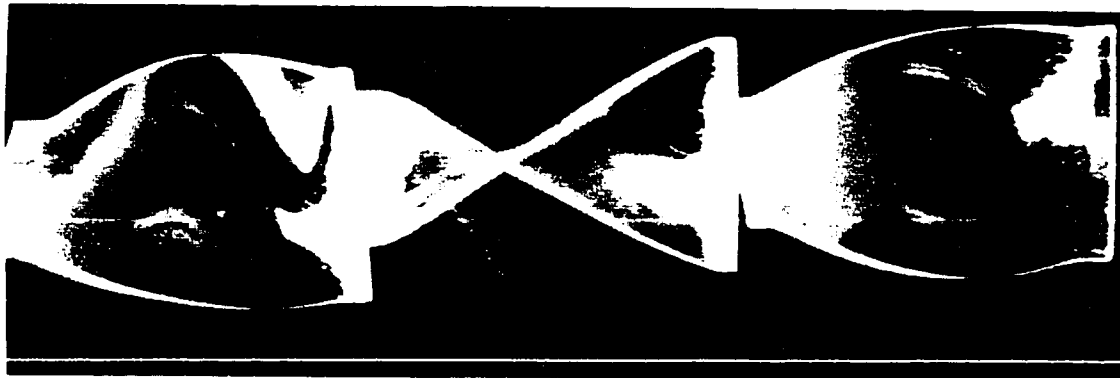


Figure 3.1.1.1. – Static Mixer Elements, Acrylic, Aspect Ratio of 1.5.

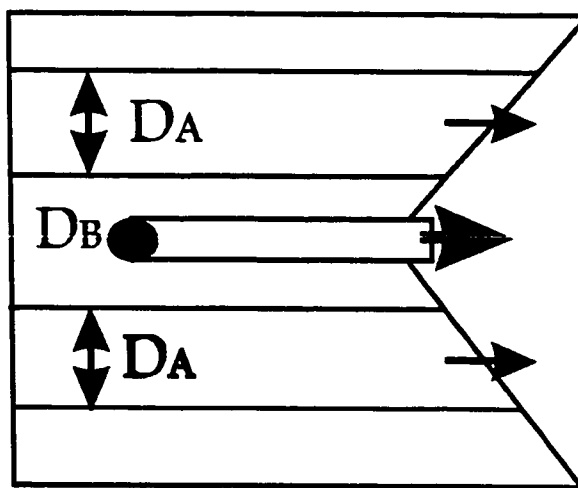


Figure 3.1.1.2. - Axial Cross Section of Komax L/H[®] Series Distributor, $D_A/D_B = 4$.

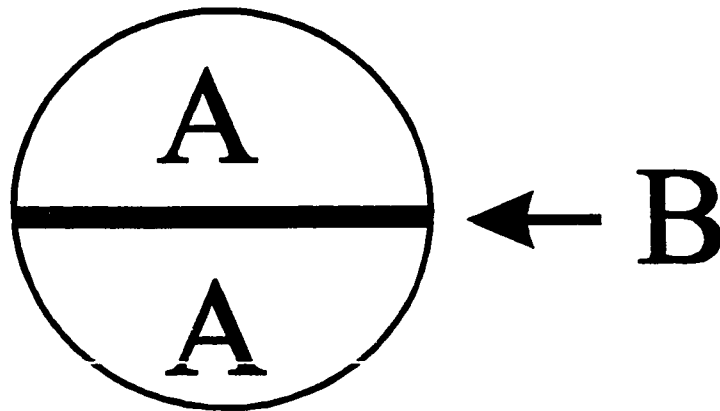


Figure 3.1.1.3 - Flow Field Exiting Komax L/H[®] Distributor, A (Clear oil), B (Dyed Oil).

3.1.2. Intermeshing Co-Rotating Twin Screw Extruder

The twin screw extruder (TSE) was modelled after a Werner & Pfleiderer (WP) ZSK 30[®]. The housing of the extruder was a rectangular block of acrylic, 250 mm x 125 mm x 75 mm, with two 30 mm holes bored out lengthwise forming a figure eight and is shown in Figure 1.2.3. The specifications for the extruder are given in Table 3.1.2.1. The shafts were constructed from acrylic with a spline allowing for the conveying elements and kneading discs to be keyed onto the shaft. The TSE has special seals on the end of the shafts to prevent leaks. A GKH motor, 0-2300 rpm, coupled with a reducing gear box of 10 to 1, drives the shafts of the extruder over a range 0 -230 rpm.

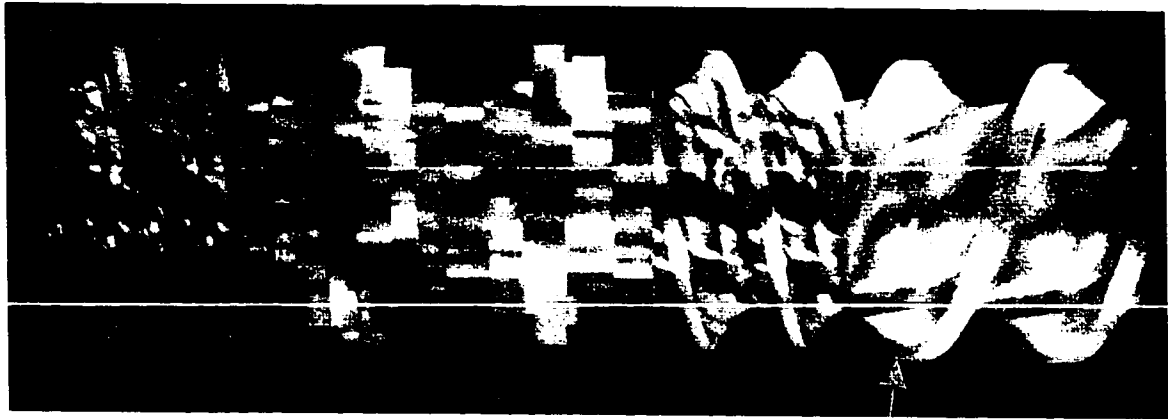
Barrel bore diameter (D_b)	30.85 mm
Screw outside diameter (D_o)	30.7 mm
Screw root diameter (D_i)	21.3 mm
Flight depth (t)	4.7 mm
Centre distance of screws (C_L)	26.2 mm
Clearance between discs (G)	0.2 mm
Clearance disc-barrel (B)	0.075 mm

Table 3.1.2.1. - Technical data for ZSK 30[®] extruder.

All of the conveying elements and kneading discs were fabricated out of acrylic and keyed for the shafts. The keyed elements allowed for a modular design, permitting various geometries to be studied. The screw profiles (sequence of elements) used for the LIF studies are shown in Figure 3.1.2.1. and their specifications are given in Table 3.1.2.2. The main difference in the two profiles is the location of the back-pressure or reverse conveying element.

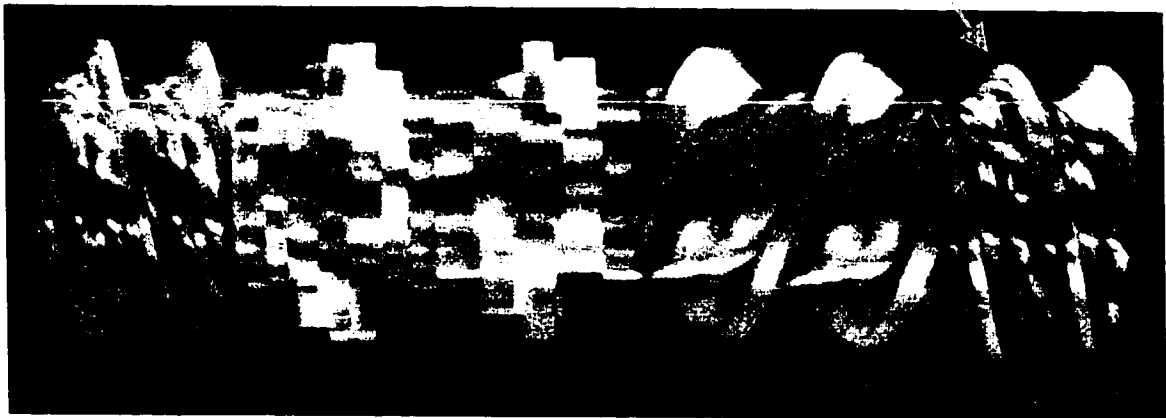
The kneading blocks are classified to the number of discs per block, the length of the block and the stagger angle between the discs. A cross section of the kneading discs used in this study is shown in Figure 1.2.1. The stagger angle is defined as the angle between adjacent discs on the kneading block. This angle can be classified as forward,

reverse or neutral. This classification implies whether the discs provide forward, reverse or no conveying flow. The kneading blocks studied here were all forward stagger with angles of thirty and forty-five degrees between adjacent discs. An example of the nomenclature that is used in industry to describe these kneading blocks is RH-KB/45/20. The KB stands for kneading block; 45 stands for the angle between discs; 20 stands for the length of the block in millimetres and the RH stands for right handed. Right handed elements are forward conveying elements and left handed, LH, are reverse conveying elements. The nomenclature for the conveying elements are described as RH/20, meaning right handed with a pitch of 20 mm. The pitch is defined as the distance required for the screw flight to make one full 360° turn. The screw flights are shown out in Figure 3.1.2.1. The conveying elements used for this study all were double-flighted. This means there were two flights revolving around the screw root, 180 degrees to one another.



a)

Screw Flights



b)

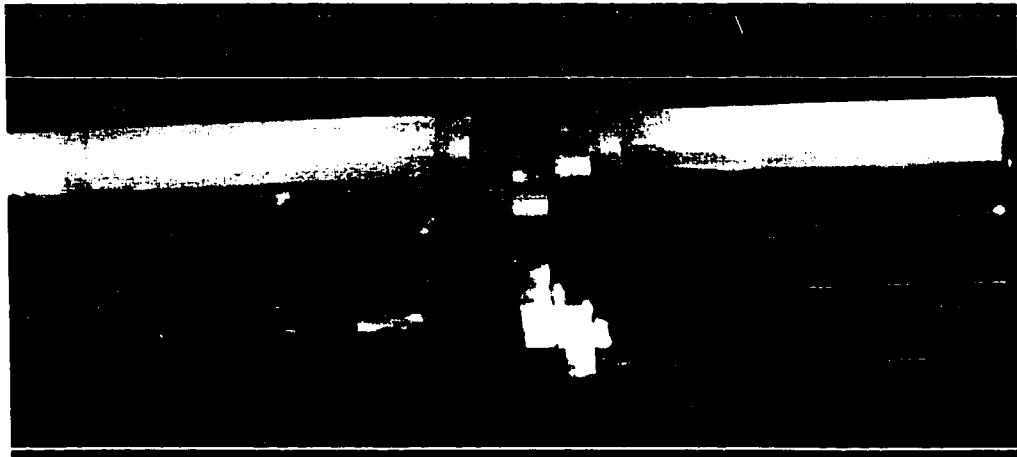
Figure 3.1.2.1. – Screw profiles for flow visualisations - a) Geometry C b) Geometry D.

	Geometry C	Geometry D
Pre-Kneading Block Conveying Length and [Profile]	1.93D, [2-RH/28]	1.6D, [1-RH/28, 1-RH/20]
Kneading Disc Section	1.33D, [1-KB/30/20, 1- KB/45/20]	1.33D, [1-KB/30/20, 1- KB/45/20]
Post-Kneading Block Conveying Length and [Profile]	2.9D, [1-RH/28, 1-LH/28, 1-RH/28]	1.6D, [1-LH/28, 1-RH/28]

Table 3.1.2.2 - Specifications of Screw Profiles (Figure 3.1.2.1.).

For the velocity measurements two geometries were considered (Figure 3.1.2.2.). The main objective was to study the effect of the adjacent discs on the flow pattern in the kneading discs and to help determine the appropriate boundary conditions for CFD simulations.

Figure 3.1.2.2. displays the configuration of elements placed on the shafts of the extruder for the two screw profiles. A special configuration, as shown in Figure 3.1.2.2a. (Geometry A), was fabricated to study the effect of the boundary condition used for mathematical models as well as to isolate the individual discs. Long discs (an extended kneading disc 60 mm in length) were placed before and after the 45/5/20 kneading blocks. For the configuration shown in Figure 3.1.1.2b. (Geometry B), 20 mm pitch, forward conveying elements (double flighted) were placed before and after the 45/5/20 kneading blocks. The conveying element provided a more realistic boundary condition.



(a)



(b)

Figure 3.1.2.2. - Geometry of the elements for the experimental measurements.

a) **Geometry A** - From left to right: 40 mm straight element, 20 mm, 45° stagger angle forward kneading block, 40 mm straight element; b) **Geometry B** - From left to right: 20 mm forward conveying element, 20 mm, 45° stagger angle forward kneading block, 20 mm forward conveying element.

3.2. Equipment and Materials

The use of clear acrylic for the mixer body, elements, shafts and flow distributors facilitates the optical experimental methods of LIF and PIV. The working fluids are bright (clear) mineral oils of differing viscosities but of indices of refraction ($n_d=1.465$) nearly matching that of the acrylic ($n_d=1.47$).

The light source is a 6W Coherent argon ion laser that creates a beam of light roughly 1 mm in diameter. The beam is passed through a cylindrical lens to create a sheet of light, which is then focused with a convex lens to create a sheet with a thickness between 100 and 500 μm . This sheet is produced in the r and θ plane for a cylindrical lens defined in cylindrical co-ordinates (Figure 3.2.1). This sheet can be adjusted to pass through the acrylic model at different angles, creating two dimensional visualisations of the flow field. Since the indices of refraction for the oil and acrylic are nearly the same, diffraction of the light sheet and optical distortion are reduced. This benefits the techniques of LIF, LDA and PIV.

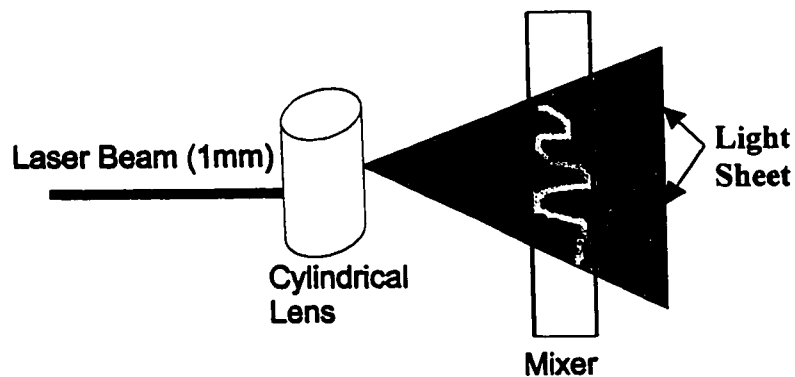


Figure 3.2.1. – Laser Sheet Schematic.

3.3. Experimental Techniques

3.3.1. *Flow visualisation and laser induced fluorescence (LIF)*

Flow visualisation studies were accomplished using the LIF technique. A soluble dye (BASF fluorol yellow 80) is dissolved in the mineral oil of one stream. This dye fluoresces when excited by light with a wavelength range of 460 to 530 nm (provided by the Ar-ion laser). In this study, the two streams of mineral oil to be mixed were called A and B. Stream B was dyed and mixed with the clear A stream. The thin laser light sheet was directed through the mixer (radial or axial cross-sections) exciting the dyed fluid. The resulting 2D flow visualisations are recorded with a CCD video camera (Panasonic WV310) and a SVHS video tape recorder (Panasonic AG1830). Still photographs were obtained with a Nikon F3 35-mm camera with 400 - 1600 ASA film. The benefits of this technique are:

- 1) the entire flow field may be visualised,
- 2) the mixing process is readily visible,
- 3) the method is non-intrusive,
- 4) the degree of mixing can be quantified using digital image analysis techniques.

However, the major draw back of this method is that the resulting mixture can not be separated once mixed. Therefore, clear mineral oil is continuously used up while the dyed oil accumulates requiring disposal.

3.3.2. Image Analysis From LIF Visualisation

From the recorded LIF visualisations on video, images were acquired via a 'frame grabbing' technique. Frame grabbing refers to the converting of the analogue signal from a video recorder to a digital signal that is recorded in computer memory. Each video frame contains 480 lines that are converted to 512 pixels per line where each pixel is 8 bits long. These frames are grey-scale images having a range of 0 to 255 in pixel intensity with 0 being pure black and 255 being pure white. The image capture board was a TSI 600066 PCI analogue to digital installed in a Dell dimension XPS 166 computer with the software TSI Insight NT 1.0 (PIV and image acquisition software). A second software package, Sigma Scan/Image measurement (Jandel Scientific), was used to analyse the digitized image quantitatively. This package allowed pixel intensity, distance (striation width), perimeter (interfacial area) and area measurements over a stored image. The perimeter and area measurements use a pixel threshold criterion to determine the edges of black and white in a grey-scale image. The threshold pixel intensity was set at 180. Any intensity above this threshold was classified as dyed fluid, and below it, as clear. This threshold value was determined from measuring the pixel intensities of the pure species in the mixer. Striation thickness was measured at radial planes at the beginning and end of each element. The beginning and end of each striation was determined by the pixel intensities. If there was a jump over 20 units in pixel intensity between neighbouring particles, this point marked the interface between striations. The distances between these interfaces was measured and classified as a striation width.

3.3.3. *Laser Doppler Anemometry (LDA)*

Laser Doppler Anemometry (LDA) was used to determine the velocity field in the static mixer for a limited number of cases. A brief overview of the principles of LDA follows, however, greater detail regarding the theory and practice of LDA is given in Drain (1980) and Durst et al. (1981).

The LDA apparatus shown in Figure 3.3.3.1. consists of a 25 mW helium-neon (He-Ne) laser, an optical train, frequency selector, counter processor and a computer. The laser beam enters the optics train where it is split into two equally intense beams. One beam passes through the Bragg cell (to shift its frequency) and both then pass through a beam expander and finally a focusing lens. The end of the optic train consists of a receiving lens and a photomultiplier tube (PMT). The underlying principle behind LDA is the creation of an intersection of two laser beams causing a fringe pattern of “light and dark” bands due the interference of the wave fronts. These fringes correspond to the constructive and destructive interference pattern created when two light waves intersect. This intersection region is called the probe volume. Small particles (1–10 μm), which scatter the light of the probe volume as they pass through the light and dark bands, are used to seed the flow. The reflected light from the particles is focused onto a photomultiplier, which causes the PMT to produce a voltage signal with the frequency of the reflected light. The LDA counter resolves the frequency of the voltage signal. This frequency is called the Doppler frequency and is related to the velocity of the particle intersecting the interference pattern of the probe volume by

$$f_d = \frac{2u}{\lambda} \sin\left(\frac{\alpha}{2}\right)$$

where

f_d frequency obtained at the detector

λ wavelength of the laser light

u particle velocity to be measured

α angle between laser beams

and

$$\alpha = 2 \tan^{-1} \left(\frac{L_B}{2F} \right)$$

where

F focal length of lens

L_B beam separation distance.

Since all of the geometric parameters and the wavelength of the light are known, the velocity, u , is directly proportional to the Doppler frequency.

A fundamental problem with LDA is the discrimination of the directionality of the measured velocity. With this technique, the Doppler frequency created is greater or lower than the reference wavelength of the laser. However, the measured frequency is the difference between the Doppler shifted and reference frequencies. Therefore, it is only possible to determine the magnitude of the velocity but not the direction. Hence, the technique of frequency shifting is utilised and requires a Bragg cell to shift the frequency of one of the laser beams.

Figure 3.3.3.2. illustrates the technique of frequency shifting. The frequency value on the y -axis corresponds to the frequency at the detector, f_d . The direction of the fringe motion created in the probe volume is set to oppose the mean positive flow. Frequency shifting permits the Doppler negative and positive values to be discriminated since the corresponding beat frequencies after shifting the reference are $(f_i - f_D)$ for positive Doppler shift and $(f_i + f_D)$ for the Doppler negative shift. Typically, most Bragg cells operate at a fixed shift frequency of 40 MHz and the frequency is down mixed to a value corresponding to two times the maximum positive mean velocity to ensure that the frequency shifts do not become ambiguous (or, if known, two times or greater the maximum negative velocity of negative mean velocities). The shift frequency was chosen to a velocity twice the maximum axial velocity of the parabolic profile in a semi-circular duct for the static mixer.

The data sampling frequency is selected according to the measured data rate and percentage of these data measurements that are validated. For the static mixer, the data rate was around 1 kHz and the percent of validated signals 50%. Therefore, 1000 points were being measured per second and only 500 were valid. As a result, according to Drain (1980), a sampling frequency of one-tenth the validated data rate should be used to ensure that true velocities are measured. Hence, the sampling rate was set at 50 Hz. However, measured velocities occasionally are not valid because of overlapping signals and must be discarded. Therefore, the LDA uses a sample and hold system where it keeps the last validated measurement in memory and places that as the next measured velocity if the velocity measurement just made must be discarded. Every time a valid measurement is

made, it replaces the current velocity in memory. When the probe volume is moved into a curved solid wall, the light is diffracted causing no light emissions to be detected by the photomultiplier (PMT). Since no signals are created by the PMT, the LDA holds the previous validated result. To distinguish velocities that are zero or false readings, the root mean square (rms) of each measurement are determined. If the rms value is too low ($\text{rms} < 10^{-3}$), then the measurement is discarded since the velocity measured is only the result of the velocity held in memory (usually this corresponds to a measurement in an element).

The choice of particles to seed the flow with is not as trivial as it may appear. Signal to noise ratios and visibility factors are dependent on the size of particle to fringe spacing ratio. The complexities involved in determining the optimum ratio of particle size to fringe spacing is given in Drain (1980). The optimum ratio is 0.586 and consequently indicates that for this experimental setup, the particle size should be in the order of one to two microns in diameter. The mineral oil used as the working fluid was filtered of all particles above $1\mu\text{m}$ and then was seeded with mono-dispersed poly(divinylbenzene) microspheres of 1 or $2\mu\text{m}$. These particles had a density close to that of the oil and hence, gave an accurate representation of the fluid velocity.

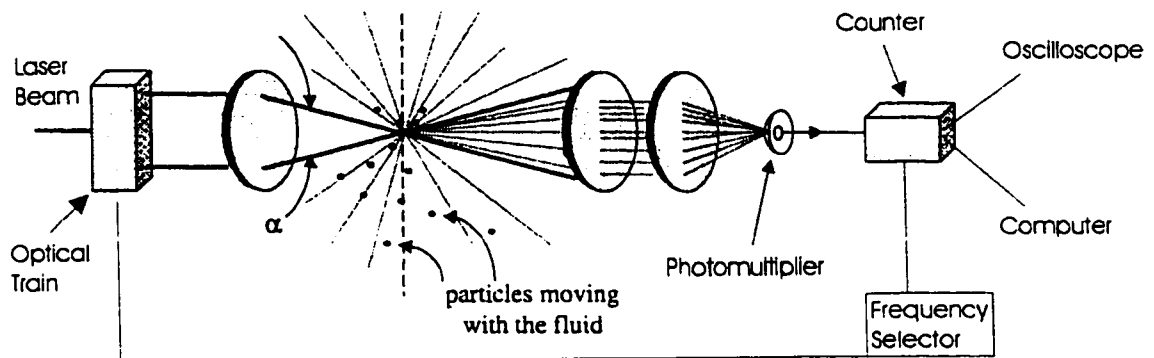


Figure 3.3.3.1. – Schematic of Laser Doppler Anemometry Apparatus [TSI (1998)].

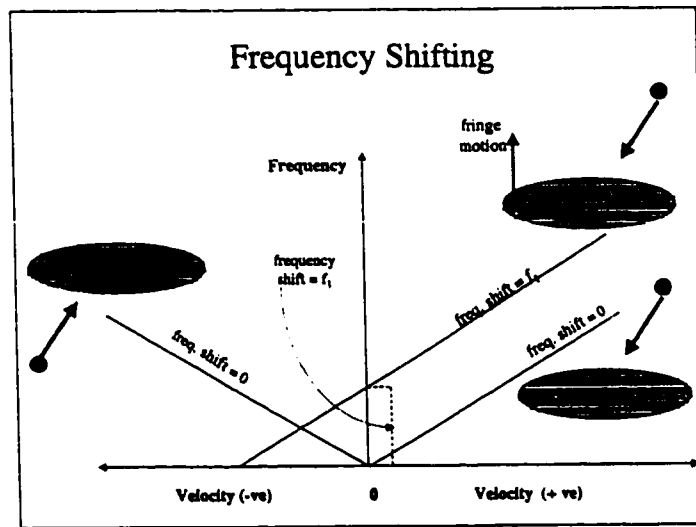


Figure 3.3.3.2. – Schematic of Frequency Shifting Technique for LDA [TSI (1998)].

3.3.4. Particle Image Velocimetry (PIV)

Particle image velocimetry falls within a broader range of experimental techniques known as pulsed-light velocimetry (PLV). This class of measuring techniques has a commonality in that all members observe the motion of small marked regions of fluids. These fluid elements are observed at two or more times and the marked fluids are recorded on an image or images. Markers can be classified according to their size: molecular or particle. Molecular markers can be either fluorescent or photochromic and are analysed separately of particle markers. Further reading on these techniques can be found in Miles et al. (1989). The fluid elements that are marked by particles are illuminated through a pulsed light source and recorded giving either a speckle pattern or particle trajectory image.

All of the PLV methods return to the fundamental definition of the velocity for its measurement and estimate the local velocity, u_x , based on the displacement of the marker, Δx , over the time, Δt , between pulses.

$$u_x = \frac{\Delta x}{\Delta t}$$

The technique of particle image velocimetry, PIV, follows the movement of particles, which are of neutral density and hence represent the flow field well.

The benefits of PIV are:

- 1) an entire flow field can possibly be measured in a single image,
- 2) the method is non-intrusive,

- 3) reduced times for measuring flow fields compared to point-wise measuring methods.

The drawbacks of this technique are:

- 1) the loss of time dependent structures due to computer and illumination limitations,
- 2) the weighting of the technique towards higher velocities for flows with strong velocity gradients.

The light source can be pulsed at distinct frequencies and periods. In the double pulse operation mode, the image obtained would contain pairs of particles as seen in Figure 3.3.4.1. These pairs of particles are analysed using various techniques to resolve the velocity components. These techniques can include Yonge's fringes coupled with optical fast Fourier transforms (FFT) to digital FFT. The various techniques of analysing PIV images are discussed in a review article by Adrian (1991). The technique used in this thesis was the cross-correlation method and is discussed in the following section.

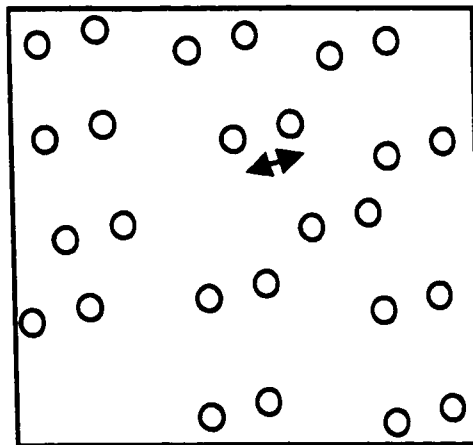


Figure 3.3.4.1. – PIV image containing a Doubled Pulsed Image.

A Coherent 6W argon ion laser was used as the light source to illuminate the flow. A laser light sheet was created through the use of cylindrical lenses as discussed in section 3.2. The laser source was pulsed using a TSI pulse modulator (in essence, a beam ‘chopper’). The modulator allows the pulse frequency and the period of the pulses to be manipulated allowing for a wide range of flow fields to be analysed. Metal-coated particles were mixed in with the flow and caused the laser light to be scattered. A Panasonic CCD video camera was used to monitor the flow field. The modulator was connected to a frame grabbing board in a computer and to the CCD video camera. The pulse frequency and period were set and a trigger switch was activated between the computer and the chopper. When the laser light sheet was pulsed, the trigger switch signalled the computer to start taking the data from the camera. The pulsed image was captured via the frame grabbing board [explained in section 3.1.2.] and stored for later image analysis to obtain the velocities.

3.3.5. Cross-Correlation, PIV

Cross-correlation requires two images, each having a single pulse, to be captured within a short time interval, Δt . These two images are superimposed creating a single image, which would appear to have been double pulsed (Figure 3.3.4.2.). This technique has a significant advantage over the double pulse technique. Namely, the directionality ambiguity is resolved as each pulsed particle is labelled as 1 or 2, depending which image it originated from. Therefore, the velocity calculations can only occur for pairs of particles labelled as 1 and 2. A double pulse technique could not be used since there is no

a priori knowledge of the velocity field (as seen in Figure 3.3.4.1.). Therefore, there is no way of determining which was the first pulse and hence the direction of the particle. The double pulse technique is usually coupled with image shifting techniques to resolve directionality [Adrian (1991)]. Image shifting is similar to frequency shifting in LDA.

A detailed discussion of the PIV technique and procedure is given in chapter 4.

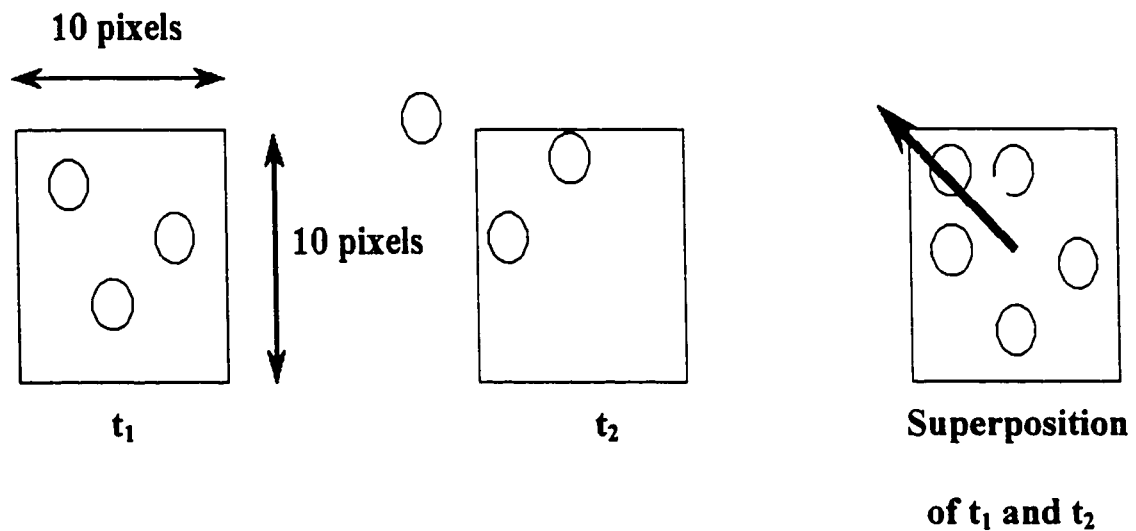


Figure 3.3.4.2. - Principle of particle image velocimetry: cross correlation.

3.4. Experimental Procedure Static Mixer

3.4.1. Flow Visualisation

For the first inlet condition, the two entering streams into the static mixer were kept separate by a divider plate in the mixer to ensure a fully developed flow entering the mixing zone. Their flow rates were controlled by variable speed progressive pumps

(Moyno # 33104) and rotameters (Brooks 8602-162153). Initially, the dyed stream flowed continuously through the mixer while the clear stream was kept within a recirculating circuit. Once the camera was positioned and focused, the clear stream was fed into the mixer until sufficient video images were recorded for image analysis. The exiting stream from the mixer was diverted at the same time such that the resulting mixture was accumulated instead of returning to the reservoir of dyed oil. This mixture was then either reused or discarded. The density of the mineral oil was given by the supplier to be 840 kg/m^3 with viscosities ranging from 0.003 to 0.4 Pa·s (3 to 400 cP). The viscosity for these experiments ranged from 3 to 70 cP and were measured using a Brookfield LVT viscometer.

For the second inlet condition, the Komax L/H[®] (Figure 3.1.1.2.) distributor, the bulk of the flow (clear stream) was fed through the larger two inlets while the dye was fed through the smaller inlet. The flow rate ratio of the dyed stream to clear stream (bulk) was set at 0.2 for a viscosity ratio, μ_{ratio} , of dye to clear stream of 0.1. The second case run through the Komax L/H[®] distributor was for a flow rate ratio of 0.25 and a μ_{ratio} of 1.

3.4.2. LDA

For LDA experiments, the first inlet condition (splitter plate) was used. The two streams were clear and flowed continuously through the mixer. LDA studies were conducted for a flow rate ratio and viscosity ratio of one for the entering streams (i.e. the same fluid was used in both streams). The apparatus was mounted on a computer controlled stage that could be moved in the three Cartesian co-ordinate directions with an

accuracy of $\pm 5\mu\text{m}$ per co-ordinate direction. This stage was fully automated and integrated with the LDA software. Therefore, a data collection grid could be set up and velocities would be measured at these points. The LDA software collected 1000 data points for each grid node and an average velocity of these measurements was then determined and recorded. The instantaneous monitoring of the Doppler shifted frequencies indicated a steady flow regime. In addition, since the flow regime was steady and laminar, a time series analysis of the collected data was unnecessary. The Reynolds number, based on a circular tube, was determined using the total flow rate of the two streams. This value ranged from 20 to 100 for the LDA measurements.

3.4.3. PIV

The static mixer was placed on a stage that had an accuracy of $\pm 0.05\text{mm}$. The flow rate was set such that the Reynolds number was 0.1. The viscosity of the oil was $1\text{ Pa}\cdot\text{s}$ and the aspect ratio of the elements used was 1.5. The mixer was measured over a series of 2D planes constant in x or z , thereby obtaining the y and z -components and y and x -components of velocity respectively. The pulse separation time used was 20 ms. Thirty pairs of images were taken for each plane. The images were cross-correlated and the velocities at each point were averaged.

3.5. Experimental Procedure for Twin Screw Extruder

3.5.1. Flow Visualisation

Flow visualisation studies were accomplished using the LIF technique described in section 3.3. A soluble dye (BASF fluorol yellow 80) dissolved in mineral oil was introduced through one of the dye ports. The dye location for geometry C (Figure 3.1.2.1a.) was introduced at the front edge of the kneading disc section and for geometry D (Figure 3.1.2.1b.) one conveying element in front of the kneading disc section. A thin laser light sheet was directed through the mixer (creating axial cross-sections) exciting the dyed fluid. The resulting 2D flow visualisations were recorded with a CCD video camera (Panasonic WVB310) and a SVHS video tape recorder (Panasonic AG1830). Images were then acquired using the frame grabbing technique describes earlier. The flow rates for the experiments conducted are listed in Table 3.5.1.1.

Geometry	Bulk Flow Rate (mL/s)	Bulk Viscosity (Pa·s)	Dyed Flow Rate (mL/s)	Dye Viscosity (Pa·s)	RPM
C	5	1.00	1	.55	100, 150, 200
D	5	1.00	1	.55	100, 150, 200

Table 3.5.1.1. – Flow Visualisation Experimental Conditions.

3.5.2. *Image Analysis from LIF Visualisations*

There are many different methods to analyse digitized images for information relating to flow and mixing. A good measure that helps determine the axial dispersion of the dye is the normalised intensity measure. The normalised intensity is calculated by taking the intensity of the dye in the visualisations and dividing by the intensity for pure dye (previously calibrated) (Section 3.3.2. explains digitised images and intensity). This value corresponds to dye concentrations where the normalised intensity of 1 is pure dye and 0 corresponds to the pure bulk stream. Each measurement is the average intensity over 5 pixels in the radial direction for each location in the axial direction. Intensity measurement locations are shown in Figure 3.5.2.1.

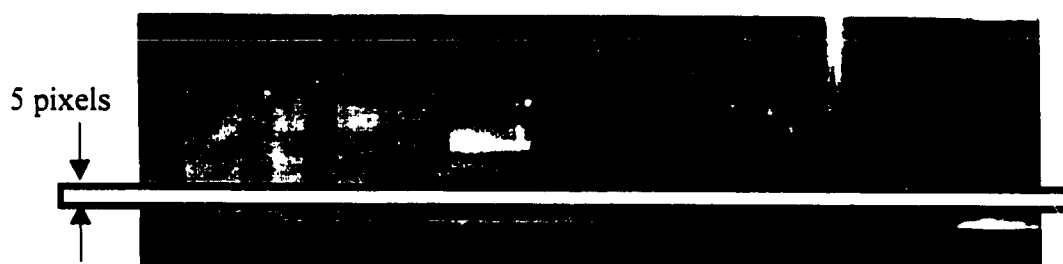


Figure 3.5.2.1. – Image Analysis, Intensity Measurements Location.

3.5.3. *PIV*

A laser light sheet was passed through the TSE along constant axial planes (constant in the z co-ordinate). This is illustrated in Figure 3.5.3.1. at a constant plane of $z=25$ mm ($z=0$ mm at bottom of the barrel). Thirty instantaneous image pairs were

obtained for each location in the TSE for a fixed rotation angle of the screws (90 degrees shown in Figure 3.5.3.1.). The images were interrogated with TSI's Insight NT 1.0, which determined the velocity vectors over each pair of images. The interrogation area used was 10 by 10 pixels in size, which corresponds to an actual area of about 1 by 1 mm. The kneading block, composed by 5 discs staggered at 45° in a forward configuration, have a total length of 20 mm. As a result, the mesh chosen for velocity measurements was a 21 by 21 node such that the areas of interrogation did not overlap as shown in Figure 3.5.3.2. The thirty sets of data were processed giving thirty instantaneous flow fields for one specific orientation of the discs. The 30 velocity measurements were averaged for each node.

Experiments were carried out for different experimental conditions: varying flow rate, rpm and the geometry of the elements before and after the region of study. The conditions for these experiments are listed in Table 3.5.3.1.

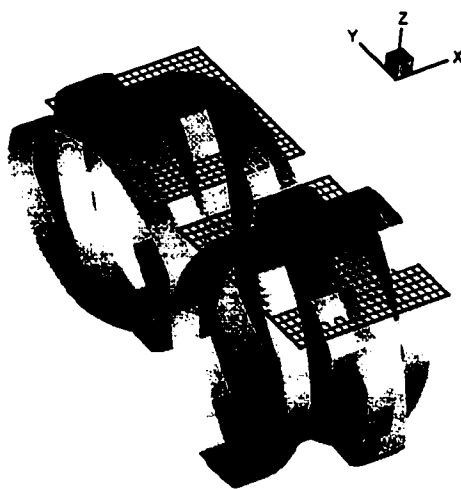


Figure 3.5.3.1. Light Sheet Plane at $z=25$ mm.

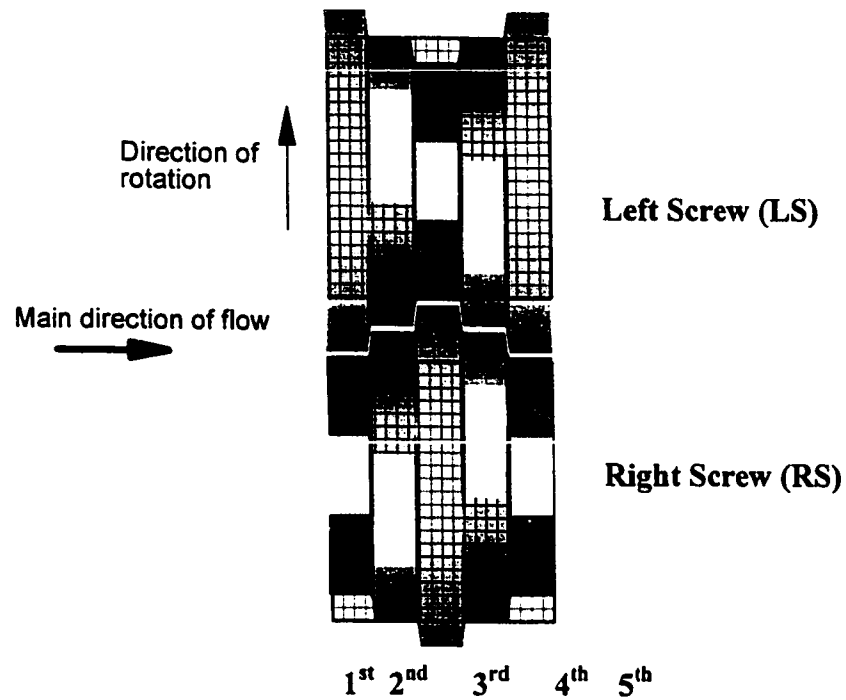


Figure 3.5.3.2. View of Interrogation (Data) Mesh.

Rpm	Flow rate (mL/s)	Location	Geometry
30	5.0	25mm	A
60	5.0	25mm, 20mm, 15mm	A
100	5.0	25mm	A
150	5.0	25mm	A
60	8.5	25mm	A
100	8.5	25mm, 15mm	A
200	8.5	25mm	A
60	5.0	25mm, 15mm	B
100	5.0	25mm	B
60	8.5	25mm	B
100	8.5	15mm	B

Table 3.5.3.1. - PIV Experimental conditions.

4.0. Validation of PIV Technique

4.1. Introduction

Before the implementation of PIV to the flow fields of interest in this study, the technique needed to be validated and a study of operational parameters had to be made. This was the main motivation for studying the jet driven recirculation cavity. Since data exist from previous studies made by Johnson (1995) with LDA, a comprehensive evaluation of the PIV technique was feasible, and the sensitivity of the set-up to operational parameters could be studied.

The recirculation cavity is a well defined flow field and is depicted in Figure 4.1.1. The flow is jet driven, with a turbulent wall jet entering from one corner of the cavity and exiting at another corner. The entering wall jet drives the recirculation with high velocity along the walls and a fairly stagnant zone in the middle. This flow is of interest for a number of applications: combustion chambers, ventilation and cooling of nuclear reactors. The flow field is considered to be fairly two-dimensional and presents a well defined problem for the PIV measurement technique. With the high velocity gradients, the PIV technique will be well tested.

This study focuses on the cavity examined at the sensitivity of the parameters in the PIV set-up, and helped to determine the operational procedure for measurements in the

ICRTSE and static mixer. The key parameters are time separation between laser pulses, signal to noise ratios, interrogation areas and particle size.

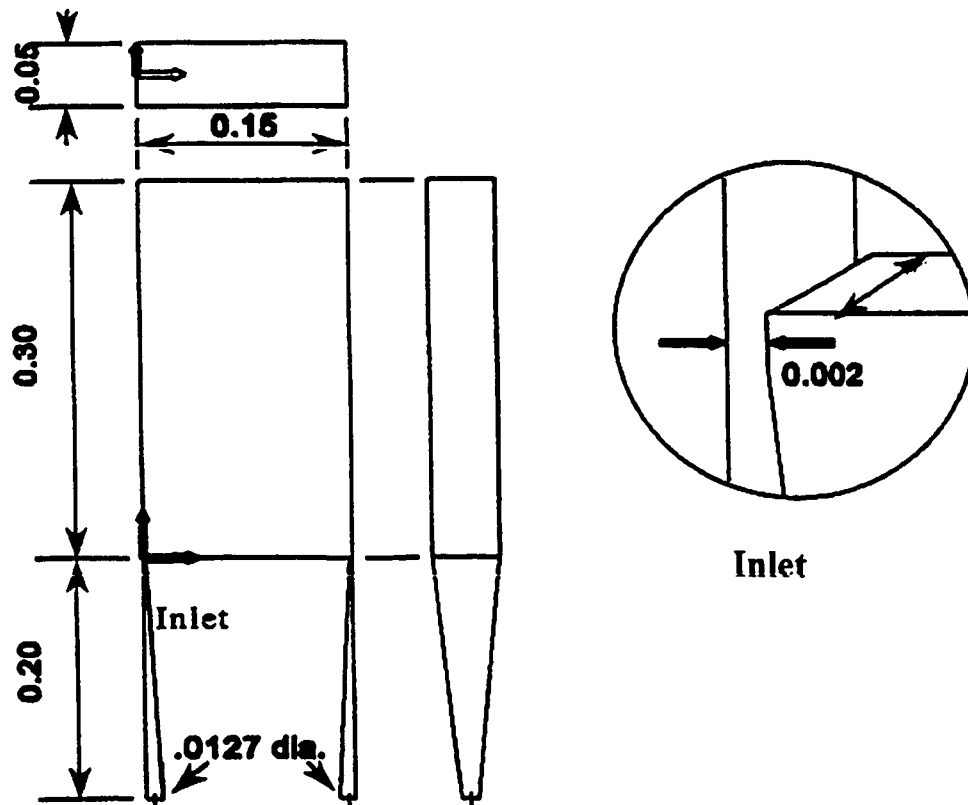


Figure 4.1.1. – Recirculation Cavity (units are meters) from Johnson (1995).

4.2. Background

PIV has been discussed briefly in chapter 3 to give a flavour of the technique in very general terms. This section will give more specifics on the technique. The general procedure used to set-up the PIV experiments is given in detail step by step.

4.2.1. PIV

There has been a tremendous amount of work that has concentrated on trying to improve PIV, to reduce its errors [Boillot and Prasad (1996), Sinha (1988)] and improve the range of measurable velocities. More recently, research focused on techniques that measure all three components simultaneously, using multiple cameras or orthogonal imaging [Cheng et al. (1984), Racca and Dewey (1988)], or single camera or in plane determination [Stolz and Köhler (1994)]. However, these improvements and refinements in the technique have filtered into commercial PIV equipment fairly slowly. The power of this technique can be utilised only when a strong understanding of the influential parameters on the technique are understood.

As with most measurement technologies of fluid flow, some *a priori* knowledge of the velocity field must be available. This includes the relative velocity range, the magnitude of velocity gradients and the relative strength of back flow. All this knowledge is critical in setting up the experiment. There is an iterative approach to achieving the best PIV set-up but to be in the right ballpark at the beginning, some previous knowledge is needed.

The general PIV measurement process is comprised of four steps:

- 1) seed the flow field with small tracer particles,
- 2) illuminate the flow field,
- 3) record the visualisation via frame 'grabbing' from video,

- 4) and determine the velocity from correlation of grey scale values on digital images.

Figure 4.2.1. shows a general picture of a set-up of PIV illustrating these steps.

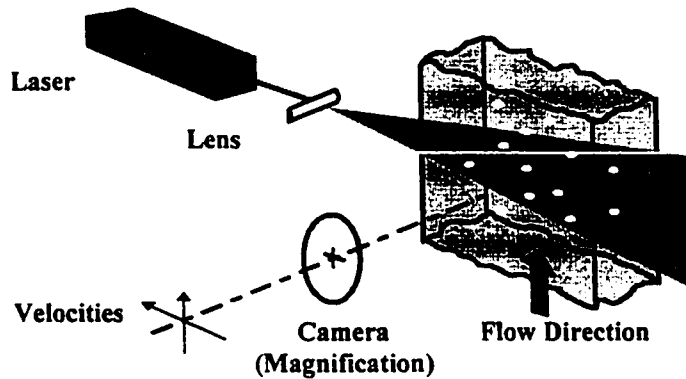


Figure 4.2.1. Schematic of PIV Set-up [Dantec (1998)].

4.2.2. Errors in PIV

The main sources of error in the PIV technique are [Boillot and Prasad (1996)]:

- 1) random error due to noise created during frame recording and digitization, and subsequent noise in the interrogation of the image;
- 2) acceleration error caused by the measurement of the Eulerian velocity (the acceleration of particles within the interrogation region);
- 3) gradient errors caused by the rotation and deformation of the flow within the interrogation region;
- 4) bias error due to the choice of the correlation peak detection algorithm;

- 5) tracking error due to the inability of the particle to faithfully follow the flow without slip;
- 6) pulse separation error caused by the mechanical shutters used to pulse the light which have a finite duration of time;
- 7) particle image blurring caused by the distance moved by the particle over the light pulse duration.

Random error due to noise can be minimised but can not be eliminated and is therefore inherent for PIV. This noise is usually the result of scatter light reaching the CCD chip of the camera. This scattered light can be minimised with the aid of shields and proper set-up of the beam modulator. This is explained further at step 7 in section 4.3.2. The noise created by the correlation of particle images not belonging to the same pair can not be eliminated.

The acceleration and gradient errors are inherent in PIV and can be minimised by choosing an interrogation region size (the area over which the local fluid velocity is measured for one point) that minimises the gradients within it and the choice of a time separation that reduces the error due to acceleration.

Detailed discussion of the error in estimating the location of the signal peak to sub-pixel accuracy by various algorithms is discussed in detail in Lourenco and Krothapalli (1995).

Tracking errors can be minimised with the choice of particle. This is discussed in more detail in section 4.3.2., step 1. Essentially, the optimal particle has good light reflective properties and is neutrally buoyant, thereby eliminating slip.

The light pulse used to illuminate the particle has a discrete duration usually $1/10$ of Δt (pulse separation). Within the pulse duration, the particles will move some finite distance. This causes blurring of the particle on the image. The error due to the accuracy of the time separation between the light pulses is usually fairly small for the current technology used. The electro-mechanical shutters or light choppers usually have an error of $0.001\Delta t$.

4.3. Experimental Design

4.3.1. Experimental Procedure and Set-up

Figure 4.1.1. shows the geometry of the recirculation cavity. The dimensions of the cavity are 300mm by 150mm by 50mm. The cavity was fabricated from clear acrylic and the recirculating fluid was water. A 0.5 Hp centrifugal pump was used to pump the fluid around the recirculation circuit shown in figure 4.3.1.1. A 12.5 mm needle valve was used to control the flow rate precisely, and a calibrated rotameter was used to measure the flow rate. The temperature of the tank of water was kept constant using a water cooling coil submersed in the tank.

The laser light sheet for PIV was set at a Z plane of 25mm, through the centre of the wall jet. Specifics on the PIV procedure are given in section 4.3.2.

The flow rate was set to 70 mL/s matching the conditions of the LDA experiments conducted by Johnson (1995). The temperature of the water was kept constant at 20°C.

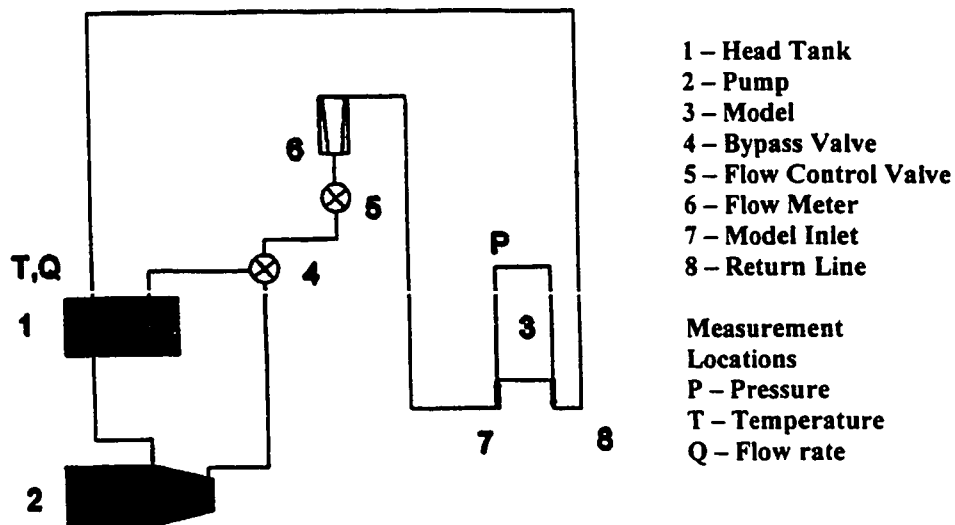


Figure 4.3.1.1. – Recirculation Pumping Circuit.

4.3.2. PIV Procedure and Set-up

This section describes the steps involved to set-up the experimental PIV measurement of a general flow field. The procedure outlined is described as generally as possible for the PIV set-up shown in figure 4.3.2.1. utilising the software by TSI, Insight NT[®] 1.0. (Other software programs are similar in their respective set-ups.) The description is outlined as a series of steps.

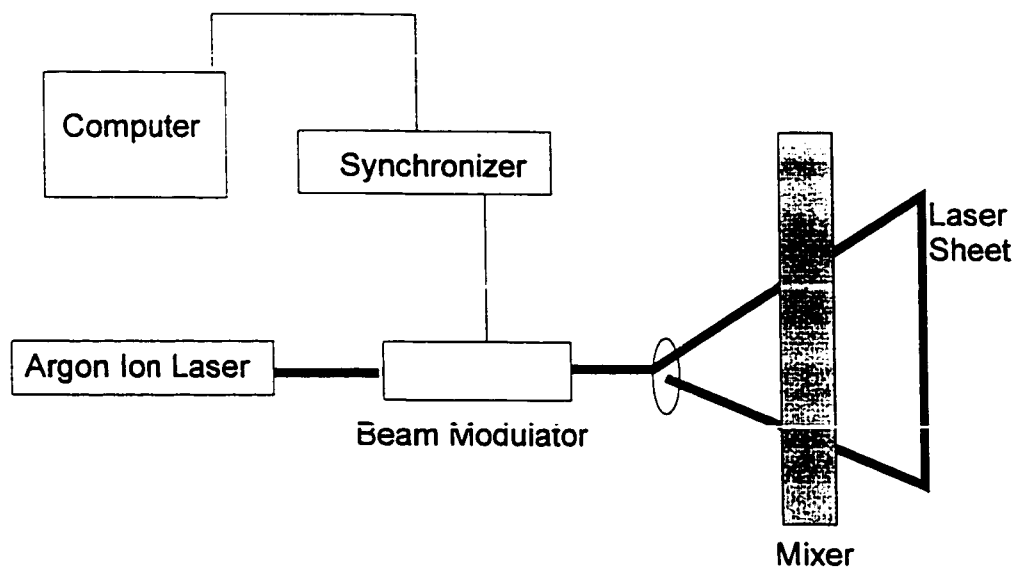


Figure 4.3.2.1. - PIV Set-up Schematic.

1. Choose Particle Size and Type.

The particles chosen must faithfully follow the flow with negligible slippage and buoyancy effects. LDA typically uses particles in the 1-10 μm range whereas PIV uses particles in the 10-100 μm range. This is mainly due to the optics which observe the scattered light. PIV is limited by the sensitivity of the video camera imaging chip or photographic film speed and the power of the illumination source (laser), thus, larger particles are preferred.

Typically, the solid particles with high reflective capabilities and in the range of 10-100 μm have problems with high settling velocities (e.g. TiO_2). As a result, neutrally buoyant particles with good reflective capabilities have been developed to reduce these difficulties. These can be solid or hollow. The trade-off for the latter has been reduced light scattering abilities compared to solid particles.

The particles chosen for these experiments were 50 μm hollow glass spheres, which were neutrally buoyant in water and were coated with aluminium to scatter light better.

2. Calculation of Magnification

The magnification, M , is set such that the particle in the camera video frame is approximately 0.5 to 2 pixels in diameter. Given that the chosen particle size is 50 μm and that the least magnification can be 0.5 pixels/diameter of the particle, the magnification is calculated to be 100 μm / pixel for the maximum value for M .

Digital video images can range in size but for this set-up the video frames acquired from the video camera and the frame grabbing board was 480 pixels by 560 pixels. With the given magnification, M , the physical viewing area is thus limited to be 48 mm by 56 mm (for particles with diameters of 50 μm). Given these limits the video camera optics can be chosen to give the required magnification. For these experiments a 50 mm camera lens coupled with a 10 mm tube extension gave the desired magnification.

3 Choose Interrogation Spot Size

Each digitised video image is divided into a mesh of interrogation regions (Figure 4.3.2.2.). Over each interrogation regions or 'areas', the fluid velocity is estimated for the centre of the interrogation region or 'spot' by correlating the particles that are inside

the area with the next video frame for the same area. The average Eulerian velocities in the two co-ordinate directions are estimated from the mean displacement of the particles in each co-ordinate direction.

The interrogation spot size can be chosen to be in the range of 0 – 144 pixels (For TSI NT[®] 1.0). The size is set based on some prior knowledge of the flow and the approximate time separation between successive light pulses. This step requires some iteration with the 4th step in which the time separation between the pulses is calculated. The spot size can be a square or rectangle, with any ratio between length and width. This allows the length of the rectangle to be oriented in the direction of flow. For these experiments due to the strong two dimensionality of the flow, the interrogation spot was kept as a square.⁷

As the size of the interrogation spot increases, the process time increases since more particles have to be located and correlated with the other particles in the same interrogation area. Therefore, there is a balance needed between minimising the spot size and having the particles travel distances at least one to two diameters such that the particle pairs may be detected [Boillot and Prasad (1996)]. Also the maximum distance travelled by particles should be approximately thirty percent of the interrogation spot size's smallest side. For these experiments this was 3 pixels for a 10 by 10 pixel interrogation spot. The reason for this maximum limitation is that the interrogation spot for the second frame is located in the same co-ordinates. Therefore, as in the case with auto-correlation schemes, the number of particles that fall outside the interrogation spot

on the second frame needs to be limited [Keane and Adrian (1990)]. This permits an accurate representation of the velocity in the interrogation area.

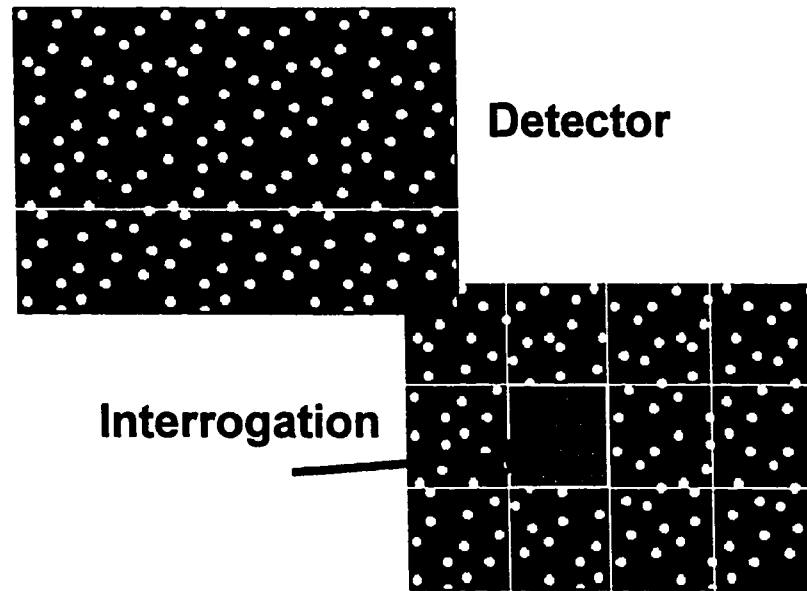


Figure 4.3.2.2. – Interrogation of PIV Images, Interrogation Area (Grey)
and Interrogation Mesh.

4 Calculate Time Separation Δt Between Light Pulses

The time between successive light pulses is calculated by restricting the maximum distance travelled by the particle to be only 3/10 of the length of the interrogation spot, Δx_{int} . Therefore, the maximum local velocity, v_{max} must be estimated in order to calculate Δt . The equation that estimates Δt is [Keane and Adrian (1990)]:

$$\Delta t = \frac{\Delta x_{\text{int}} M(0.3)}{V_{\text{max}}}$$

This equation gives a very good starting point to obtain the optimum Δt . Δt can then be adjusted in order to maximise the correlation peak, reduce noise and maximise the illumination of the particle.

5 Calculate Pulse Delay Sequence

Each video frame is composed of an even and an odd field. That is each video frame signal sends the pixel information for all the odd lines in a video frame first and then all the pixel information for even field second. The composition of these two video field comprises a single image.

The video camera's signal is used as the trigger for the synchronizer when it is placed in Video Camera Triggered Mode. The synchronizer uses the even field of the video frame as its trigger. In order to capture two images with a single pulse between them and have a small Δt between pulses, the pulses must be synchronized with the video camera frame rate. Therefore, the timing master for this set-up is the video camera's 30 frames a second or 33 ms/frame. To achieve the desired two frame cross-correlation, the first pulse must be delayed until the end of the first frame and the second pulse generated at the beginning of the second frame. Figure 4.3.2.3. describes graphically the technique of pulse delay. The benefit of this technique is that an ordinary CCD camera (30 Frames / Second) may be used rather than an expensive PIV camera. However, the major drawback to having the video camera be the timing master is that a maximum of 15 velocity measurements per second can be made (15 image pairs). This can also be less if

the computer frame grabbing board and memory on the board are limited. For the equipment described, 30 frames per second was the maximum frame digitization rate but the maximum number frames that could be stored at this frame rate was 12. This limits the set-up to 6 measurements (12 image pairs) with separation time between measurements of 66 ms. This was not a major concern for the static mixer or recirculation cavity since time dependency of the velocity field was not as important. However, this limited the measurement in the twin screw extruder, whereby there was at least 66 ms between measurements. This was not satisfactory for determining the velocity fields time dependency.

The minimum pulse separation time that may be used is limited by the frame straddling time. This is the time required by the camera to refresh the image information, which is to then be sent out as the next frame (Figure 4.3.2.3.).

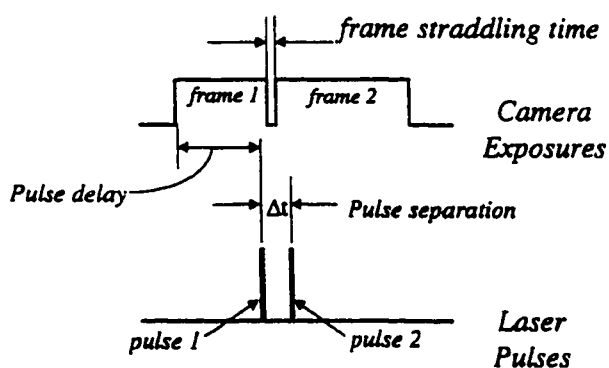


Figure 4.3.2.3. – Illustration of Pulse Delay for a Standard CCD Camera.

6 On-Line Measurement with Parameters

Once this point has been reached the equipment set-up should be tested. Two images are taken and cross-correlated to observe the quality of the correlation peaks. A schematic is shown demonstrating the correlation peak and its relation to the mean particle displacements in Figure 4.3.2.4. The position of the peak in the correlation plane is the same as the mean particle displacement. Insight NT[®] has a Status Box that permits the operator to monitor the correlation spectrums. This requires the operator to have *a priori* knowledge of good and poor correlations. Figure 4.3.2.4. shows a good correlation with very little noise that would be seen as secondary spikes in the correlation plane. If there is no peak or the peak is in the centre of the correlation spectrum, there are a number of possible errors. The particles may have travelled out of the interrogation spot and therefore the time separation needs to be reduced and the pulse delay is changed accordingly. If the time separation is already at the lowest possible value for maximum illumination, a solution is to increase the area of the interrogation spot. This change would increase the processing time for each set of images, thereby decreasing the data rate. With a strong peak at the centre giving a very small velocity or zero velocity, the time separation needs to be increased.

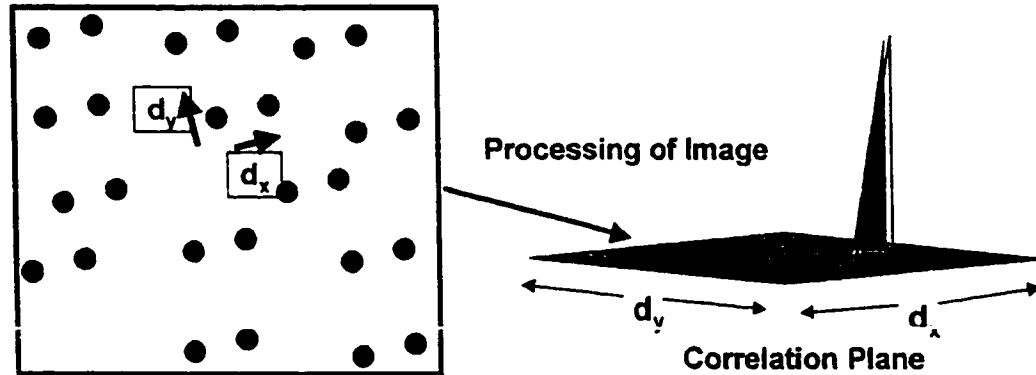


Figure 4.3.2.4. – Schematic of Correlation Plane [Dantec (1998)].

7 Check Signal to Noise Ratios (SNR)

There are three SNR values that must be set to create bounds for the correlation. That is, if a correlation peak is too weak then the measurement is excluded. These parameters can be adjusted on-line as with the time separation. The operator will need to use his or her own judgement to determine the appropriate values for the SNR values. The three SNR values are:

SNR1 – The Velocity peak intensity divided by the zero peak intensity. (This is only adjusted for auto-correlation mode operation.)

SNR2 – The Velocity peak intensity divided by the first noise peak intensity.

SNR 3 – The Velocity peak intensity divided by the average intensity of non peak pixels (i.e. the summation of the pixels in the correlation area excluding zero

peak, and velocity peak areas divided by the number of pixels in the correlation area).

The largest sources of noise are scattered light, noise created by analogue to digital conversion and poor set-up of the beam modulator. These sources can be reduced by careful set-up, especially of the beam modulator. This requires that the modulator only permit the primary beam to exit.

8 Take Measurements

The system is ready to take measurements. The post-processing or batch function of Insight NT[®] is described in detail in the operating manual [TSI (1997)].

4.4. Results

4.4.1 Influence of Separation Time Between Pulses

The guideline for setting the time separation between pulses is to take the smallest dimension of the interrogation spot and divide by the maximum velocity in the interrogation area and multiply by 0.3. This requires some knowledge of the velocity field. Unfortunately this is usually what the unknown is and as a result setting the time separation is quite difficult. Therefore, to some extent the process of setting the time separation is a process of trial and error. The time separation between pulses, Δt , is

optimised by checking the signal to noise ratios, SNR, of the correlation. The strongest peak or correlation is desired.

Even with previous knowledge of the velocity field in the recirculation cavity, choosing a separation time was not trivial. This was primarily due to the strong velocity gradients created by the wall jet. There was a velocity range from 0.5 m/s to 0.1 m/s over a distance of 10 mm at a constant y-plane of 60 mm which is the core of the jet. The interrogation area's smallest dimension was ~ 0.5 mm which corresponds to a range of Δt from 1 ms to 5 ms. However, from figure 4.4.1.1. at $\Delta t = 1$ ms the velocity gradient of the jet core was not well captured when compared to results at $\Delta t = 0.5$ ms. This can be attributed to the fact that the higher velocity particles at a time separation of 1 ms have a higher probability of leaving the interrogation spot over a sequence of two images. Hence, at a smaller time separation between pulses the particles have a less probability of leaving the interrogation spot.

At a smaller time separation, small velocities are difficult to measure, as the particles do not move sufficient distance to accurately determine the sub pixel displacements. Since the error in the interpolation schemes used to determine the sub pixel displacements have errors in the range of sub-pixels, for particles that have displacements in this range, the error can be quite large as results. This typically creates large variances in data. The correlation scheme used in TSI NT[®] 1.0 would show the error of small time separations by assigning a value of zero or extremely small ($\sim 10^{-8}$). This would then result in a lower averaged velocity than the true velocity. This is

illustrated in Figure 4.4.1. where the velocity profile flattens out ($\sim x = 10\text{mm}$), and the poor comparison of the PIV to LDA data at Δt of 0.5 ms. At the larger Δt of 1ms, the plateau in the velocity profile shows a better agreement between the PIV and LDA measurements.

The pulse separation time limit for this set-up is 0.5 ms due to the illumination strength. The argon ion laser produces a 5 W beam which then passes through the beam modulator where only the first order beam is used to illuminate the flow. This beam's power is anywhere from 5 to 20% of the initial beam strength. Therefore, the flow is illuminated with 1 W at the maximum. This corresponds to 0.05 mJ of energy for a 0.5ms pulse time separation where the pulse duration is only 1/10 of the pulse time separation. This value was used to set the pulse duration. For example if the pulse separation time was increased to 1 ms, the pulse duration could be reduced to a minimum of 5 percent of the pulse separation time. Therefore, this limits the error due blurring of the particle in an image (see section 4.2.2).

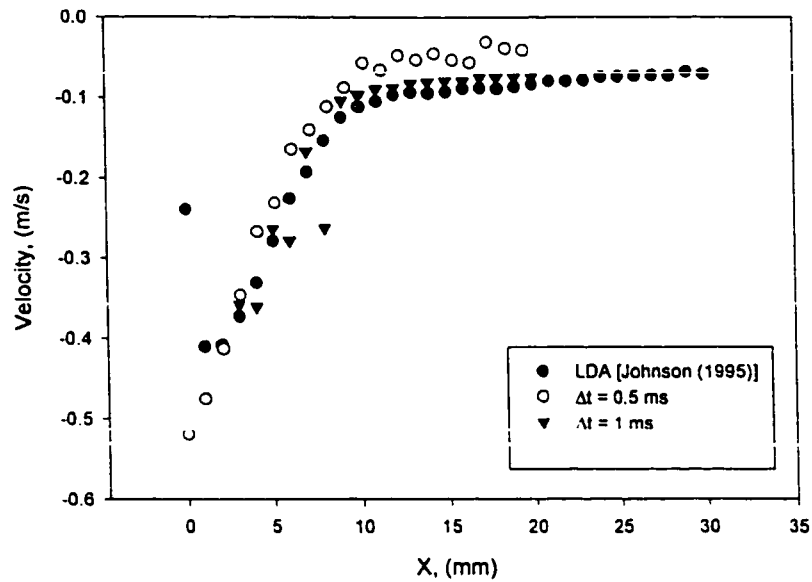


Figure 4.4.1.1. – Influence of Time Separation of Laser Pulses,
Wall Jet Core at $Y = 60$ mm.

4.4.2 Interrogation Size

Every set of images will be further broken into interrogation spots or areas. Each of the interrogation areas will be assigned as 1 grid point as depicted in figure 4.4.2. The particle velocities are determined for each area from the correlation of the sequential images and are averaged, giving the average velocity of the particles in each area. The choice of the size of this area is not trivial. Too small an area will result in particles leaving the interrogation area between sequential images. If the area is too large, there is an error associated with assigning a single velocity to a large physical area and hence loss of resolution as well as being computationally expensive. Hence, a discussion follows

that demonstrates some of the key parameters and choices for the selection of the interrogation size.

The technique of cross correlation can track all particles in an interrogation area from the first image to the second if the second interrogation area chosen is slightly larger than the first, and if the area is moved in the direction of the mean velocity. However, this technique is extremely expensive numerically and is an iterative process as the area must be moved once the velocity is approximated. Commercial software as a result (to keep processing times low) use the same size and location of the interrogation area as in the first image.

With this limitation in mind, setting an appropriate separation time can be quite difficult since at least 80 percent of the particles should remain within the interrogation area [Adrian (1991), Boillot and Prasad (1996)] to have strong correlations. Hence, small time separations between pulses are required. This in turn, if chosen poorly, leads to the bias and errors associated with too small of a Δt , as discussed in section 4.4.1.

These limitations resulted in the following general guidelines for setting up the interrogation size:

- 1) particle size of 0.5-1 pixel.
- 2) movement of particles not to exceed 3-4 pixels
- 3) interrogation sizes of 9 X 9 pixels or larger up to a maximum of 12 X 12.

With these guidelines the measurements of the recirculation tank were undertaken at various planes and compared to LDA. Section 4.4.3 discusses these results.

4.4.3 PIV and LDA Comparison

A schematic of recirculating cavity is shown in Figure 4.1.1. Fluid enters as a wall jet and travels downward along the vertical wall. Detailed velocity profiles [v (y -component of velocity) vs. x] are shown in Figures 4.4.3.1., 4.4.3.2., 4.4.3.3. and 4.4.3.4. for four different values of y . The maximum jet velocity occurs very near the vertical wall. As the jet travels it entrains low momentum fluid from the bulk of the cavity. The width of the jet increases and the maximum velocity decreases with increasing y . The maximum velocity gradient ($\partial v / \partial x$) occurs very near the wall. Very small velocities exist in the centre of the recirculation cavity. The data obtained with PIV is compared to the point-wise LDA data measurements of Johnson (1995).

Figure 2 shows the velocity profile at $y = 60$ mm (i.e. 60 mm from the entrance). The agreement between the PIV and LDA results is excellent in the wall-jet region ($0 < x < 10$ mm). The maximum velocity and jet width are in excellent agreement. The closest, that PIV measurements could be made at the wall, is approximately 0.5 mm. This would provide a large enough width for the interrogation area. (LDA has an advantage over PIV in that it can get much closer to the wall, approximately 0.1 mm.)

The PIV results show more scatter than the LDA measurements in the centre of the cavity at $y = 60$ mm. At y values of 120 mm, 180 mm and 240 mm, there is much less scatter in the centre of the cavity. For $y = 120$ mm, in the wall-jet region the maximum velocity and jet width are in very good agreement whereas at $y = 180$ mm, the maximum

jet velocity measured is higher than the LDA data. For the rest of the cavity at $y = 180$ mm, the LDA and PIV are in excellent agreement.

The results in Figure 4.4.3.4. show one of the difficulties with PIV. That is calibrating the image location correctly. The PIV data between $0 < y < 30$ mm appears to be shifted in the negative x direction as compared to the LDA data. The maximum velocity and the width of the jet are in excellent agreement but the PIV data is shifted. The PIV measurements were measured in blocks of 30 mm per set of PIV images. It appears that the calibration of the image is slightly misaligned. This would account for the slight shift on this set of data ($0 < y < 30$ mm).

In Figure 4.4.3.2., at the far wall (vertical wall at the exit) the PIV data and LDA data have poor agreement. The cause of this was uncertain but the speculation was that since this model was a replica of that used in Johnson (1995), there may have been a slight difference in the exit specifications, slightly altering the flow field near the exit. At $y = 60$ mm, near the far wall the PIV data shows high scatter. Therefore, this data did not shed any light on the deviations at the far wall at $y = 120$ mm.

4.5. Conclusions

The main result of this study is that the difficulties associated with setting up the PIV equipment and testing and learning the method on this simple flow, provided a strong base of knowledge and guidelines for future studies in devices where the velocity is not known. Hence, this knowledge will help measure the velocities in the static mixer and twin screw extruder with the PIV technique.

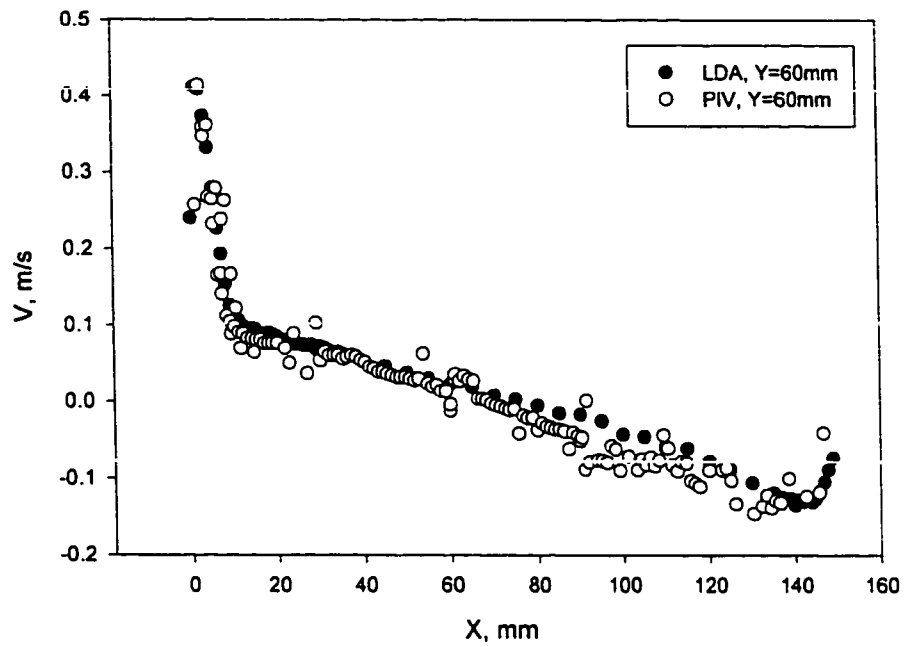


Figure 4.4.3.1. - PIV and LDA Measurements at a plane of $Y=60$ mm.

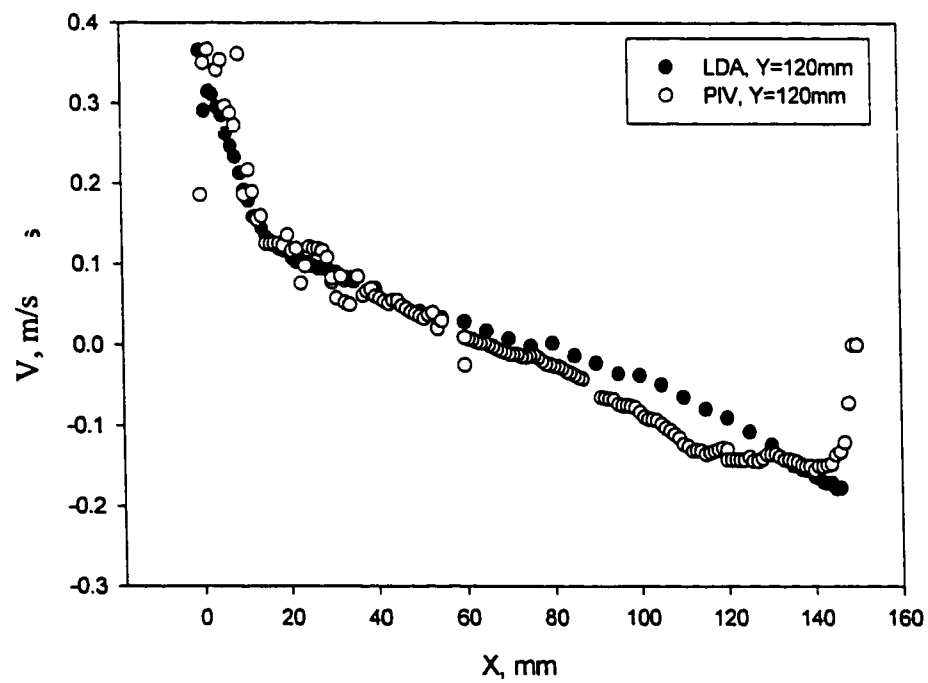


Figure 4.4.3.2. - PIV and LDA Measurements at a plane of $Y=120$ mm.

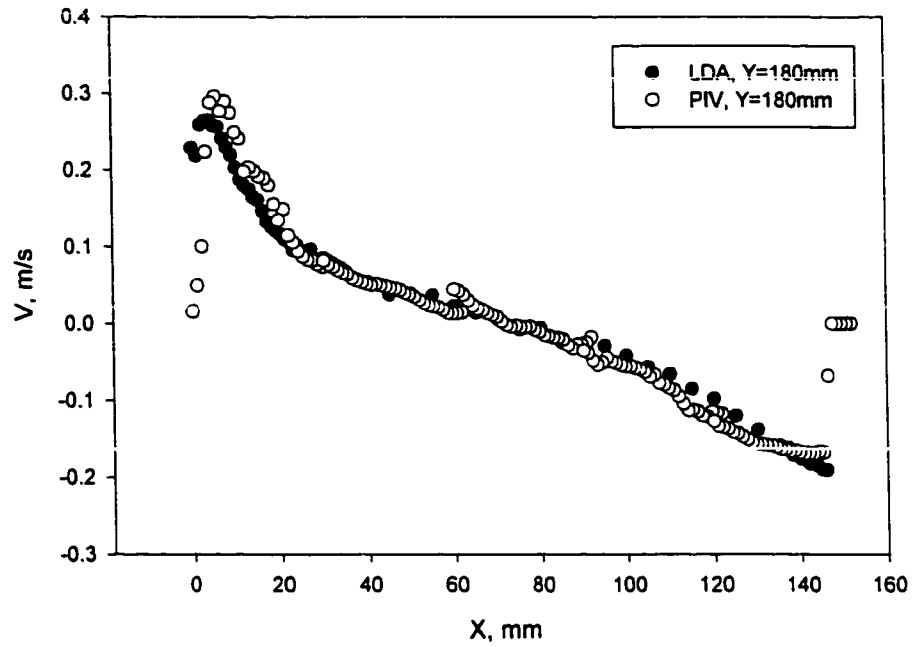


Figure 4.4.3.3. – PIV and LDA Measurements at a Plane of $Y=180\text{mm}$.

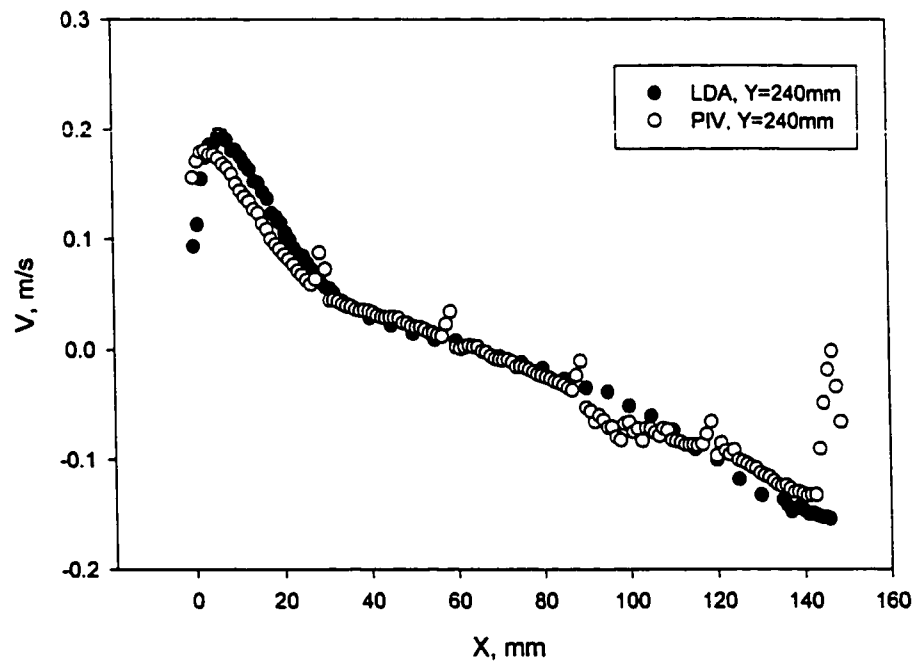


Figure 4.4.3.4. - PIV and LDA Measurements at a Plane of $Y=240\text{mm}$.

The main concern of using PIV in a static mixer and twin screw extruder is that these flows are highly three dimensional compared to the recirculation cavity measured. However, the errors associated with three dimensional flow measured using the two dimensional PIV technique can be minimised by the proper choice of interrogation area and time separation. The objective is to reduce the number of particles that flow out of the illuminated plane within the pulse separation time and to take an adequate number of data at each measurement location. From the works of Adrian (1991) and Boillot and Prasad (1996), the error in the velocity measurement due to particles falling out of the illuminated plane between pulses can be reduced to approximately ten percent for the range of velocities in the static mixer and twin screw extruder.

From the validation of the PIV technique presented in this chapter and the knowledge that with proper choice of the PIV parameters, the measurement of the fluid flow field in the static mixer and twin screw extruder could be measured with a high level of confidence in the results. Chapter Five presents the mixing quantification of the static mixer and chapters 6 and 7 present the PIV measurements in the static mixer and twin screw extruder respectively.

5.0. Quantification of Laminar Mixing in the Kenics KM[®] Static Mixer

5.1. Introduction

There have been very few published experimental studies of laminar mixing in the Kenics KM[®] static mixer. The mixing efficiencies and energy requirements for various mixer designs for laminar mixing applications have been studied by Heywood et al (1984). Micro-mixing studies such as those of Baldyga et al (1997) are in the literature and cover the turbulent mixing regime but so far, the research on laminar mixing has mainly centred on determining mixing from computational fluid dynamics simulations of the mixer's velocity field [Dackson and Nauman (1986), Arimond and Erwin (1985a,b), Ling and Zang (1995)]. The present work was primarily motivated by the need for experimental measurements of mixing in the open literature. A great deal of research is being carried out using computational fluid mixing (CFM) for predicting mixing [Byrde and Sawley (1996a,b,c), Hobbs et al (1998)]. CFM tracks the trajectories of many particles ($10^4 \sim 10^6$) in a simulated fluid flow field to model different species mixing. The particle trajectories are used to determine the lamellar structure created. However, the limitation of CFD and CFM has been that very little experimental data exists to validate simulation results. Hence, questions still remain about the accuracy of these mathematical models of fluid flow and fluid mixing.

5.2. Flow Visualisation

The flow visualisations yielded some unexpected results compared to previously published pictures (Figure 5.2.1.) of striation development through the mixer [Devellian (1972)] and the expected 2^n increase in the number of striations where n is the number of mixing elements. In Figure 5.2.2., the Reynolds number is 43 (based on the total flow rate through an empty tube of diameter, D). The elements have an aspect ratio of 1.0 and the flow rate and viscosity ratios of the two streams are 1.0. The flow pattern is similar to that expected from Figure 5.2.1. The measured striation widths or thicknesses decrease with distance along the mixer as shown in Figure 5.3.1. As the Reynolds number is increased above a critical value, re-circulating vortices begin to appear in the flow field. In Figure 5.2.3., at a Re of 97, a single vortex is visible above the first element and also a second vortex (not visible in the visualisation) resides below the first element and is hidden by the element. For this case, the measured striation thickness decreases dramatically after the first element as shown in Figure 5.3.1. From our experimental studies it was observed that the critical value of the Reynolds number for the onset of the vortex appearance for this configuration is Re_{crit} of 55 ± 2 (for $L/D=1.0$). A second critical Reynolds number was observed to be $Re_{crit} = 105 \pm 2$ (for $L/D=1.0$). Above this value, a second vortex (Figure 5.2.4.) appears above the second element (with a partner, invisible beneath the element). The onset of the second vortex at $Re=105 \pm 2$ can be seen in Figure 5.2.5. This picture clearly shows how the dye is being folded over in the recirculation.

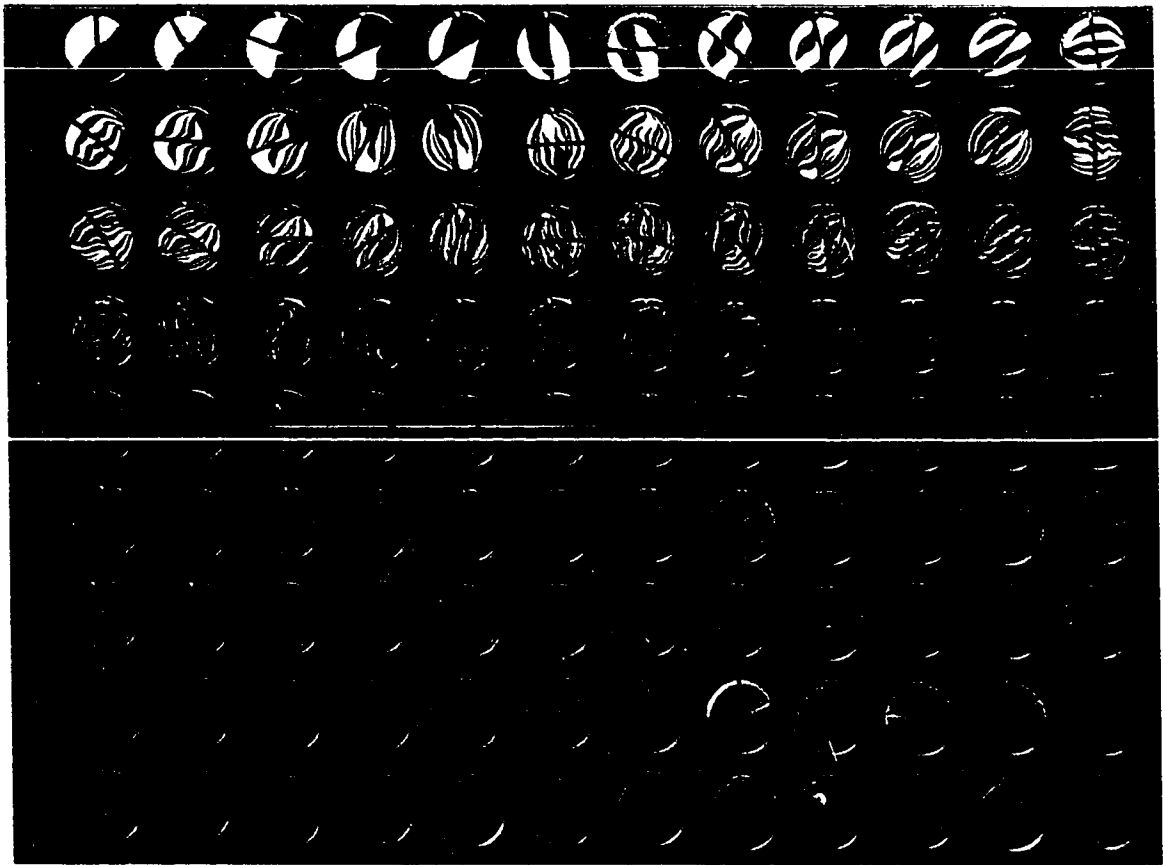


Figure 5.2.1. - Lamellar Structure Created in the Kenics KM[®] Static Mixer, (courtesy of Chemineer, Dayton, Ohio.).

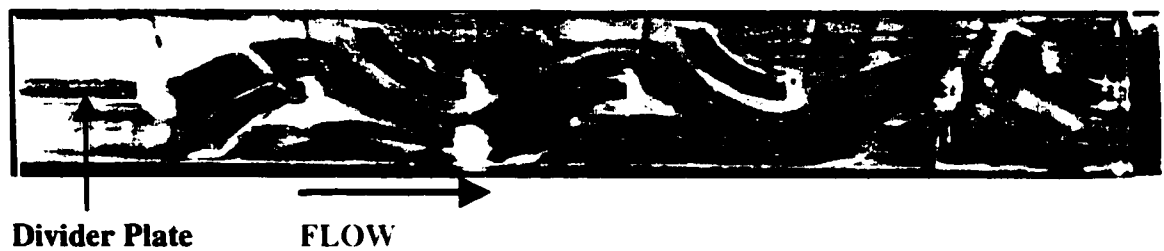


Figure 5.2.2. - Flow Visualisation at $Re=43$ for $L/D=1.0$.

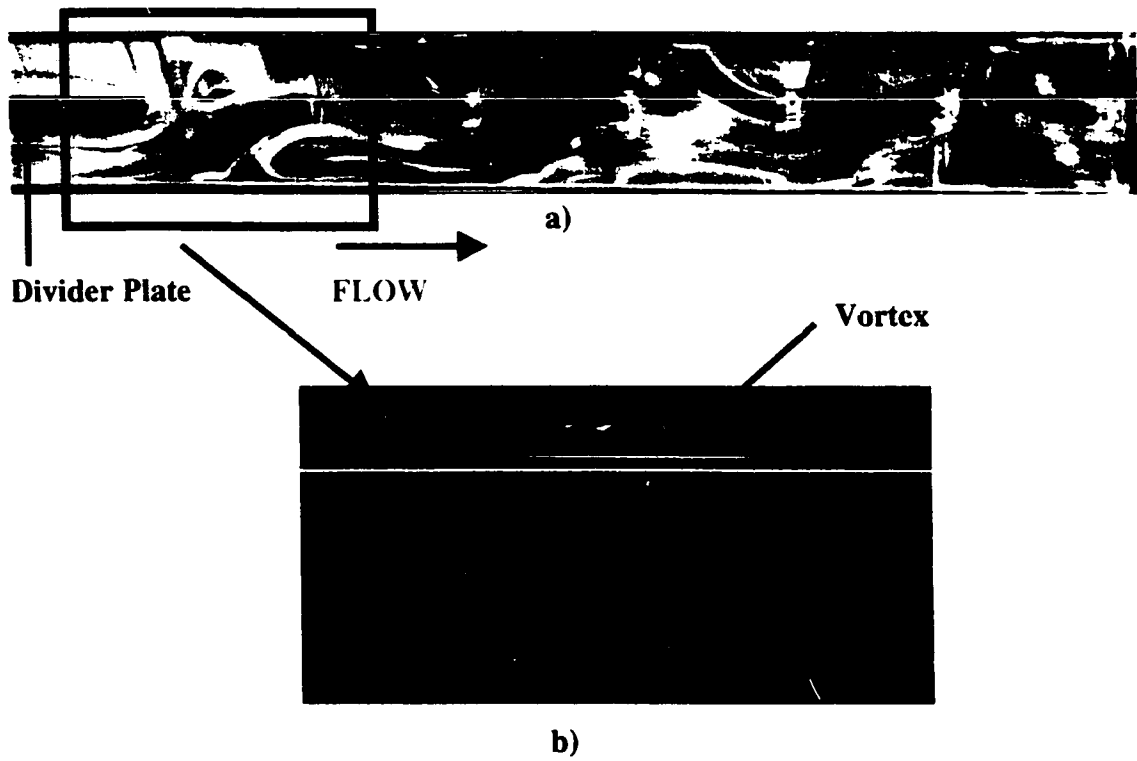


Figure 5.2.3. - Flow Visualisation at $Re=97$ for $L/D=1.0$, a) Full Flow Field, b) Close-up of Element 1.

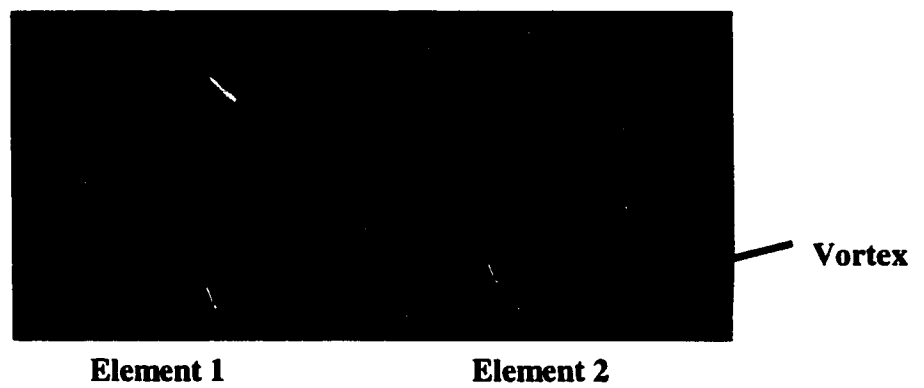


Figure 5.2.4. - Flow Visualisation at $Re=125$ for $L/D=1.0$.

These critical Reynolds numbers are distinct for each element geometry. For aspect ratios of 0.8, the onset of these vortices at the first and second elements, occurs at Re of 43 ± 5 and 90 ± 5 respectively. The reason for the large range of Re is that the precise location of the transition would require a large number of runs, which would not add any additional information.

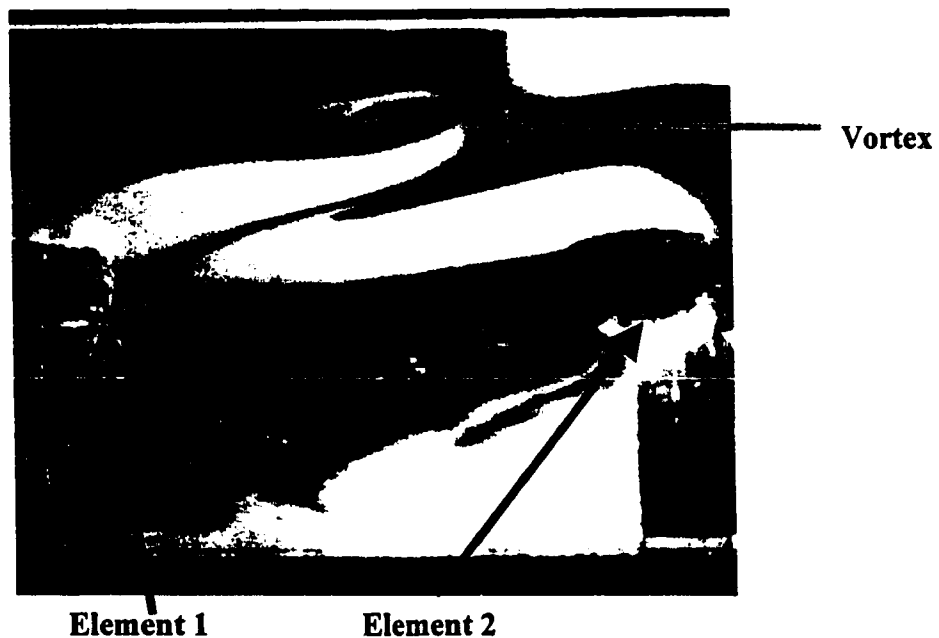


Figure 5.2.5. - Onset of Vortex above Second Element.

5.3. Image Analysis: Mixing Quantification

As shown in Figure 5.3.1., as the Re is increased, the average striation thickness decreases except for measurements at $Re = 97$ and $Re = 114$ for element 4. The observed exception is within the experimental error of the measurements. This is explained further

below. Above a Re of 105, a second vortex appears above the second element (with a partner, invisible beneath the element). These vortices have a less dramatic effect in reducing the striation width as illustrated in Figure 5.3.1. After the fourth element, the resolution required and the blurring of interfaces due to molecular diffusion does not permit accurate measurement of the striation thickness.

The difficulty with the number averaged striation width measurements is that the results can be easily biased due to very small or large striations. For example, a flow field with many thin striations but having a single large unmixed region would have a small number averaged striation thickness but would not be considered well mixed. A second measure of the distribution of striation widths is the variance. The goal of a mixer is not only to reduce average striation thickness but also to reduce the variance of the striation widths. Figure 5.3.2. shows the measurement bias very well. Even though at higher Reynolds numbers the average striation thickness has decreased, the variance first increases before it decreases after the first element. For values of Re above 105, the second vortex causes the variance at the second element to remain approximately constant before decreasing. Although Figure 5.3.1. indicates that higher Reynolds numbers lead to 'better' mixing based on number average striation thickness measurements, the variance measurement shows that after four or five elements, the variances of all the cases have attained approximately the same value. Hence, Figures 5.3.1. and 5.3.2. show that if the mixer is operated at lower Reynolds numbers it can reach the same result as when the mixer is operated at higher Reynolds numbers, with each having approximately the same average striation thickness and variance after four or

five elements. The advantage of operating the mixer at lower Re is that the power requirement is lower and suggests that increased energy input does not always lead to better mixing.

The errors associated with the measurements in Figures 5.3.1. and 5.3.2. are in the range of 3 to 5 percent. These errors were determined by replicating a few of the runs, but there were insufficient runs to have a representative sample to measure standard deviation. Due to the lengthy time required for each set of measurements, replicating all the experiments was not feasible.

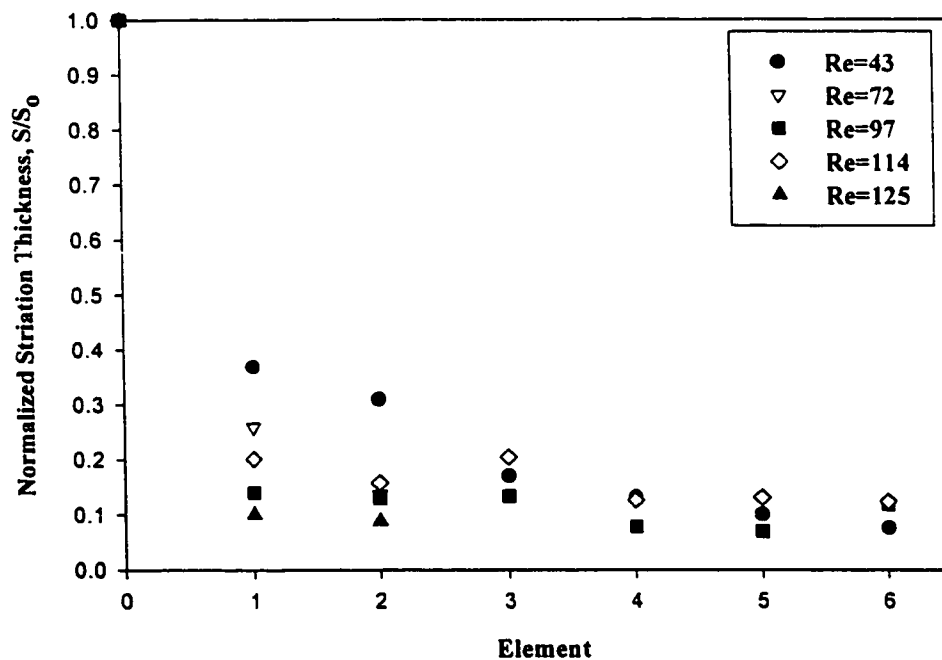


Figure 5.3.1. - Normalised Number Average Striation Widths for $L/D=1.0$.

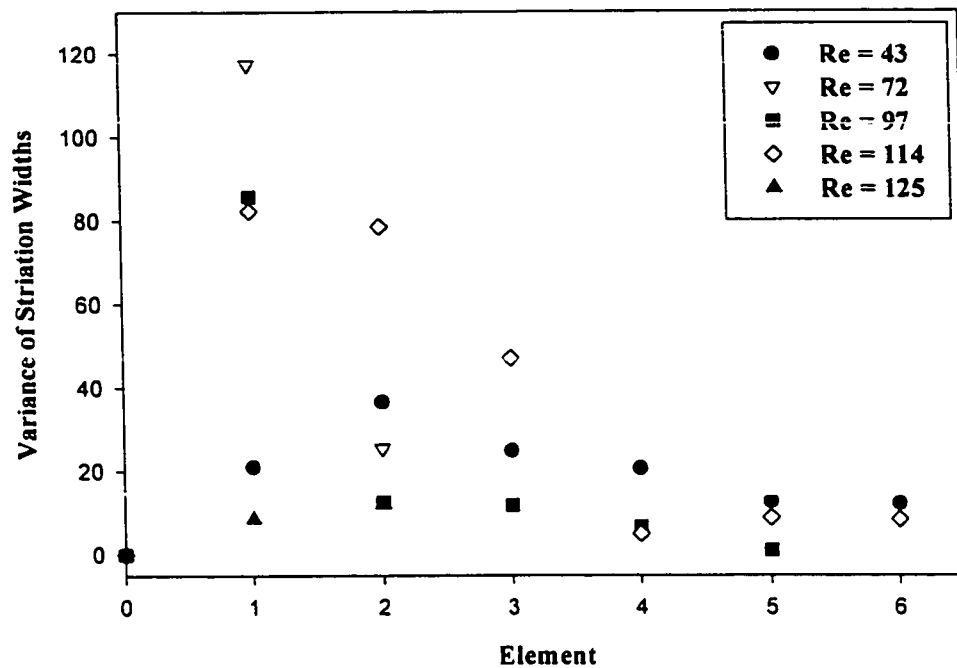


Figure 5.3.2. - Variance of Striation Widths for $L/D=1.0$.

5.4. Effect of Viscosity on Mixing

Figure 5.4.1. shows a series of radial cross-sections along the axial direction from the first element to the sixth element. In this case, the geometry of the elements is $L/D=1.5$ with a twist of 90 degrees. The Komax L/H[®] distributor was used at the inlet for distributing the minor phase (dyed oil) into the bulk stream (clear oil). These visualisations were obtained at Re of 4. The two streams being mixed had a viscosity ratio, μ_{ratio} of 0.1 (0.1 Pa·s/1 Pa·s) and a flow rate ratio, Q_{ratio} of 0.2 for the dyed (appears white) to clear (appears black) mineral oil. In Figure 5.4.2., a similar series of visualisations is shown at $Re=4$ for a viscosity ratio of 1 (1 Pa·s) and a flow rate ratio of 0.25 (clear oil to dyed oil).

The interfacial area growth was estimated for each axial location for the series of images shown in Figures 5.4.1. and 5.4.2. Using a threshold value on pixel intensity as

explained in section 3.3.1.1., the edges of the dyed fluid were determined and the perimeter was measured for each cross-section. These results are shown in Figure 5.4.3. This plot shows that the flow with a viscosity ratio of 1 has a faster interfacial area growth rate (better mixing) than the flow with the lower viscosity ratio.

The average striation width measurements along the axial direction for Figures 5.4.1. and 5.4.2. are shown in Figure 5.4.4. The reduction in thickness follows trends similar to those shown in Figure 5.3.1. These measurements were made from radial cross-section images as compared to Figure 5.3.1., where the measurements are from axial cross-section images.

Figure 5.4.5. shows the variance of the striation width measurements for Figures 5.4.1. and 5.4.2. From Figures 5.4.4. and 5.4.5., the conclusions that may be drawn are that at a viscosity ratio of 1, the striation widths are larger with better uniformity than at the lower viscosity ratio. This is due to the fact that if we assume constant shear stress and negligible surface tension across an interface, the less viscous material will experience a higher shear rate [Tadmor and Gogos (1979), Chella and Ottino (1983)]. Hence, larger strains cause the less viscous material to stretch at faster rates. Therefore, very fine striations are created and the number average striation thickness is reduced compared to a viscosity ratio of 1. However, the distribution has thick and thin striations as a result and therefore, a higher variance of striation widths. This is evident in Figure 5.4.5.

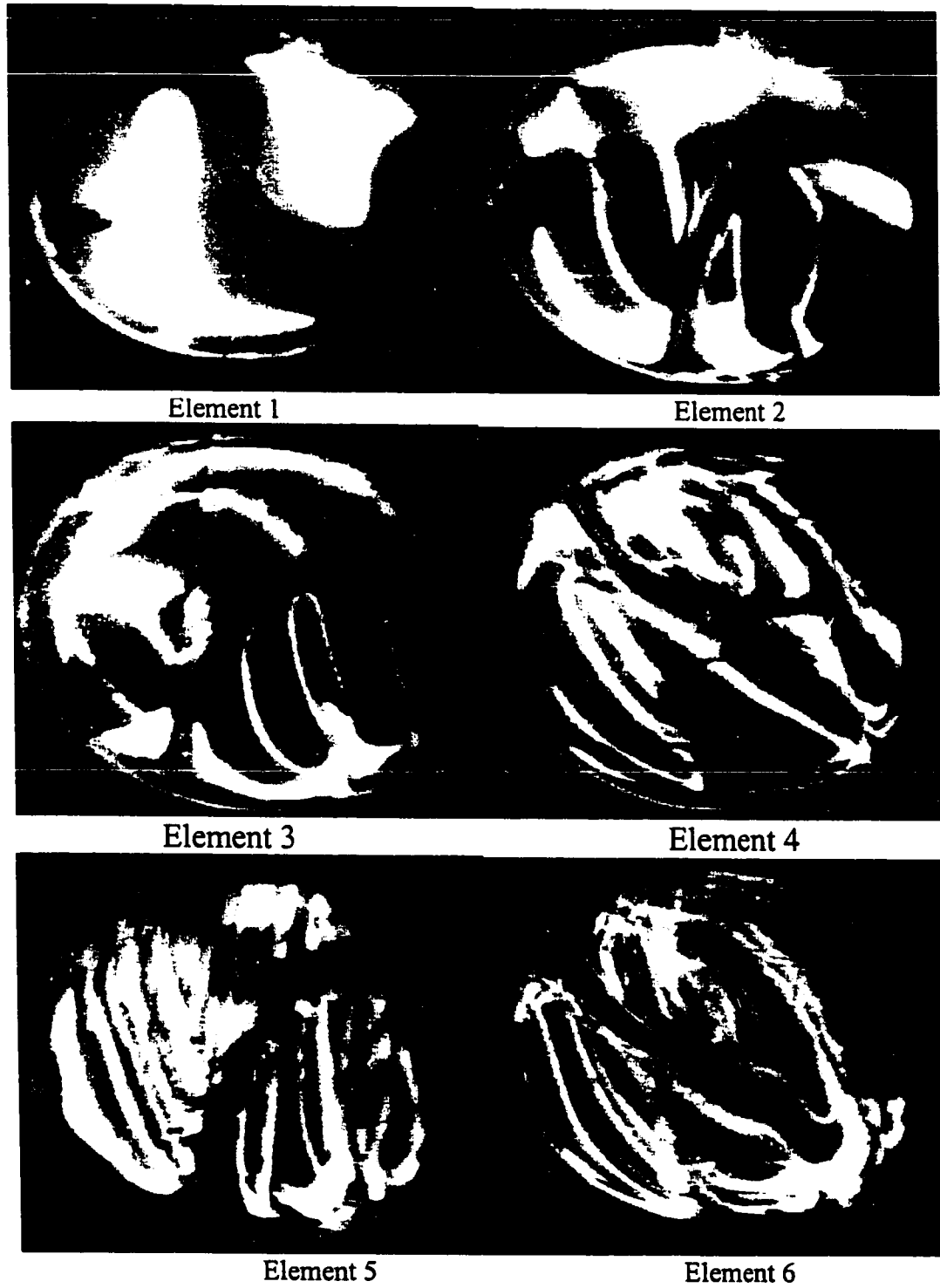


Figure 5.4.1. - Radial Cross Section Image Series for $\mu_{\text{ratio}} = 0.1$ and $Q_{\text{ratio}} = 0.2$.

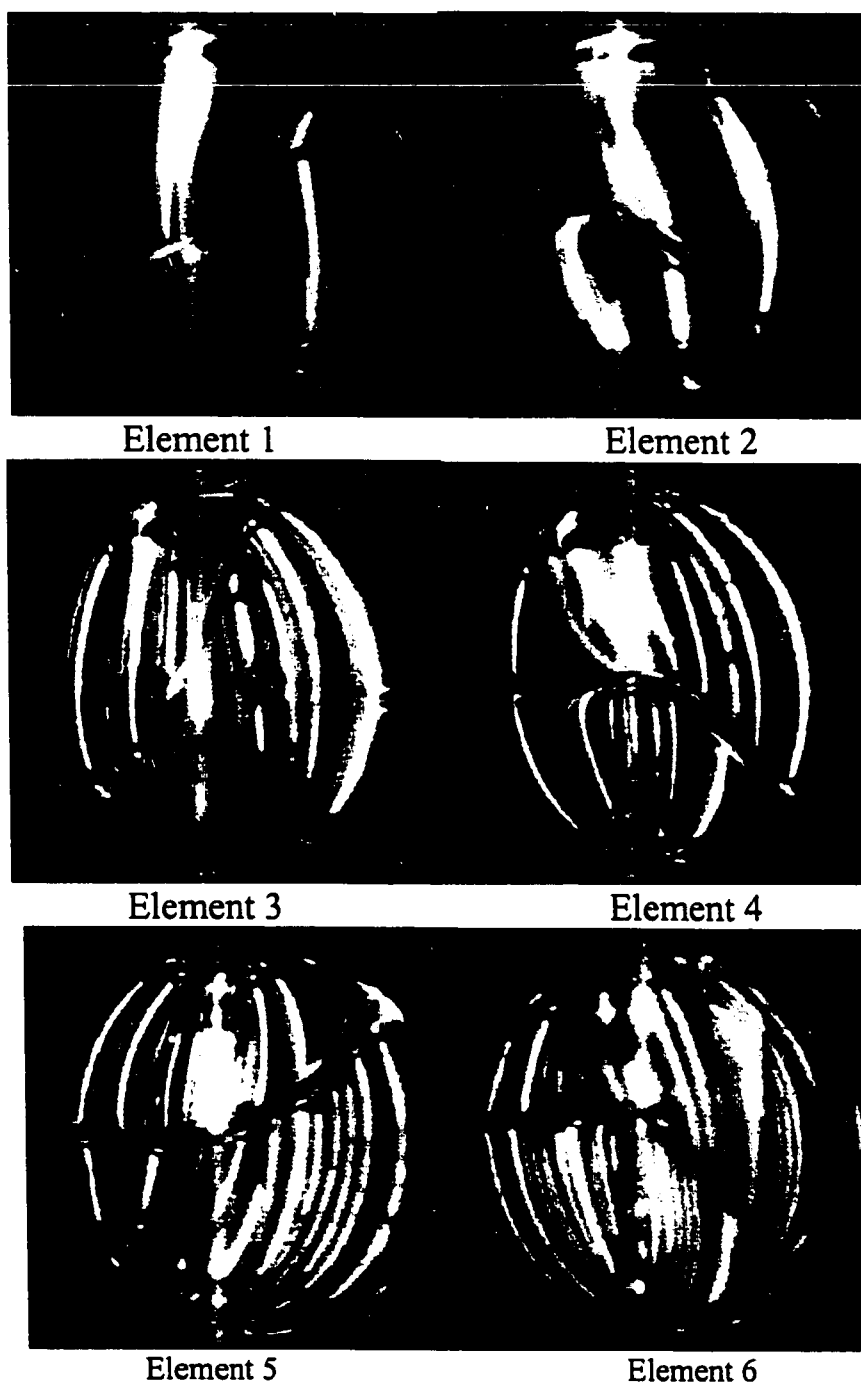


Figure 5.4.2. - Radial Cross Section Image Series for $\mu_{\text{ratio}} = 1$ and $Q_{\text{ratio}} = 0.25$.

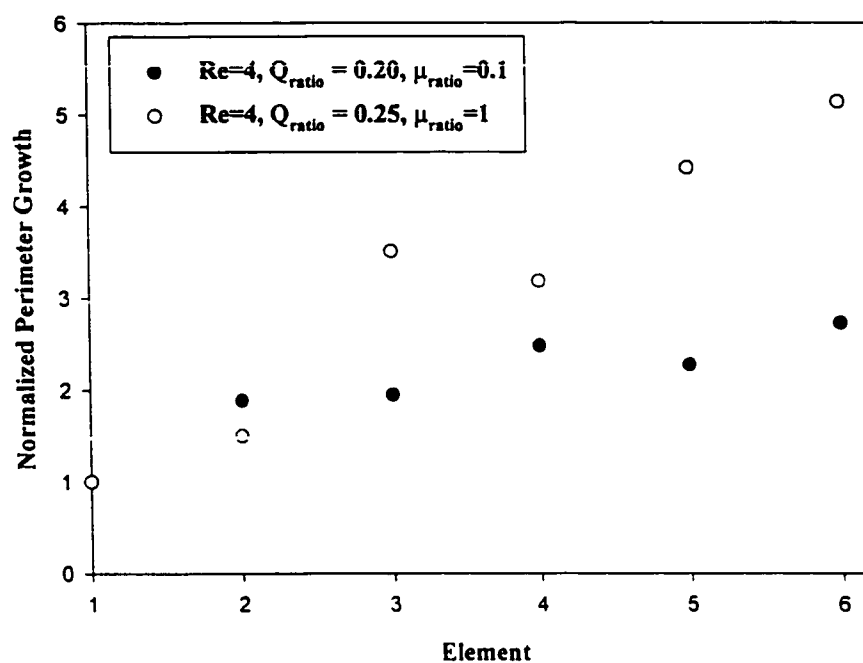


Figure 5.4.3. - Normalised Perimeter (Interfacial area) Growth for $L/D=1.5$.

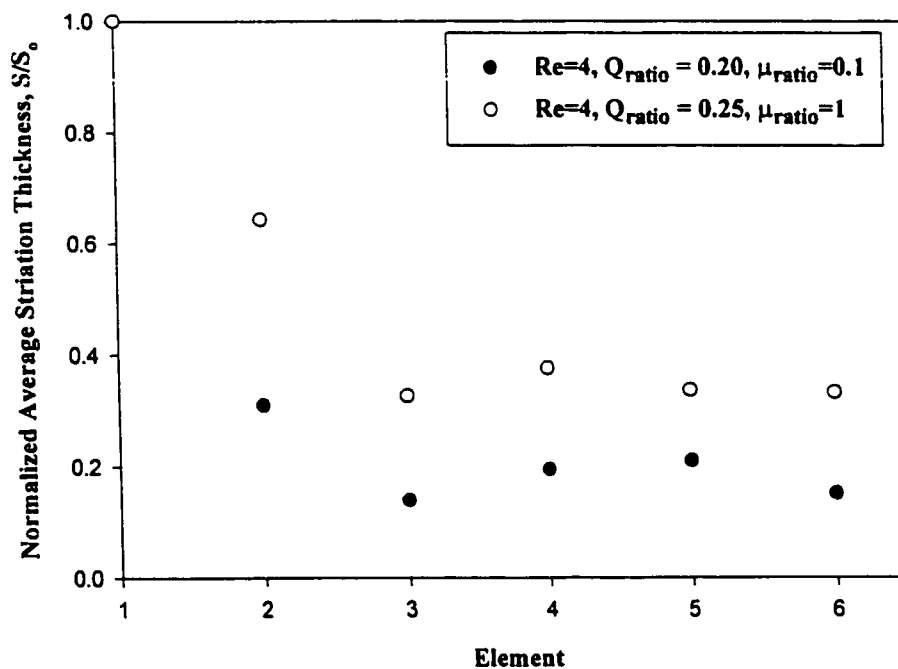


Figure 5.4.4. - Normalised Average Striation Widths for $L/D=1.5$.

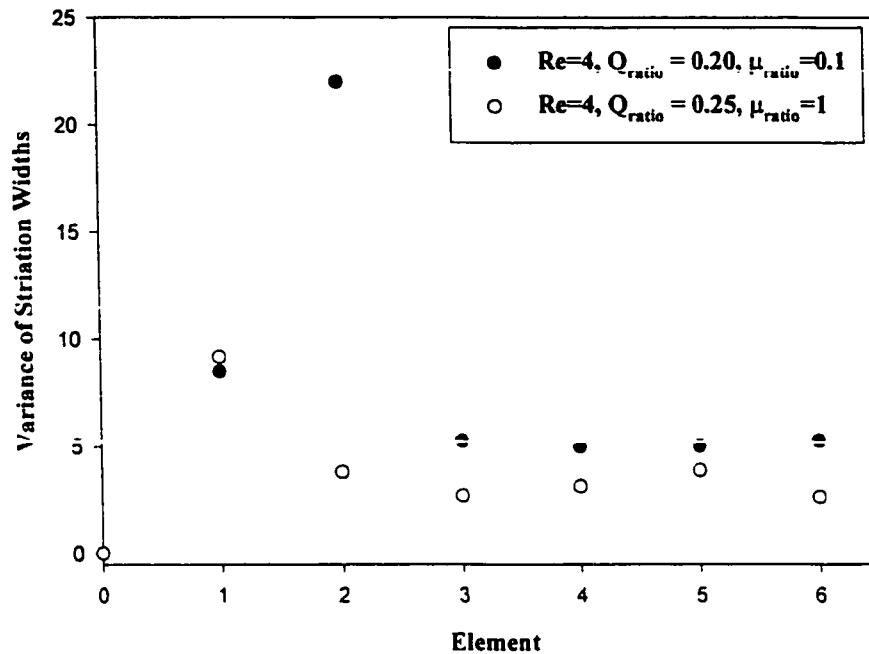


Figure 5.4.5. - Variance of Striation Widths for $L/D=1.5$

5.5 Effect of Aspect Ratio

Figures 5.5.1 and 5.5.2 demonstrate the effect of aspect ratio on the average striation thickness and variance of striation widths, respectively. From Figure 5.5.1, it is evident that the aspect ratio has little effect on the number average striation thickness. All three geometries, at the low Reynolds numbers, give relatively the same decrease in thickness after 6 elements. An aspect ratio of 0.8 produces thinner striations early but by the end of the mixer very little change in the mean width is observed. The variance also shows that the longer elements with aspect ratios of 1.5 produce a more uniform mixture compared to an aspect ratio of 1.0 or 0.8. Hence, these results indicate that for a given rotation or twist per element, the performance of an element with an aspect ratio of 1.5 is

better than one with an aspect ratio of 0.8 and 1.0. From previous studies of Shah and Kale (1991) and Heywood et al (1984), longer aspect ratios have less pressure drop for the same twist per element. Therefore, elements with aspect ratios of 1.5 give better mixing for less cost.

These results are contrary to the CFD results of Ling and Zhang (1994), Dackson and Nauman (1987) and Arimond and Erwin. (1985a,b). Ling and Zhang (1994) looked at the final mixture resulting from tracking many particles in the flow field. Dackson and Nauman (1987) and Arimond and Erwin (1985a,b) looked at the deformation of an interface simulated with tracer particles for a solved flow field. The one commonality these CFD simulations had was that they looked at a small number of particles in comparison to the CFM work of Hobbs and Muzzio (1997a,b) and Bryde and Sawley (1996a,b,c). Hobbs and Muzzio (1997b) varied the dye injection location and the flow rate of a stream of passive tracer particles and concluded that elements with an a twist of 120 degrees and an aspect ratio of 1.5 provided similar mix quality as to the standard 180 degree configuration but had much less pressure drop across the mixer. There was no optimisation of the aspect ratio presented for this work.

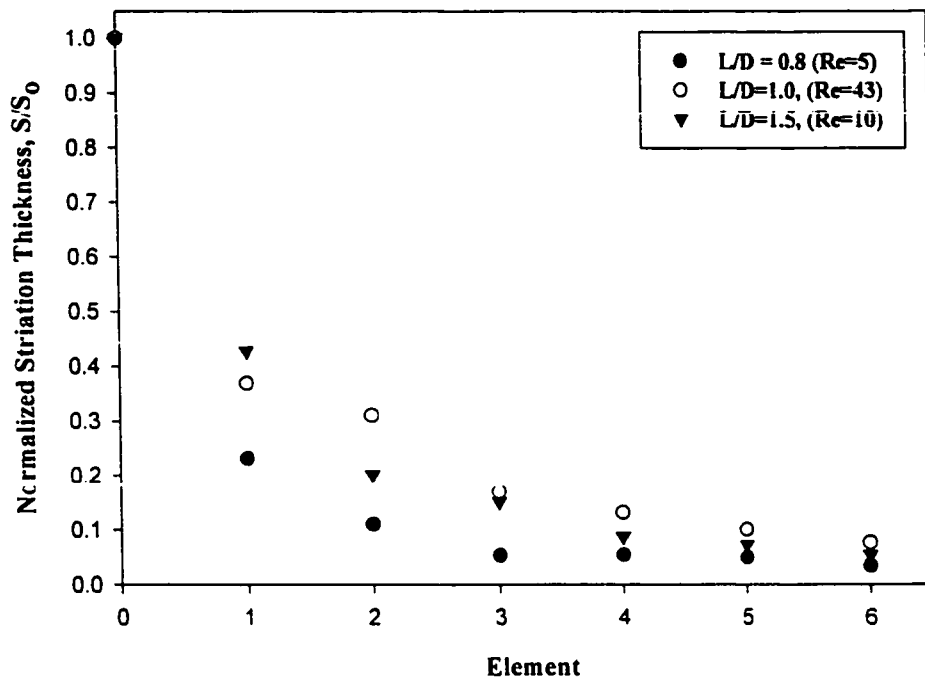


Figure 5.5.1. - Effect of Aspect Ratio on Striation Thickness.

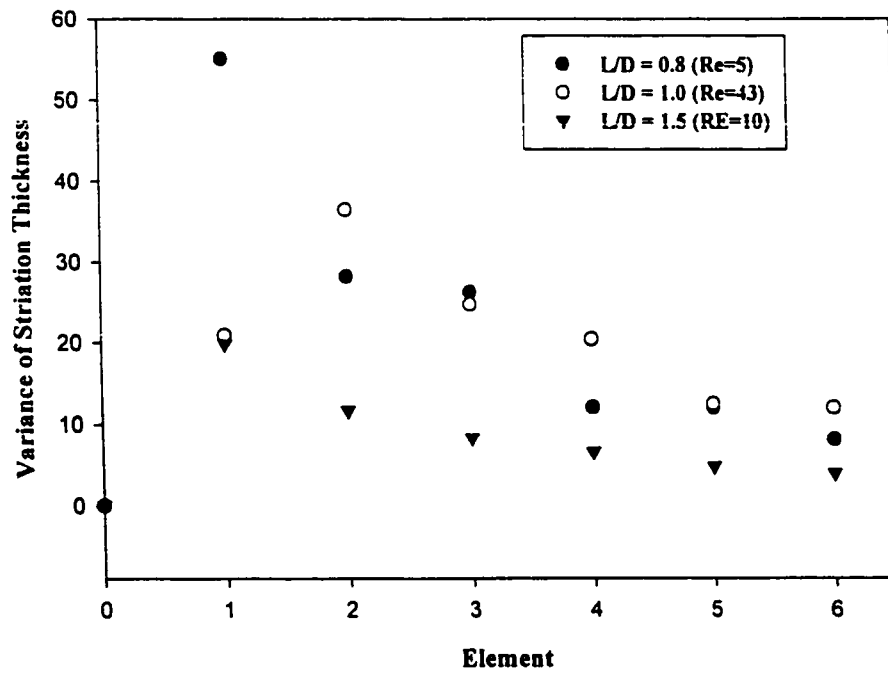


Figure 5.5.2. - Effect of Aspect Ratio on Variance of Striation Widths.

5.6. Summary

The laminar flow field in a Kenics KM[®] static mixer has been studied using laser induced fluorescence and digital image analysis. Mixing was quantified by measurement of the number average striation thickness, variance of striation widths and interfacial area, for elements of length to diameter (L/D) ratios of 0.8, 1.0, and 1.5 with 90° twist per element. From flow visualisations, transitions were observed in the flow where vortices developed above the first and second elements at Reynolds numbers of 43 and 90 for L/D=0.8 and Reynolds numbers of 55 and 105 for L/D=1.0. It was found that these vortices did not appreciably enhance mixing based on striation thickness and variance of striation widths measurements after 4 to 5 elements. The variation of viscosity ratio showed that a viscosity ratio (dyed stream/bulk stream) of 1 had faster interfacial area growth and created more uniform mixtures compared to a viscosity ratio of 0.1 for flow rate ratio of 0.2.

The experimental measurements of striation thickness showed that smaller element aspect ratios initially created thinner striation widths with a high variance compared to elements with larger aspect ratios. However, after the fluid had passed five to six elements, the striation widths were essentially the same for all three aspect ratios for the given 3 to 5 percent error in the measurements. Therefore, these results show that an aspect ratio of 1.5 for a 6 element mixer (as compared to aspect ratios of 1.0 and 0.8), provided better mixing efficiency since the mixture had the same mean number averaged striation widths, a lower variance of striation widths and a lower pressure drop [Heywood et al. (1984)]. These results are contrary to published results from CFD simulation

[Dackson and Nauman (1987), Airmond and Lewis (1985a,b) and Ling and Zhang (1985)] that found that as aspect ratios were reduced mixing efficiency increased.

6.0. Velocity Measurements in the Kenics KM[®] Static Mixer

6.1. Introduction

This chapter presents the laser Doppler anemometry and particle image velocimetry measurements of the velocity field in the Kenics KM[®] static mixer. For the LDA experiments, the objective was to measure the fluid flow field for elements with an aspect ratio of 1.0 with an inlet boundary condition of a splitter plate. The main concern was to determine if recirculations at the first element existed and their relative magnitude. The second concern was to determine the entrance velocity profile to conclude whether or not the inlet condition was responsible for the vortices. For the PIV experiments, the aspect ratio of the elements investigated was 1.5. The inlet condition was fully developed Poiseuille flow in a circular tube. The Reynolds number (based on an empty tube) was 0.1. The contours of the three velocity components and the magnitude of the deformation tensor are presented for the first four elements.

6.2. LDA Measurements

To ensure the entering streams had fully developed flow, the two streams were kept separated by a splitter (divider) plate with a length of three tube diameters. This entrance length ensures that the mixing is a result of the elements and not any impingement mixing of the streams or entrance effects. The co-ordinates of the mixer are defined in Figure 6.2.1. Figure 6.2.2. displays the axial velocity profile of the entering

stream at $Re=60$ at the end of the splitter plate just before the first element. Figure 6.2.3. shows a two dimensional profile of the entering velocity along the plane $z=0$ (perpendicular to the splitter plate plane). This figure shows duplicate measurements (two arrows superimposed) made for the same flow conditions to demonstrate the validity of the LDA measurements. Each of the velocities plotted is an average of ten thousand measurements, having a variance no larger than three percent. Any measurements with larger variances were discarded since most of these were the result of the laser light scattered from the elements. Figures 6.2.2. and 6.2.3. are very important in the analysis of the flow field since they indicate that a steady, parabolic velocity field entered the mixer and entrance effects were not possible causes of the vortices present.

The two entering streams are split by the first element causing half of each stream to be combined with the opposite half from the other stream. Just after the two streams were divided, at the top edge of the first element, the velocity profile was measured on one side of the element and is given in Figure 6.2.4. The two streams are separated by the splitter plate which is defined by the plane $x = 0$ mm (note - there is a finite distance where the splitter plate and the first element are joined, 0.005m) with the front edge of the first element defined by the plane $z = 18-19$ mm. Therefore, the zero velocities measured at $x = 0$ mm are due to the presence of the divider plate. These measurements were taken at $Re=57$ (where the vortices are present). The measured flow field does not exhibit any instabilities as indicated by a low variance in each measurement and from the time series of the data. (Note that this time series was recorded and the velocity measurements were plotted as a function of time. The resulting curve showed no

measurements deviating more than three percent of the mean velocity.) Consequently, the thickness associated with the leading edge of the first element does not create any instabilities in the flow field based on these measurements.

At $Re = 53$, LDA results show the onset of the vortices with negative velocities in the axial direction and are shown in Figure 6.2.5. The results show that the vortices develop at $Re = 53 \pm 2$ for an element aspect ratio of 1.0.

The flow field at $Re = 60$ across element 1, at a plane parallel to the splitter plate is given in Figure 6.2.6. as the element rotates into this plane. Measurements beyond $z = 20\text{mm}$ were not possible due to the diffraction of the laser beams as a result of the twist in the element. Some duplicate measurements were made and are also given. From $18\text{ mm} < y < 30\text{mm}$, the velocities were measured along a plane perpendicular to the divider plate with the trailing edge of element 1 perpendicular to the measured plane (leading edge of element 1 is parallel with measured plane). These results are presented in Figure 6.2.7. and show the velocity profile progressing from an essentially flat profile with small magnitude to a parabolic profile (at the end of the element). In Figures 6.2.6., measuring on the opposite side of the element was not possible due to the bending of the laser beams by the element. Therefore, the measurements beyond $z = 20$ are poor.

The LDA results show the presence of a vortex at the first element for $Re = 53 \pm 2$ with aspect ratios of 1.0. These results eliminated the entrance condition as the cause of the vortices. No instabilities were found at the leading edge of the first element or the end edge of the splitter plate.

Chemineer (Dayton, Ohio), the manufacturers of the Kenics® elements, sharpen the edges of the elements for situations where thermally sensitive materials are flowing through the mixer. They had found material was burning in the static mixer with elements with blunt edges due to the stagnant zones being created. Their solution was to sharpen the elements leading and trailing edges. LDA showed that the measured vortices were static and stable. These could have caused material to burn if fluid had been trapped in the vortex for a long period of time. Unfortunately, Chemineer's solution could not be tested as sharpening the elements was not possible.

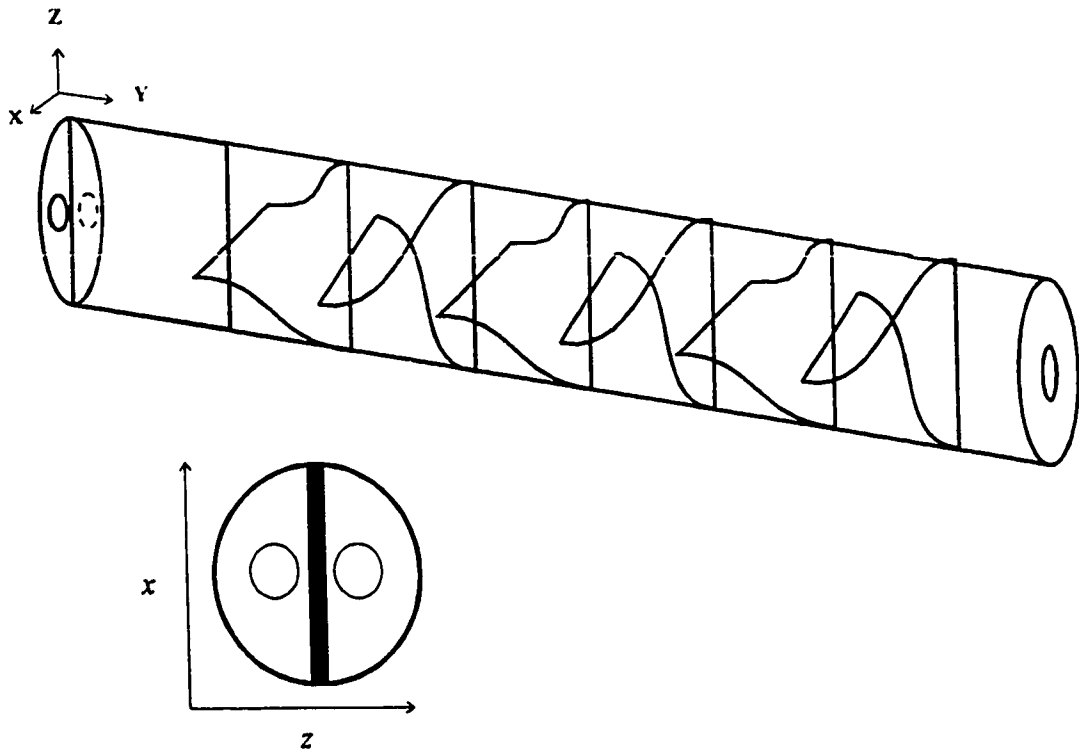


Figure 6.2.1. – Definitions of co-ordinates for LDA measurements.

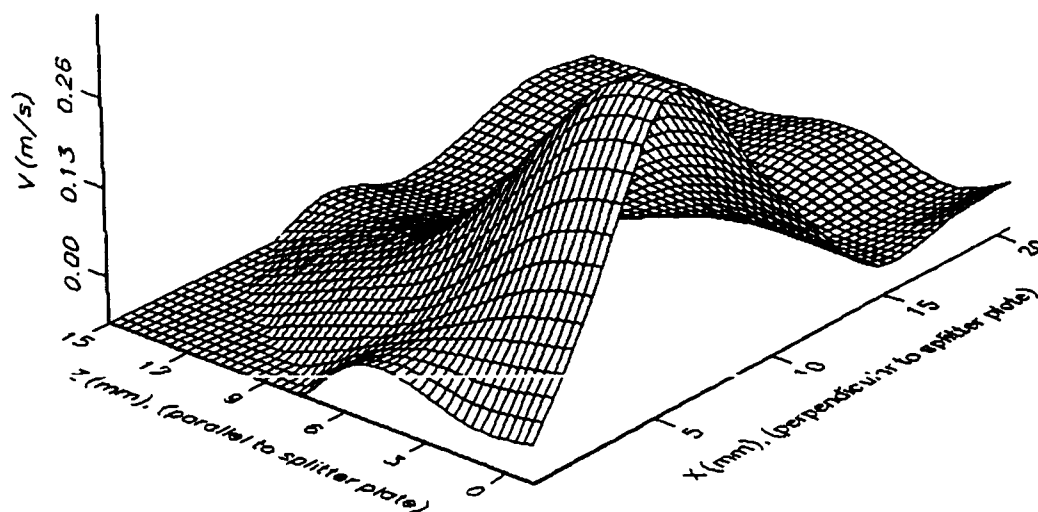


Figure 6.2.2. – Axial Velocity Profile at $Re=60$ at the end of the Splitter Plate.

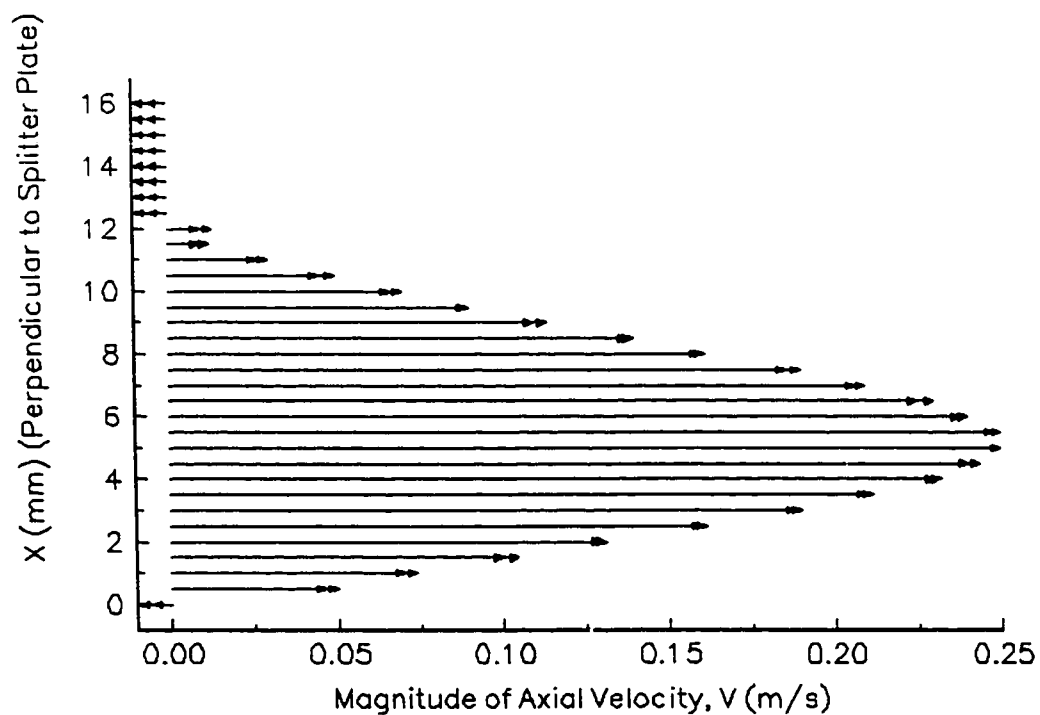


Figure 6.2.3. – Axial Velocity Vector Plot at the End of the Splitter Plate at $Re = 56$ and $Z = 0$ mm.

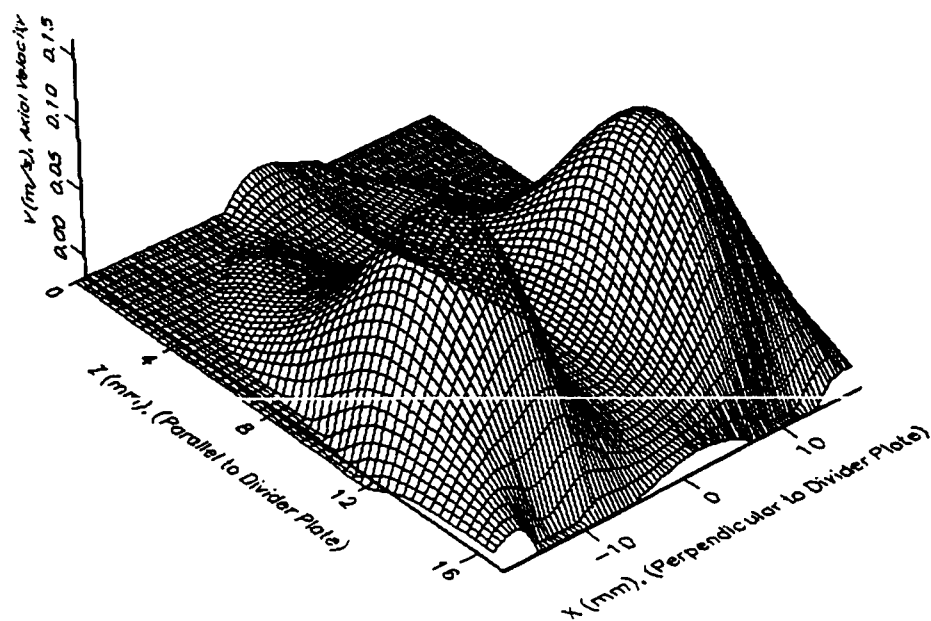


Figure 6.2.4. – Axial Velocity Profile at $Y = 5$ mm at Junction of Splitter Plate and Element 1 at $Re=57$.

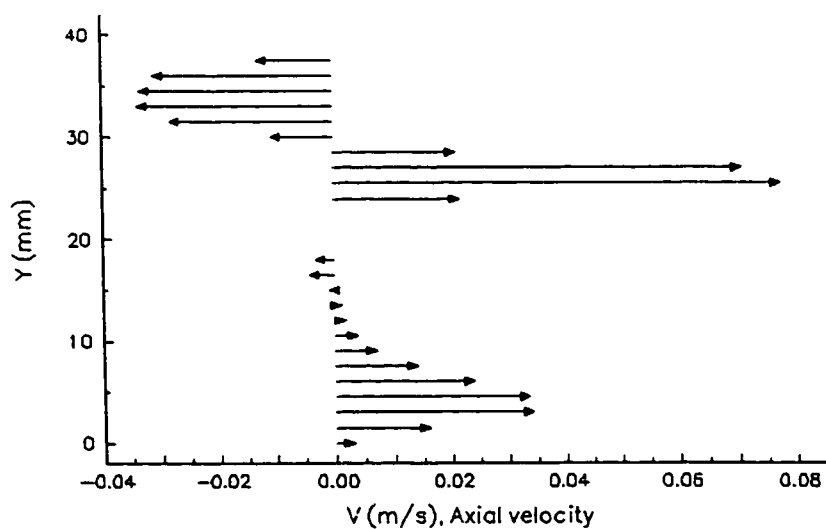


Figure 6.2.5. – Axial Velocity Vector Plot for Element 1 at $Re=53$ at $Y=10$ mm and $X=16$ mm.

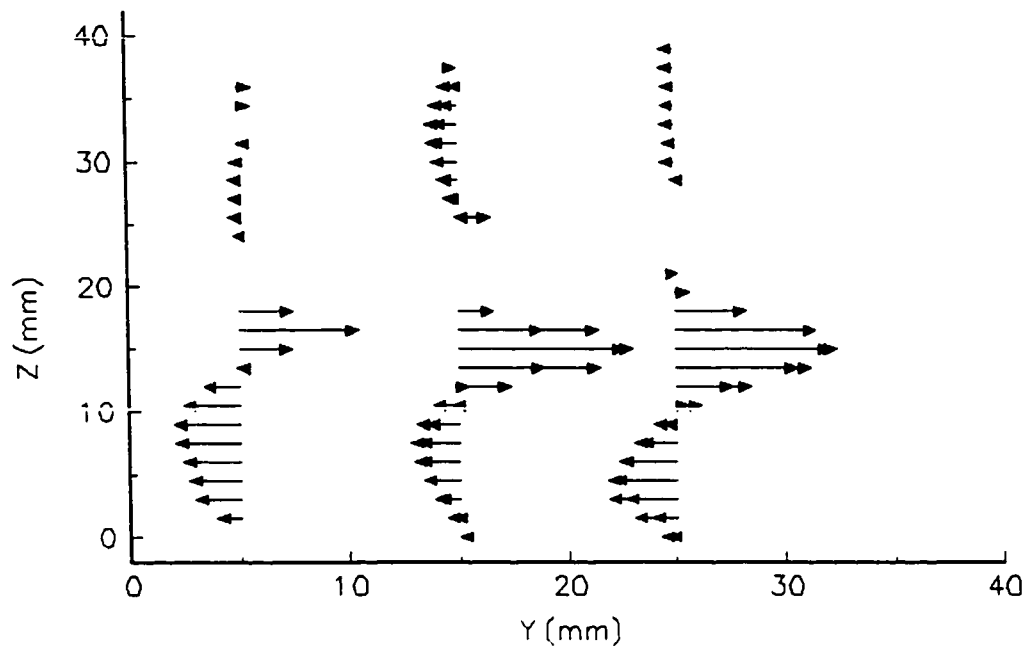


Figure 6.2.6. – Axial Velocities for Element 1 at $Re=6$ at $X = 16$ mm.

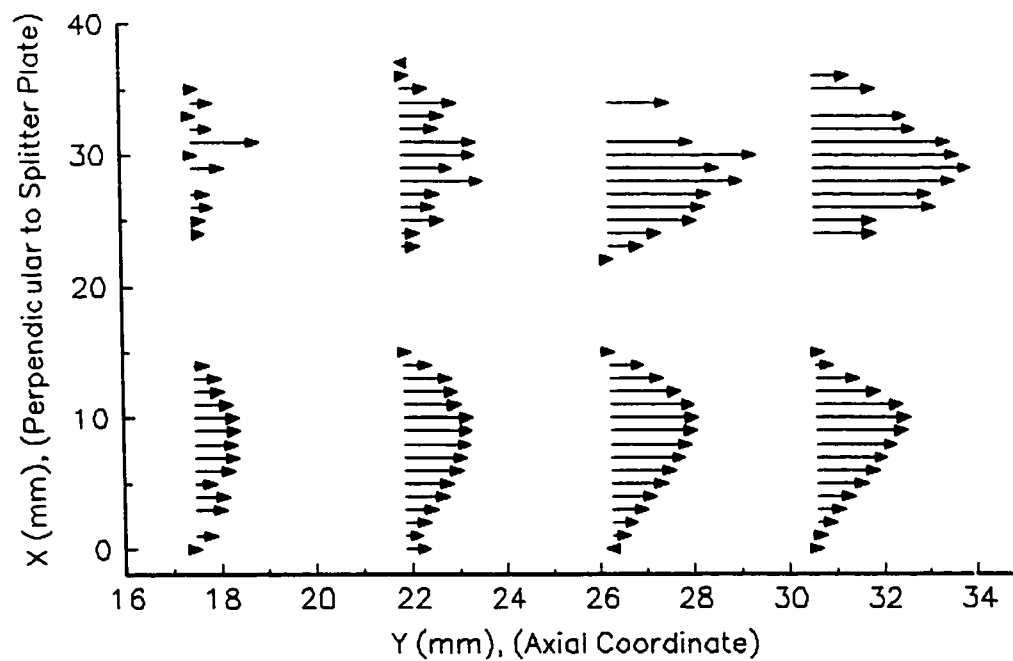


Figure 6.2.7. – Axial Velocity Vector Plot for Element 1, at $Z = 0$ mm and $Re = 60$.

6.3. PIV Measurements

The velocity contours for the axial and two radial components in the static mixer are presented in Figures 6.3.1 to 6.3.13 for the first four elements. The fluid flow field in the mixer was measured by visualising a series of axial planes constant in the x or z directions and determining the axial and two transverse velocity components. The flow field around an element was measured one half the elements distance per set of data due to the limitation imposed on the magnification by the diameter of the seeded particles. As a consequence, slight discontinuities in the contour plots at an axial location of $y \sim 30\text{mm}$ for the first element and $y \sim 85\text{ mm}$, 135mm and 205mm for subsequent elements are observed. The diameter of the tube was used to calibrate the PIV images and the location of the flow field was determined from the top and bottom of each element. The images for all the planes were measured based from the calibrated images at $x = 0\text{ mm}$ and $z = 0\text{ mm}$. The interrogation area and mesh were chosen based on the centre axial planes ($X = 0\text{ mm}$ and $Z = 0\text{ mm}$). At the outer edges of the contour plots (near the tube wall), there is data that appear as blue or red contours which look like spots or squares. These are the result of measurements near the tube wall. Near or within an element, a similar behaviour in the plot is observed. This is an inherent problem with PIV near solid objects since the closest the PIV measurement can be made near the wall is 0.5mm (see section 4.4).

Figure 6.3.1i. shows a schematic of the fluid flow around the first element. This schematic shows the view for the axial cross section contour plots shown in Figures 6.3.1. and 6.3.2. The axial cross section planes for these two figures are

$-16.3\text{mm} \leq x \leq 16.3\text{mm}$. Unfortunately, the solid element could not be depicted in these plots. Figures 6.3.1. and 6.3.2. show results for the y -component (axial) of velocity for $-16.1\text{ mm} \leq x \leq -2.7\text{ mm}$. The axial fluid flow starts at $y=0\text{mm}$ and is directed by the element from the left to the right (of the plots). This flow is expected from intuition as the fluid is redirected by the counter-clockwise twist of the element (viewed from the entrance plane). For $2.7\text{ mm} \leq x \leq 16.3\text{ mm}$, the fluid moves from the bottom right to the top left. The flow field at $x = 0\text{ mm}$ (Figure 6.3.1g.) would be expected to show symmetry about $z = 0\text{ mm}$ but the velocity contours on the right side of the element (of the plot) shows larger regions with high axial velocity. In fact, the entire right side of the mixer shows more fluid having higher axial velocities than the left side for their symmetric partner planes (i.e. $x = 2.7\text{ mm}$ and $x = -2.7\text{ mm}$ planes should be symmetric). The right side of the element is the blue fluid shown in schematic 6.3.1i. Figure 6.3.3 shows the results for the axial velocity measurements for element 1 from an orthogonal view to the one presented in Figure 6.3.1 and 6.3.2. These results show how the parabolic profile entering the mixer is divided at the leading edge of the first element ($x = 0\text{ mm}$) (Figure 6.3.3b.). At $z = 0\text{ mm}$, the left side or blue fluid side (Figure 6.3.3h.) shows larger regions of fluid with high axial velocities as seen in the measurements at the planes of $z = 10.9\text{ mm}$ and -10.9 mm . This asymmetry in the flow was not expected for the given inlet condition of a fully developed parabolic velocity profile. The possible reasons for this are discussed below.

Figures 6.3.4. and 6.3.5. show the contour plots of the transverse velocity (u) component in the x co-ordinate direction. The results are presented for planes of

$-16.3\text{mm} \leq z \leq 16.3\text{ mm}$. The magnitude of the maximum velocity in the x co-ordinate direction is approximately three times smaller than the axial velocity at the first element. The results for the x – component of velocity are close to being symmetric with slightly larger regions with high velocities for the positive z planes (red side of flow). Figure 6.3.6. shows the velocity contours of the z - component (w) of velocity at element 1. The flow is fairly symmetric for these results. From the visualised planes, the average fluid velocity magnitude in the z direction is smaller when compared to the results for the x component of velocity (the complimentary radial component). These results show that the fluid sees more rotation in the x -co-ordinate direction compared to the z -co-ordinate direction. This would be expected, given that the element only rotates 90 degrees mainly causing fluid to be pushed to tube wall in the x -direction at the first element. This is quite an important result for heat transfer applications. If the goal is to move the fluid from the centre of the tube to the tube wall, this has only been partially achieved as there has been very little movement of the fluid in the z co-ordinate direction compared to the x co-ordinate direction. For the first element, the results seem to indicate that ninety degrees of rotation may not be enough to create strong fluid motion from the centre to the wall of the tube. These results do suggest that the conclusions of Hobbs and Muzzio (1997b) from CFM that the optimal twist per element is 120 degrees are valid.

The red (left) side (Figure 6.3.1i.) of the fluid flow around element 1 had larger regions with high radial velocity components and lower axial velocity component compared to the blue fluid flow side. This asymmetry may be explained by the element geometry itself. The method by which the elements are made, may not create a helix

with a constant helix angle, α (amount of rotation/ aspect ratio). The helix was assumed to be very close to having a constant helix angle throughout the element since the elements were twisted gradually during fabrication (see section 3.1). This variability in the element geometry may have caused the observed asymmetric flow.

Measurements across element 2 are shown in Figures 6.3.7. and 6.3.8. The element shows larger regions with high axial velocities on one side of the element when compared to the other side. The flow field shows that the fluid entering the element has a lower axial velocity than the fluid entering the first element. The fluid at the second element shows higher radial velocity in the z - co-ordinate direction at an earlier point (lower axial position) than for element 1. At $x = 10.9$ mm and 5.4 mm, the fluid is subjected to strong radial velocities within the first half of the element ($57 \text{ mm} \leq y \leq 85 \text{ mm}$). The x - component of velocity is not shown for the second element but displays similar results to the z - component of velocity (for the second element) in magnitude and flow field for the x -component of velocity at element 1. The axial velocity contour plots in Figure 6.3.7. show how the fluid recombines above the trailing edge of the first element ($y \sim 60$ mm).

One of the most interesting results of the PIV measurements can be seen in Figure 6.3.8e. ($x = -10.9$ mm). At $y = 110$ mm and $z = -10$ mm, there is positive flow in the z - co-ordinate direction. This captures the flow recirculation in the radial plane, where at the high pressure side of the element (the front of the rotating element), fluid moves to the outer wall and at the suction side of the element, fluid flows toward the centre of the

mixer. This confirms the flow pattern predicted by simulations in literature [Hobbs et al. (1997a,b,1998), Dackson and Nauman (1987)].

The axial and radial velocity contour plots for element 3 are presented in Figures 6.3.9. and 6.3.10. These velocity contours show a fair degree of noise. This was due to large reflections of light off this element. No explanation as to why this particular element gave more reflection than others can be given. The reflections are seen as red or blue spots (square shaped). This data captures the fluid flow division and recombination across the element. These results show fairly good symmetry for the axial but not the radial components of velocity. The fluid recirculations in the radial plane can be seen in Figure 6.3.10a. to 6.3.10f ($y \sim 165\text{mm}$ and $z \sim 10\text{mm}$). The maximum velocity in the z – co-ordinate direction is approximately thirty percent higher than the first two elements. The w – velocity component maximum is approximately 0.004m/s compared 0.003m/s for the first two elements. This increase is beneficial to mixing, as more fluid is being moved from the centre to the wall of the mixer and back again creating recirculation in the radial plane. The results for element 3 show that the magnitudes of the x and z components of velocity are approximately equal. This indicates that there is a development length for the radial flow. Even though the first element does not create large radial flows by the third element the amount and magnitude of radial flow has increased.

Figures 6.3.11 to 6.3.13. show the fluid velocity contour plots for element 4 for the y , z , and x components of velocity respectively. In Figure 6.3.11f., the fluid reorientation is captured well where the fluid from the third element ($y \sim 170\text{ mm}$) on the

left side ($0 \text{ mm} < z < -19 \text{ mm}$) is being directed to the right side of element 4 ($y \sim 200 \text{ mm}$). This image shows a fairly strong 'core' of fluid with high axial velocity (also seen in Figure 6.3.11g. and 6.3.11h.). This may not appear to be very beneficial for mixing since channelling of the fluid flow would be expected. However, the flow shows a strong radial component that keeps the fluid moving in and out of the 'core'. This would explain the plug flow behaviour for residence time distributions observed by Nauman (1982) for the Kenics® static mixer.

The Re number for the simulations of Hobbs et al. (1998) was 0.15. Their fluid velocity contour plots show very similar profiles to those reported here even though an element of 180 degrees of twist was simulated for the same aspect ratio. Over a 90 degree twist (half the element), the trends and relative magnitudes of the velocity are in fairly good agreement. Hobbs et al. (1998) results are shown in Figure 6.3.14. The results show the axial (V_x) and radial velocity ($V_y + V_z$) and the absolute magnitude of the radial component ($|V_y + V_z|$). The figure shows the velocity contours for half the element or 90 degrees of twist. Given that the inlet condition to the element is flow from an element with 180 degrees of twist, the inlet flow to the this element (figure 6.3.14e.) has a fair amount of radial flow (magnitude ~ 0.5 the maximum radial velocity across the element). The results presented here do not show as strong a radial component at the junction of two elements. Significant differences would be expected in the radial velocity component for elements with different degrees of twists (for the same aspect ratio).

The measured fluid flow field showed small magnitudes of the radial velocity components near the centre of the mixer ($x \sim 0 \text{ mm}$ and $z \sim 0 \text{ mm}$). However, there was still

sufficient velocity to move the fluid from the centre outwards. This disagrees with the results of Byrde and Sawley (1986a,b,c), who reported from their simulations that fluid at the centre would experience small deformations. This is in contrast to Hobbs et al. (1998) analysis based on the magnitude of the rate of deformation tensor, which showed higher magnitudes of strain rate at the centre (near the elements) than in the centre of the hemispheres (between the element and mixer wall).

To determine the relative magnitude of mixing in the static mixer, the magnitude of the deformation tensor was calculated and is presented in the next section.

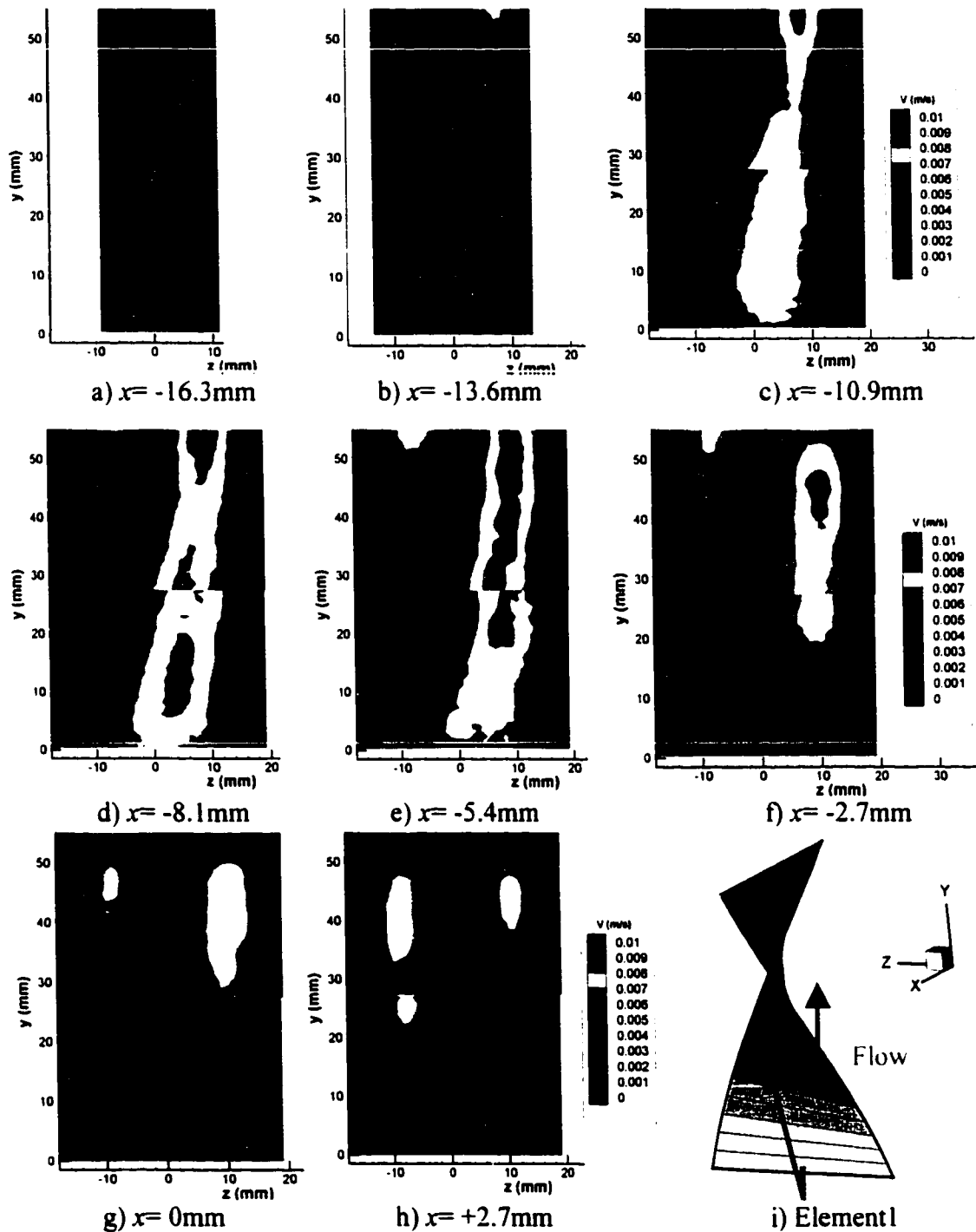


Figure 6.3.1. – Contour Plots of y -component (v) (axial) of Velocity, Axial Cross Sections of Element 1, PIV Measurements at $Re=0.1$.

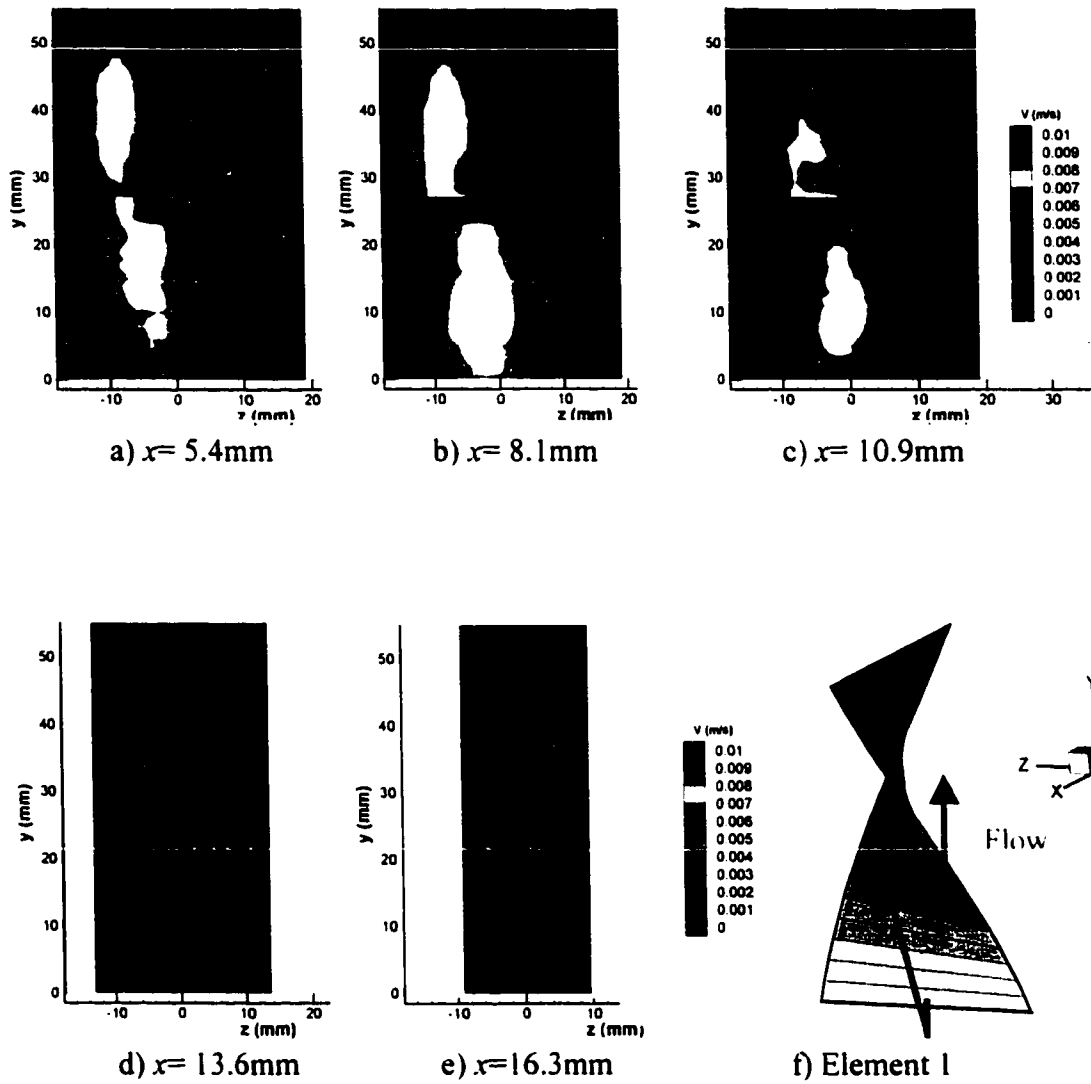


Figure 6.3.2. – Contour Plots of y -component (v) (axial) of Velocity, Axial Cross Sections of Element 1, PIV Measurements at $Re=0.1$.

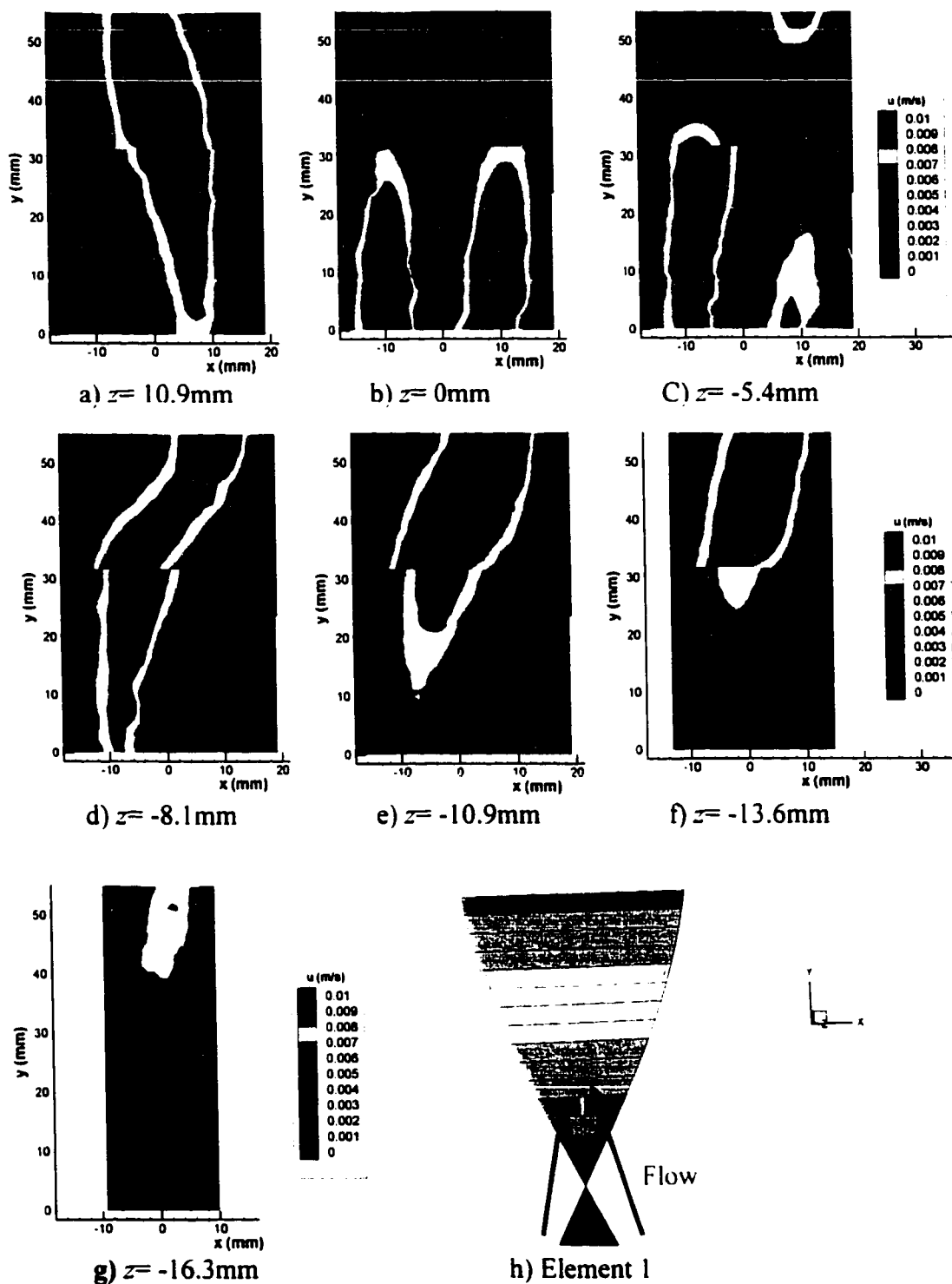


Figure 6.3.3. – Contour Plots of y -component (v) (axial) of Velocity, Axial Cross Sections of Element 1, PIV Measurements at $Re=0.1$.

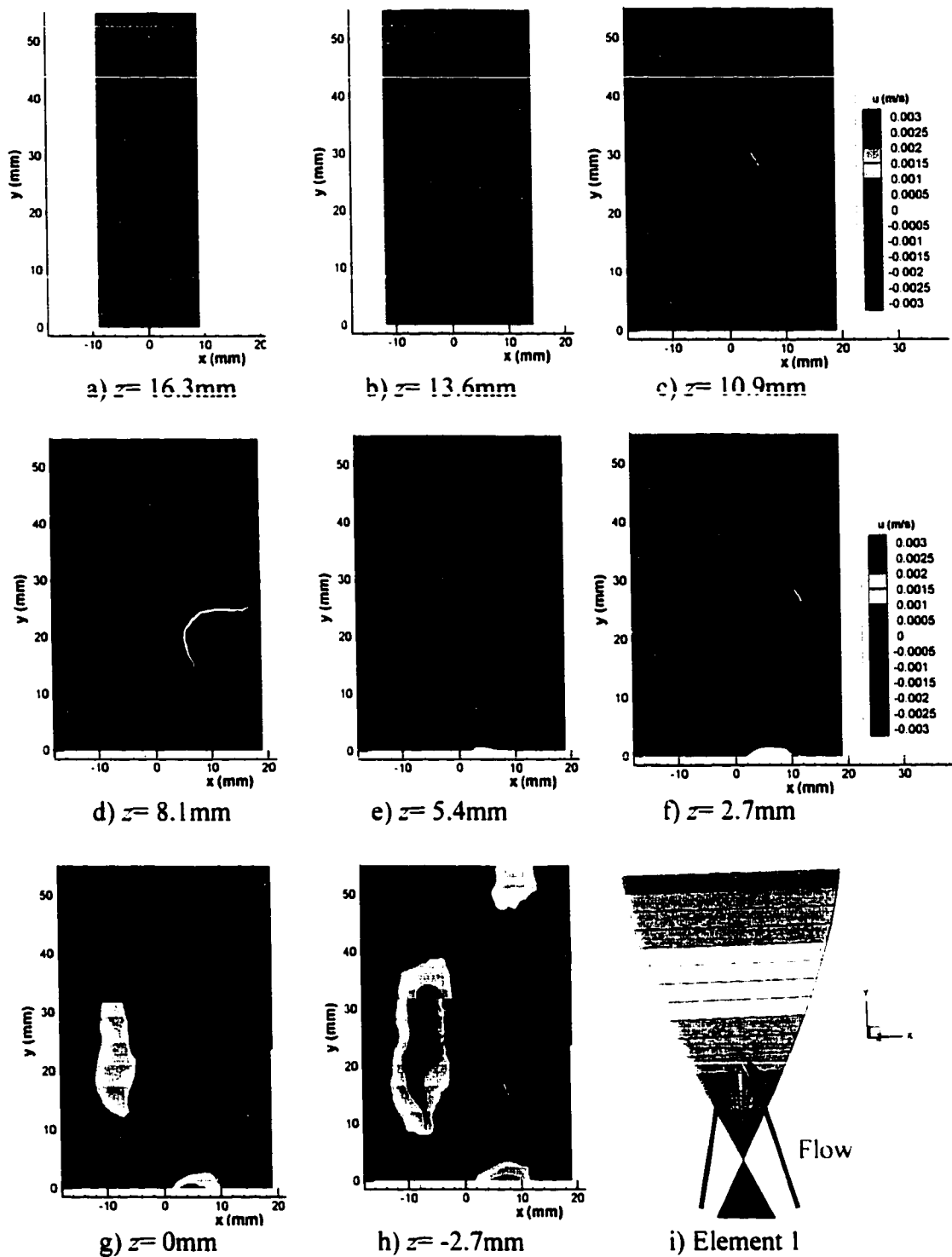


Figure 6.3.4. – Contour Plots of x -component (u) (radial) of Velocity, Axial Cross Sections of Element 1, PIV Measurements at $Re=0.1$.

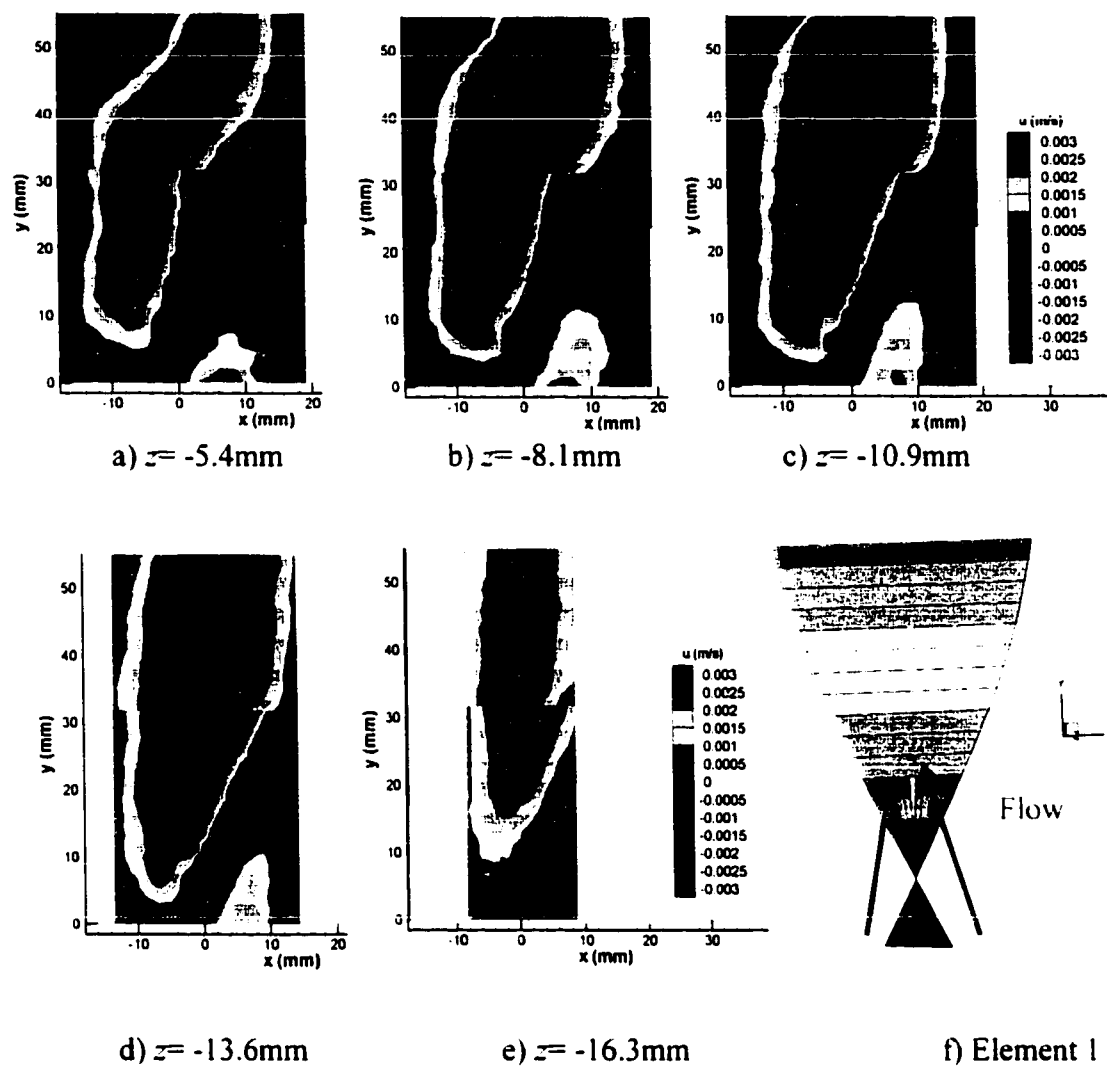


Figure 6.3.5. – Contour Plots of x -component (u) (radial) of Velocity, Axial Cross Sections of Element 1, PIV Measurements at $Re=0.1$.

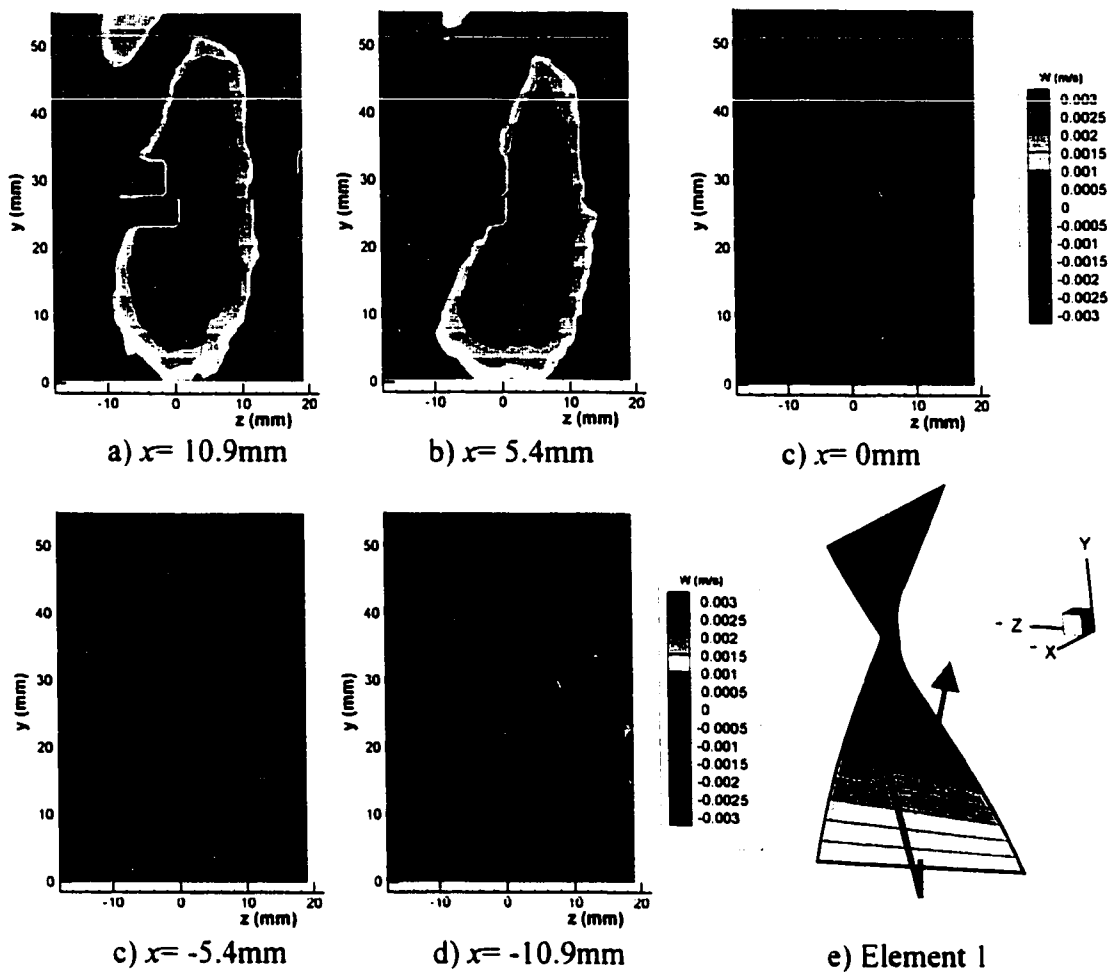


Figure 6.3.6. – Contour Plots of z -component (w) (radial) of Velocity, Axial Cross Sections of Element 1, PIV Measurements at $Re=0.1$.

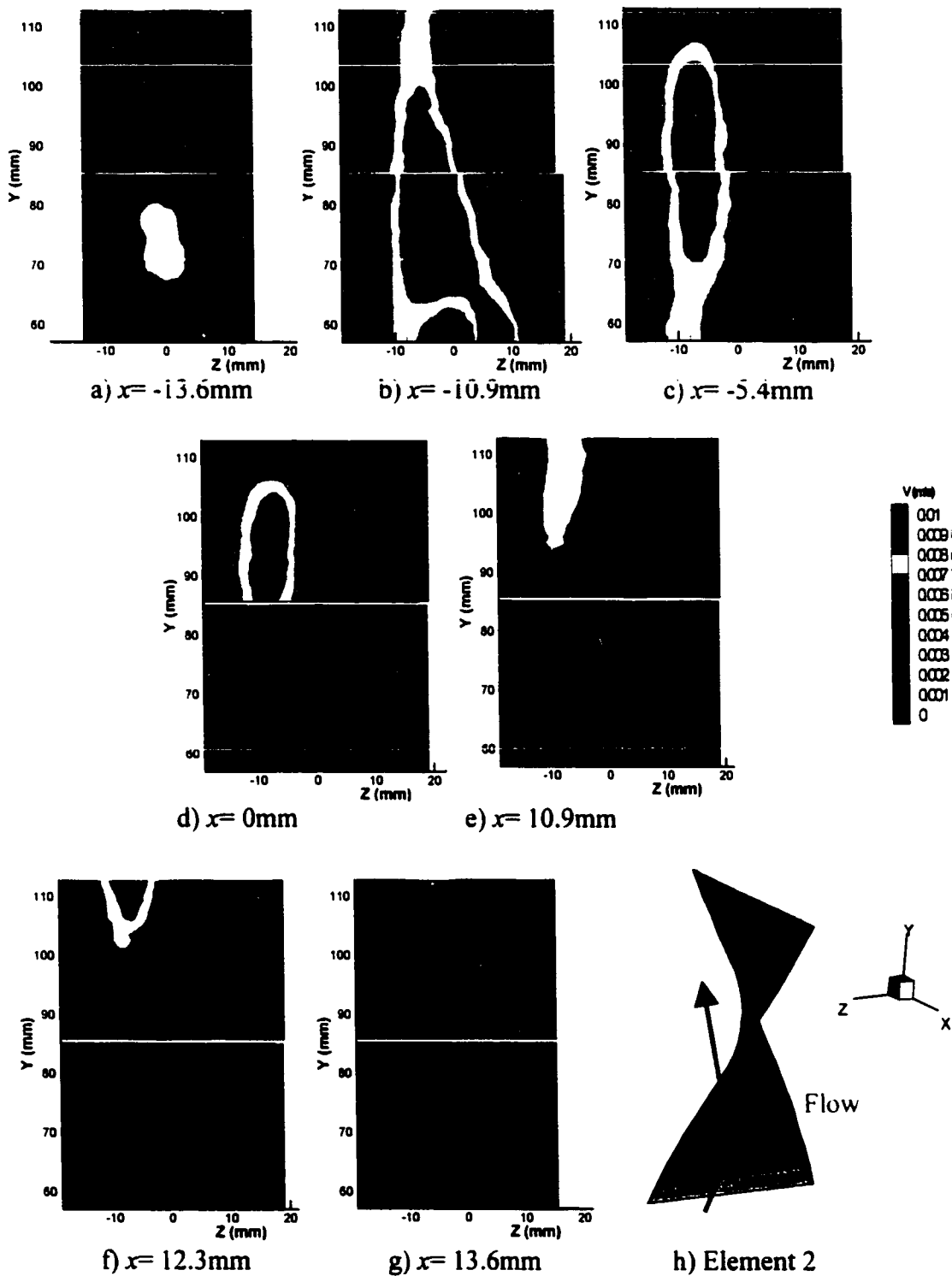


Figure 6.3.7. – Contour Plots of y -component (v) (axial) of Velocity, Axial Cross Sections of Element 2, PIV Measurements at $Re=0.1$.

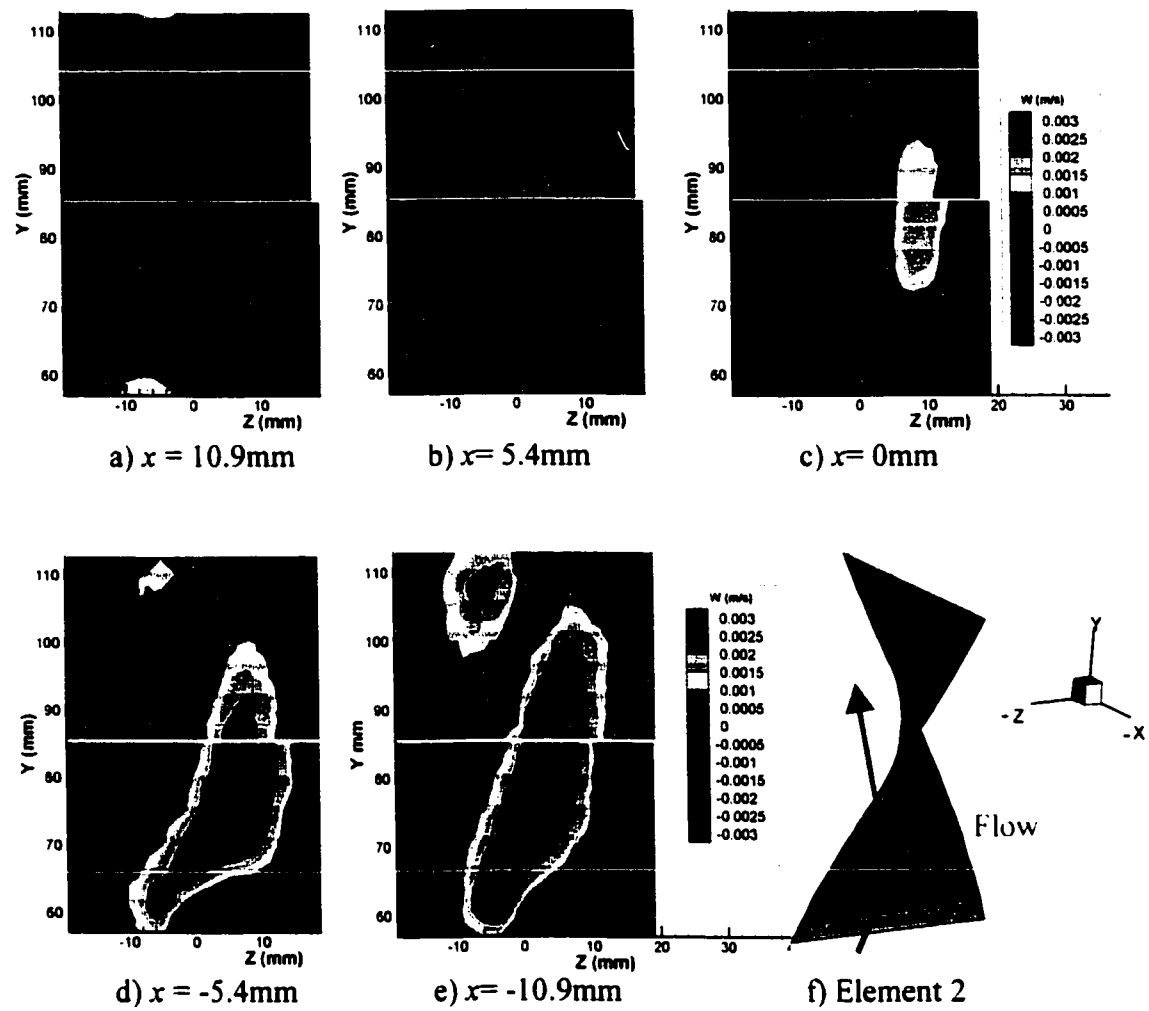


Figure 6.3.8. – Contour Plots of z-component (w) (radial) of Velocity, Axial Cross Sections of Element 2, PIV Measurements at $Re=0.1$.

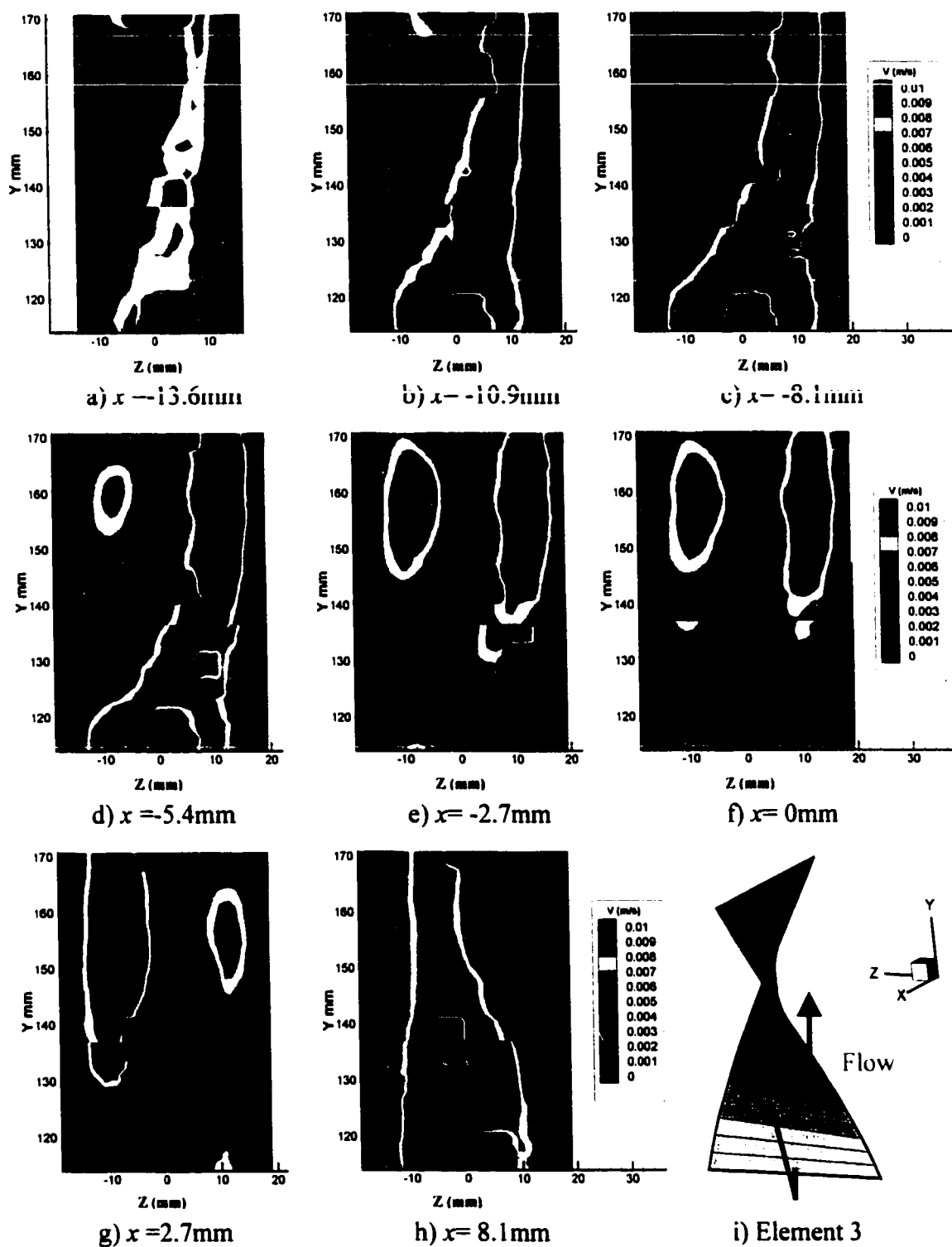


Figure 6.3.9. – Contour Plots of y -component (v) (axial) of Velocity, Axial Cross Sections of Element 3, PIV Measurements at $Re=0.1$.

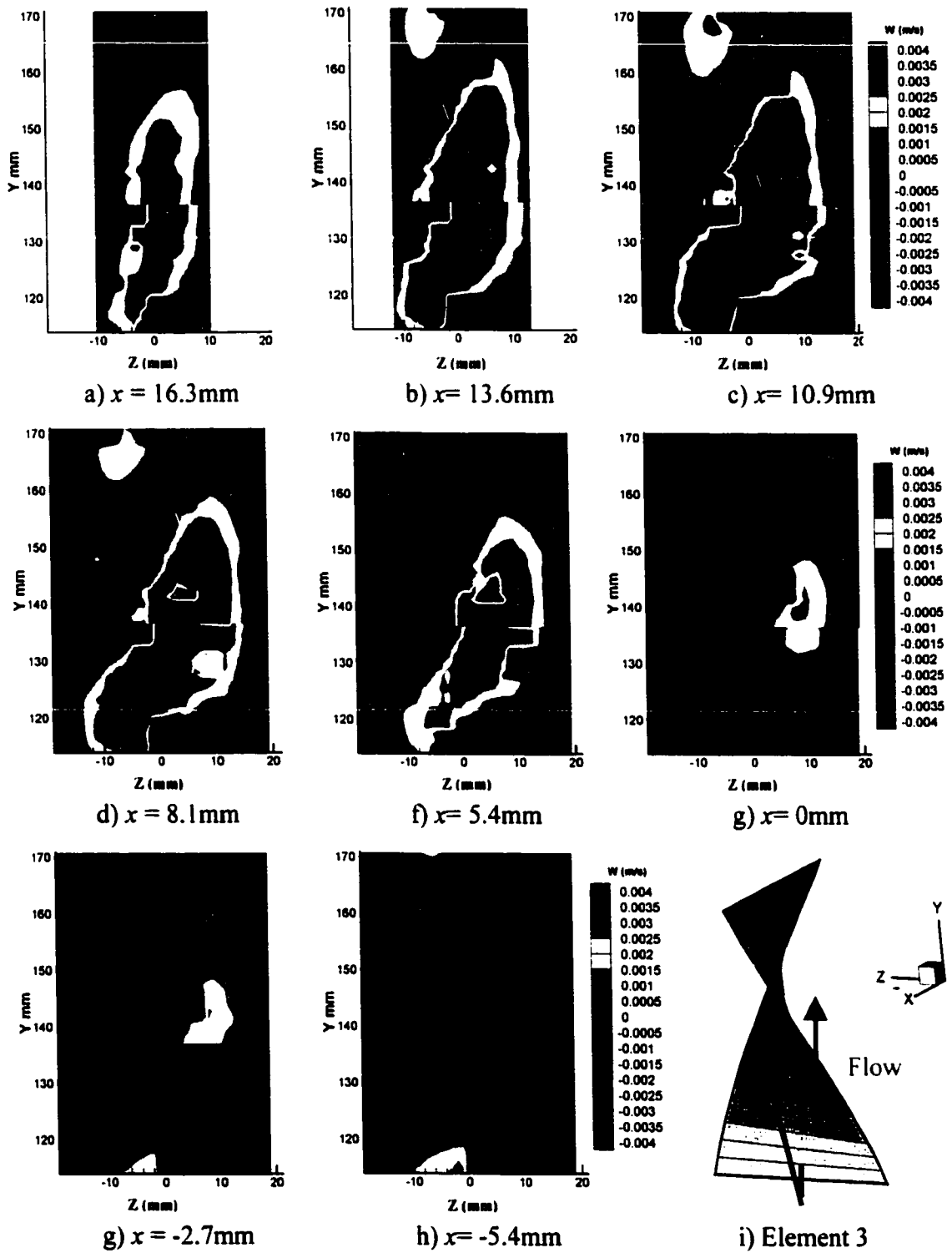


Figure 6.3.10. – Contour Plots of z -component (w) (radial) of Velocity, Axial Cross Sections of Element 3, PIV Measurements at $Re=0.1$.

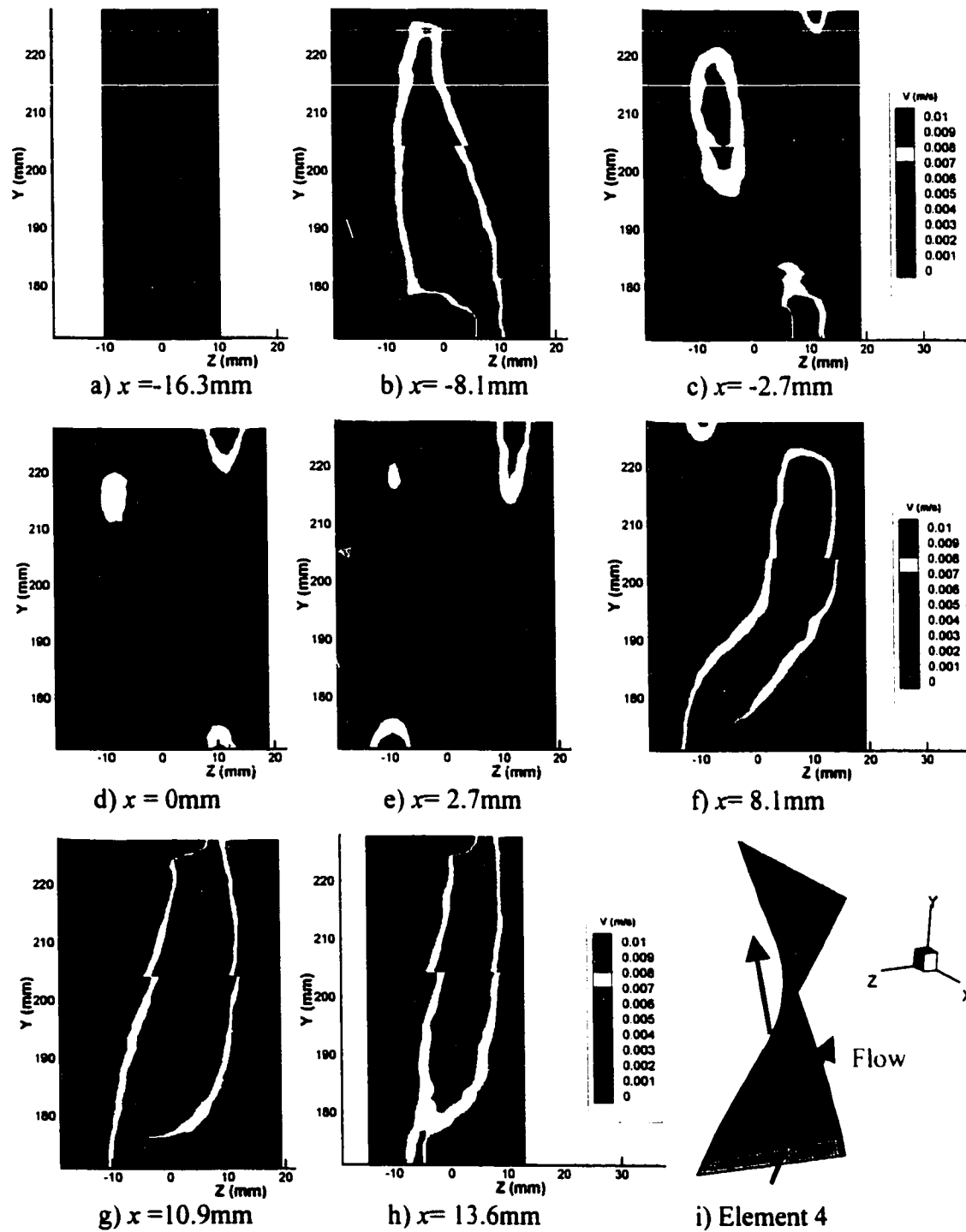


Figure 6.3.11. – Contour Plots of y -component (v) (axial) of Velocity, Axial Cross Sections of Element 4, PIV Measurements at $Re=0.1$.

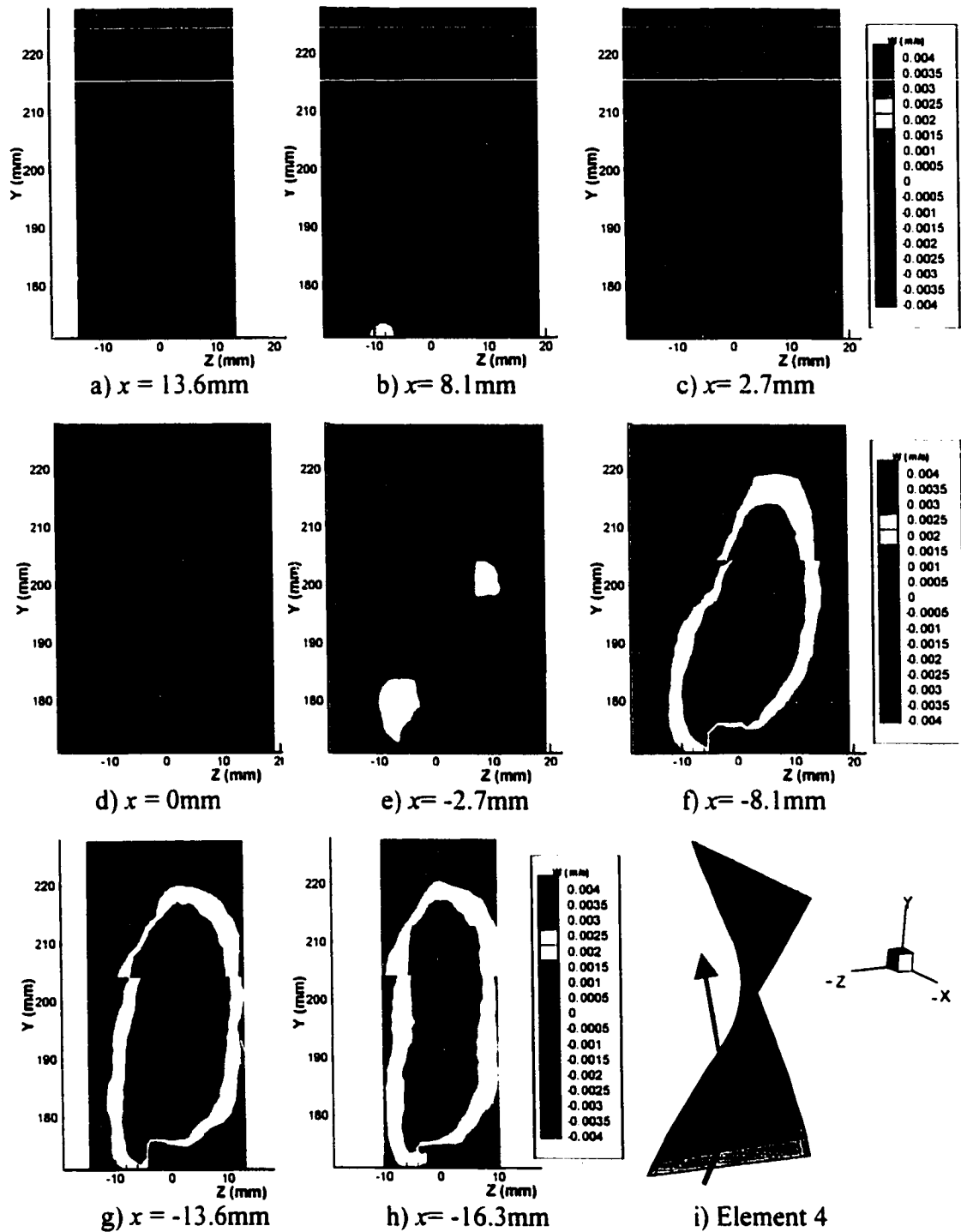


Figure 6.3.12. – Contour Plots of z -component (w) (radial) of Velocity, Axial Cross Sections of Element 4, PIV Measurements at $Re=0.1$.

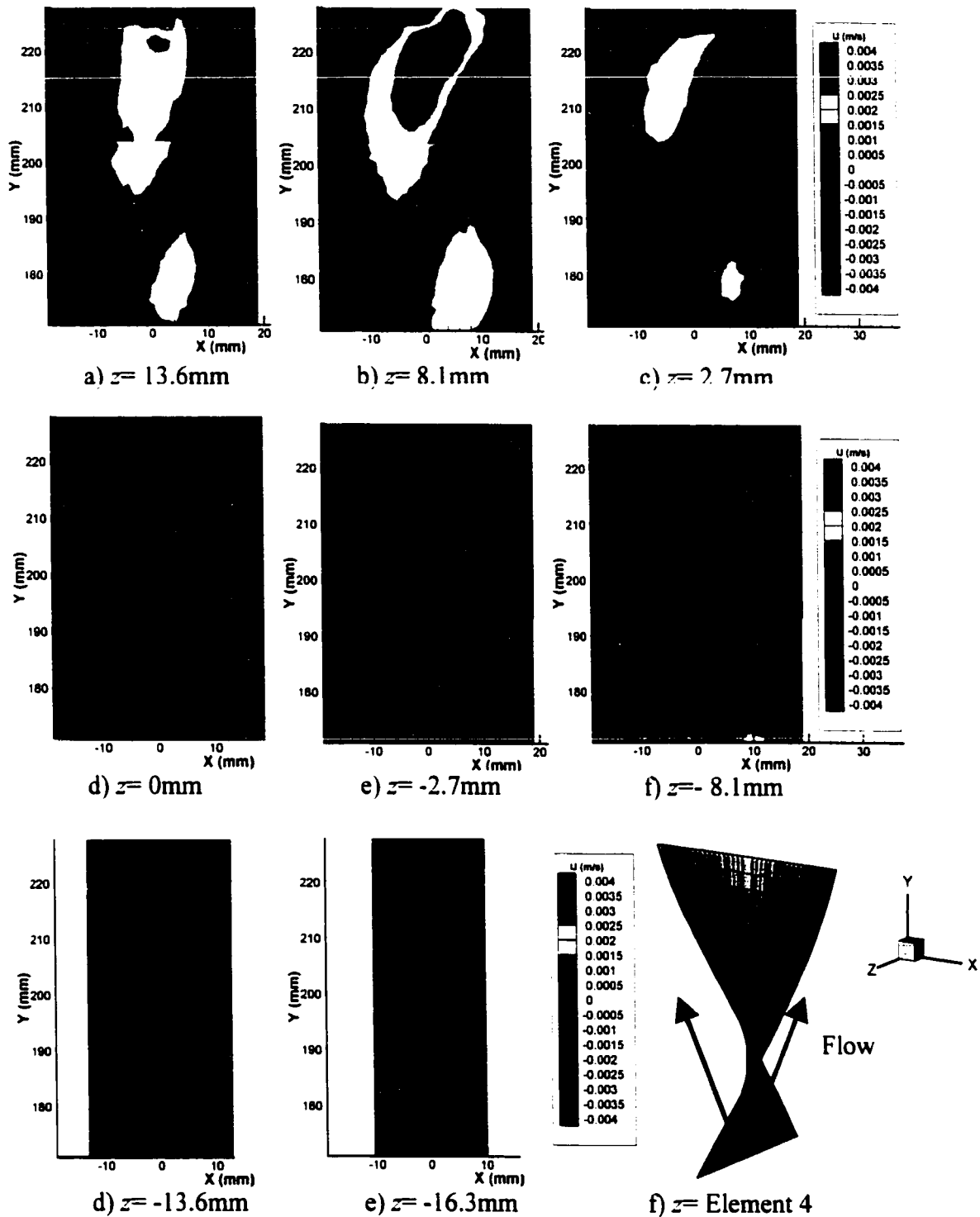


Figure 6.3.13. – Contour Plots of x-component (u) (radial) of Velocity, Axial Cross Sections of Element 4, PIV Measurements at $Re=0.1$.

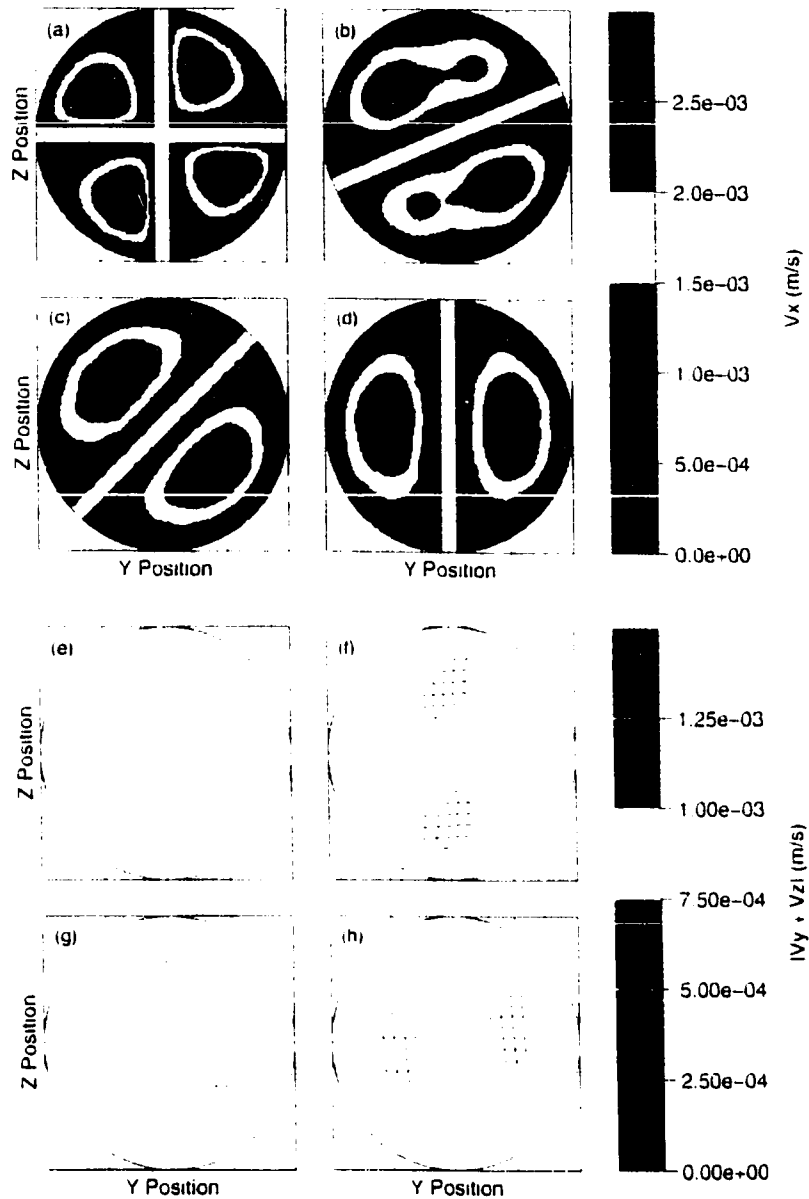


Figure 6.3.14. Fluid Flow Simulation Results from Hobbs et al. (1998) for Aspect Ratio of 1.5, $Re=0.15$ and a twist of 180 degrees per element. (a) – (d): contours of the axial velocity component (v_x); (e)-(h): velocity vectors for radial components (v_y+v_z). Velocity Magnitude ($|v_y+v_z|$) is Color coded. $X=0$ for (b,f); $X=L/8$ for (c,g); $X=L/2$ for (d,h); L = length of element. (Reprinted from CHEM. Eng. Sci., Vol 53, D.M. Hobbs, P.D. Swanson and F.J. Muzzio, 'Numerical Characterization of low Reynolds number flow in the Kenics static mixer', pp. 1565-1598, Copyright 1998, with permission from Elsevier Science)

6.4. Rate of Deformation Analysis

The magnitude of the rate of deformation tensor, $\dot{\gamma} = [1/2(\mathbf{D}:\mathbf{D})]^{0.5}$, was calculated based on the velocity gradients at each grid point. The velocity gradients were calculated from the measured velocities by a simple forward finite difference [i.e. $\frac{\partial v_i}{\partial x_j} = \frac{\Delta v_i}{\Delta x}$]. The magnitude of the deformation tensor is related to the local energy consumed to stretch, elongate and shear the fluid element. The value of $\dot{\gamma}$ is a maximum for the energy consumed to mix the fluids at a given point. In actuality, all the energy may not be dissipated for fluid deformation [Ottino (1989)]. This is explained in section 2.5.

For each measurement plane, $\dot{\gamma}$ was calculated for the two dimensional flow only (using only the two components of shear and elongation). To have a complete three dimensional calculation of the magnitude required some sophisticated interpolating schemes. Keane and Adrian (1990) point out that to estimate the deformation tensor (resolving all three components) with an error of five to 10 percent, the resolution of the grid required for the static mixer would require the magnification to be doubled. This would be too costly in time and effort for the little gain compared to the results presented herein.

Figures 6.3.15 to 6.3.18. show contour plots of the magnitude of the rate of strain tensor at element 1 and 4. Figure 6.3.15. and 6.3.16. show $\dot{\gamma}$ for x and z planes. It was expected that the first element would display high levels of deformation since the element would create a transition in the flow thereby, creating strong mixing [Middleman (1977)]. The highest values of $\dot{\gamma}$ were calculated along the surfaces of the element and tube wall

with a maximum of 0.7 s^{-1} . From the earlier discussion in the previous section, due to the smaller transverse velocity components in the z – co-ordinate direction, larger regions experience high levels of deformation in the xy planes (Figure 6.3.16.) as compared to the yz planes (Figure 6.3.15.). The first element displayed less overall deformation across its entire volume compared to elements 2, 3 and 4. The results for elements 2 and 3 not presented as the results from element 4 are very similar.

Figures 6.3.17. and 6.3.18. show the contour plots for $\dot{\gamma}$ at constant x and z planes for element 4. They show that the highest regions of deformation occur due to the fluid shearing at the element surfaces and tube walls. Most of the images in Figures 6.3.1.7. and 6.3.1.8., show that the highest levels of deformation occur at the element to element junctions. This can be seen at $y = 180 \text{ mm}$ for the constant x planes (Figure 6.3.17.) and $z \cong 0 \text{ mm}$ where the trailing edge of the third element has high deformation rates at and near its surface. In Figure 6.3.18., the leading edge of the fifth element is seen to create a high level of deformation ($y = 225 \text{ mm}$, and $x \cong 0 \text{ mm}$). These images also demonstrate that the fluid in the ‘core’ (refer to section 6.3. - Figure 6.3.11.) of the flow has very low magnitudes of deformation, $\dot{\gamma} \cong 0 \text{ s}^{-1}$.

Figure 6.3.19. displays the results of $\dot{\gamma}$ for Hobbs et al. (1998) for aspect ratio of 1.5 and 180 twist per element. Their results predict high levels of deformation along the element surfaces and at the junction of elements (Figure 6.3.19a.). Hobbs showed that the deformation along the element surfaces is due mainly to shear and that at the element junctions elongation and shear caused deformation. Their mathematical models also predicted low deformations in the core of the flow (the centre of the flow between the

element and mixer wall). Their simulation results match very well with the experimental measured deformation fields. The relative magnitudes for deformation predicted are very close at the element junctions. Here the simulation predicted a maximum $\dot{\gamma}$ of 0.5 to 0.6s^{-1} and experiments measured a value of 0.9 to 1.0 s^{-1} . Along the surfaces of the elements the simulation predicted $0.3\text{-}0.4\text{ s}^{-1}$ for $\dot{\gamma}$ while the experimentally measure value was $\dot{\gamma}=0.7\text{s}^{-1}$. Even though the flow conditions and mixer geometry are not the same for these experiments and the simulations of Hobbs et al. (1998), there is good agreement on the relative magnitude of the rate of strain and the location of high deformation.

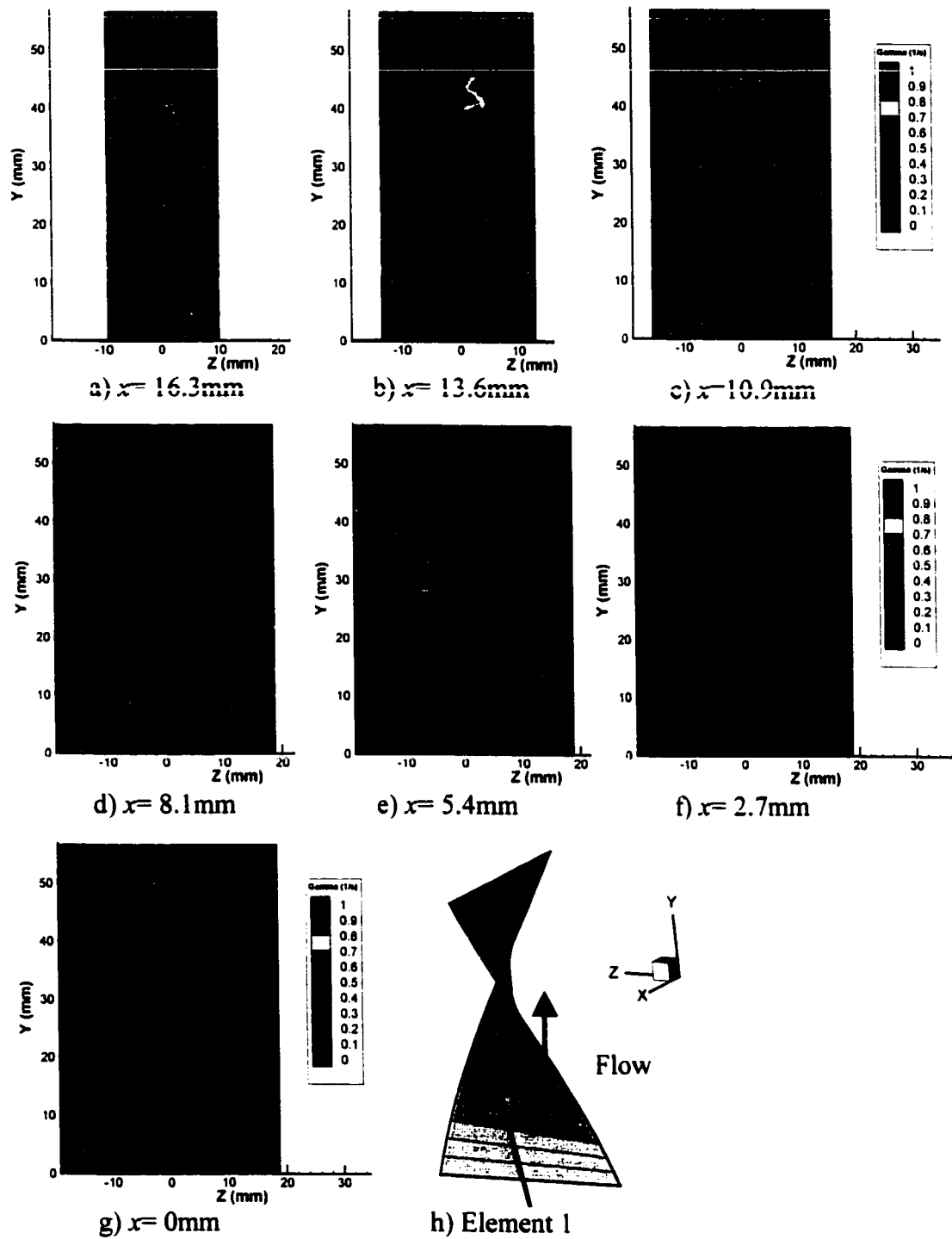


Figure 6.3.15. – Contour Plots of the Magnitude of the Rate of Strain Tensor, Axial Cross Sections of Element 1, PIV Measurements at $Re=0.1$.

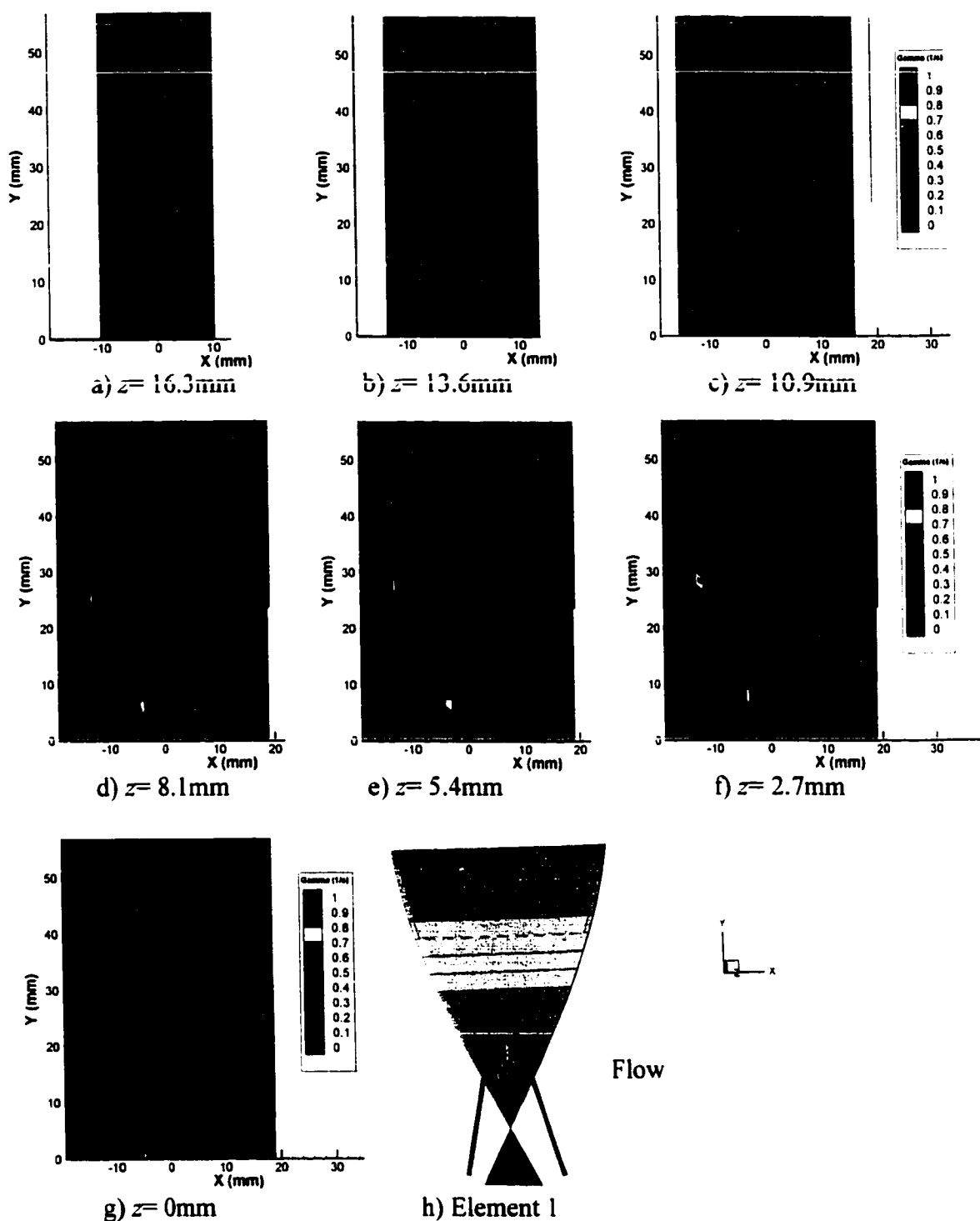


Figure 6.3.16. – Contour Plots of the Magnitude of the Rate of Strain Tensor, Axial Cross Sections of Element 1, PIV Measurements at $Re=0.1$.

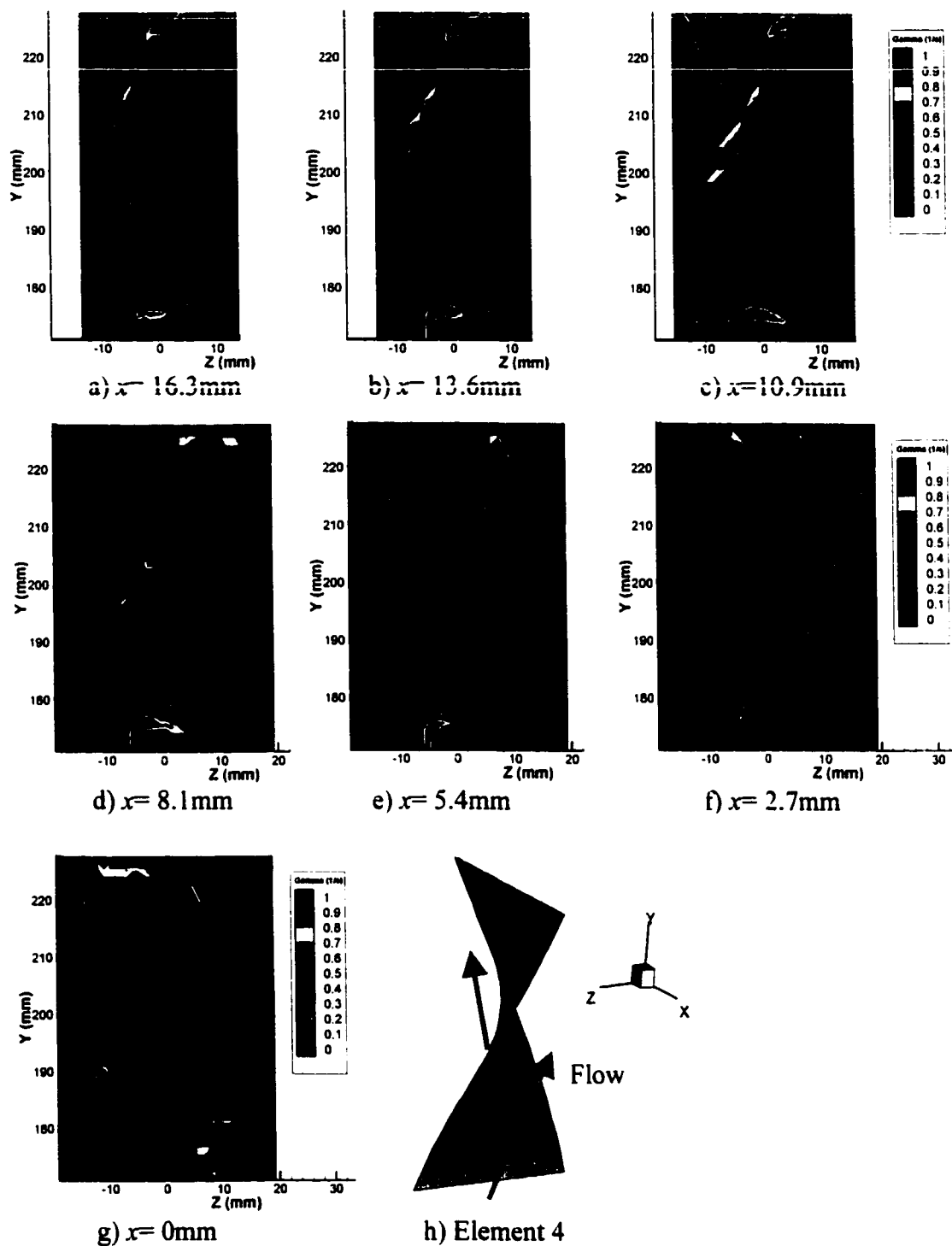


Figure 6.3.17. – Contour Plots of the Magnitude of the Rate of Strain Tensor, Axial Cross Sections of Element 4, PIV Measurements at $Re=0.1$.

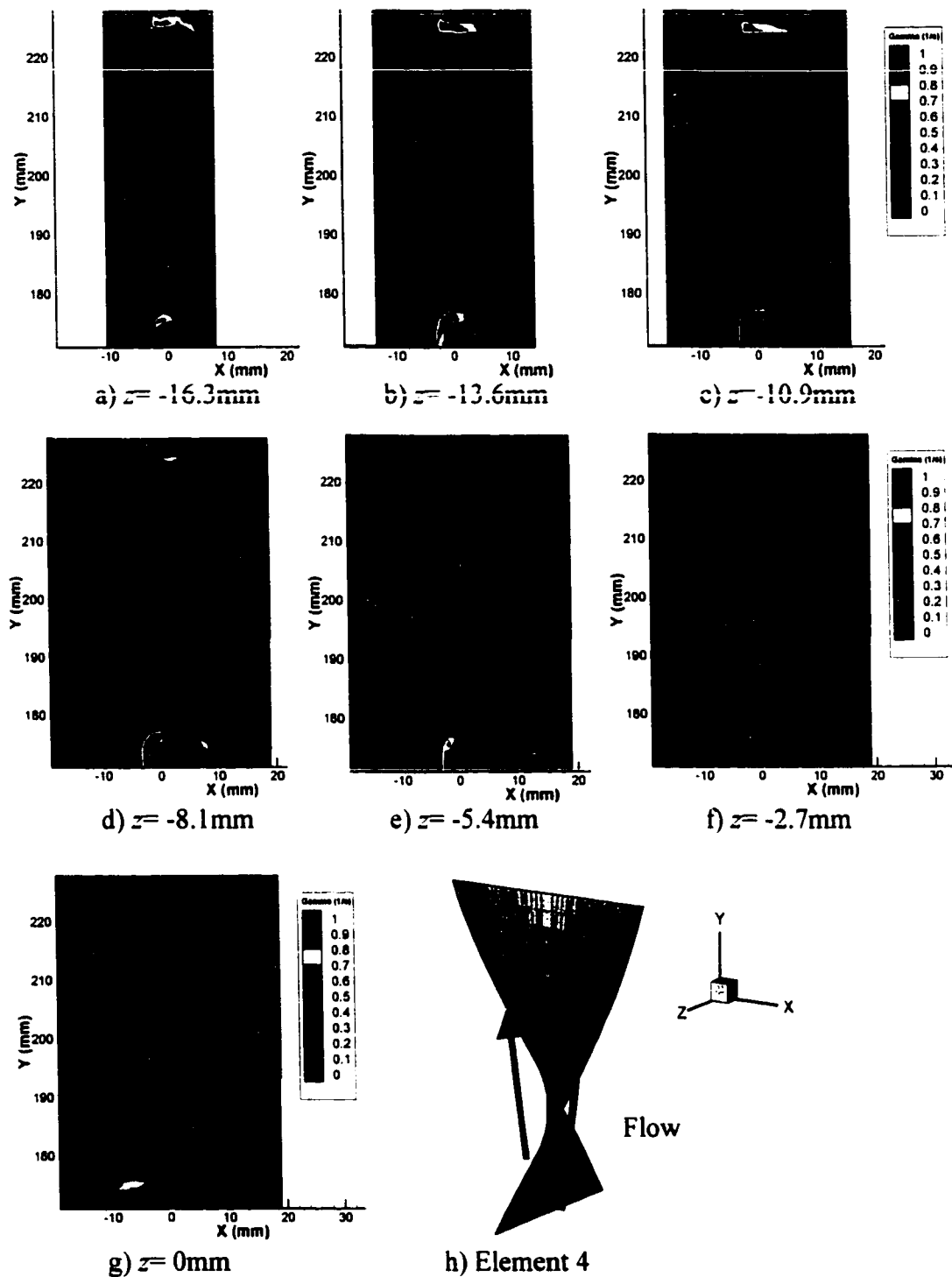


Figure 6.3.18. – Contour Plots of the Magnitude of the Rate of Strain Tensor, Axial Cross Sections of Element 4, PIV Measurements at $Re=0.1$.

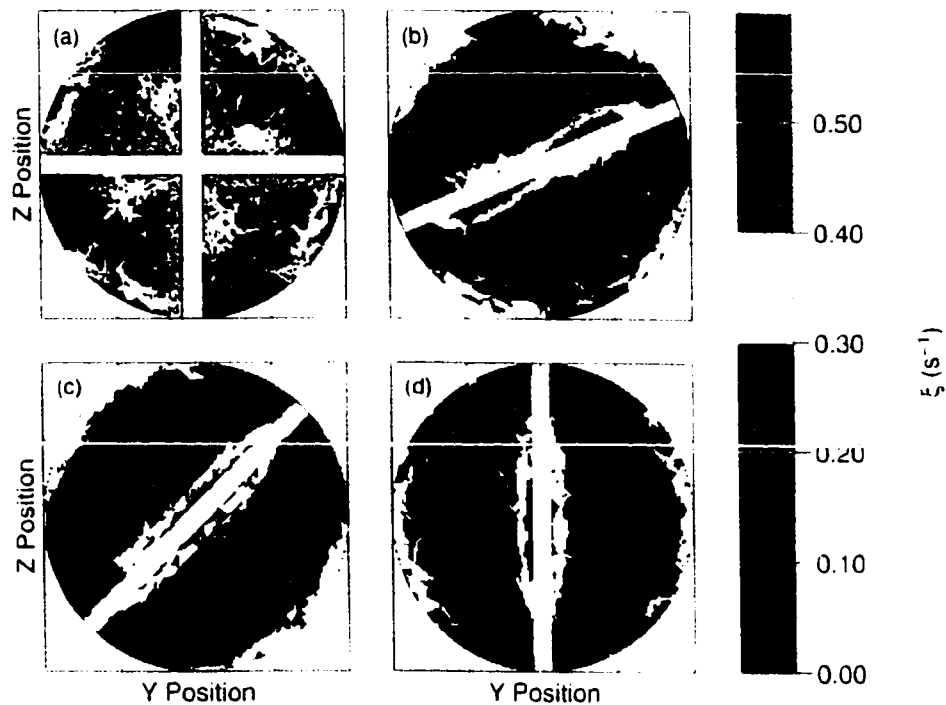


Figure 6.3.19. –Cross sectional profiles of the magnitude of the rate of strain tensor (ξ) for the mixer cross sections shown in Figure 6.3.14 from Hobbs et al. (1998). [(a): $X=0$; (b) $X=L/8$; (c): $X=L/4$; (d): $X=L/2$, where L =length of Element] (Reprinted from CHEM. Eng. Sci., Vol 53, D.M. Hobbs, P.D. Swanson, and F.J. Muzzio, 'Numerical Characterization of low Reynolds number flow in the Kenics static mixer', pp. 1565-1598, Copyright 1998, with the permission of Elsevier Science).

6.5. Summary

The lack of experimental data has proven to be a major stumbling block for mixer designers as their levels of confidence in simulation were not high due to the inability of CFD codes to be validated. The experimental measurements of velocity and mixing, provide benchmarks that have not been in published literature before. With this new data, the importance for CFD can already be seen. Comparisons with the work from Hobbs et al. (1998) have shown that the mathematical model results of the fluid flow in the Kenics® mixer are quite similar to these experimental results. The objective of future simulations should be to test CFD codes against the experimental measurements presented. The experimental results are summarised below.

The experimental fluid velocities in a static mixer having elements with an aspect ratio of 1.5 and 90 degrees of twist per element have been measured over four elements. The velocity field measured captured the mixing nature of the static mixer, where the flow was split at the leading edges of the elements and recombined at the trailing edge. The flow followed the path created by each element in the direction of the helical twist. Recirculations in the radial plane were observed that would flow from the high pressure side of the element out along the tube wall to the low pressure side or suction side of the element. The magnitude of the radial flow was approximately 30 percent of the maximum axial flow for the first two elements and then increased to 40 percent by the fourth element. These results indicated that the radial flow field required time to develop. The axial velocities reduced after the first element as the parabolic entering velocity profile was split into two. The axial velocity profile for the elements showed high

velocity regions between the element and the tube wall resembling the flow in a semicircular duct. The magnitude of this velocity reduced at the leading edge of each element as the developed flow from the previous element was split. But for this element geometry studied, results showed that the flow had short development lengths for the axial velocity profiles to re-establish the 'core' of the flow.

The flow field also exhibited differences in the magnitudes of the two transverse velocity components (the two complementary radial components). The flow showed lower magnitudes of velocity in the z – co-ordinate direction compared to the x – co-ordinate direction at the first element. Thereafter, the fluid had similar magnitudes of x and z components of velocity at later elements. The conclusion to be drawn from this was that the mixer required a development length to allow the radial flow to build in magnitude.

The rate of deformation analysis on the fluid flow field indicated that mixing efficiency would be increased if the elements had a larger helix angle (amount of rotation/ aspect ratio) at the first element. This became apparent from the reduced velocity magnitudes in the transverse z – co-ordinate direction compared to the complementary transverse x – co-ordinate direction. The lower magnitude in velocity resulted in a reduced magnitude of the rate of deformation, which translates into less stretching and elongation. This indicated that mixing would benefit if more radial flow could be generated in the z – co-ordinate direction at the first element. The rate of deformation analysis showed that the largest magnitude of deformations occurred at the

junction between elements, the element surfaces and the mixer tube surface and that the core of the fluid flow experienced little deformation.

From these results, mixing efficiency could be possibly increased if higher deformations could be created at the first element. Even though the striation thickness reduces by one half at this first element (for $L/D=1.5$), this is due to the flow division. If the magnitude of deformation could be increased at this element perhaps a further reduction in thickness would be seen. A possible solution would be to exchange the first element for an element that had a larger helix angle to create more radial flow. The helix angles studied in chapter 5: $\pi/3$, $\pi/2$ and $5\pi/8$, showed that the shortest (aspect ratio of 0.8) with the larger helix angle reduced the striation thickness over the first element by eighty percent. The penalty would be an increase in pressure drop and the increase in mixing would have to be sufficient to justify the increase in energy.

These experimental results help eliminate many questions for the mixer designer but in the process have shown the need for more analysis when approaching mixer design with the idea of using elements with different geometrical characteristics in combination. However, the experimental data presented in chapters 5 and 6, have opened up a whole new avenue for mixer designers. The mathematical models of fluid flow fields in the static mixer available, now have the data that will allow for them to be validated not only for fluid velocities but also for validation of the computational fluid mixing simulations. If one of these models, could be validated with these results, it could be used as a design tool in a similar way to the works of Byrde and Sawley (1996a,b,c), Hobbs and Muzzio (1997a,b) and Hobbs et al. (1998).

The recommendation of creating mixers where the first element has a large helix angle leads naturally to the recommendation of testing designs with elements with different geometrical parameters in combination. The problem that mathematical models would face is that the entire mixer would have to be simulated compared to the current method of combining the periodic profiles over two elements. For example, Hobbs et al. (1998) solved the flow field for a six element mixer. The simulated velocity profiles over elements 3 and 4 were cut and pasted in between the 4th and 5th elements, creating the velocity profile for an eight element mixer. This could be done over and over creating any size of mixer. Therefore, simulations of entire mixers with no periodicity in element geometry would be extremely numerically expensive, requiring many more hours than the current simulations (~100 hours).

7.0 Flow and Mixing in the Twin Screw Extruder

7.1. Introduction

The primary roles of twin screw extruders (TSE) in the polymer industry are compounding, reactive extrusion, modification processes and blending. Typically, designs of these machines use screw elements that can be combined in many different configurations to create screw profiles that have significant effects on the performance of the twin screw extruder. In order to ascertain the effect on flow and mixing by changing screw elements, studies on individual elements have been conducted to further the understanding in the design process.

The velocity field was measured for the kneading blocks (KB/45/20) for two screw profiles (Figure 3.1.6.) and for one orientation of the discs (rotation angle). Extended discs [see section 3.1.2.] were used to isolate the kneading discs such that upstream and downstream influences could be eliminated. This allowed for the characterisation of the performance of the discs (KB/45/20). The second screw profile utilised forward conveying elements placed before and after the kneading discs (KB/45/20). The flow conditions and measurement locations are given in Table 3.5.2.

The main motivation for measuring the velocity field in the kneading disc section was to create a database that would help validate the computer simulations of

Bravo (1998). Secondly, the velocity fields help characterise the mixing nature within the kneading disc section. The shear and elongation fields are quantified and provide valuable design information.

7.2. Flow Visualisations

For all the flow visualisations, the dye and bulk flow rates were kept constant at 1 mL/s and 5 mL/s respectively. The details are listed in Table 3.5.1. The main difference between the two screw profiles studied was the position of the back pressure element. The screw profiles are shown in Figure 3.1.5. Sections 7.2.1. and 7.2.2. discuss the digitized images acquired from video sequences. The digitized images are limited in their resolution and as a result some of the structures are difficult to see. A few colour photographs are shown in section 7.2.3. to help illustrate some of the structures present in the kneading section of the twin screw extruder

7.2.1. Geometry C

Figures 7.2.1.1. to 7.2.1.7. show results for 100 rpm for screw profile C where the dye is introduced at the front edge of the kneading disc section. Figure 7.2.1.1. is taken just after the dye is injected at the right screw (RS) and it shows that there is a strong forward convection in the kneading disc section. A small amount of dye is seen to coat

the elements and barrel in the second disc section (KB/30/20). This dye exits the section early and unmixed. Figure 7.2.1.2. and 7.2.1.3. show that after 5 to 6 seconds after introducing the dye, there is still a fair amount of poorly mixed material exiting the kneading disc section.

Figures 7.2.1.4. and 7.2.1.5. show the mixing within the nip region. Figure 7.2.1.4. shows the folding action of the KB 30/7/20 discs and Figure 7.2.1.5. shows the cutting and elongation for the KB 45/5/20 discs. From Figure 7.2.1.5., the radial nips created by two discs passing by one another are as important as the axial nip regions since both nip regions cause the flow to continuously rearrange orientation and, hence, the elongation and shear fields have a much stronger influence.

Figures 7.2.1.6. and 7.2.1.7. show the structures created after 4 to 5 rotations at the left screw (LS). It is evident that the dye seems to be held up in the first set of kneading discs with a small amount of dye passing to the second set of discs. This material is stretched and exits the kneading discs section early compared to the bulk of the dye.

Figures 7.2.1.8. to 7.2.1.10. show snapshots in time of the mixing in the kneading disc at 150 rpm. There are still filaments or striations present, but the striations are thinner compared to those at 100 rpm. Figure 7.2.1.10. shows the extremely strong mixing action as the dye is compressed in the radial and elongated in the axial directions as the dye passes through the gap between the disc and barrel (outlined by box).

Figures 7.2.1.11. to 7.2.1.14 show a series of snapshots at 200 rpm. Figure 7.2.1.11. shows that at 200 rpm, after the dye has been introduced, there are still

large pockets of unmixed zones in the first set of discs and at the second set of discs (Figure 7.2.1.12.). Figure 7.2.1.13. shows that material is convected forward without being mixed. Portions of the dye are channelling and are hardly being mixed before they exit the kneading disc section. Figure 7.2.1.14. shows this as well, with the lamellar structure above the second kneading disc being comprised of fairly thick striations (outlined by the box).

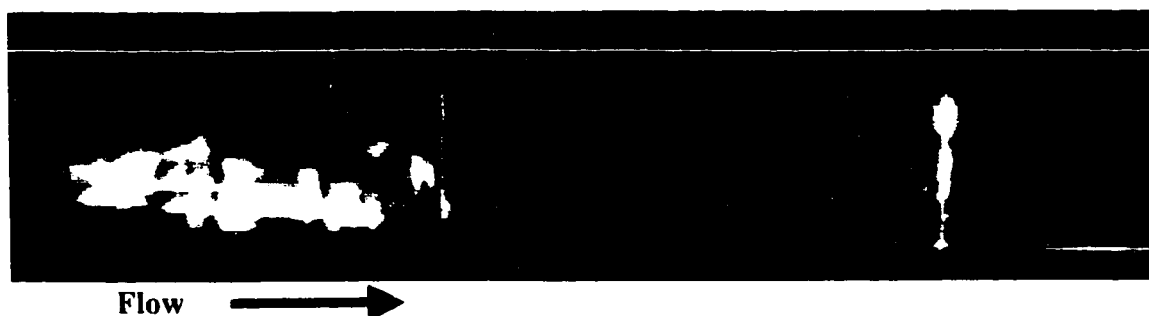


Figure 7.2.1.1. - Location: Right Screw Kneading Disc Section, 1st and 2nd set of Discs.
~1 to 2 Rotations (~1s) after Dye Injection, 100 rpm.

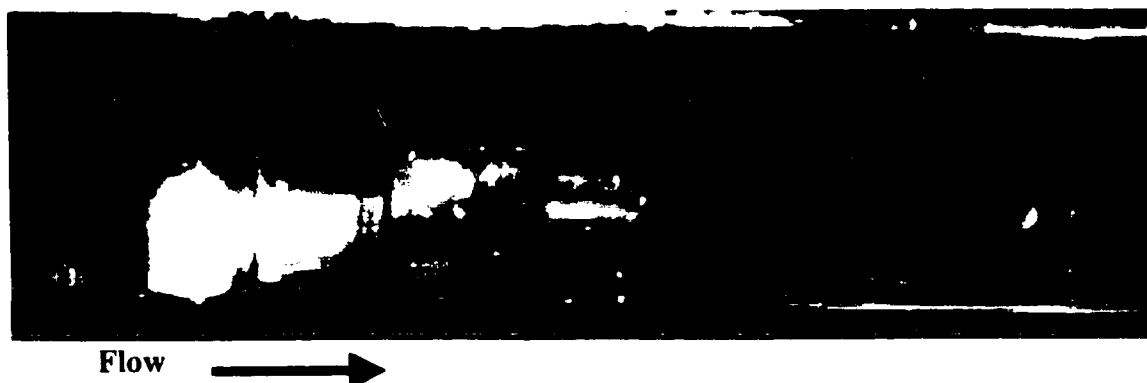


Figure 7.2.1.2. - Location: Right Screw Kneading Disc Section, 1st set of discs after ~10
Screw Rotations (~5-6s), 100 rpm.



Figure 7.2.1.3. - Location: Right Screw Kneading Disc Section, 2nd set of discs after
~10 Screw Rotations (~5-6s), 100 rpm.

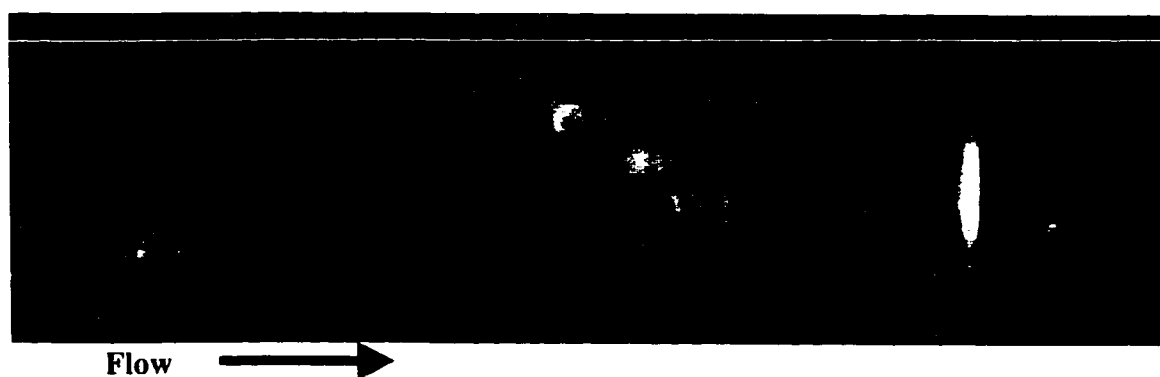


Figure 7.2.1.4. - Location: Nip Region Kneading Disc Section, 1st set of discs after ~10 Screw Rotations (~5-6s), 100 rpm.

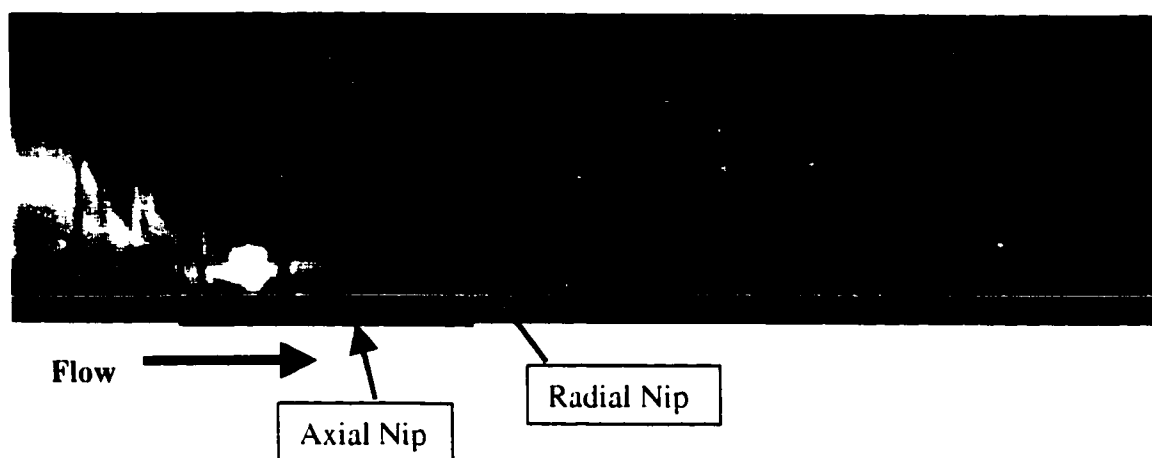


Figure 7.2.1.5. - Location: Nip Region Kneading Disc Section, 2nd set of discs after ~10 Screw Rotations (~5-6s), 100 rpm.

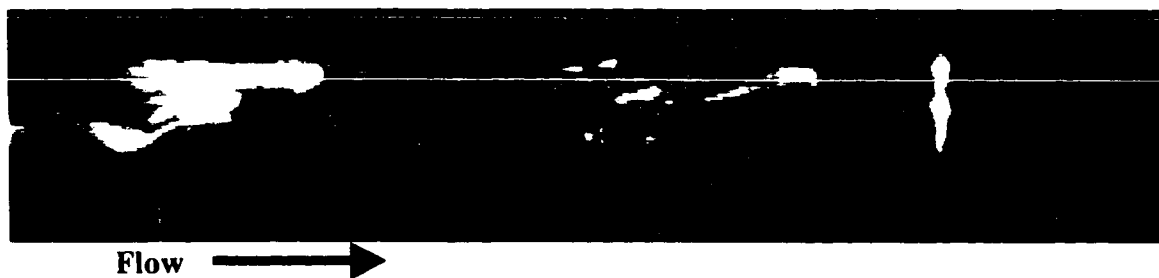


Figure 7.2.1.6. - Location: Left Disc Kneading Disc Section, 1st set of discs after ~5 Screw Rotations (~3s), 100 rpm.



Figure 7.2.1.7. - Location: Left Disc Kneading Disc Section, 2nd set of discs after ~5 Screw Rotations (~3s), 100 rpm.



Figure 7.2.1.8. - Location: Right Screw Kneading Disc Section, 1st set of Discs, ~5 to 6 Rotations after Dye Injection (~3s), 150 rpm.

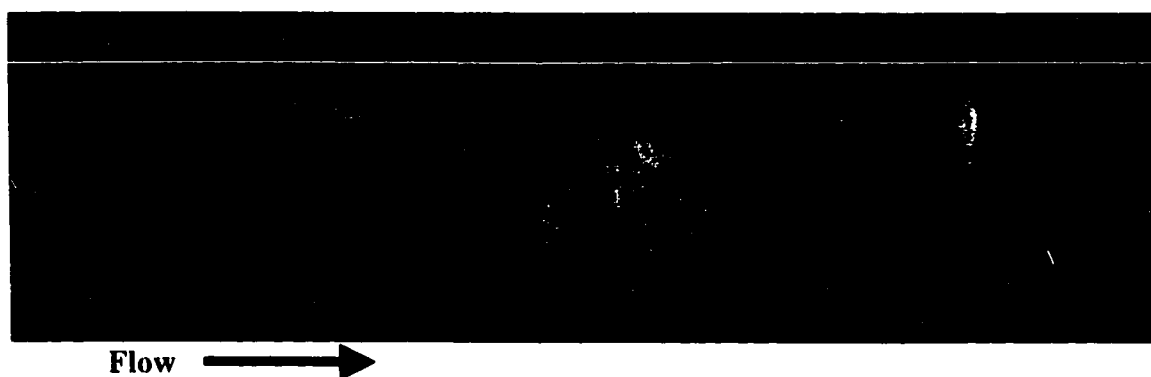


Figure 7.2.1.9. - Location: Nip Region of Kneading Disc Section. 1st set of Discs. ~5 to 6 Rotations after Dye Injection (~3s), 150 rpm.

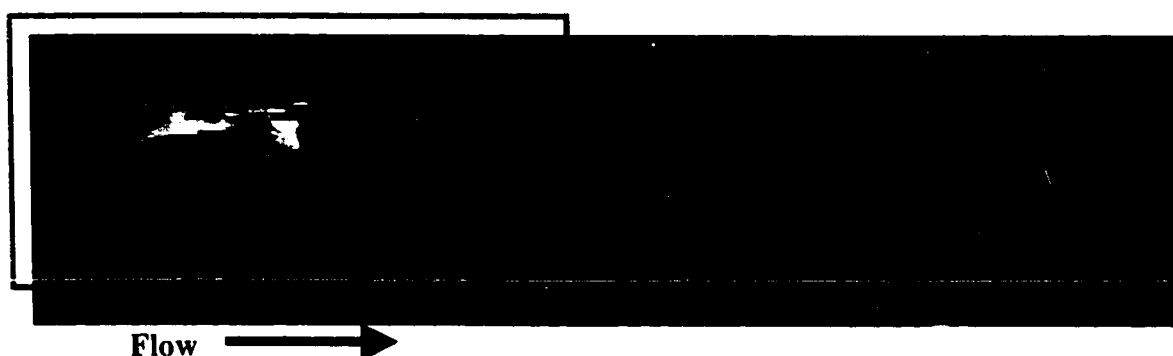


Figure 7.2.1.10. - Location: Left Screw Kneading Disc Section. 1st set of Discs. ~1 to 2 Rotations after Dye Injection.

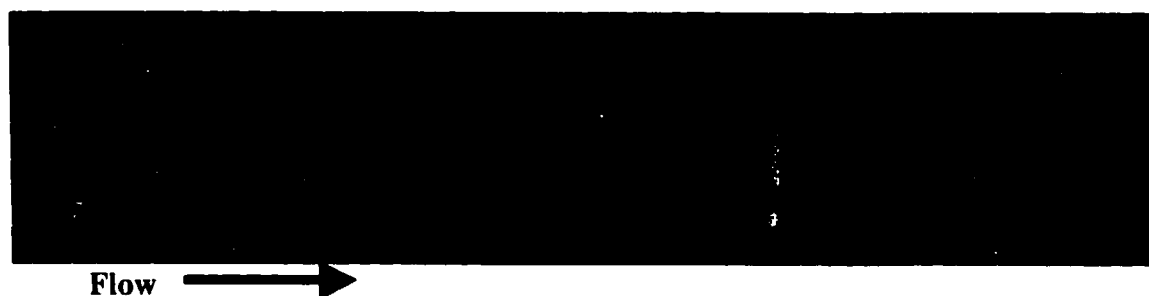


Figure 7.2.1.11. - Location: Right Screw Kneading Disc Section. 1st set of Discs. ~5 to 6 Rotations after Dye Injection (~2s), 200 rpm.

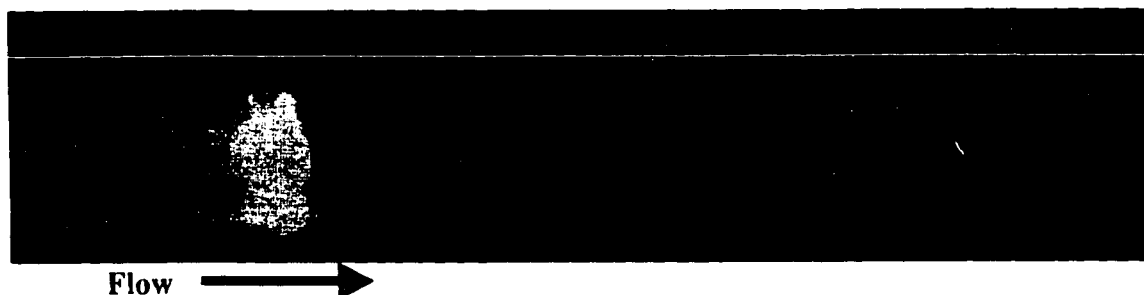


Figure 7.2.1.12. - Location: Right Screw Kneading Disc Section, 1st and 2nd set of Discs, ~10 to 12 Rotations after Dye Injection (~3-4s), 200 rpm.

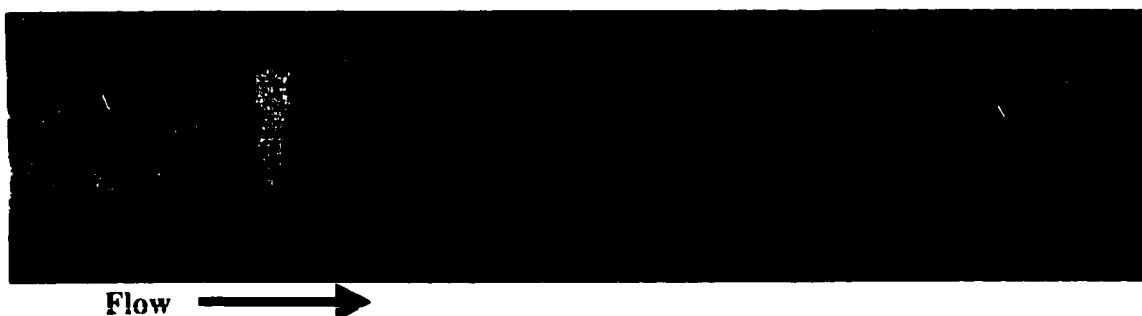


Figure 7.2.1.13. - Location: Left Screw Kneading Disc Section, 2nd set of Discs, ~5 to 6 Rotations after Dye Injection (~2s), 200 rpm.

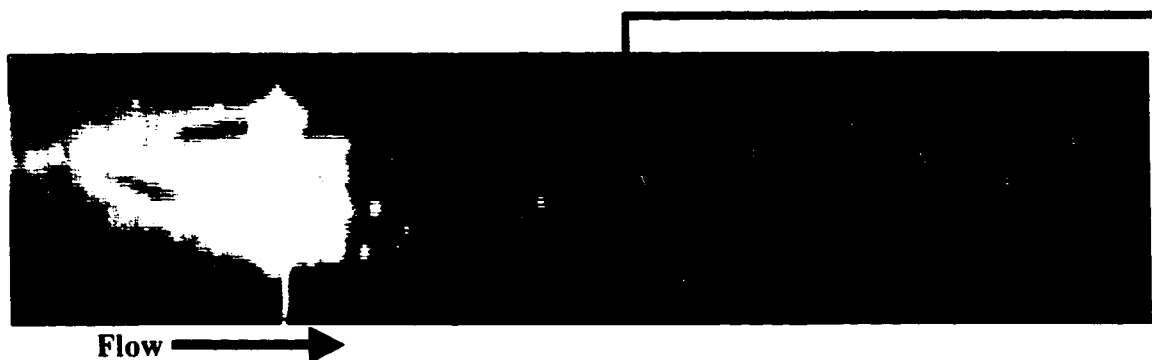


Figure 7.2.1.14. - Location: Left Screw Kneading Disc Section, 1st and 2nd set of Discs, ~10 to 12 Rotations after Dye Injection (~3-4s), 200 rpm.

7.2.2. Geometry D

Figures 7.2.2.1. to 7.2.2.6. show a series of pictures tracing the dye over three elapsed times, 5 s, 10 s and 15 s at 100 rpm. With geometry D, compared to geometry C, there is less channelling of the dye due to the back flow created by the reverse conveying element. The dye is held up longer in the kneading disc section and as a result the flow is continuously recirculating due to the presence of the reverse elements.

Figures 7.2.2.7. and 7.2.2.8. show the dye at 5 s after injection into the kneading zone at 150 rpm. The reverse conveying element at the end of the kneading disc section creates a flow pattern which holds up the dye within the first set of discs (KB/30/20). This produces more of a plug flow behaviour through the discs compared to having a forward conveying element at the end of the kneading disc section (geometry C).

Figures 7.2.2.9. and 7.2.2.10. show digitised images obtained at 200 rpm. The flow exhibits greater back mixing and there is little lamellar structure in the first set of discs, as compared to the lower rpm cases. Figure 7.2.2.10. captures the folding and reverse flow created by the reverse element. A striation which has been folded over is evident and is outlined by the box in Figure 7.2.2.10.

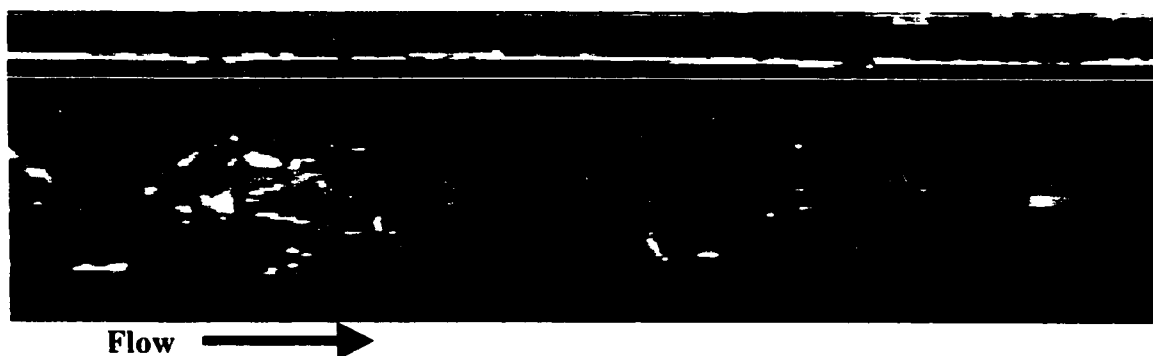


Figure 7.2.2.1. - Location: Right Screw Kneading Disc Section, 1st set of Discs, ~5 Seconds after Dye Injection, 100 rpm.



Figure 7.2.2.2. - Location: Right Screw Kneading Disc Section, 1st set of Discs, ~10 Seconds after Dye Injection, 100 rpm.



Figure 7.2.2.3. - Location: Right Screw Kneading Disc Section, 1st set of Discs, ~15 Seconds after Dye Injection, 100 rpm.

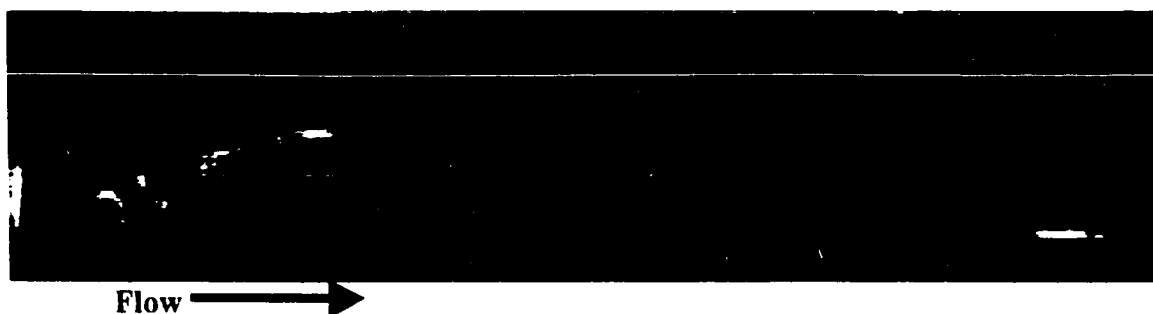


Figure 7.2.2.4. - Location: Right Screw Kneading Disc Section, 2nd set of Discs, ~5 Seconds after Dye Injection, 100 rpm.



Figure 7.2.2.5. - Location: Right Screw Kneading Disc Section, 2nd set of Discs, ~10 Seconds after Dye Injection, 100 rpm.

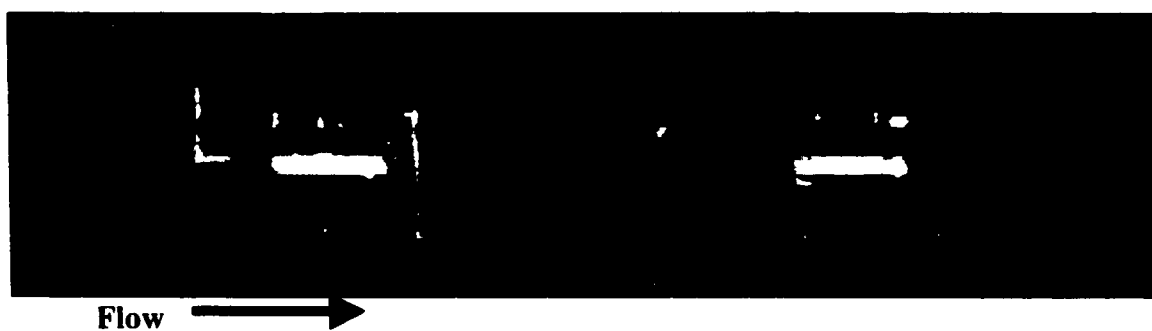


Figure 7.2.2.6. - Location: Right Screw Kneading Disc Section, 2nd set of Discs, ~15 Seconds after Dye Injection, 100 rpm.

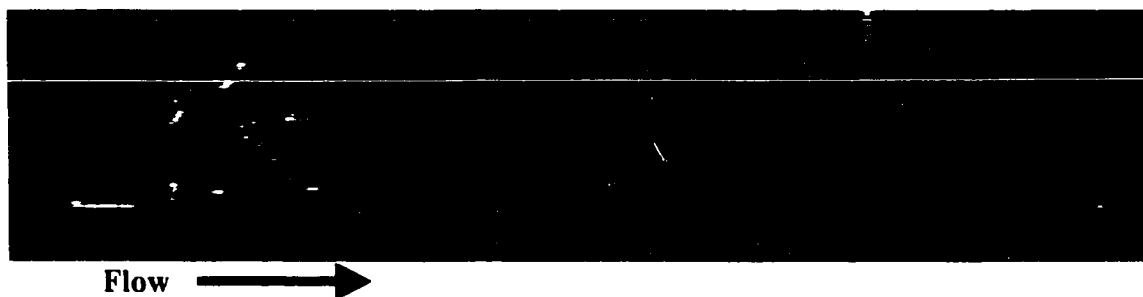


Figure 7.2.2.7. - Location: Right Screw Kneading Disc Section, 1st set of Discs, ~5 Seconds after Dye Injection, 150 rpm.

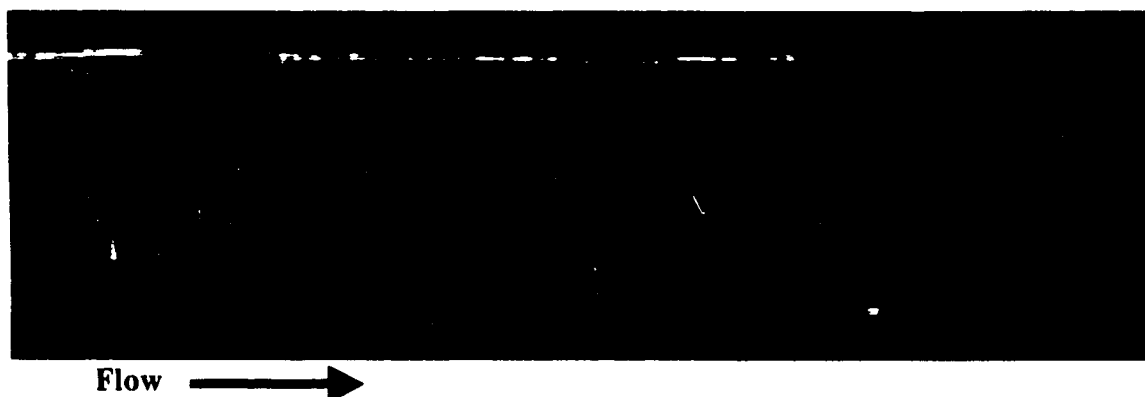


Figure 7.2.2.8. - Location: Right Screw Kneading Disc Section, 2nd set of Discs, ~5 Seconds after Dye Injection, 150 rpm.

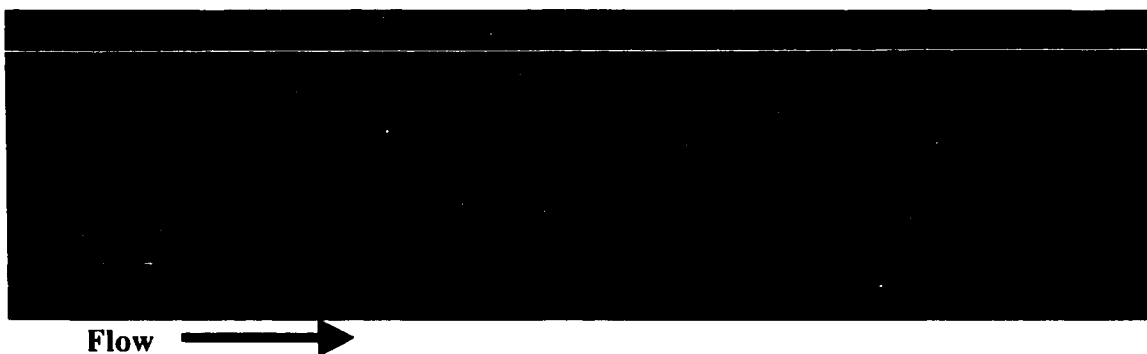


Figure 7.2.2.9. - Location: Right Screw Kneading Disc Section, 1st set of Discs, ~5 Seconds after Dye Injection, 200 rpm.

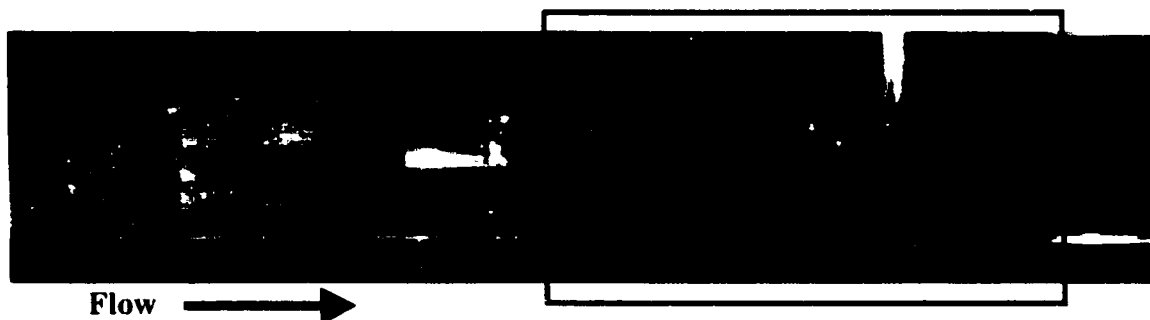


Figure 7.2.2.10. - Location: Right Screw Kneading Disc Section, 2nd set of Discs, ~5 Seconds after Dye Injection, 200 rpm. A folded striation is outlined by the box.

7.2.3 Colour Photography

Figure 7.2.3.1. to 7.2.3.3. show colour still photos of the TSE left screw and nip region 3 to 4 seconds after the dye pulse. These are presented mainly to help show some of the fluid structures that are difficult to discern from the digitised images. These images were taken for geometry C at a flow rate of 10 mL/s with a viscosity ratio of 0.1 of dyed to bulk streams. Figures 7.2.3.1. and 7.2.3.3. show how the dyed fluid elements have been folded over and have recirculated in the channels of the screws and kneading discs at 30 and 60 rpm. In these two figures, there is a core of dye originating from the pulse at the second set of kneading discs. Above the first set of kneading discs and in the conveying element channel, the lower viscosity dye wets the surfaces of the barrel, screw and disc surface. These photos show this wetting more dramatically than the digitised images of Figures 7.2.1.1., 7.2.1.11. and 7.2.1.14, which are at higher screw rotation speeds.

Figure 7.2.3.2. shows how the fluid is stretched very thin in the nip region. The picture shows an axial cross section of the fluid which is being stretched in the x - z -plane and compressed in between elements in the x - y -plane.

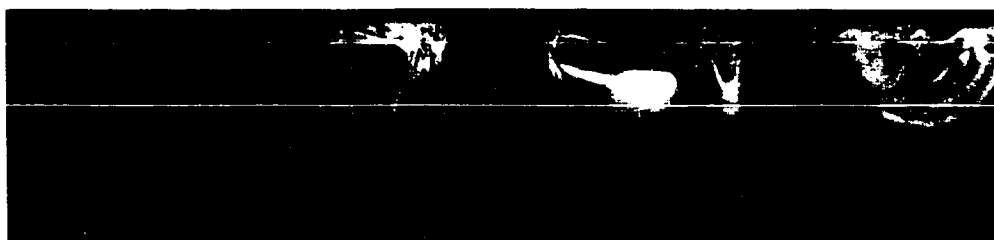


Figure 7.2.3.1. – Left Screw Visualisation at 30 rpm and 10 mL/s (Clear)
and 1 mL/s (Dye).

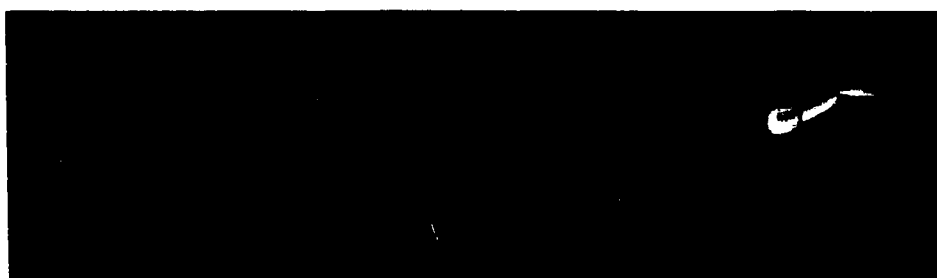


Figure 7.2.3.2. – Nip Region Visualisation at 30 rpm and 10 mL/s (Clear)
and 1 mL/s (Dye).

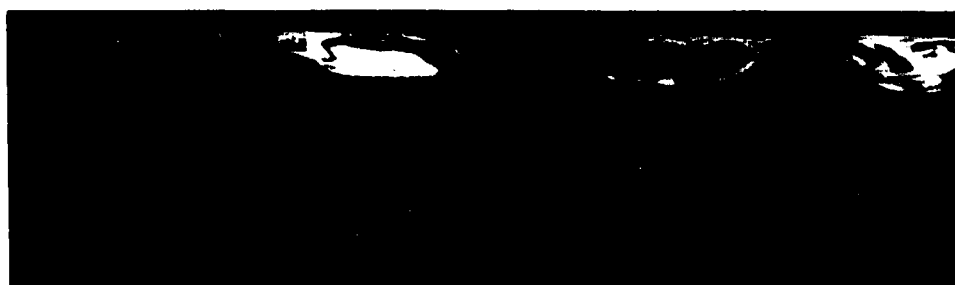


Figure 7.2.3.3. – Left Screw Visualisation at 60 rpm and 10 mL/s (Clear)
and 1 mL/s (Dye).

7.3 Image Analysis

7.3.1 Intensity Measurements

Figures 7.3.1.1. to 7.3.1.7. show measurements of the intensity (concentration) of the dye tracer from visualisations for the right screw. In Figures 7.3.1.1. to 7.3.1.7., the x-axis shows the distance in pixels. The magnification is 50 $\mu\text{m}/\text{pixel}$ which corresponds to 400 pixels = 20 mm (length of one set of kneading discs).

Figures 7.3.1.1. to 7.3.1.3. show that geometry D creates much better back-mixing than geometry C. The concentration of the dye is fairly uniform throughout the kneading discs after 5, 10 and 15 seconds. Geometry D reduces high concentration zones and increases the residence time of the dye in the kneading zone.

In Figure 7.3.1.4., geometry C shows the progression of the dye as it moves from the first disc at 5 seconds to the middle of the kneading disc zone at 10 seconds and then to the second set of discs after 15 seconds. This indicates a fairly narrow residence time distribution for geometry C. Figure 7.3.1.5. shows the progression of dye in geometry D. There is no significant trend in Figure 7.3.1.5. but a long residence time in the kneading disc zone is indicated.

The influence of rpm is shown in Figures 7.3.1.6. and 7.3.1.7. for times of 5 and 15 seconds after the dye pulse. No conclusions may be drawn from these results. The variance of the results is shown in Figures 7.3.1.8. and 7.3.1.9. These plots show improvement in homogeneity as indicated by the reduced variance over time, with geometry D showing better performance in this respect. However, the influence of

rotation rate is not clear. The results indicate that geometry D produces lower variance of intensity, mainly due to the back mixing that is created by the screw profile, which causes material to have longer residence times in the kneading disc section.

The average intensity measured across the highlighted region in Figure 3.5.2.1. gives some indication of the residence times that the material spends in the kneading disc section. If the average intensity is high this indicates the region between the discs and barrel is predominantly filled with dye. With respect to screw rotation rate, in Figure 7.3.1.10., for geometry D, the maximum intensity is observed after 10 seconds, indicating that the dye has been mixed throughout the kneading section. By 15 seconds, the majority of the dye has left the kneading disc region. At 200 rpm, the dye is held up longer in the disc region since at 10 seconds the lowest average intensity of the three rotation speeds is observed, while at 15 seconds the highest average intensity is observed. This indicates a broader residence time distribution for 200 rpm compared to that at 100 rpm. Comparing the two geometries (C,D) at 150 rpm (Figure 7.3.1.11.), the average intensity at 5 seconds is a maximum for geometry C and thereafter decreasing with time. This indicates, as seen in earlier results, that this geometry has very short residence times, thereby allowing dye to escape the kneading disc zone with very little deformation.

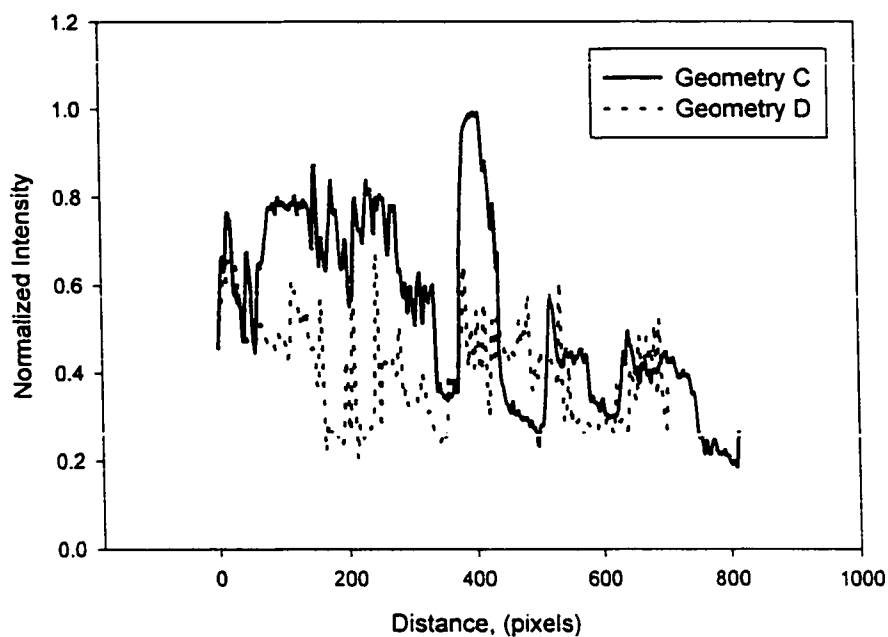


Figure 7.3.1.1. – Intensity Plots for Right Screw, 150 rpm, 5 mL/s (Clear), 2 Second Pulse of Dye, Configurations C and D, 5 Seconds After Pulse

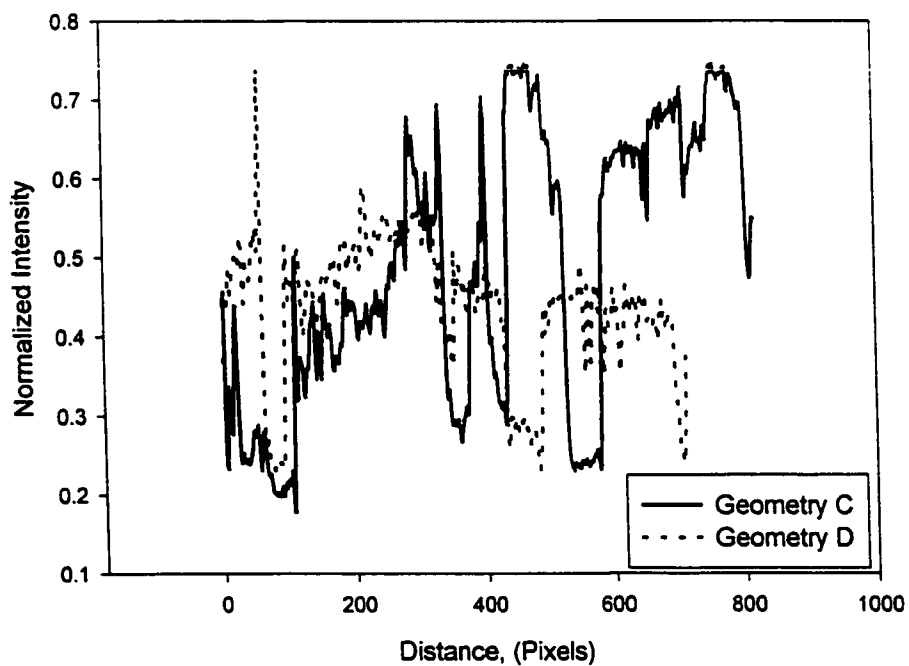


Figure 7.3.1.2. – Intensity Plots for Right Screw, 150 rpm, 5 mL/s (Clear), 2 Second Pulse of Dye, Configurations C and D, 10 Seconds After Pulse.

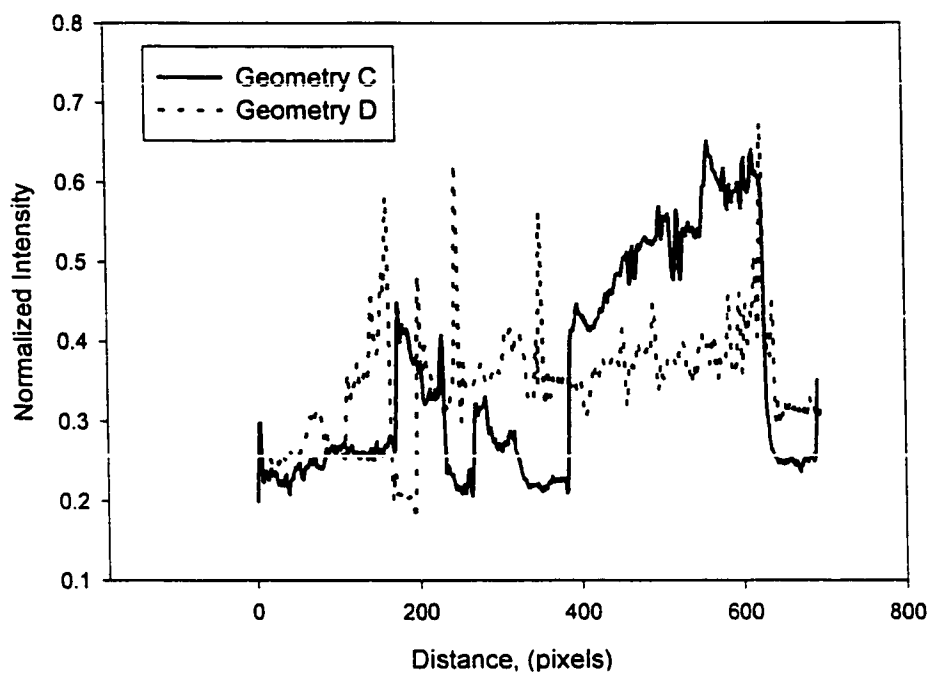


Figure 7.3.1.3. – Intensity Plots for Right Screw, 150 rpm, 5 mL/s (Clear), 2 Second Pulse of Dye, Configurations C and D, 15 Seconds After Pulse.

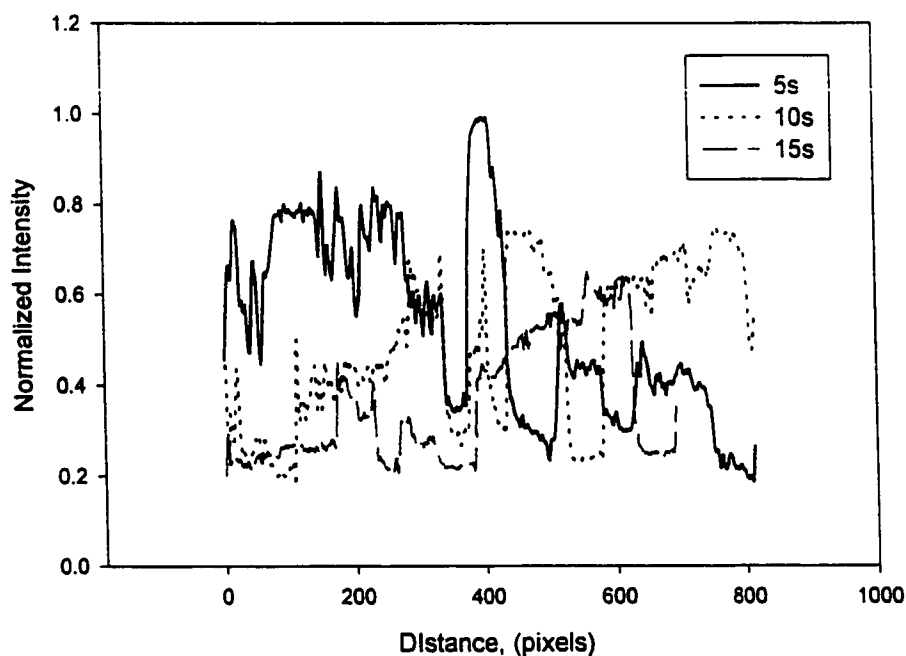


Figure 7.3.1.4. – Intensity Plots for Right Screw, 150 rpm, 5 mL/s (Clear), 2 Second Pulse of Dye, Configuration C, Progression of Tracer Pulse.

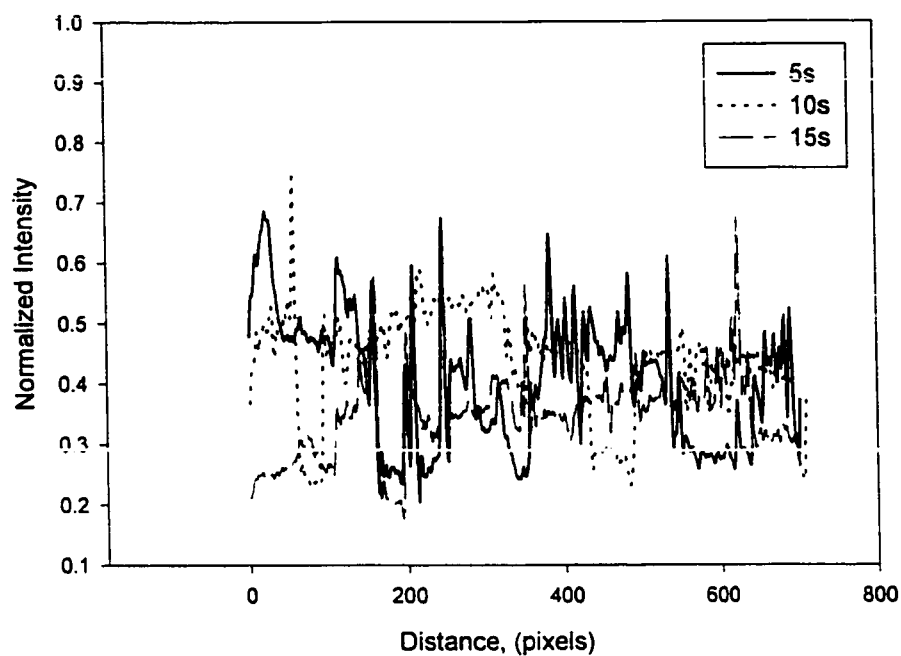


Figure 7.3.1.5. – Intensity Plots for Right Screw, 150 rpm, 5 mL/s (Clear), 2 Second Pulse of Dye, Configuration D, Progression of Tracer Pulse.

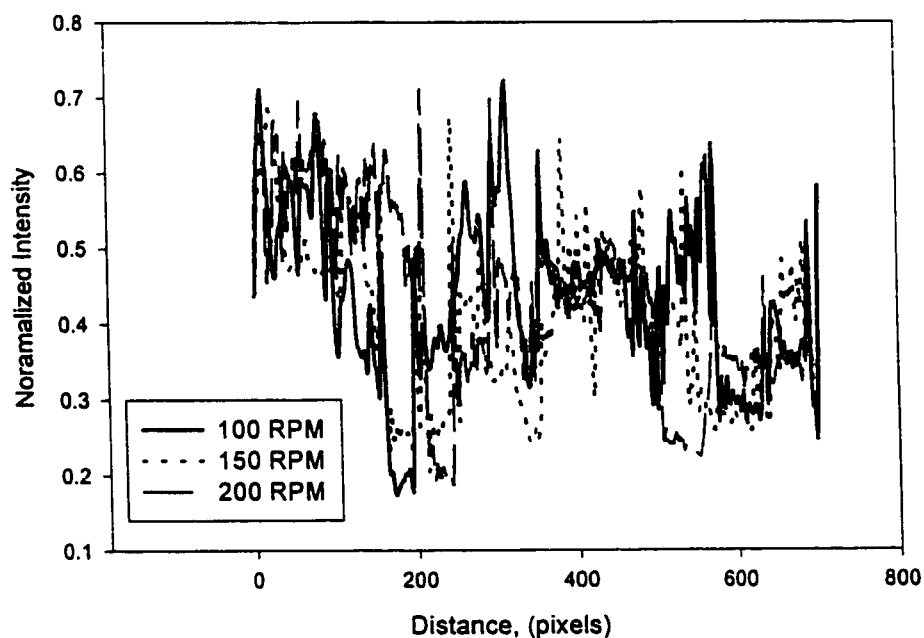


Figure 7.3.1.6. – Intensity Plots for Right Screw, 5 mL/s (Clear), 2 Second Pulse of Dye, Configuration D, Influence of rpm 5 Seconds after Pulse.

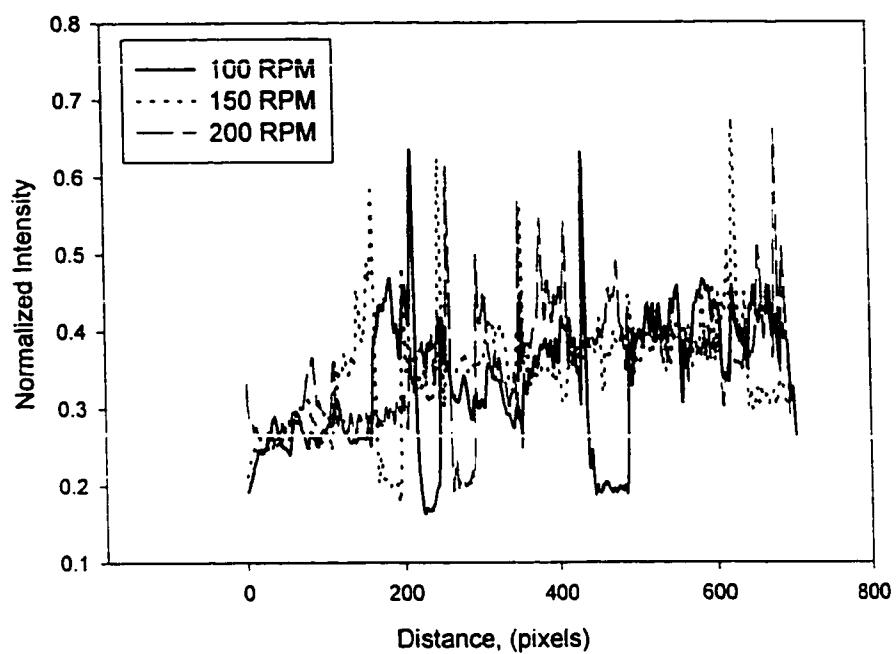


Figure 7.3.1.7. Intensity Plots for Right Screw, 5 mL/s (Clear), 2 Second Pulse of Dye, Configuration D, Influence of rpm, 15 Seconds After Pulse.

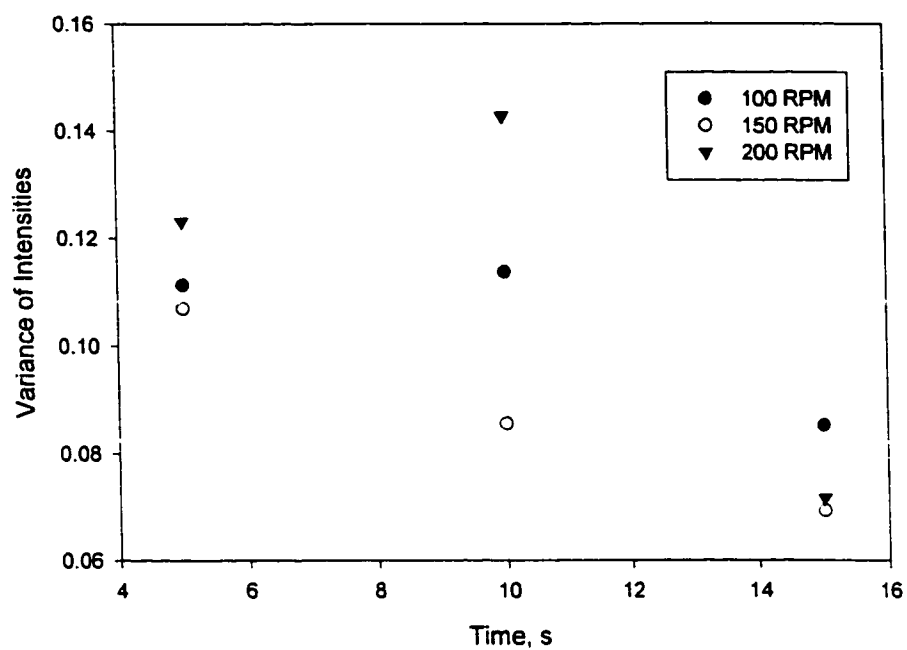


Figure 7.3.1.8. – Variance of Intensities versus time for Geometry D.

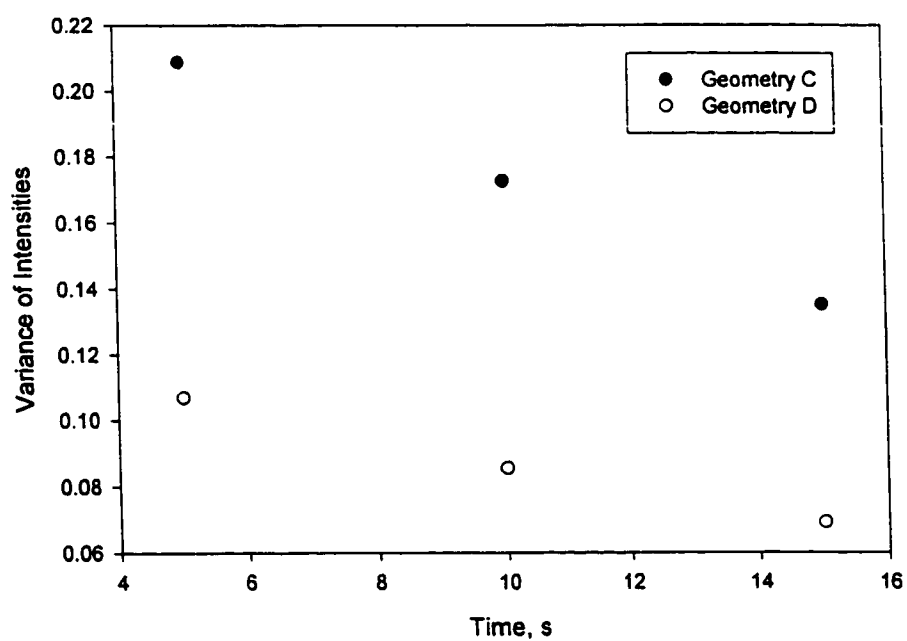


Figure 7.3.1.9. – Variance of Intensities versus Time for 150 rpm for Geometries C and D.

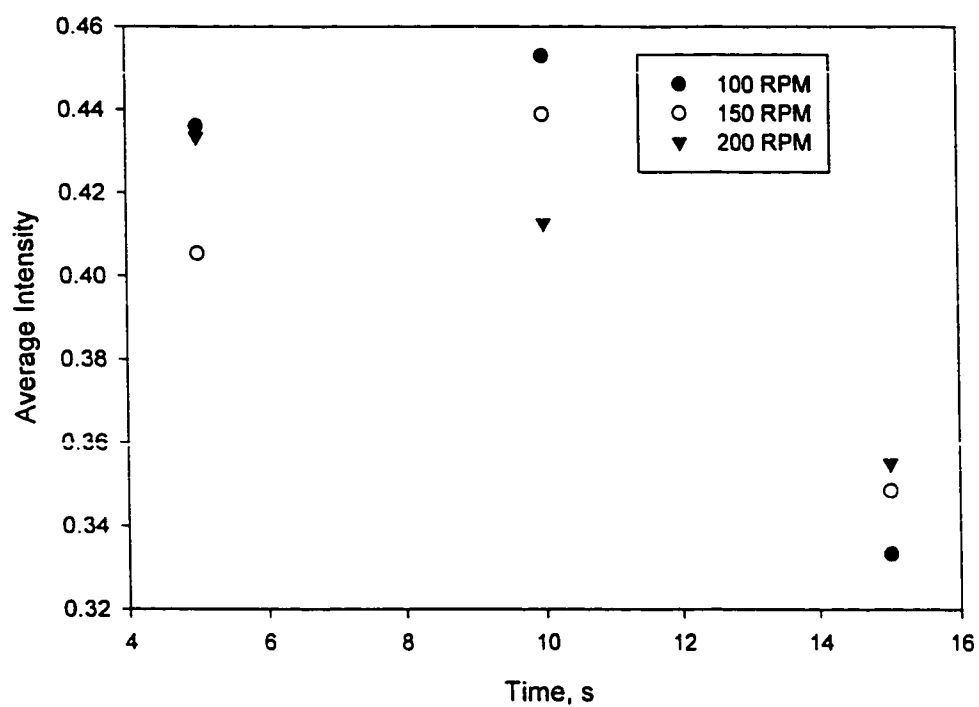


Figure 7.3.1.10. – Average Intensity versus Time, Geometry D.

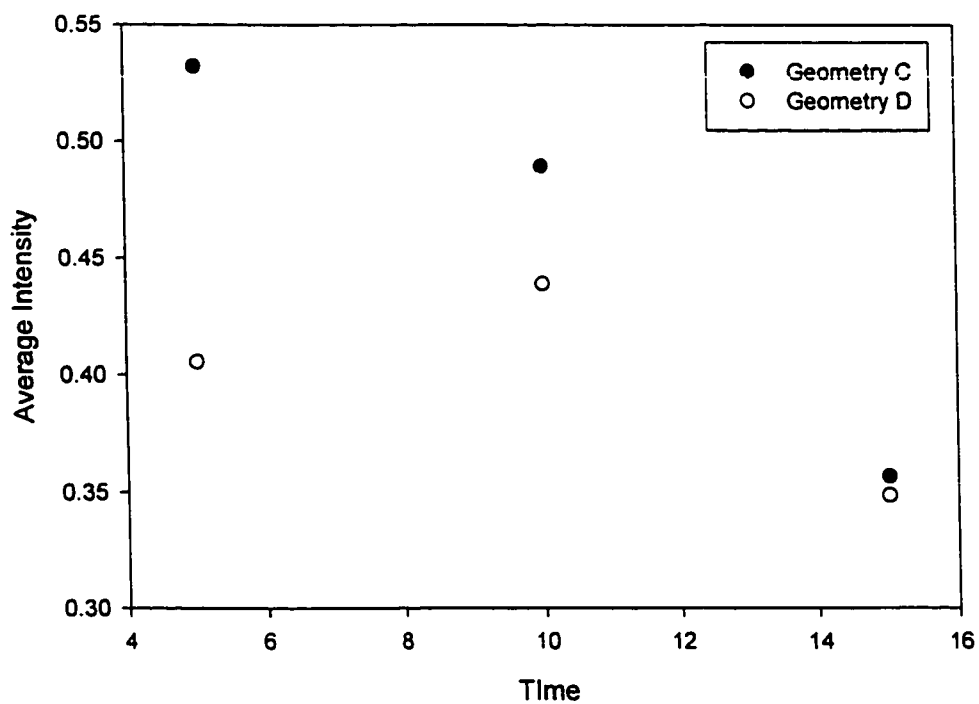


Figure 7.3.1.11. – Average Intensity versus Time, 150 rpm, 5 mL/s.

7.3.2 *Striation Measurements*

The striation thickness was measured for the right screw visualisations at the first disc, at the interface between the two sets of discs (KB/45/20 and KB/30/20) and at the last disc in the kneading disc zone. The striation thickness was measured along a radius perpendicular to the barrel wall. The thicknesses of the dyed striations were measured based on pixel intensity. If there was a jump of 20 units in pixel intensity of adjacent pixels, this was marked as the interface between striations. There was also the possibility of intensity spikes where a single pixel may be higher or lower by a significant amount compared to surrounding pixels. This was created by signal noise and was disregarded. Consequently, the striations must be larger than two pixels in width to be recorded.

Figure 7.3.2.1. shows the average striation thickness (non-dimensionalised with respect to barrel diameter) for the right screw, five seconds after the dye pulse. Geometries C and D show similar trends, with D creating thinner striations.

Figure 7.3.2.2. compares the performance of geometry D for 100 and 150 rpm. Noticeably, the striation thickness for 100 rpm at the end of the kneading disc section increases abruptly. By the end of the kneading disc section, there are no discernible structures and hence the dye appears as one large striation. At 150 rpm, the reason for the small striation thickness at $x = 4.0$ mm, is that the fluid is held up in the front end of the kneading disc section and only a small amount of the dye has entered the back end of the kneading disc section, similar to the visualisation in Figure 7.2.1.7.

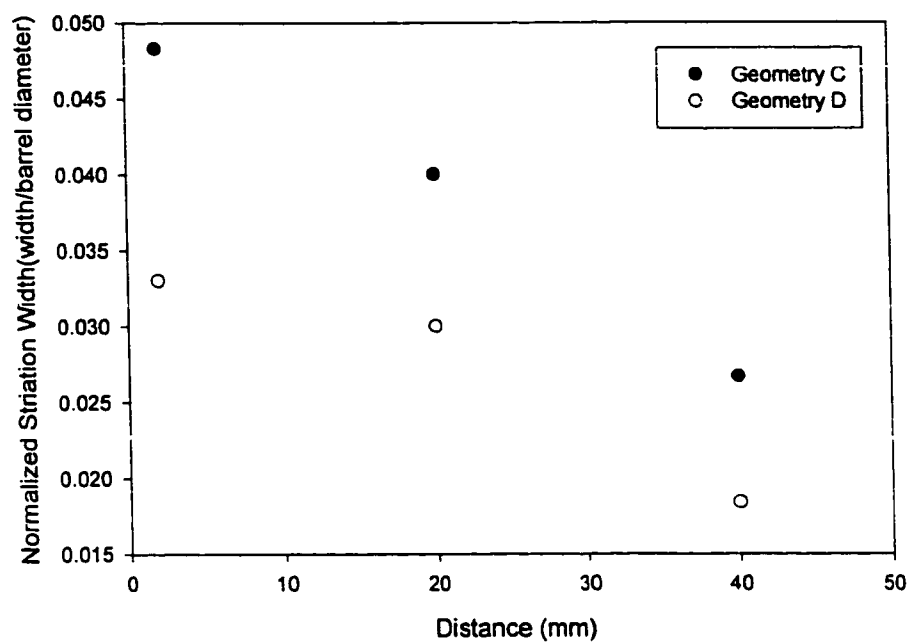


Figure 7.3.2.1. – Normalised Striation Thickness versus Axial Distance, 5 Seconds After Pulse, 5 mL/s, 150 rpm.

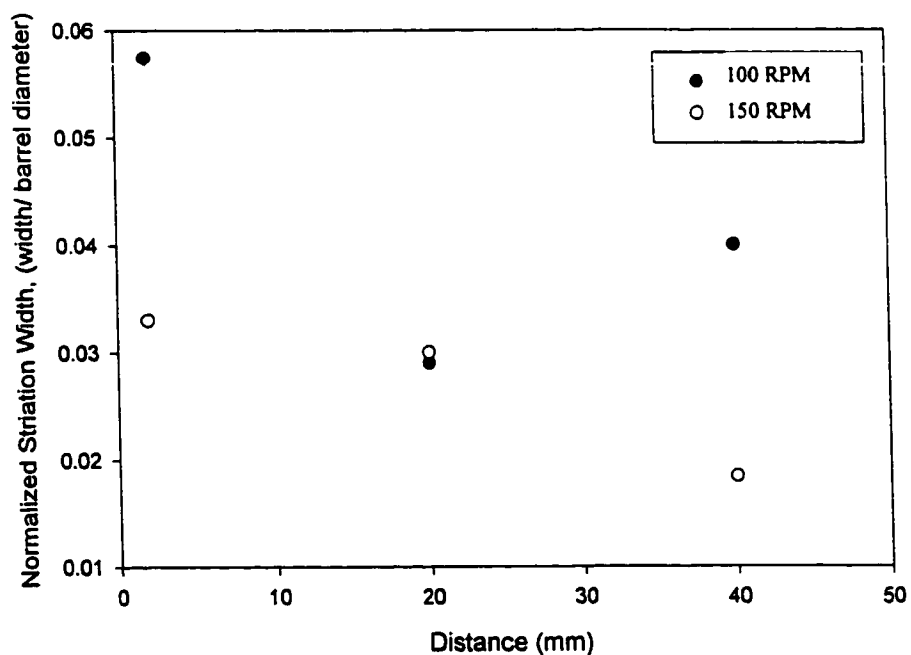


Figure 7.3.2.2. – Normalised Striation Thickness versus Axial Distance, 5 Seconds After Pulse, 5 mL/s, Geometry D.

7.4 PIV Results

Figures 7.4.1. to 7.4.11. show velocity vectors results, obtained by PIV, for configuration A, where extended discs were used to isolate the kneading discs (KB/45/20). The goal of these extended discs was to reduce some of the complexity of the flow field. The objective was to determine the flow field created by the kneading discs in isolation. By isolating the discs, characterisation of the performance of the kneading discs is possible without questions arising as to the effect of upstream and downstream elements.

Figure 7.4.1. shows two dimensional velocity vectors for geometry A operating at 30 rpm and 2.5 mL/s and an axial plane at $z = 25$ mm ($z = 0$ mm is the bottom of the barrel). An interesting result, which is prominent in most of the results for geometry A, is the split of the flow at the first disc at the left and the right screw (defined in Figure 3.5.3.2.). The pressure flow has a greater momentum than that generated by the rotating discs causing the flow to channel through the right screw (RS) in the channel created at this orientation. The flow also exhibits reverse flow in the axial direction (u -component) behind the first disc on the right screw. There is also back flow at the fifth disc, again behind the left screw (LS). This figure captures a large component of the back mixing in the kneading disc zone, which is the back flow or reverse flow as fluid fills in behind the rotating discs. On the fifth disc of the left screw, the effect of the front of a passing disc is visualised. The flow is pushed in both the positive and negative axial direction as the front of the disc is about to pass through the visualised plane.

Figure 7.4.2. shows the flow field for $Q = 5.0 \text{ mL/s}$ and 60 rpm at a z plane of 25 mm. There is very little channelling of the flow except behind the 4th and 5th disc on the right screw. Back-mixing is also seen behind the 5th LS disc and the 2nd RS disc. The pressure driven flow has a strong axial component in the gap between the first and second discs and the barrel wall. Figure 7.4.3. and 7.4.4. show the velocity fields for the same screw speed and flow rate for z planes of 20mm and 15mm (centre of barrel). At $z = 20 \text{ mm}$, the forward conveying nature of the KB/45/20 kneading discs is seen at the 3rd and 4th RS discs (bottom right side of figure). With the 3rd disc preventing back flow, the 4th disc's front edge is causing flow in the positive axial direction. At $z = 15 \text{ mm}$, an interesting flow pattern is seen for the left screw. There is back flow predominantly between the disc and barrel. We would expect, as the disc continues to rotate, that the flow would reverse and flow forward. This would then create a recirculation of the fluid. This can be seen in experimental flow visualisations at the plane of $z = 15 \text{ mm}$. Figures 7.2.1.6. and 7.2.1.11. show this recirculation where it is evident the dye is on the outer perimeter in the gap and the centre core is unmixed material.

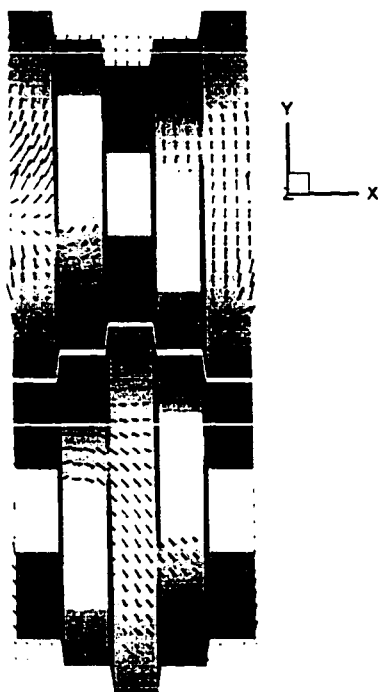


Figure 7.4.1. - Velocity Vectors, $Q=2.5$ mL/s, 30 rpm. Geometry A.

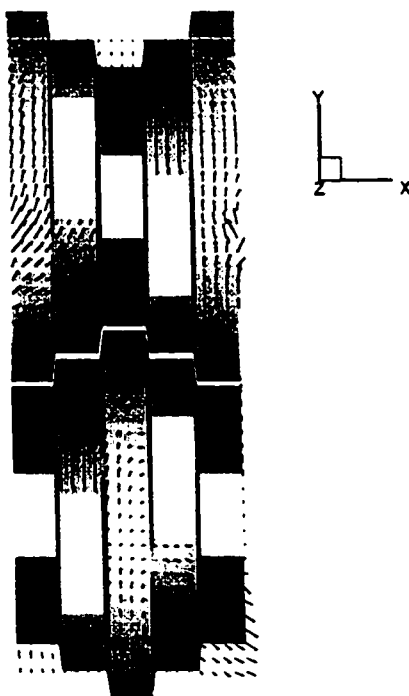


Figure 7.4.2. - Velocity vectors, $Q=5.0$ mL/s, 60 rpm. Geometry A.

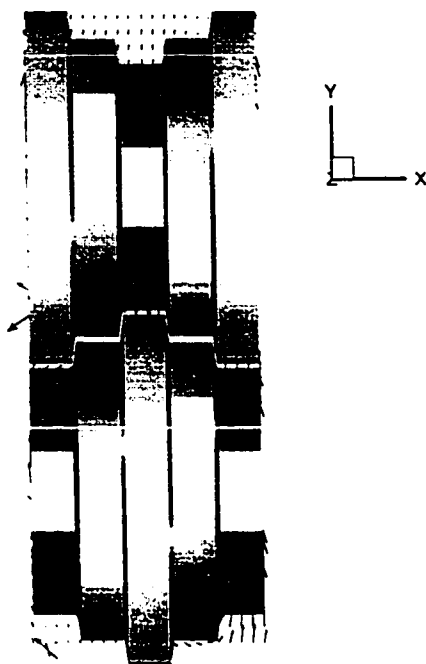


Figure 7.4.3. - Velocity Vectors, $Q=5.0\text{ mL/s}$, 60 rpm, $z=20\text{mm}$. Geometry A.

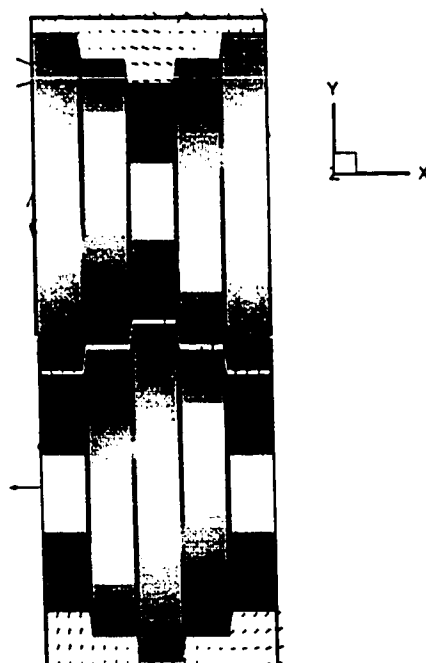


Figure 7.4.4. - Velocity Vectors, $Q=5.0\text{ mL/s}$, 60 rpm, $z=15\text{mm}$. Geometry A.

Figure 7.4.5. shows the flow field for 100 rpm and $Q = 5.0 \text{ mL/s}$ at $z = 25 \text{ mm}$. The flow field exhibits fluid channelling through the right screw but is forced back by the 4th disc (RS). At the higher rotation speed, the flow can not escape the kneading disc region without being aligned by a rotating disc. There is extremely strong back mixing behind the 5th LS disc and in front of the 4th LS disc. Some back mixing is also captured in front of the 3rd LS disc.

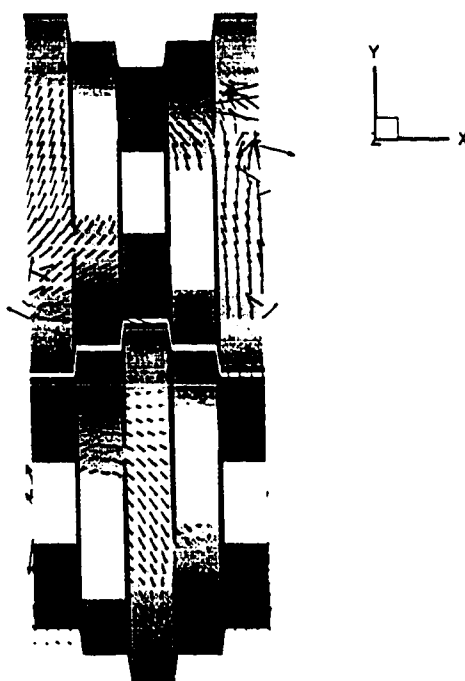


Figure 7.4.5. - Velocity vectors for $Q=5.0 \text{ mL/s}$ and 100 rpm. Geometry A.

Figure 7.4.6. shows the flow field for 150 rpm and $Q = 5.0 \text{ mL/s}$. A re-circulation or vortex is present in front of the 3rd LS disc. At the front edge of the 5th LS disc, back flow is observed due the oncoming disc (it looks like an explosion pushing fluid in all directions).

Figure 7.4.7. shows the flow field for 60 rpm and $Q = 8.5 \text{ mL/s}$. The flow splits at the first LS disc creating negative radial flow. There is not as much back mixing as was observed in earlier cases with lower flow rates. The pressure driven flow has too large a momentum to be overcome by the drag forces. Hence, less back mixing is seen and strong axial velocity components are evident.

Figure 7.4.8. to 7.4.12. show the results for geometry B previously described in Figure 3.1.2.2b. The conveying elements align the flow with the kneading discs and the drag flow created by the discs is assisted by the pressure driven flow. The flow shows very little back mixing or reverse flows, hence very little shear or elongation results within this screw profile. Flow rate and rotation speed changes created very little change in the flow pattern observed. The split within the flow field for geometry A is not observed here and the majority of the flow is in the direction of the rotating discs.

The technique of PIV has proven to be a powerful tool for visualising a large section of the flow field in the TSE. PIV lends itself extremely well to this complicated geometry mainly due to the optical accessibility. Observations of the flow in the very small gaps is also possible, providing large insight into characterising high shear zones from the velocity field.

The limitation in illumination from the laser and the frame speed of the camera places an upper bound on the current PIV setup of about 1 ms for the pulse separation time. Typically, the maximum screw rotation that should occur between the laser pulses is about 1 to 2 degrees. This is so that particles do not move out of the visualised plane

and errors due to the third component of velocity are minimised. Therefore, the maximum screw speed with this setup is about 300 rpm (based on 2 degrees/1 ms).

The error due to the neglect of the z – component of velocity was estimated from the maximum measured velocity in the y – co-ordinate direction. This values was assumed to represent the maximum velocity normal to the visualised plane. For a case of 100 rpm and 5 mL/s, the maximum value was 0.05 m/s. From previous studies [Bravo (1998)], the maximum velocity from computer simulation of this case was also 0.05 m/s. For a time separation between pulses of 2ms, and a velocity of 0.05 m/s, the maximum distance travelled perpendicular to the plane of light is 100 μm . Given that the sheet thickness is in the range of 100 to 500 μm , the number of particles that leave the visualised plane between successive pulses is quite small [Keane and Adrian (1990)].

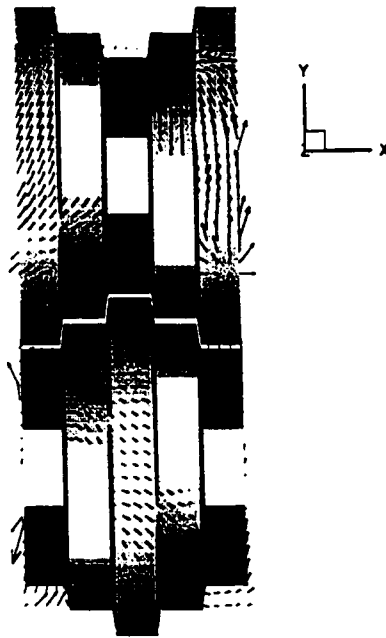


Figure 7.4.6. - Velocity Vectors for $Q=5.0$ mL/s and 150 rpm. Geometry A.

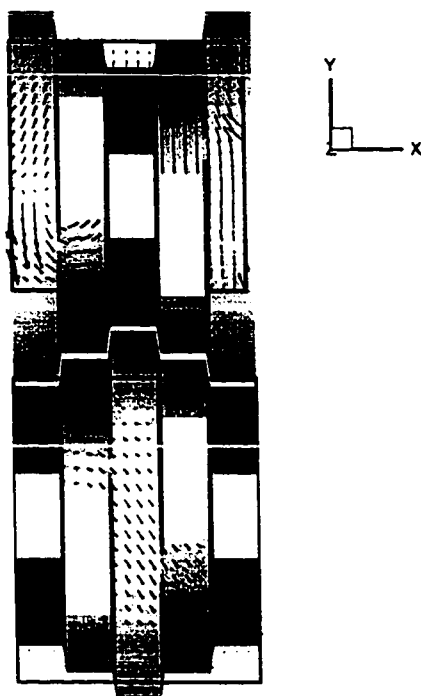


Figure 7.4.7. - Velocity vectors, $Q=8.5$ mL/s, 60 rpm. Geometry A.

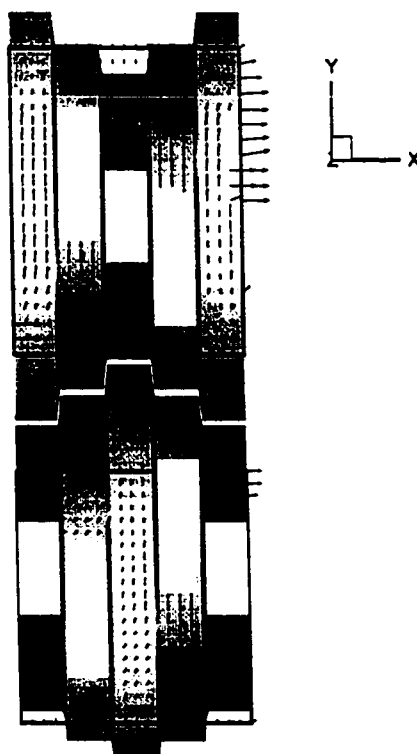


Figure 7.4.8. - Velocity vectors, $Q=5.0$ mL/s, 60 rpm. Geometry B.



Figure 7.4.9. - Velocity vectors, $Q=5.0$ mL/s, 60 rpm, $z=15$ mm. Geometry B.

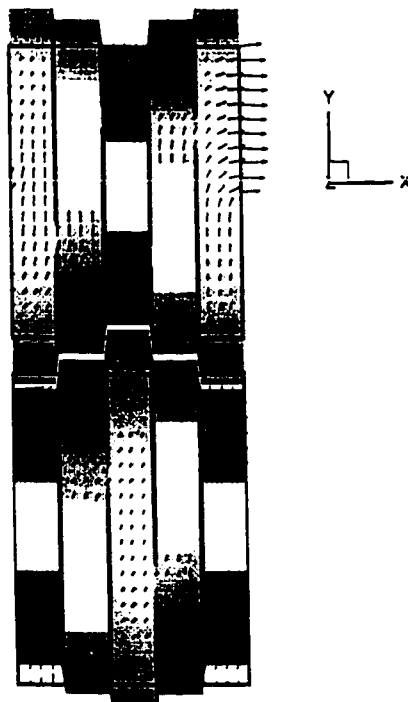


Figure 7.4.10. - Velocity vectors, $Q=8.5$ mL/s, 60 rpm. Geometry B.

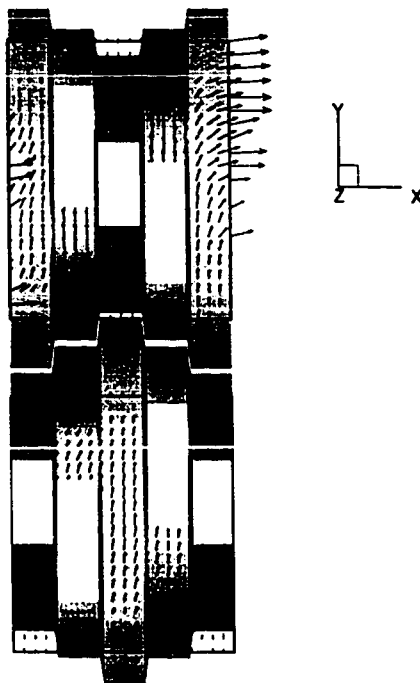


Figure 7.4.11. - Velocity vectors, $Q=5.0$ mL/s, 100 rpm. Geometry B.

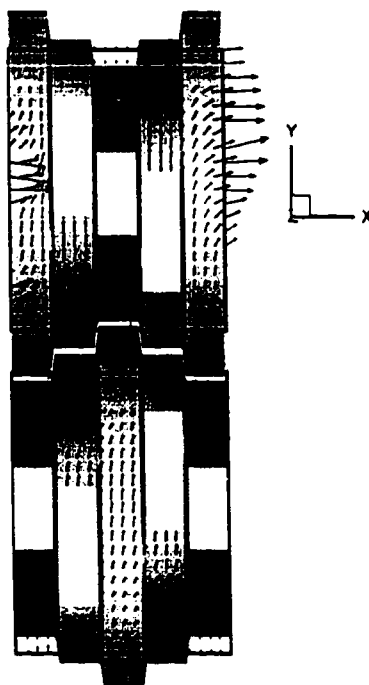


Figure 7.4.12. - Velocity vectors, $Q=8.5$ mL/s, 100 rpm. Geometry B.

7.5 Validation of Finite Element Simulation

One of the main objective for obtaining these PIV results was to validate simulations of the kneading disc section. Bravo (1998) performed a finite element simulation of the KB/45/20 kneading discs which were validated with the results presented herein. This section summarises these results. Further details on the validation of the simulation are presented in Jaffer et al. (1998).

7.5.1 Computer Simulation – Governing Equations

Bravo (1998) modelled the flow of molten polymers within the kneading discs region assuming that the flow is steady state, isothermal, creeping, incompressible and with no body forces.

The governing equations are the momentum equations (without inertia terms) and the continuity equation, which can be written in dimensionless tensorial form as:

$$\Delta \cdot \tau - \Delta P = 0 \quad (7.5.1.1)$$

$$\Delta \cdot u = 0 \quad (7.5.1.2)$$

where τ is the extra stress tensor, P the pressure and u the velocity vector. A Generalised Newtonian constitutive equation is used to model the stress-strain relation for polymers:

$$\tau_{ij} = \eta \left(\frac{\partial u_i}{\partial x_j} + \frac{\partial u_j}{\partial x_i} \right) \quad (7.5.1.3)$$

For the results presented, a Newtonian fluid was modelled with a viscosity of 1 Pa.s. The dimensionless groups used in equation 1 to 3 are:

$$\begin{aligned} x &= \frac{x'}{D} & u &= u'/U \\ P &= \frac{P'D}{\mu_0 U} & \tau &= \frac{\tau' D}{\mu_0 U} \\ \mu &= \frac{\mu'}{\mu_0} \end{aligned} \tag{7.5.1.4}$$

where D is the characteristic diameter (in this case, the outer diameter of the screw), U is the total average superficial velocity (total flow rate over (total area – area occupied by disc)), μ_0 is the zero-shear viscosity of the fluid and the prime (') denotes a dimensional variable.

7.5.2. Boundary Conditions

Bravo (1998) used the standard no-slip boundary condition at the barrel wall and disc surfaces. The fluid at the barrel surface remains stationary, whereas the fluid at the rotor surfaces moves according to the local rotational speed.

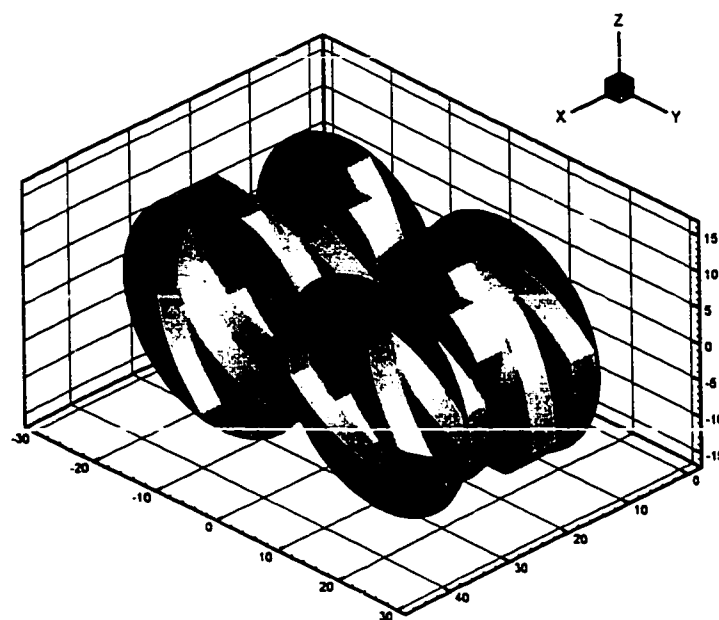
The boundary conditions at the disc section inlet and outlet were more complicated to address since the simulation is limited to the kneading disc section. Therefore, providing an accurate representation of the boundary conditions at the inlet and outlet plane is very difficult without any previous knowledge. As Yang (1993) points out, it is very difficult to calculate *a priori* the true velocity profiles at the entrance and exit planes of the kneading blocks. The kneading disc sections are usually fed by screw

conveying sections. The boundary condition at the inlet of the kneading disc section should be the exit values of the preceding conveying section. The complete specification of the inlet velocity profile would require the calculation of the flow field in the screw conveying section in conjunction with the kneading disc section. This becomes extremely computationally expensive and with limited resources this is not feasible.

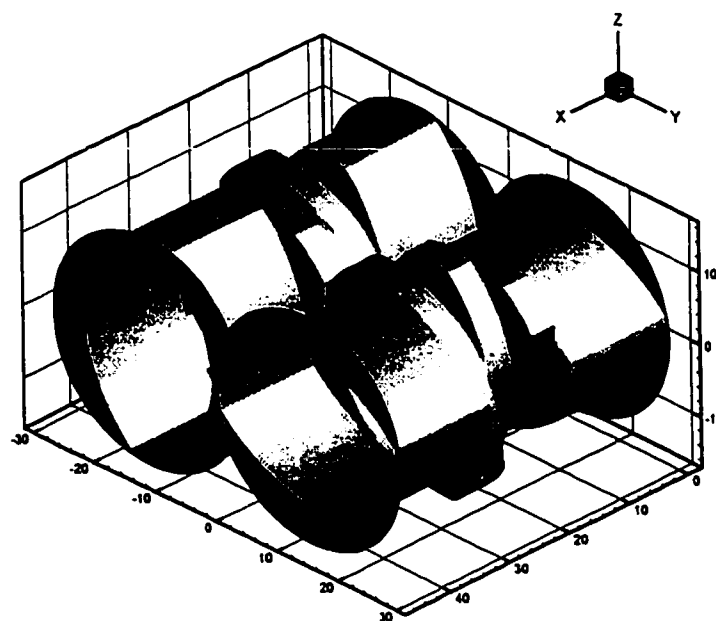
Bravo (1998) used the normal stress difference ($\sigma_{xx} = -p + \tau_{xx}$) between the entrance and exit surfaces as the inlet and outlet boundary conditions. The normal stress difference was set and then changed until the desired flow rate was obtained. The normal stress boundary condition was applied at a specific distance from the area of interest. With this approach, the effect of the constant normal stress on the flow field is reduced due to the creeping nature of the flow and the resultant short flow development lengths.

The numerical solution of the governing equations is obtained according to the method explained in Bravo (1998) using the finite element method. For a flow rate of 5 mL/s, at 60 rpm, the normal stress difference imposed was 200 Pa. For the case of 8.5 mL/s and 60 rpm, the normal stress difference was 800 Pa. The solution is obtained using 27 node triquadratic brick elements for the three velocity components. Each triquadratic element is subdivided into 8 trilinear elements, for the purpose of interpolating the data values onto a 2D plane corresponding to the plane interrogated with PIV. The interpolation of the data values is done from the original 3D field onto the 2D mesh using linear interpolation. A mesh density of 21 by 21 nodes was used for each one of the two kneading blocks, as shown in Figure 3.5.2.

The effect of inlet and outlet boundary conditions was studied by using the long straight elements shown in Figure 3.1.6. Two different finite element meshes were necessary to simulate the flow field with and without the long elements. In both cases, the normal stress boundary condition was applied. Figure 7.5.2.1. shows the surface finite element mesh for the two cases studied. In case (a) the inlet and outlet boundary conditions are imposed at the ends of the kneading blocks, whereas in case (b) long straight elements are deployed before and after the kneading blocks to move the inlet and outlet boundary conditions away from the kneading blocks. The main purpose was to establish the effect of the adjacent elements on the measured flow field and to analyse the ability of the proposed numerical model and boundary conditions to describe the experimentally observed flow field.



(a)

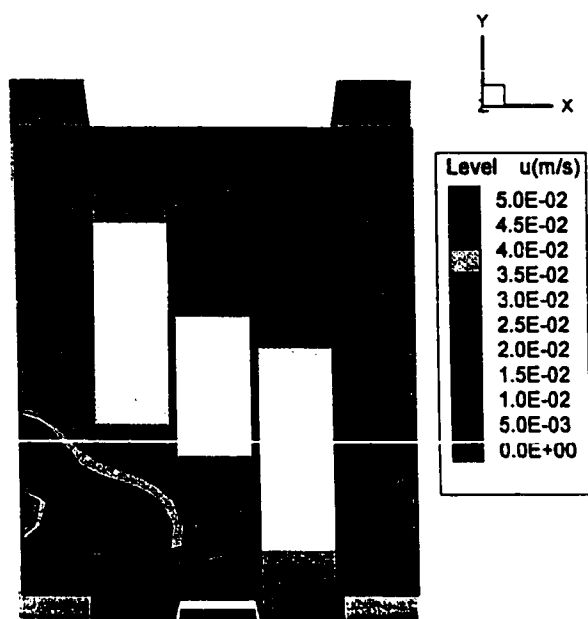


(b)

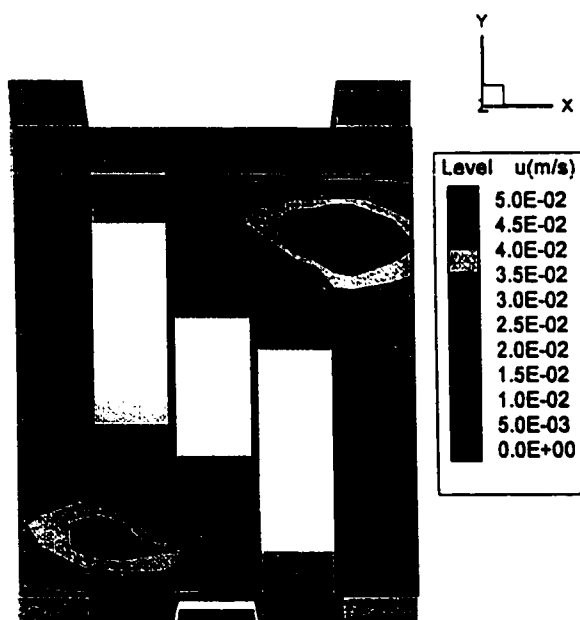
Figure 7.5.2.1. - Kneading disc configuration and location of inlet/outlet boundary conditions. a) Inlet and outlet boundary condition at the ends of the kneading blocks; b) Inlet and outlet boundary condition at the ends of long elements. [Bravo (1998)].

7.5.3. Velocity Comparison

The velocity contours for the axial (x) component are shown in Figure 7.5.3.1a. and Figure 7.5.3.1b. for the left screw and Figure 7.5.3.2a. and Figure 7.5.3.2b. for the right screw. The simulation results were obtained for the boundary condition depicted in Figure 7.5.2.1b. and the experimental results were obtained using the extended first and last disc for the kneading blocks (Figure 3.1.6a.). The rotation rate was 60 rpm at a flow rate of 5 mL/s. The magnitudes of the velocity vectors in Figure 7.5.3.1a. and Figure 7.5.3.1b. show good qualitative agreement between the experimental and simulation results. The measured axial component of velocity is larger than that simulated in the bottom left part of the field (Figure 7.5.3.1.) where the axial gap is wide and material is being pushed by the right screw into the intermeshing region. Simulation results in the top right part of the field of Figure 7.5.3.1b. predict an axial component larger than the experimental measurements in Figure 7.5.3.1a. These differences are attributed to the effect of the adjacent long elements in the experimental runs. Figure 7.5.3.1b. demonstrates that the maximum predicted axial velocity components (~ 0.05 m/s) are located at the widest axial gaps. The computed minimum axial velocity components are located near the discs because the kneading discs present an obstacle to the pressure driven flow. Figure 7.5.3.2a. and Figure 7.5.3.2b. display the axial component of velocity contours for the right screw. The order of magnitude of the predicted velocities (0-0.05 m/s) is in good agreement with the experimental measurements.

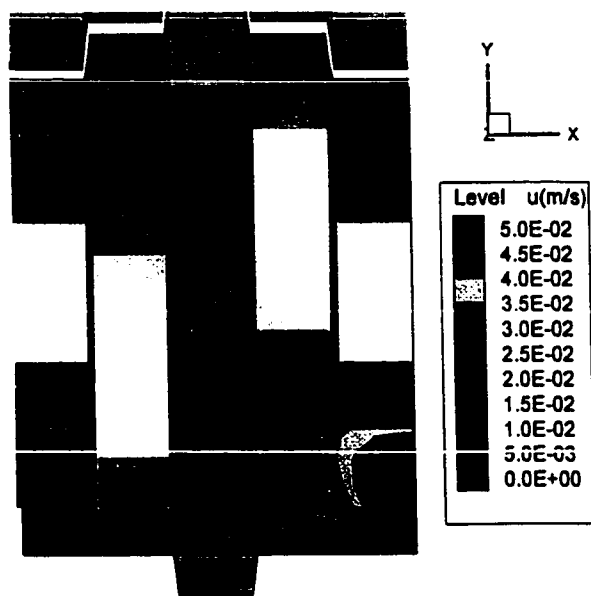


a)

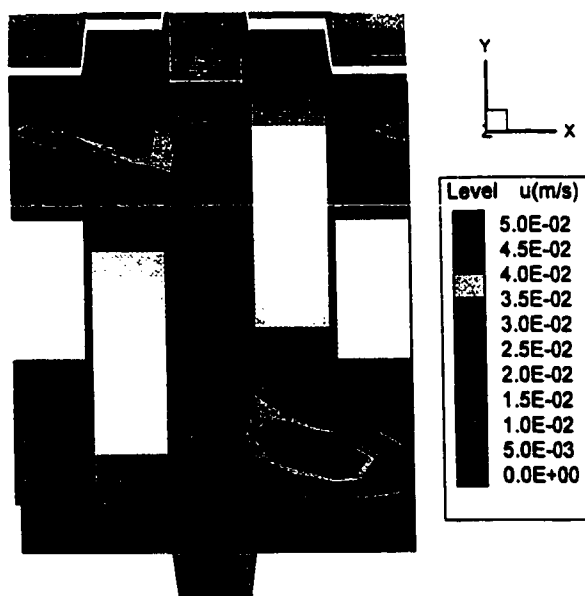


b)

Figure 7.5.3.1. - Contours of the x-component of velocity. Left screw, 60 rpm, 5 mL/s. Long straight elements are deployed before and after the kneading blocks.
a) Experimental b) Simulation.



a)

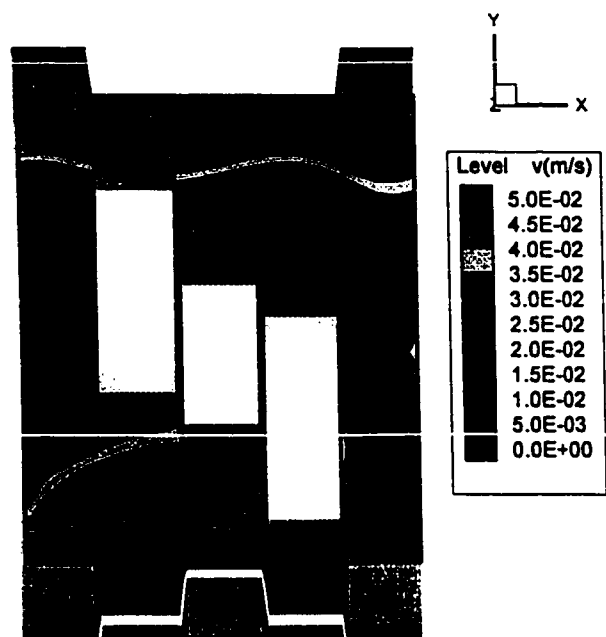


b)

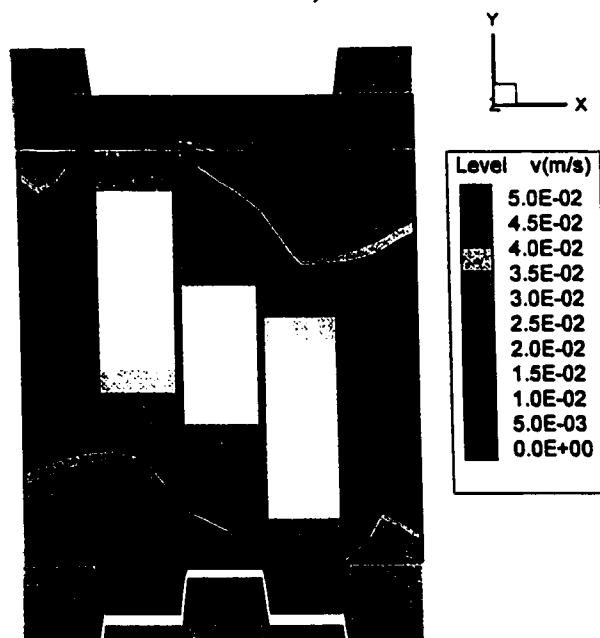
Figure 7.5.3.2. - Contours of the x -component of velocity. Right screw, 60 rpm, 5 mL/s. Long straight elements are deployed before and after the kneading blocks.
a) Experimental b) Simulation

Figure 7.5.3.3a. and Figure 7.5.3.3b. show that the radial velocity (y -component) contours for the left screw obtained via experiment and simulation have good qualitative agreement. Both simulation and experimental results show a velocity magnitude of approximately 0.05 m/s around the discs, with a decreasing gradient where the fluid approaches the barrel walls within the measured plane. Figure 7.5.3.4a. and Figure 7.5.3.4b. show the radial velocity contours for the right screw. Simulation results (Figure 7.5.3.4b.) consistently predict the largest magnitude of the radial velocity component to be near the discs. Experimental results in Figure 7.5.3.4a. show that the highest values of the y -component of velocity are in the vicinity of discs 1 and 2 but show very small values near discs 4 and 5.

Analysis and comparison between experimental and simulation results is complex with two-dimensional plots. Velocity components extracted from the two dimensional planes onto one-dimensional lines in the plane can facilitate the quantitative analysis of results. The extraction line is located at $x=2.83$ mm, 2.87 mm $\leq y \leq 26.08$ mm, $z=11$ mm which is the middle of the first disc on the left screw. This location was chosen to compare the simulated inlet condition with the measured velocity profile. The velocity components were extracted for 21 points along the extraction line from the two dimensional plane. Figure 7.5.3.5. shows the results obtained for the extracted data where 0 mm is at the outer barrel wall and 20 mm near the apex of the TSE (Figure 1.2.1.). The axial component of velocity shows a maximum difference of 20% between simulation and experimental results at a distance of 2.5 mm, whereas the maximum difference

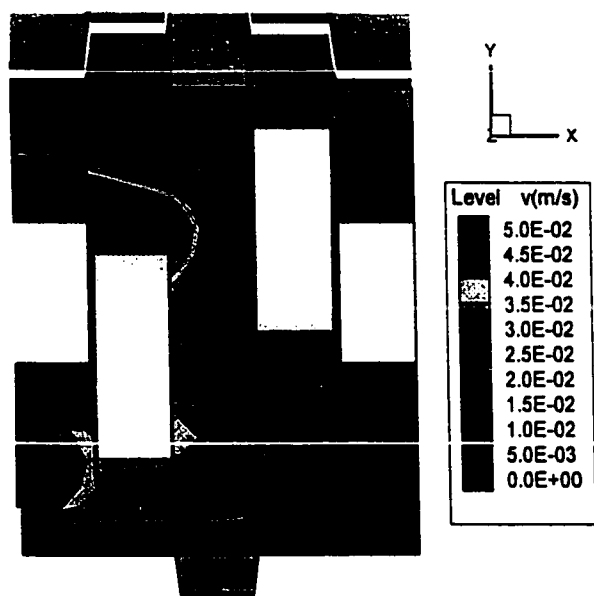


a)

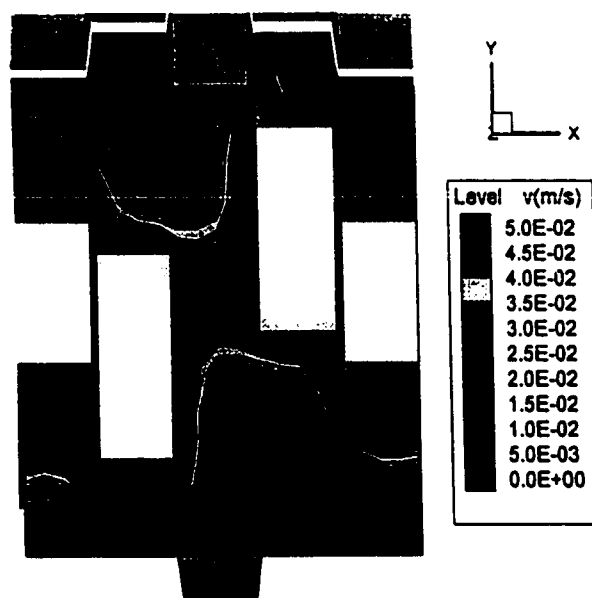


b)

Figure 7.5.3.3. - Contours of the y -component of velocity. Left screw, 60 rpm, 5 mL/s. Long straight elements are deployed before and after the kneading blocks. a) Experimental b) Simulation.



a)



b)

Figure 7.5.3.4. - Contours of the y -component of velocity. Right screw, 60 rpm, 5 mL/s. Long straight elements are deployed before and after the kneading blocks.
a) Experimental b) Simulation.

for the y component is less than 10%. The trends observed in the experimental data are well reproduced by the simulations for both x and y velocity components.

The results for the axial component vector for the left screw obtained for the boundary condition depicted in Figure 7.5.2.1a., and the experimental velocity vectors using conveying elements before and after the kneading blocks (Figure 3.1.6b.) at 60 rpm and 5.0 mL/s may be found in Bravo (1998). Computed and experimental results show good qualitative agreement for the axial velocity component for the complete field. The simulation results for the y -component of velocity are not in good agreement with the experimentally measured y -component. The results for the extracted data at the first disc on the left screw are shown in Figure 7.5.3.6. There is a pronounced quantitative difference between experimental and simulation results for both x and y velocity components, although the prediction of the experimental trend is still reasonable. The maximum differences for the x -component are 57%, whereas for the y -component the maximum difference is 28%. This is believed to be the result of the estimated inlet condition, which does not truly capture the true velocity profile.

The second case kept the rotation speed constant at 60 rpm while the flow rate was increased from 5 mL/s to 8.5 mL/s. For the experimental and simulation results using extended discs for the boundary condition (Figure 3.1.6a. and Figure 7.5.2.1b.), all the results for 60 rpm at a flow rate of 8.5 mL/s show a poor correlation between experiments and simulation [Bravo (1998)]. It is presumed that the creeping flow assumption under the higher flow rate may be no longer valid and results in the poor agreement between simulation and experiments.

The most interesting results are obtained for the flow rate of 8.5 mL/s using the conveying elements before and after the kneading blocks. The qualitative agreement between experimental and simulation results is surprisingly better than for the case with the long straight elements. Again, the helical-type of motion created by the conveying elements is not altered drastically by the kneading blocks. On the contrary, the kneading blocks tend to maintain the same type of ordered helix-type motion. Figures 7.5.3.7. to 7.5.3.10. show the contour plots of the x and y velocity components for the case of 60 rpm at 8.5 mL/s, using conveying elements before and after the kneading blocks for the experimental runs. The comparison between experimental and simulation results shown in Figure 7.5.3.11. indicates a good prediction of the trends. The quantitative agreement is very good for the x -component of velocity, and reasonably good for the y -component

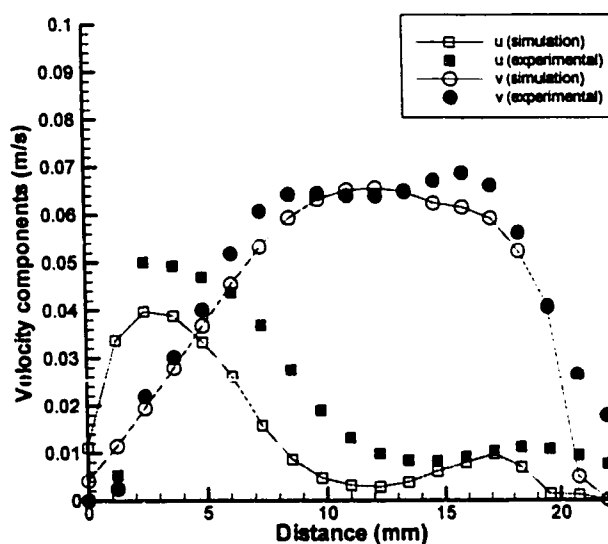


Figure 7.5.3.5. - Comparison between simulation and experimental u and v components of velocity at $x = 2.836$ mm. Left screw, 60 rpm, 5 mL/s. Long straight elements are deployed before and after the kneading blocks.

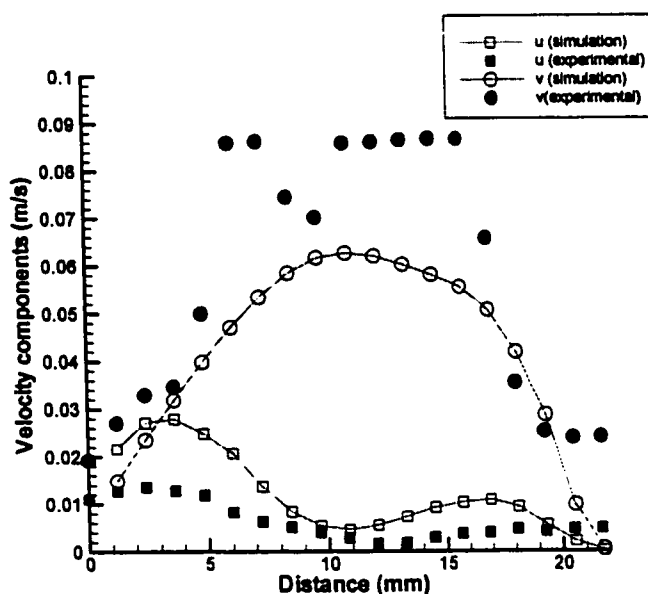


Figure 7.5.3.6. - Comparison between simulation and experimental u and v components of velocity at $x = 2.836$ mm. Left screw, 60 rpm, 5 mL/s. Conveying elements are deployed before and after the kneading blocks.

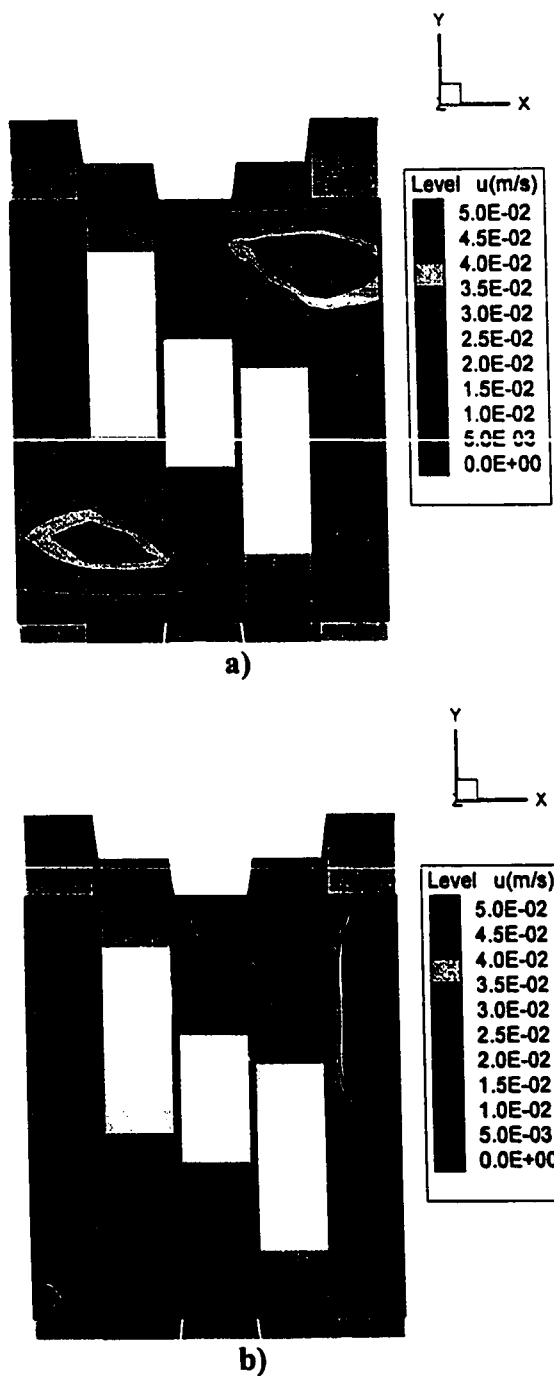


Figure 7.5.3.7. - Contours of the x-component of velocity. Left screw, 60 rpm, 8.5 mL/s. Conveying elements deployed before and after the kneading blocks. a) Experimental b) Simulation.

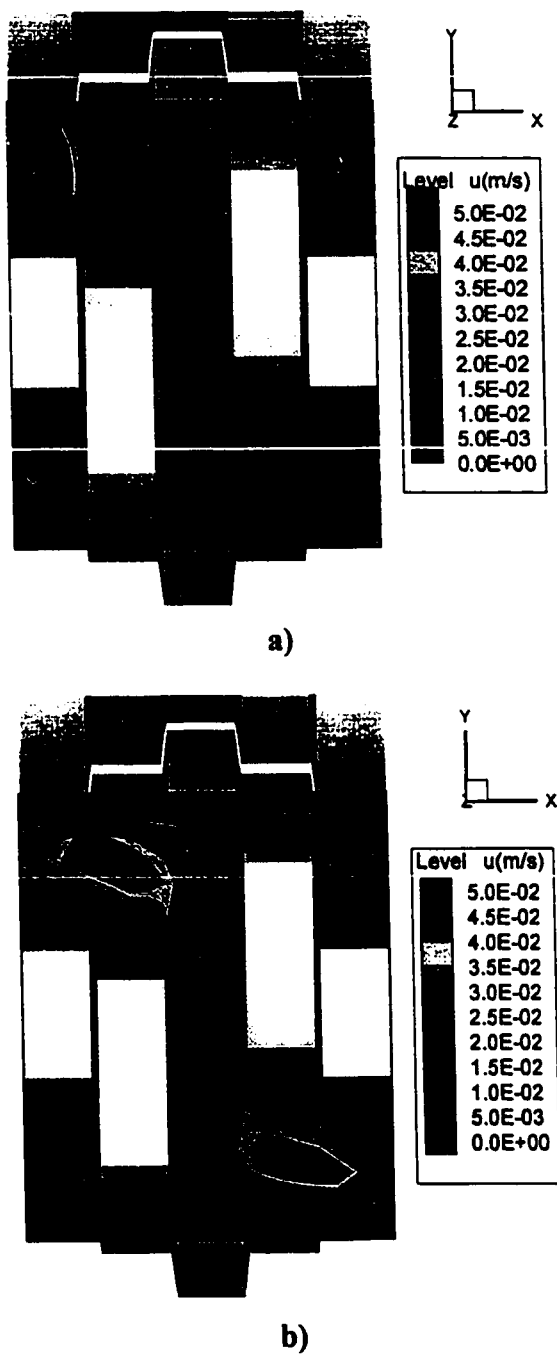


Figure 7.5.3.8. - Contours of the x-component of velocity. Right screw, 60 rpm, 8.5 mL/s. Conveying elements deployed before and after the kneading blocks.
a) Experimental b) Simulation.

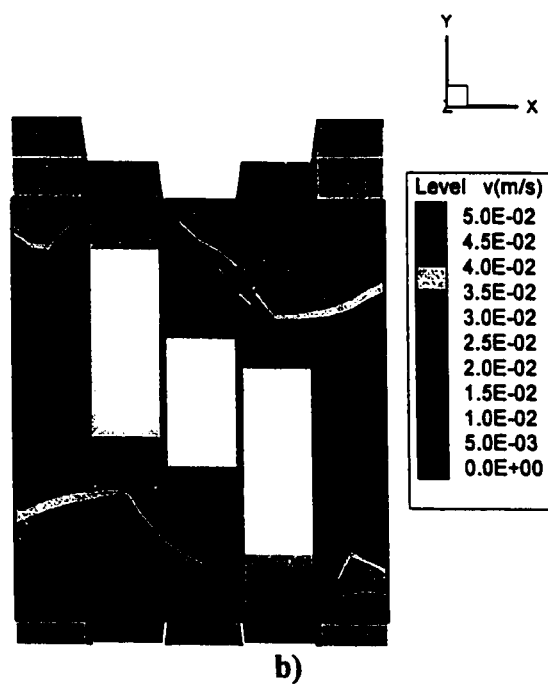
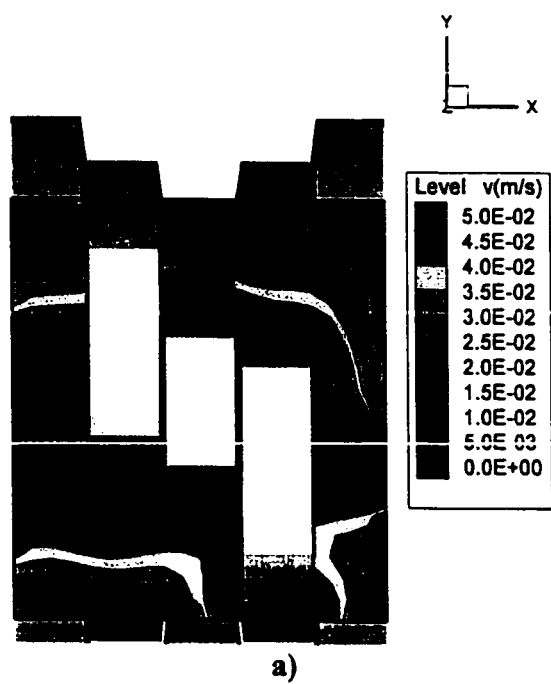
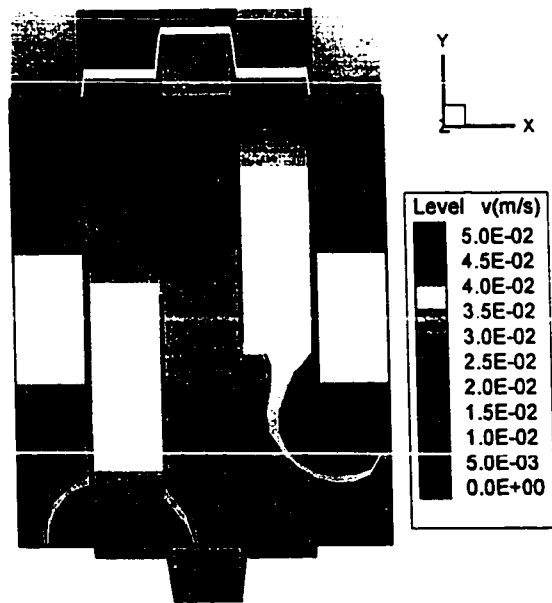
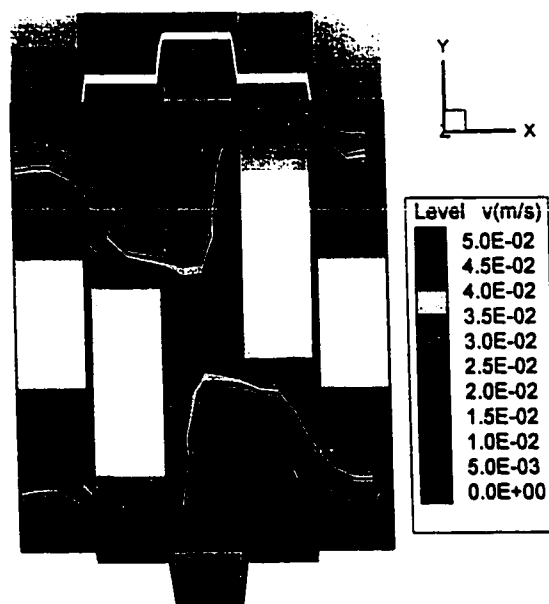


Figure 7.5.3.9. - Contours of the y -component of velocity. Left screw, 60 rpm, 8.5 mL/s. Conveying elements deployed before and after the kneading blocks. a) Experimental
b) Simulation.



a)



b)

Figure 7.5.3.10. - Contours of the y -component of velocity. Right screw, 60 rpm, 8.5 mL/s. Conveying elements deployed before and after the kneading blocks.
a) Experimental b) Simulation.

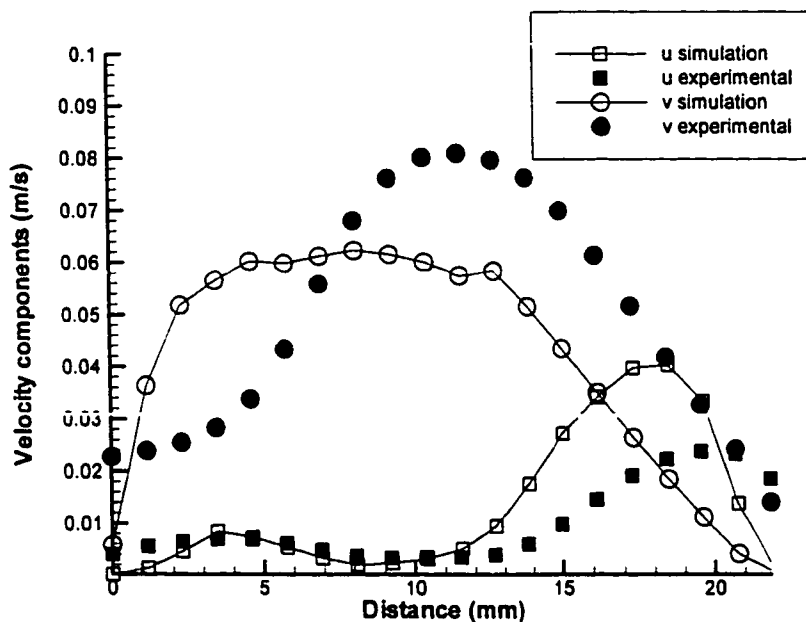


Figure 7.5.3.11. - Comparison between simulation and experimental u and v components of velocity at $x = 2.836$ mm. Left screw, 60 rpm, 8.5 mL/s. Conveying elements are deployed before and after the kneading blocks for the experimental runs.

7.6. Characterisation of Disc Mixing Performance

The mixing characteristics of the kneading discs were evaluated based on three criteria. These were chosen to quantify the amount of shear, elongation and magnitude of the overall deformation tensor. The experimental velocity measurements on the TSE were made over two dimensional axial planes. The third component of velocity was not able to be measured and as a result the mixing analysis described herein is two dimensional.

The magnitude of shear was determined from the summation of the absolute values of shear rates measured. This was defined as Total Absolute Shear, TS. A simple forward difference between neighbouring velocities is calculated ($du/dy = \Delta u/\Delta y$) to estimate the velocity gradients.

$$TS = \left| \frac{du}{dy} \right| + \left| \frac{dv}{dx} \right|$$

This measure was used primarily to give an estimate of the high shear regions. The individual shear components contour plots gave essentially the same information as this single measure.

The degree of elongation or compression created in the two dimensional plane was obtained from

$$TE = \left(\frac{du}{dx} \right) + \left(\frac{dv}{dy} \right) = - \left(\frac{dw}{dz} \right)$$

where TE was defined as total elongation. For an incompressible fluid total elongation is equal to the magnitude of the elongation in the z- component from the continuity equation.

The magnitude of the two dimensional deformation tensor was determined from the calculation of the second invariant of the deformation tensor. This is defined as Tadmor and Gogos (1979)

$$\dot{\gamma} = \sqrt{\frac{1}{2}(\mathbf{D} : \mathbf{D})}$$

The second invariant quantifies regions of high deformation and subsequently high viscous dissipation rates. In other words, it tells us where the energy is being dissipated to deform fluid elements, thereby illustrating the performance characteristics of the geometry. This magnitude of the deformation tensor is the value for the maximum efficiency from the mixing efficiency equations of Ottino (1989). [Section 2.5.]

Figure 7.6.1a. to 7.6.6a. show contour plots of the total absolute shear, total elongation and second invariant of the rate of deformation tensor. Figures 7.6.1. to 7.6.3 have extended discs before and after the kneading blocks, KB/45/20, whereas Figures 7.6.4. to 7.6.6. are cases with conveying elements before and after the kneading block. In all six figures, the total absolute shear shows high values at the entrance and exit planes, especially for the geometry B cases. The maximum total shear is approximately 70 s^{-1} . For a distance of 1mm this translates into a change in velocity of 0.07 m/s (looking at a single component of shear only). The maximum velocities measured were approximately 0.05 m/s . Therefore, there is a fair amount of acceleration or deceleration over a very short distance. This indicates that there is a significant reorientation of the flow creating a strong mixing action. This would be expected for geometry B at the first and last disc as there is a fairly distinct reorientation of the flow as it moves from a conveying element to a kneading disc. For the comparable conditions the extended discs have lower shear components as the extended discs orient the flow in the same direction as the flow in the kneading discs.

The total elongation plots for 100 rpm and 150 rpm (Figure 7.6.2b. and 7.6.3b.) show strong compressive forces at the LS behind the 5th disc. The compression results as the disc passes by and the fluid rushes in behind it to fill the gap, as well as the disc creating elongation in the direction of motion (z direction). Figure 7.4.5. shows the vector plots for 100 rpm and 5 mL/s. The compressive flow pattern is observed behind the LS 5th disc. Elongation is created at the front edge of the LS 1st and 5th discs (Figure 7.6.1b. to 7.6.3b.) as the oncoming disc is displacing the fluid in the positive and negative axial direction. This is seen in Figure 7.6.1b. to 7.6.3b. at the 1st and 5th kneading discs on the LS.

For the cases of geometry B, one interesting result for the total elongation shows that at the 5th element on the LS, there is a high region of elongation compared to compression for the extended discs. Figure 7.5.3.7a. shows the vector contour plot for the axial velocity at $Q=5$ mL/s and 60 rpm. It is evident that the fluid is accelerating from almost zero axial velocity to very high axial velocity in a short distance (see also Figure 7.4.10). This may be attributed to the fact that the conveying elements prevent fluid from rushing back into the kneading discs from upstream, permitting the fluid to accelerate into the conveying channel. This may also explain why in the visualisations, when a forward conveying element was placed on the end of the kneading disc section, there was an increased amount of dye escaping the kneading disc section with very little deformation.

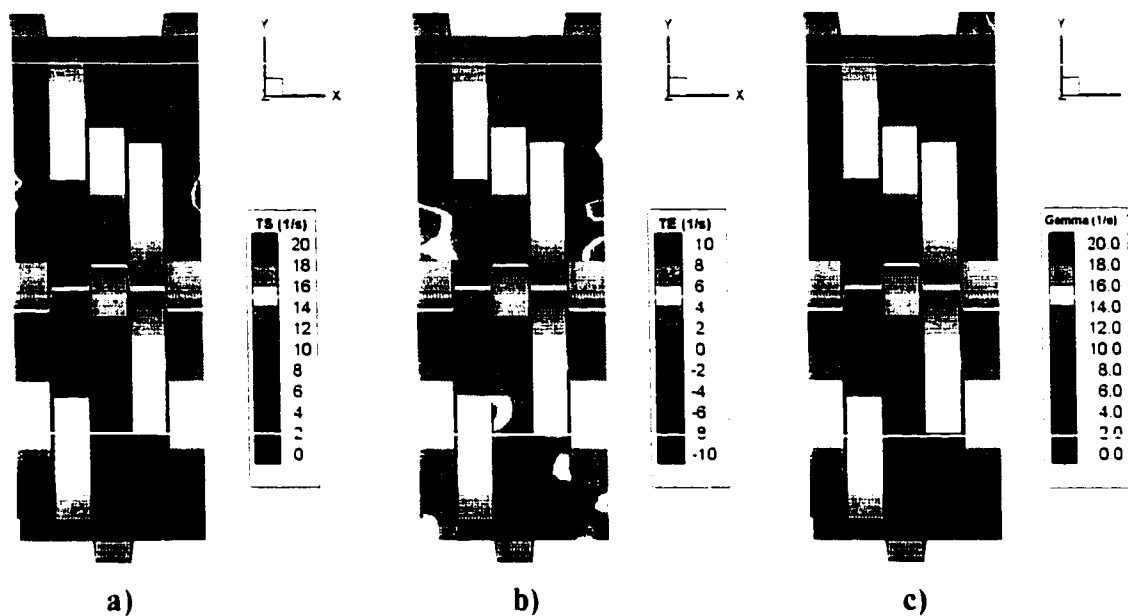


Figure 7.6.1. – Contour Plots at 60 rpm and 5 mL/s, Extended First and Last Discs (Geometry A), a) Total Absolute Shear, b) Total Elongation and c) Second Invariant.

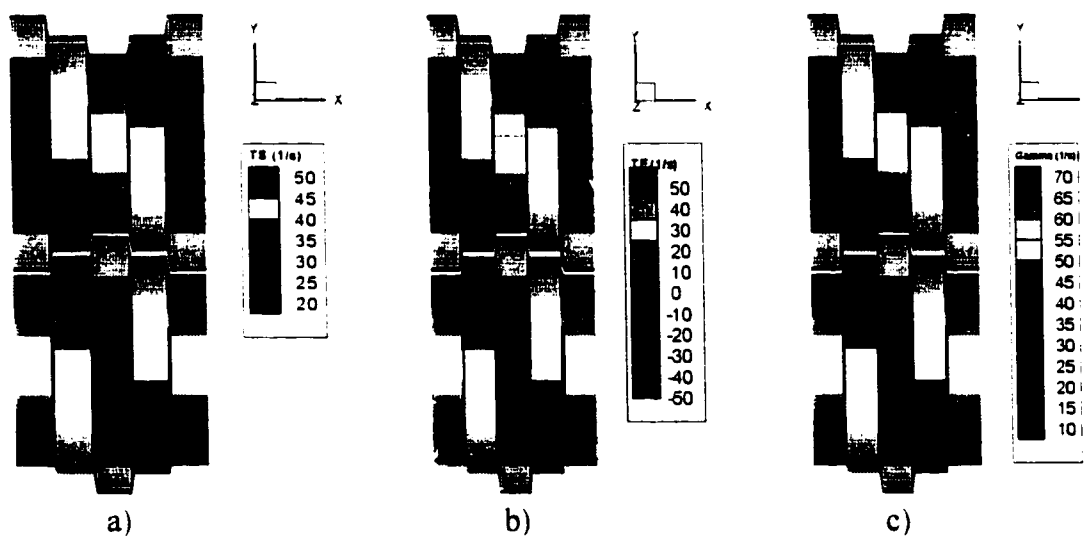


Figure 7.6.2. – Contour Plots at 100 rpm and 5 mL/s, Extended First and Last Discs (Geometry A), a) Total Absolute Shear, b) Total Elongation and c) Second Invariant.

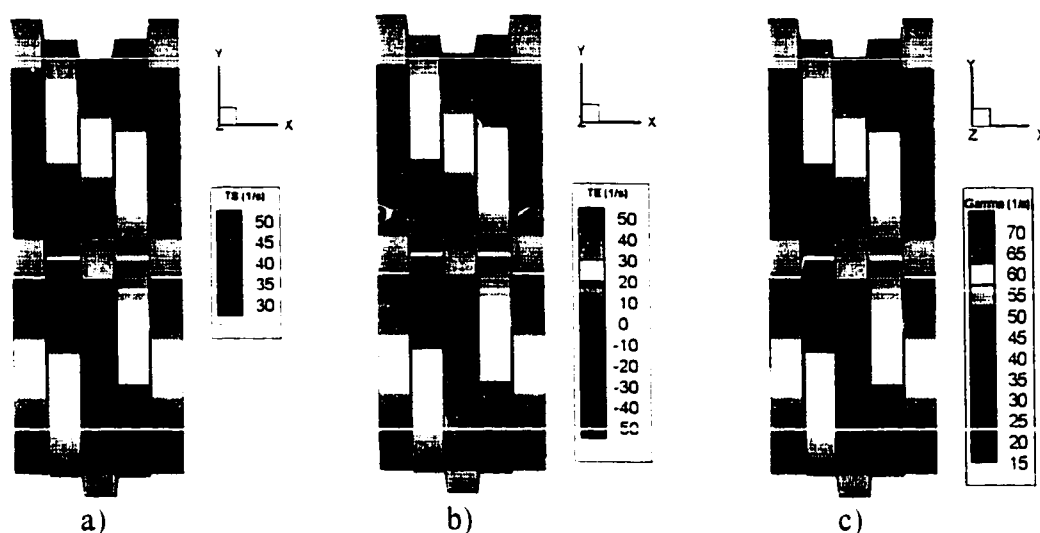


Figure 7.6.3. - Contour Plots at 150 rpm and 5 mL/s, Extended First and Last Discs (Geometry A), a) Total Absolute Shear, b) Total Elongation and c) Second Invariant.

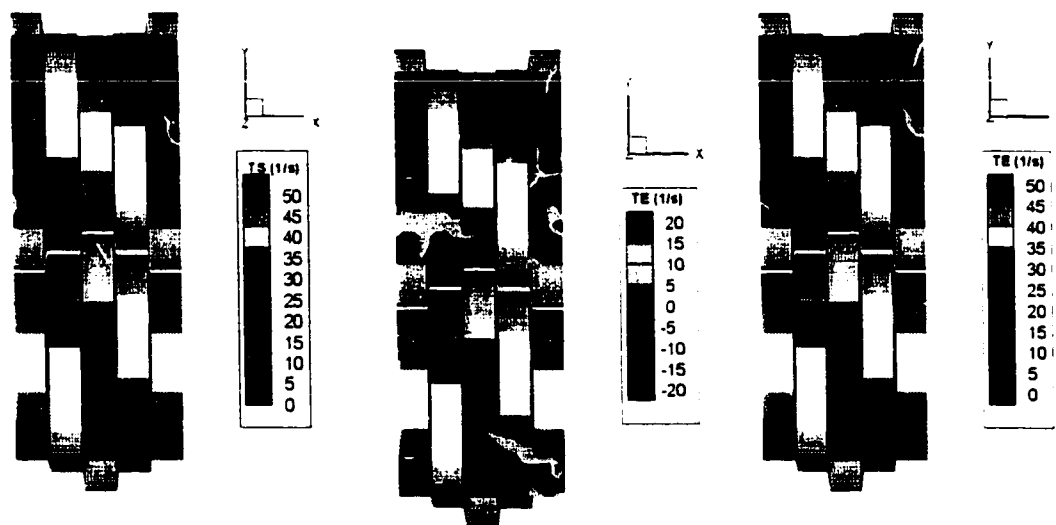


Figure 7.6.4. - Contour Plots at 60 rpm and 5 mL/s, Conveying Elements Before and After (Geometry B), a) Total Absolute Shear, b) Total Elongation and c) Second Invariant.

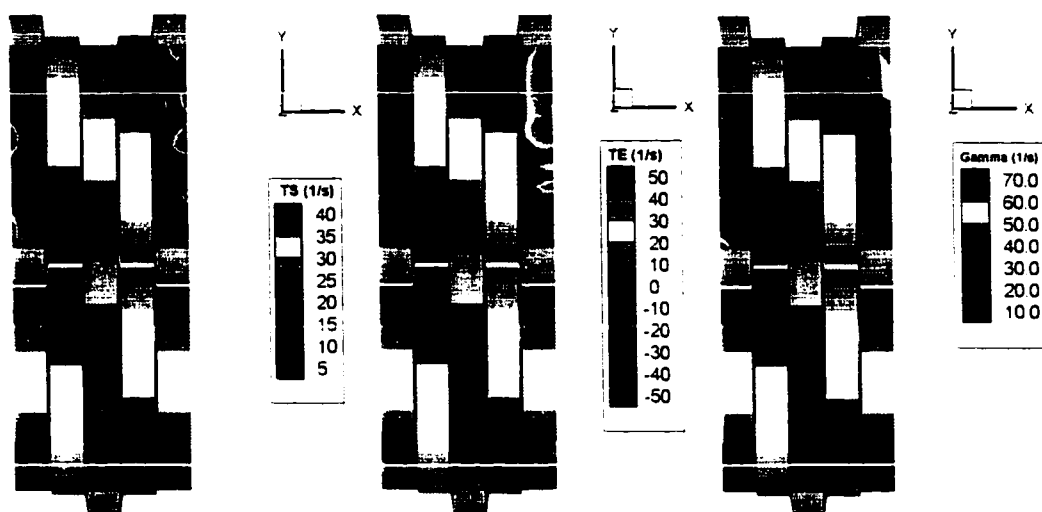


Figure 7.6.5. - Contour Plots at 100 rpm and 5 mL/s, Conveying Elements Before and After (Geometry B), a) Total Absolute Shear, b) Total Elongation and c) Second Invariant.

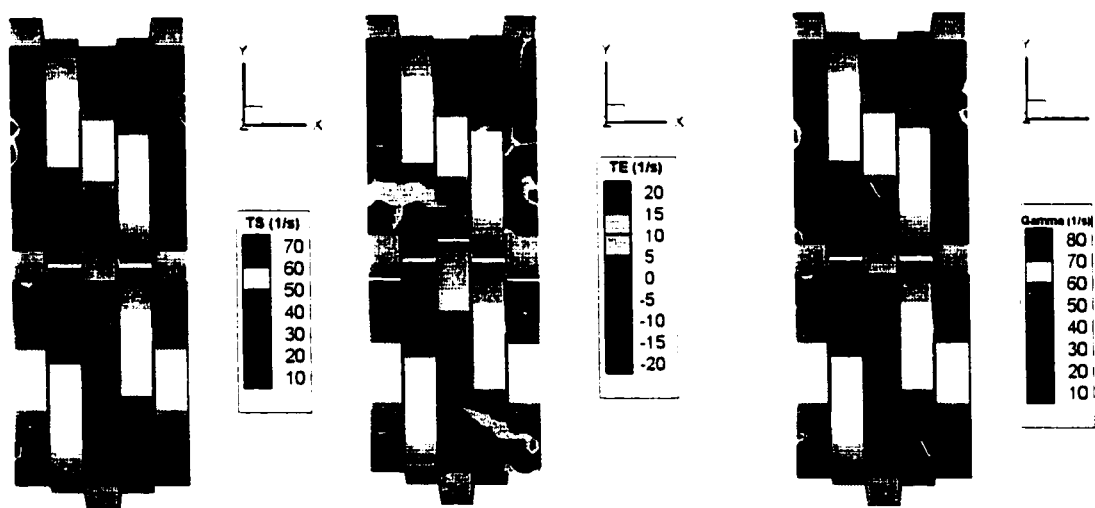


Figure 7.6.6. - Contour Plots at 100 rpm and 8.5 mL/s, Conveying Elements Before and After (Geometry B), a) Total Absolute Shear, b) Total Elongation and c) Second Invariant.

From the above discussion, there is no surprise that the regions of highest deformation are at the first and last discs of the kneading block. For most of the cases, the majority of the deformation for this measured plane and screw angle occurs at the transitions between the elements. Therefore, it would be expected that this translates into most of the mixing taking place at the transition between element types. Ottino (1989) has shown that the highest mixing efficiency would be at flow transitions or abrupt changes in the flow. These results agree with Ottino (1989) for this limited regime of the flow field.

Figures 7.6.7. to 7.6.9. show data that was extracted from the above contour plots for the left screw at 60, 100 and 150 rpm for geometry A. Data were extracted along constant axial positions at the entrance to the kneading discs and at the end of each kneading disc. Gaps in the data are the result of the solid discs (i.e. elements 2, 3 and 4 for the left screw). Values in between measured points were linearly interpolated from the experimental data. The plots for total shear are not presented, as there were no new conclusions that could be drawn that the above contour plots had not shown previously. The radial co-ordinate, y , is plotted on the x-axis of Figures 7.6.7 to 7.6.14. A value of zero for y represents the centre axial axis of the extruder. This centre axial plane (x - z plane) is called the nip region. Values for y of ± 30 represent the barrel wall (at a plane of $z=25$ mm the bounds on y co-ordinate are $3(\text{nip}) < y < 26(\text{barrel wall})$ for the LS and $-3 > y > -26$ for the RS).

Figure 7.6.7a. shows that at 60 rpm compression is created between the barrel wall and all five elements. All the elements show approximately the same magnitude of

compression. In the nip region, elongation is predominantly created with a maximum rate of approximately 12 s^{-1} . Figure 7.6.7b. shows the second invariant (called gamma) on the y -axis. The highest values for rate of deformation are seen at the 1st and 5th elements.

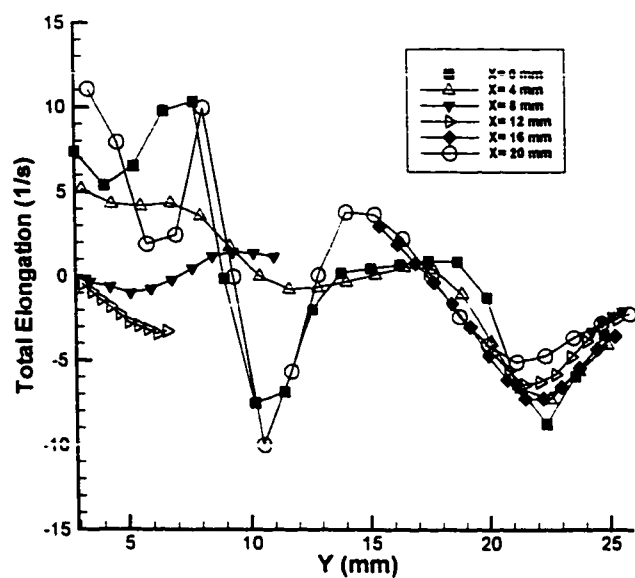
For 100 rpm, Figure 7.6.8. shows that the elongation rates and rate of deformation are significantly higher than at 60 rpm. These two graphs show how strong the elongation, compression and rate of deformation are at the 1st and 5th disc as compared to the rest of the flow field.

Figures 7.6.9. and 7.6.10. show total elongation and second invariant for the left and right screws respectively at 150 rpm and $Q = 5 \text{ mL/s}$. In the nip regions, at the 1st element, elongation is created at the LS and compression at the RS. This would be expected as the relative motion of the screws at this location are opposite to one another. For the right screw, Figure 7.6.3. shows that the flow pattern at the 1st disc near the barrel, has high shear and elongation rates which can be seen Figure 7.6.10a. The elongation rate shows strong stretching and compression over a distance of 5 mm ($20 \text{ mm} < y < 25 \text{ mm}$). This shows that within this small region the fluid is being stretched in not only the one x - y plane but is also being stretched in the x - z plane (in the third direction). At this point, the highest values of $\dot{\gamma}$ are observed. This may be explained if the geometry of the discs is studied. At this screw orientation, the first disc (RS) provides a gap between itself and the barrel wall, but the second disc provides an obstacle for the flow. The drag force created by the disc's motion causes the fluid to compress in the x - y plane (elongate in x - z), while the pressure driven flow stretches the fluid elements as they are pushed through the small gap between the barrel wall and the second disc.

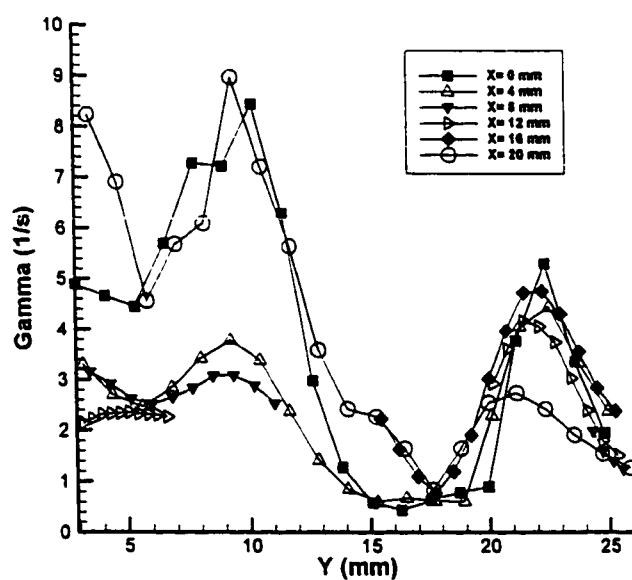
Figure 7.6.11. and 7.6.12. show the results for total elongation and magnitude of the rate of deformation tensor for varying flow rate for a fixed screw rotation speed of 60 rpm and varying rotation speed for a constant flow rate of 5 mL/s for geometry A. The data have been extracted at the 1st disc at $x=0$ mm at the left screw. This location was the basis for comparison since the maximum values for all the cases were observed at $x=0$ mm. As the flow rate increases, there is a significant increase in TE and $\dot{\gamma}$. From Figure 7.4.7. the flow shows a split at a flow rate of 8.5 mL/s explaining this sudden jump in TE and $\dot{\gamma}$. Elongation and compression in the nip and at the barrel wall respectively increase in magnitude with increasing rotation speed. The same trends are observed for $\dot{\gamma}$. This agrees with existing knowledge that higher rotation speeds create greater deformations.

Figures 7.6.13. and 7.6.14. show results from geometry B for the same data extraction location as Figures 7.6.7. The locations with significant deformation and elongation occur at elements 1 and 5. At 100 rpm, higher values for TE and $\dot{\gamma}$ are observed. The unexpected result in these plots is that at the first disc compression is created in the nip, whereas for geometry A elongation was created at the LS. A second observation is that at the fifth element at the barrel wall, elongation is created compared to compression for geometry A. The explanation for this lies in the fact that the conveying elements prevent fluid from moving back in the axial direction at the nip for the 1st LS disc. As a result, the fluid flows in the direction of rotation and is elongated in the third direction. For the fifth element at the barrel wall, after the disc passes by, fluid

can not rush back from the conveying element and is accelerated into the conveying channel as discussed earlier.



a)



b)

Figure 7.6.7. – a) Total Elongation b) Second Invariant as a Function of y -Coordinate at Different Axial Positions (x) on the Left Screw for the KB/45/20 Kneading Discs at 60 rpm and 5 mL/s (Geometry A).

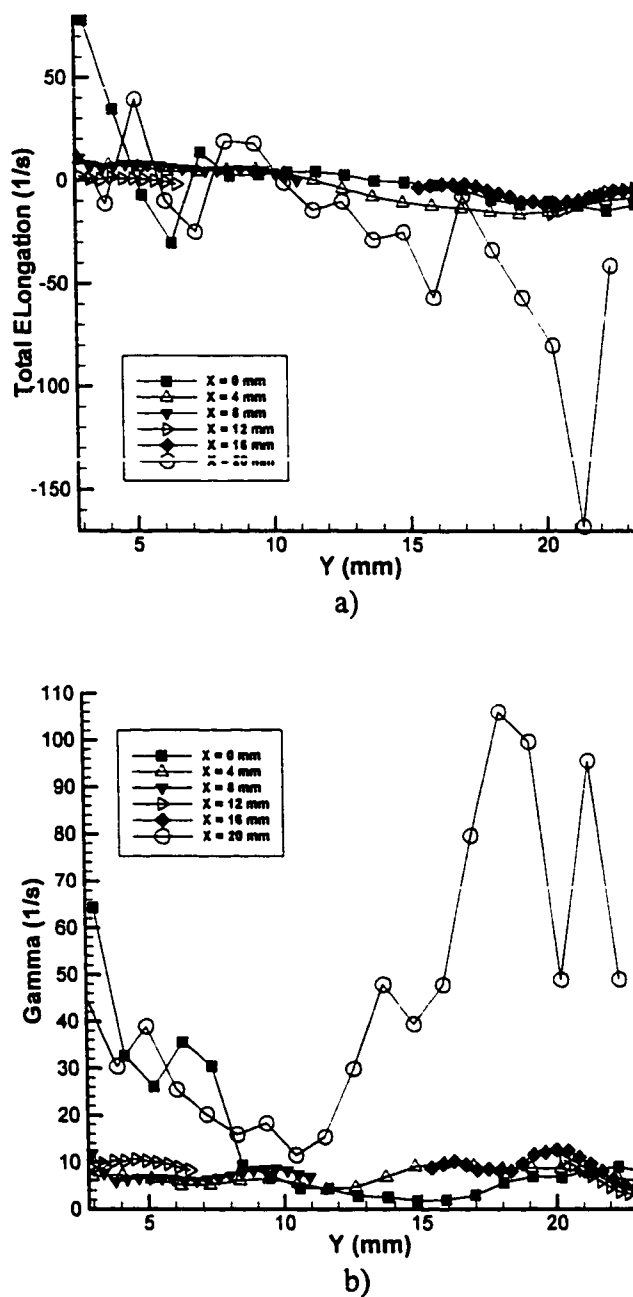
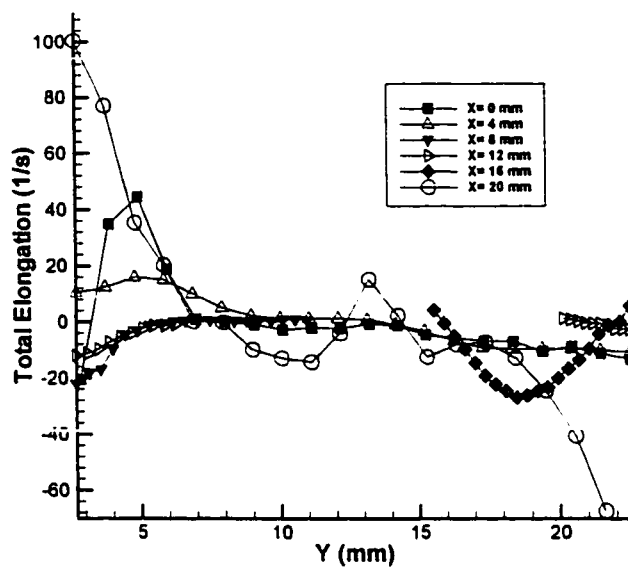
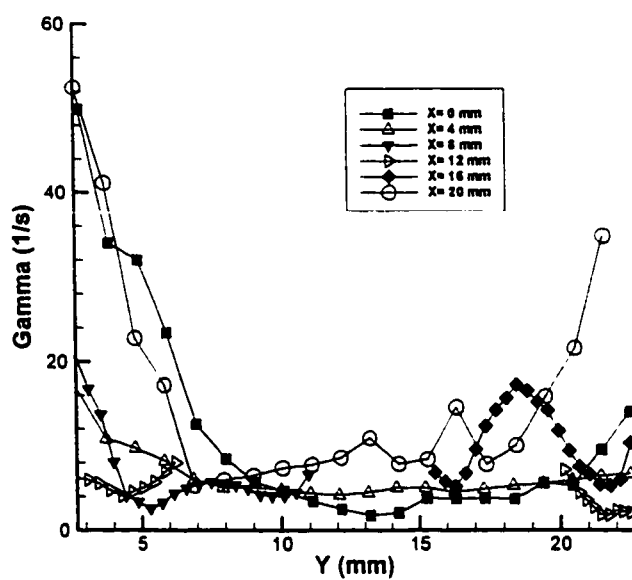


Figure 7.6.8. – a) Total Elongation b) Second Invariant as a Function of y-Coordinate at Different Axial Positions (x) on the Left Screw for the KB/45/20 Kneading Discs at 100 rpm and 5 mL/s (Geometry A).

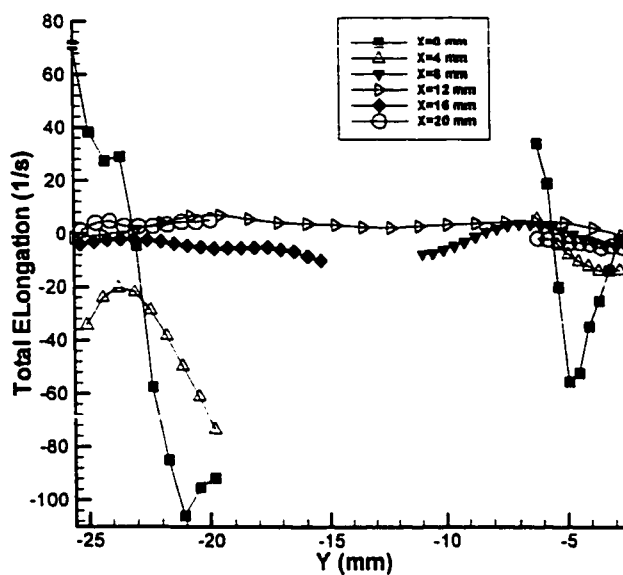


a)

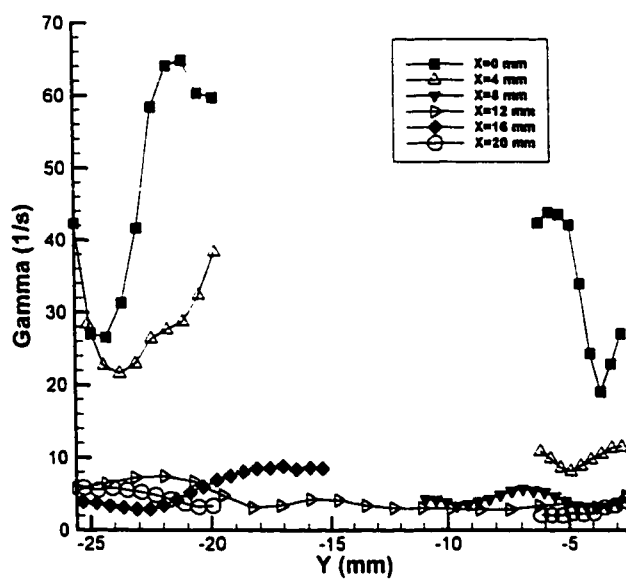


b)

Figure 7.6.9. – a) Total Elongation b) Second Invariant as a Function of y-Coordinate at Different Axial Positions (x) on the Left Screw for the KB/45/20 Kneading Discs at 150 rpm and 5 mL/s (Geometry A).



a)



b)

Figure 7.6.10. – a) Total Elongation b) Second Invariant as a Function of y -Coordinate at Different Axial Positions (x) on the Right Screw for the KB/45/20 Kneading Discs at 150 rpm and 5 mL/s (Geometry A).

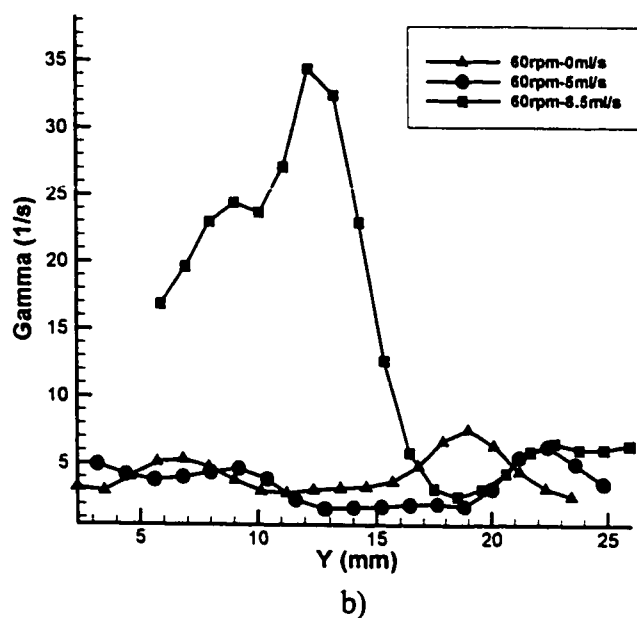
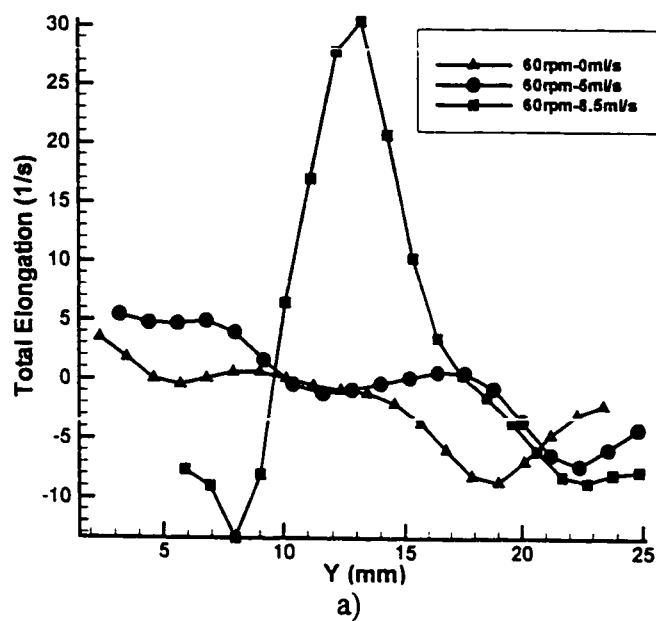
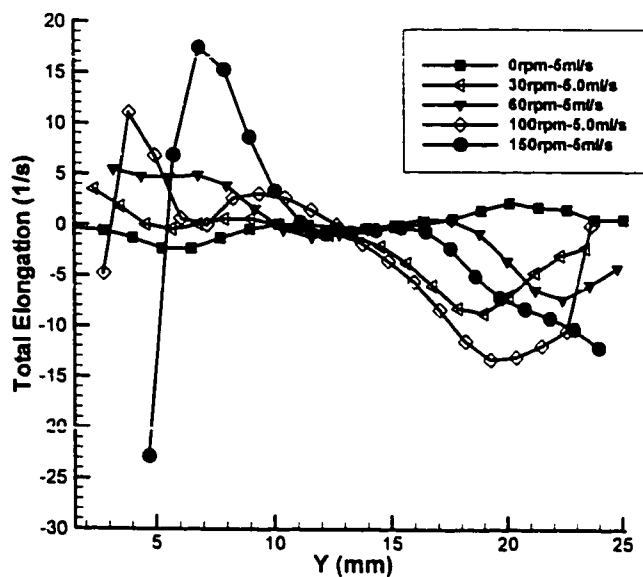
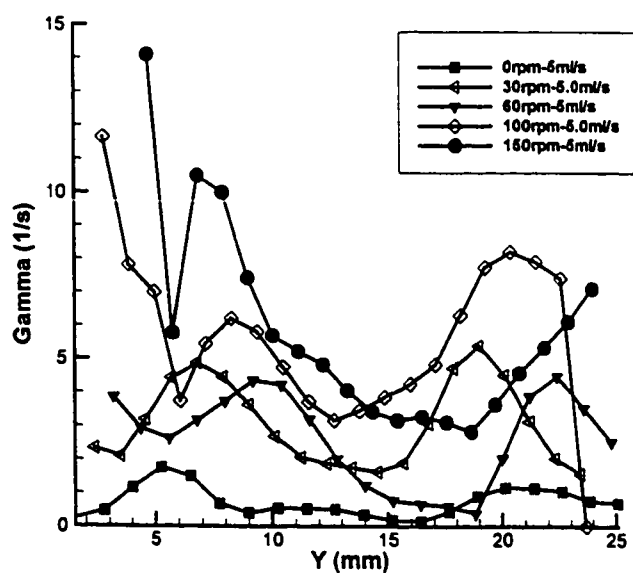


Figure 7.6.11. – a) Total Elongation b) Second Invariant as a Function of y -Coordinate Varying Flow Rate at the 1st Disc on the Right Screw for the KB/45/20 Kneading Discs at 150 rpm and 5 mL/s (Geometry A).



a)



b)

Figure 7.6.12. – a) Total Elongation b) Second Invariant as a Function of y-Coordinate Varying Rotation Speed (rpm) at the 1st Disc on the Right Screw for the KB/45/20 Kneading Discs at 150 rpm and 5 mL/s (Geometry A).

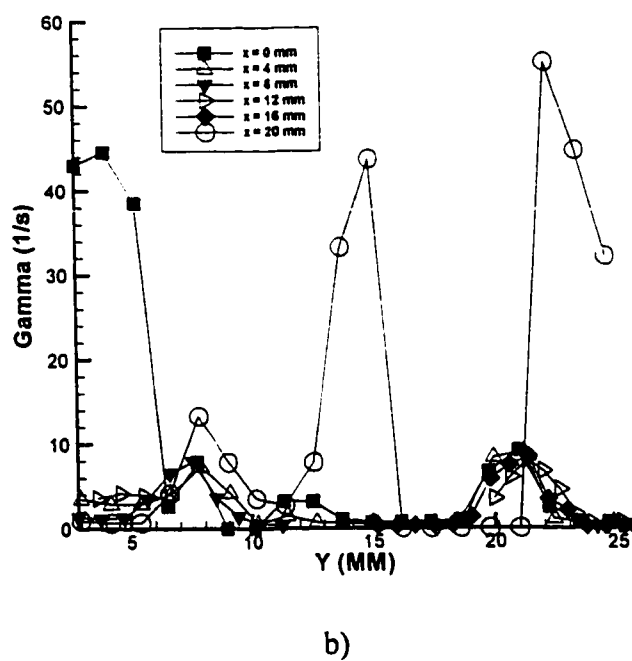
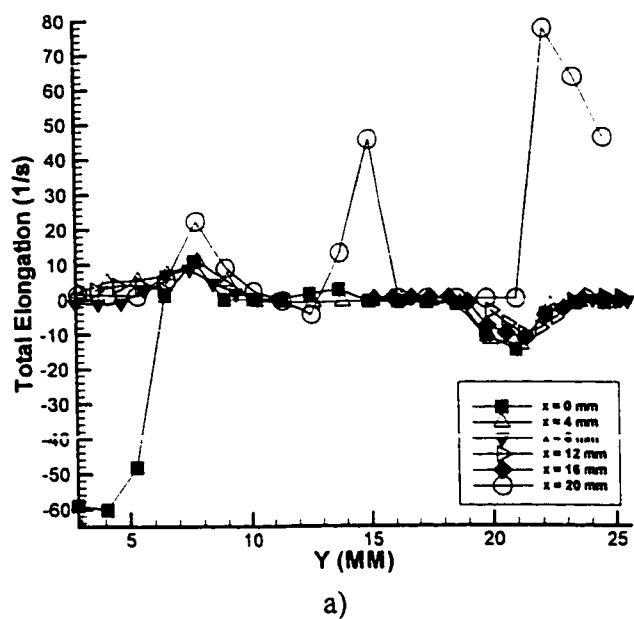


Figure 7.6.13. – a) Total Elongation b) Second Invariant as a Function of y -Coordinate at Different Axial Positions (x) on the Left Screw for the KB/45/20 Kneading Discs at 60 rpm and 5 mL/s (Geometry B).

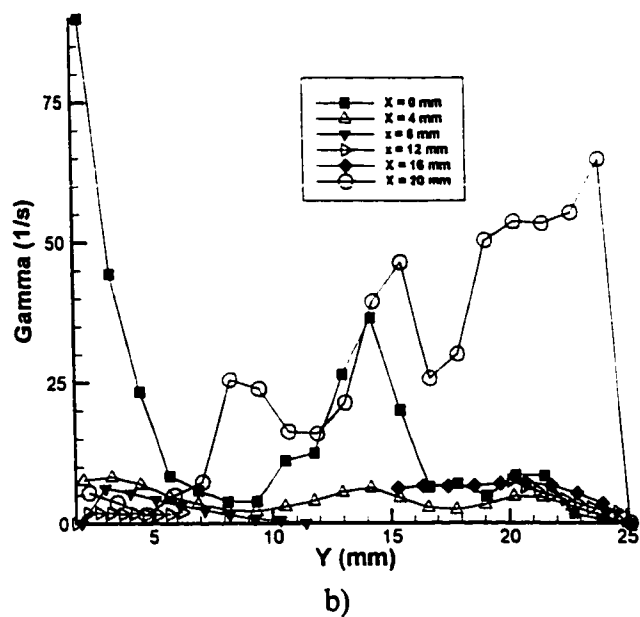
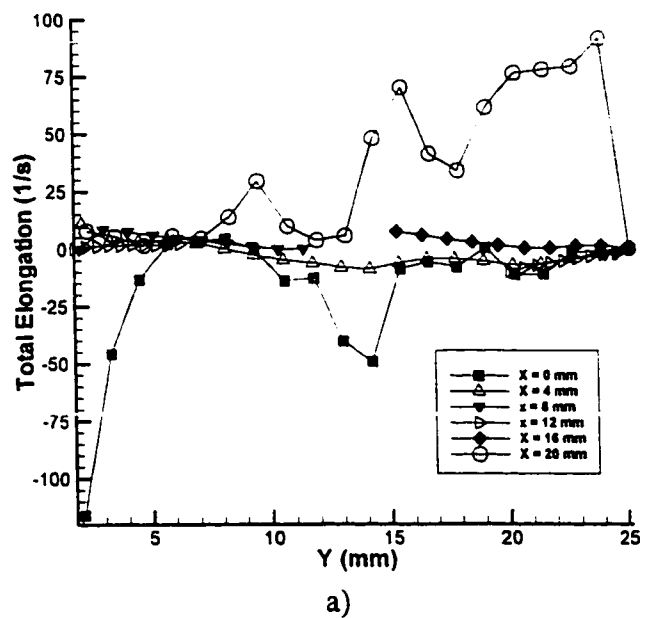


Figure 7.6.14. – a) Total Elongation b) Second Invariant as a Function of y -Co-ordinate at Different Axial Positions (x) on the Left Screw for the KB/45/20 Kneading Discs at 100 rpm and 5 mL/s (Geometry B).

7.7. Summary

The difficulty for experimenters studying the flow and mixing in the twin screw extruders has been optical access. This problem was eliminated with the fabrication of a fully acrylic ICRTSE model. The plastic model permitted the use of the experimental techniques of laser induced fluorescence (LIF) and particle image velocimetry (PIV). The flow visualisation results from LIF demonstrated the mixing mechanisms present in the kneading blocks of the twin screw extruder. Two screw profiles were studied in detail to determine the effect of the reverse conveying elements location after the mixing section (kneading blocks). The visualisations coupled with image analysis demonstrated clearly that the mixing was enhanced by placing a reverse conveying element directly after the last set of kneading discs (geometry D) in the mixing section. This would create back mixing which was vital for efficient mixing in the kneading section. When the screw profile consisted of a forward and then reverse conveying element after the last set of kneading disc (geometry C), the flow exhibited channelling and poor mixing. Geometry D produced a more uniform mixture in the kneading discs based on the mixing measure of normalised intensities. Average intensity results showed that geometry D created longer residence times in the kneading disc section compared to Geometry C.

Fluid velocities were measured for two screw profiles (geometry A and B - Figure 3.1.2.2.). The objective of these measurements was to isolate the kneading discs from the other elements to create a database of velocity measurements for comparison with simulation [Bravo (1998)]. The measured velocities were used to calculate the shear and elongation rates and the magnitude of the deformation tensor for the fluid flow field. The

velocity results for geometry A showed higher back flow and larger recirculations with increasing screw rotation. An unexpected flow pattern that was observed was the splitting of the flow at the first kneading disc where the fluid at the left screw (LS) flowed in the direction of rotation and at the right screw (RS) the fluid flowed opposite to the rotation through the channel created by the staggered discs. This channelling of the flow was observed up to a rotation speed of 150 rpm. The conclusion drawn was that this geometrical configuration of the kneading discs did not provide sufficient drag flow momentum to overcome the pressure flow momentum. For higher flow rates, the flow opposite to the direction of rotation increased and less back mixing or recirculation of the flow was observed.

The velocity field was significantly different for geometry B where a forward conveying element were used before and after the kneading discs. The conveying elements caused the flow field at the inlet to the discs to have a very different profile than geometry A. The conveying elements oriented the flow with a higher radial velocity and lower axial velocity compared to the extended discs (geometry A). As a result, the fluid flowed in the direction of rotation and no channelling of the flow reverse to the direction of rotation was observed. In fact, the fluid was aligned such that no back flow was observed. This explained our results from flow visualisation for Geometry C where there was dye exiting the kneading disc section with very little deformation.

The comparison of the measured velocity field with the finite element simulation of Bravo (1998), showed the importance of inlet boundary conditions. For the screw profile with extended first and last discs, the experimental and simulation results were in

reasonable agreement for the run at 60 rpm and 5 mL/s with poorer agreement at higher flow rates. The poor agreement at higher flow rates is believed to be the result of the assumption of creeping flow for the mathematical model. The higher flow rates are believed to create strong convective forces in the flow which could not be captured by the model. An unexpected result, was that the experimental simulation results had better agreement at higher flow rates when conveying elements were deployed before and after the kneading discs. At the higher flow rates, the conveying elements created an ordered pattern on the flow prior to entering the kneading blocks producing a similar inlet velocity profile to that used as the inlet boundary condition for the simulation.

The performance of the kneading discs was characterised based on the shear, elongation and the magnitude of the rate of deformation tensor within the measured flow fields. The results were able to capture the regions of high deformation and showed the relative magnitudes of the shear and elongation created. For geometry A, compression was created in the gap between the discs and barrel. In the intermeshing or nip region, strong compressive and elongation was observed. Higher rotation speed created higher elongation rates and compression rates. The value of the deformation tensor reflected these observations, as maximums were seen in the intermeshing and disc-barrel gap regions of the TSE. For the various cases of screw rotation speed, the largest rates of deformations (elongation and shear) were seen at the first and last disc of the kneading block. This result showed that at the entrance and the exit of the kneading discs, where flow transitions occurred, largest deformations were created. For increase in flow rate, the data showed that there was a sharp rise in elongation rate due to the flow splitting at

the first element. Overall, the elongation across the discs increased for higher flow rates, which agreed with the result of the mathematical model of Van Der Wal et al. (1996).

The results presented here have shown the feasibility of observing and measuring the flow field in a very complicated geometry. The results helped characterise the performance of screw profiles and kneading discs and provided a valuable data set that were used to validate mathematical models of the fluid flow in the kneading disc section.

8.0. Conclusions and Recommendations

8.1. Static Mixer

The experimental measurements of velocity and mixing in the Kenics[®] KM static mixer, provide benchmarks that have not been published in the open literature before. The techniques of LIF, LDA and PIV were applied to study the flow and mixing in the static mixer. The conclusions of this study are detailed below.

Mixing was observed and quantified from flow visualisation using the technique of laser induced fluorescence coupled with digital image analysis. The measurements of the number average striation thickness, variance of striation widths and interfacial area, were determined from the visualisations for elements of length to diameter (L/D) ratios of 0.8, 1.0, 1.5 with 90° twist per element. From flow visualisations, flow field transitions were observed in where vortices developed above the first and second elements at Reynolds numbers of 43 and 90 for $L/D=0.8$ and Reynolds numbers of 55 and 105 for $L/D=1.0$. These transitions were confirmed by measurements of the fluid velocity field with laser Doppler anemometry. It was found that these vortices did not appreciably enhance mixing based on striation thickness and variance of striation width measurements after 4 to 5 elements of $L/D=1.0$. The influence of viscosity ratio on mixing showed that a viscosity ratio (dyed stream/bulk stream) of 1, had faster interfacial area growth and created more uniform mixtures compared to a viscosity ratio of 0.2 for a flow rate ratio of 0.2 (dyed stream/bulk stream).

The experimental fluid velocities in a static mixer having elements with an aspect ratio of 1.5 and 90 degrees of twist per element were measured over four elements. The velocity field measured captured the mixing nature of the static mixer, where the flow was split at the leading edges of the elements and recombined at the trailing edge. The flow followed the path created by each element in the direction of the helical twist. Recirculations in the radial plane were observed where fluid would flow from the high-pressure side of the element forward out along the tube wall to the low-pressure side or suction side of the element. The magnitude of the maximum radial flow was approximately 30 percent of the maximum axial flow for the first two elements and increased to 40 percent by the fourth element.

The flow field also exhibited differences in the magnitudes of the two transverse velocity components (the two complementary radial components). The flow showed lower magnitudes of velocity in the z – co-ordinate direction compared to the x – co - ordinate direction at the first element. Thereafter, the fluid had similar magnitudes of x and z components of velocity at later elements. The conclusion to be drawn from this was that the mixer required a development length to allow the radial flow to build in magnitude.

The rate of deformation analysis on the fluid flow field indicated that mixing efficiency would be increased if the first element had a larger helix angle (amount of rotation/ aspect ratio). This became apparent from the reduced velocity magnitudes in the transverse z – co - ordinate direction compared to the complementary transverse x – co - ordinate direction. The lower magnitude in velocity resulted in a reduced magnitude of

the rate of deformation, which translated into less stretching and elongation. This indicated that mixing would benefit if more radial flow could be generated in the z – co-ordinated direction at the first element. The rate of deformation analysis showed that the largest magnitude of deformations occurred at the junction between elements, the element surfaces and the mixer tube surface and that the core of the fluid flow experienced little deformation.

These experimental results have helped to eliminate many questions for the mixer designer but in the process have shown the need for more analysis when approaching mixer design with the idea of using elements with different geometrical characteristics in combination within a mixer. However, the experimental data presented have opened up a whole new avenue for mixer designers. The mathematical models of fluid flow fields in the static mixer available, now have the data that will allow for them to be validated not only for fluid velocities but also for validation of the computational fluid mixing simulations. These models could then be used as tools for mixer design.

8.2. Twin Screw Extruder

The fluid flow and mixing mechanisms were identified in the kneading section of a twin screw extruder using the experimental techniques of laser induced fluorescence and particle image velocimetry. The flow field in this extruder was qualitatively studied from flow visualisation and the fluid mixing was characterised and quantified with image analysis techniques. The fluid velocity measurements provided invaluable data for this complicated geometry. The velocity measurements published in literature to date have

been limited to very small regions of the flow in the kneading discs. With larger regions of the flow measured, the data permitted the characterisation of the kneading discs based on calculated shear and elongation rates. Computer simulations of the kneading disc could also be validated with these data. The conclusions of this study of the twin screw extruder are summarised below.

The flow visualisation results from LIF demonstrated the mixing mechanisms present in the kneading blocks of the twin screw extruder. Two screw profiles were studied in detail to determine the effect of the reverse conveying elements location after the mixing section (kneading blocks). The visualisations coupled with image analysis demonstrated clearly that the mixing was enhanced by placing a reverse conveying element directly after the last set of kneading discs in the mixing section. This would create back mixing which is vital for efficient mixing in the kneading section. When the screw profile consisted of a forward and then reverse conveying element after the last set of kneading discs, the flow exhibited channelling and poor mixing.

Fluid velocities were measured for two screw profiles. The objective of these measurements was to isolate the kneading discs from the other elements to create a database of velocity measurements for comparison with simulation. The measured velocities were used to calculate the shear and elongation rates and the magnitude of the deformation tensor for the fluid flow field. The velocity results for the screw profile with extended first and last discs showed an increase in back flow and recirculations with increasing screw rotation. An unexpected flow pattern observed, was the splitting of the flow at the first kneading disc where the fluid at the left screw (LS) flowed in the

direction of rotation and at the right screw (RS) the fluid flowed opposite to the rotation through the channel created by the staggered discs. This channelling of the flow was observed up to a rotation speed of 150 rpm. The conclusion drawn was that this geometrical configuration of the kneading discs did not provide sufficient drag flow momentum to overcome the pressure flow momentum. For higher flow rates, the flow opposite to the direction of rotation increased and less back mixing and recirculation of the fluid flow was observed.

The velocity field was significantly different for screw geometry B, where a forward conveying element was used before and after the kneading discs. The conveying element caused the flow field at the inlet to the discs to have a very different profile than with extended discs (Geometry A). The conveying elements oriented the flow with a higher radial velocity and lower axial velocity compared to geometry A. As a result, the fluid flowed in the direction of rotation and no channelling of the flow reverse to the direction of rotation was observed.

The comparison of the measured velocity field with the finite element simulation of Bravo (1998), showed the importance of inlet boundary conditions. For the screw profile with extended first and last discs, the experimental and simulation results were in reasonable agreement for the run at 60 rpm and 5 mL/s with poorer agreement at higher flow rates. The poor agreement at higher flow rates is believed to be the result of the assumption of creeping flow for the mathematical model. The higher flow rates are believed to create strong convective forces in the flow which could not be captured by the model. An unexpected result, was that the experimental and simulation results had better

agreement at higher flow rates when conveying elements were deployed before and after the kneading discs. At the higher flow rates, the conveying elements created an ordered pattern on the flow prior to entering the kneading blocks producing a similar inlet velocity profile to that used as the inlet boundary condition for the simulation.

The performance of the kneading discs was characterised based on the shear, elongation and the magnitude of the rate of deformation tensor within the measured flow fields. The results were able to capture the regions of high deformation and showed the relative magnitudes of the shear and elongation created. For geometry A, compression was created in the gap between the discs and barrel. In the intermeshing or nip region, strong compressive and elongation was observed. Higher rotation speed created higher elongation rates and compression rates. The value of the deformation tensor reflected these observations, as maximums were seen in the intermeshing and disc-barrel gap regions of the TSE. For the various cases of screw rotation speed, the largest rates of deformations (elongation and shear) were seen at the first and last disc of the kneading block. This result showed that at the entrance and the exit of the kneading discs, where flow transitions occurred, largest deformations were created.

References

- Adrian, R.J., "Particle-Imaging Techniques for Experimental Fluid Mechanics", *Ann. Rev. Fluid Mech.*, **23**, 261-304, 1991.
- Arimond, J.; Erwin, L., "A Simulation of a Motionless Mixer", *Chem. Eng. Comm.* **37**, 105-126, 1985a.
- Arimond, J.; Erwin, L., "Modelling of Continuous Mixers in Polymer Processing", *Transactions of the ASME*. **107**, 70-76, 1985b.
- Alloca, P.T., "Mixing Efficiency of Static Mixing Units in Laminar Flow", *Fiber. Prod.* **8**, 12, 1982.
- Baker, J., "Motionless Mixers Stir Up New Uses", *Chem. Eng. Prog.*, **86**, no. 6, 32-38, 1991.
- Bakker, A., Marshall, E.M., "Laminar Mixing with Kenics In-Line Mixers", Presented at the Fluent Inc.'s 1992 Users Group Meeting, October 13-15, Burlington, Vermont, 1992.
- Baldyga, J., Bourne, J.R., Hearn, S.J., "Interaction Between Chemical Reactions and Mixing on Various Scales", *Chem. Eng. Sci.*, **52**, 457-466, 1997.
- Bigio, D., Stry, W., "Measures of Mixing in Laminar Flow", *Polym. Eng. Sci.*, **30**, 153-161, 1990.
- Biswas, A., Davis, B.A., Gramann, P.J., Stradins, L.; Osswald, T.A., "Simulating Mixing in the Extrusion Process", *SPE ANTEC Tech. Papers*, 336-340, 1994.
- Boillot, A., Prasad, A.K., "Optimization Procedure for Pulse Separation in Cross-Correlation PIV", *Exp. Fluids*, **21**, 87-93, 1996.
- Bourne, J.R., Baldyga, J., "A Fluid Mechanical Approach to Turbulent Mixing and Chemical Reaction I: Inadequacies of Available Methods", *Chem. Eng. Comm.*, **28**, 231-241, 1984a.

- Bourne, J.R., Baldyga, J., "A Fluid Mechanical Approach to Turbulent Mixing and Chemical Reaction II: Micromixing in the Light of Turbulence Theory", *Chem. Eng. Comm.*, **28**, 243-258, 1984b.
- Bourne, J.R., Baldyga, J., "A Fluid Mechanical Approach to Turbulent Mixing and Chemical Reaction III: Computational and Experimental Results for the New Mixing Model", *Chem. Eng. Comm.*, **28**, 258-281, 1984c.
- Bravo, V.E., Finite Element Simulation of Flow in Twin Screw Extruder Mixing Elements, Ph.D. Thesis, McMaster University, 1998.
- Brodkey, R.S., "Fluid Motion and Mixing", in Mixing, Vol. 1, Uhl, V.H.; Gray, J.B., eds., Academic Press, New York, Chapter 2, 1966.
- Buchave, P., *Exp. Thermal Fluid Sci.*, **5**, 586, 1992.
- Byrde, O, Sawley, M.L., "Parallel Computation of Flow in an In-line Static Mixer", ECCOMASS 96, John Wiley and Sons Ltd, (1996a).
- Byrde, O, Sawley, M.L., "Parallel Computation and Analysis of the Flow in a Static Mixer", <http://imhefwww.epfl.ch/lmf/>, (1996b) (retrieved from the internet).
- Byrde, O, Sawley, M.L., "Optimization of a Kenics Static Mixer using Numerical Flow Simulations", <http://imhefwww.epfl.ch/lmf/>, (1996c) (retrieved from the internet).
- Chandrasekaran, M., Karwe, M.V., *AIChE J.*, **43**, 24, (1997).
- Chella, R.; Ottino, J.M., "Laminar Mixing of Polymeric Liquids; A Brief Review and Recent Theoretical Developments", *Polym. Eng. Sci.*, **23**, no. 7, 357-378, 1983.
- Chella, R., Ottino, J.M., "Stretching in Some Classes of Fluid Motions and Asymptotic Mixing Efficiencies as Measure of Flow Classification", *Arch. Rat. Mech. Anal.*, **90**, 15-42, 1985.
- Chemineer, Internet Web Site, <http://www.kenics.com/km.html>, (1998).
- Chen, S.J., MacDonald, A.R., *Chem. Eng.*, **80**, 1973.

- Cheremisinoff, N.P. Polymer Mixing and Extrusion Technology. Marcel Dekker Inc., 1987.
- Christiano, J., Lindenfelzer, M., "Investigation of Mixing Patterns in Co-Rotating Fully Intermeshing Twin Screw Extruders Mixing Elements Using Dynamic Pressure Distributions", *Technical Papers, SPE ANTEC*, 78, 1997.
- Christiano, J.P., "Co-Rotating Fully Intermeshing Twin Screw Extruder Mixing Analysis", *SPE ANTEC Tech. Papers*, 3386-3396, 1993.
- Conner, J.H., Bigio, D.I., "A Numerical Analysis of the Mixing Performance of the Non-Intermeshing Twin Screw Extruder Nip", *SPE ANTEC Tech. Papers*, 31-34, 1992.
- Cooper, A.R., "Diffusive Mixing in Continuous Laminar Flow Systems", *Chem. Eng. Sci.*, 21, 1095-1106, 1966.
- Dackson, K., Low Reynolds Number Entrance Flows and Analysis of Motionless Mixers, Ph.D. Thesis, Rensselaer Polytechnic Institute, Troy, New York, 1986.
- Dackson, K., Nauman, E.B., "Fully Developed Flow in Twisted Tapes: A Model for Motionless Mixers", *Chem. Eng. Comm.*, 54, 381-395, 1987.
- Danckwerts, P.V., "The Definition of Some Characteristics of Mixtures", *Appl. Sci. Res.*, Sec. A3, 279-296, 1952.
- Danckwerts, P.V., *Chem. Eng. Sci.*, 7, 116, 1957.
- Devellian, R., "Continuous, Predictable Performance with Motionless Mixers", *Automation*, February, 46-48, 1972.
- Drain, L.E., The Laser Doppler Technique, John Wiley and Sons, Toronto, 1980.
- Erwin, L. "Principles of Laminar Fluid/Fluid Mixing", in "Polymer Mixing and Extrusion Technology", N.P. Cheremisinoff, Ed., Marcel Dekker Inc., 1987.
- Funatsu, K., Nagashima, Y., Nakamo, Y., Kajiwara, T., "Direct Simulation of 3-D Flows in Various Twin Screw Extruders", *PPS Tenth Annual Meeting*, p.46, 1994.
- Grace, C.D., "Static Mixing and Heat Transfer", *Chem. Proc. Eng.*, July, 1971.

- Gotsis, A.D., Kaylon, D.M., "Simulation of Mixing in Co-rotating Twin Screw Extruders", *Technical Papers, SPE ANTEC*, 1989.
- Gotsis, A. D., Ji, Z., Kaylon, M., "3-D Analysis of the Flow in Co-rotating Twin Screw Extruders", *Technical Papers, SPE ANTEC*, 139, 1990.
- Heywood, N.I., Viney, L.J. and Stewart, I.W., "Mixing Efficiencies and Energy Requirements of Various Motionless Mixer Designs for Laminar Mixing Applications", *Fluid Mixing II, I. Chem. Eng. Symp. Ser.*, no. 89, 1984.
- Hobbs, D.M., Swanson, P.D., Muzzio, F.J., "Numerical Characterization of Low Reynolds Number Flow in the Kenics Static Mixer", *Chem. Eng. Sci.*, **53**, 1565-1584, 1998.
- Hobbs, D.M., Muzzio, F.J., "The Kenics Static Mixer - A Three-Dimensional Chaotic Flow", *Chem. Eng. J.*, **67**, 153-166, 1997.
- Hobbs, D.M., Muzzio, F.J., "Effects of Injection Location, Flow Ratio and Geometry on Kenics Mixer Performance", *AIChE J.*, **43**, 3121-3132, 1997b.
- Jaffer, S.J., Bravo, V.L., Wood, P.E., Hrymak, A.N., "Experimental Validation of Numerical Simulations of the Kneading Disc Section in a Twin Screw Extruder", submitted to *Polym. Eng. Sci.*, May 1998.
- Janssen, J.M.H., Meijer, H.E.H., "Dynamics of Liquid-Liquid Mixing: A 2-Zone Model", *Polym. Eng. Sci.*, **35**, 1766-1780, 1995.
- Ji, Z., Kaylon, D.M., "Two Dimensional Computational Study of Chaotic Mixing in Two Tipped Kneading Paddles of Co-Rotating Twin Screw Extruders", *SPE ANTEC Tech. Papers*, 1323-1327, 1992.
- Kalyon, D.M., Gotsis, A.D., Yilmazer, U., Gogos, C., Sangani, H., Aral, B., Tsenoglou, C., "Development of Experimental Techniques and Simulation Methods to Analyze Mixing in Co-rotating Twin Screw Extrusion", *Advances in Polymer Technology*, **8**, No. 4, 337-353, 1988.

- Kalyon, D.M., Sangani, H.N., "An Experimental Study of Distributive Mixing in Fully Intermeshing Co-rotating Twin Screw Extruders", *Polym. Eng. Sci.* **29**, No. 15, 1989
- Kalyon, D.M., Jacob, C.; Yaras, P., "Experimental Study of the Degree of Fill and Melt Densification in Fully-Intermeshing, Co-rotating Twin Screw Extruders", *Plastics, Rubber and Composites Processing and Applications*, **16**, 193-200, 1991.
- Kalyon, D.M., Lawal, A., Yacizi, R., Yaras, P., Railkar, S., "Mathematical Modeling and Experimental Studies of Twin Screw Extrusion Processing of Filled Polymers", *Polyblends 97, SPE Retec*, 188-234, 1997.
- Karwe, M.V.; Sernas, V., "Velocity Measurements in the Nip Region of a Co-Rotating Twin Screw Extruder Using Laser Doppler Anemometry", *SPE ANTEC Tech. Papers*, 150-154, 1995.
- Keane, R.D., Adrian, R.J., "Optimization of Particle Image Velocimeters. Part I. Doubled-Pulsed Systems", *Meas. Sci. Tech.*, **1**, 1202-1215, 1990.
- Keane, R.D., Adrian, R.J., "Theory of Cross Correlation Analysis of PIV Images", *App. Sci. Res.*, **49**, 191-215, 1992.
- Kemblowski, Z., "Residence Time Distribution of a Power Law Fluid in a Kenics Static Mixer", *Chem. Eng. Sci.*, **43**, 473-478, 1988.
- Kim, P.J., White, J.L., "Flow Visualization and Residence Time Distributions in a Modular Co-rotating Twin Screw Extruder". *Inter. Polym. Proc.*, **IX**, 108, (1994).
- Koh, C.J., Hookham, P.; Leal, L.G., "An Experimental Investigation of Concentrated Suspension Flows in a Rectangular Channel", *J. Fluid Mech.*, **266**, 1-32, 1994.
- Komax, Internet Web Site, <http://www.komax.com/gen-pphldist.html>, 1998.
- Ottino, J, Kusch, H., "Analysis of Impingement Mixing-Reaction Data: Use of a lamellar model to generate fluid mixing information", *Ind. Chem. Res*, 302-315, 1989.
- Kwon, T.H., Joo, J.W., Kim, S.J., "Kinematics and Deformation Characteristics as a Mixing

- Measure in the Screw Extrusion Process", *Polym. Eng. Sci.*, **34**, 174-189, 1994.
- Lawal, A., Kalyon, D.M., "Simulation of Intensity of Segregation Distributions Using Three-Dimensional FEM Analysis: Application to Co-rotating Twin Screw Extrusion Processing", *J. App. Polym. Sci.*, **58**, 1501-1507, 1995.
- Ling, F.H., Schmidt, G., "Mixing Windows in Discontinuous Cavity Flows", *Physics letter A*, **165**, 221-30, 1992.
- Ling, F.H., Zhang, X., "Chaotic Mixing in the Kenics Static Mixer", Advances in Computational Methods in Fluid Dynamics ASME, Fluids Engineering Division, **196**, ASME, New York, 367-374, 1994.
- Ling, F.H., Zang, X., "A Numerical Study of Mixing in the Kenics Static Mixer", *Chem. Eng. Comm.*, **136**, 119-141, 1995.
- Lourenco, L. Krothapalli, A., "On the Accuracy of Velocity and Vorticity measurements with PIV", *Exp. Fluids*, **15**, 421-428, 1995.
- Manas-Zloczower, I., Cheng, J., *Polym. Eng. Sci.*, **29**, 1059, 1989.
- Manas-Zloczower, I., Wong, T.H., *SPE ANTEC*, 1788, 1992.
- McCullough, T.W., Hilton, B.T., "The Extrusion Performance of Co-rotating Intermeshing Twin Screw Extruder Screw Elements - An Experimental Investigation", *Technical Papers SPE ANTEC*, 3372, 1993.
- Mckelvey, J.N., Polymer Processing, John Wiley and Sons, New York, 1962.
- Middleman, S., Fundamental of Polymer Processing, McGraw-Hill, New York, (1977).
- Miles, R.B., Connors, J.J., Markovitz, E., Howard, P.J., Roth, G.J., "Instantaneous profiles and turbulence statistics of supersonic free shear layers by Raman excitation plus laser induced electronic fluorescence (Relief) velocity tagging of oxygen", *Expt. Fluids*, **8**, 17-24, 1989.
- Mohr, W.D., Saxton, R.L., Jepsen, C.H., "Mixing in Laminar Flow Systems", *Ind. Eng.*

- Chem.*, **49**, 1855-1856, 1957.
- Mokhtarian, F., Erwin, L., *SPE ANTEC Tech. Papers*, **28**, 476, 1982.
- Naumann, E.B., "Enhancement of Heat Transfer and Thermal Homogeneity with Motionless Mixers", *AIChE J.*, **25**, 246-258, 1979.
- Naumann, E.B., "On Residence Time and Trajectory Calculations in Motionless Mixers", *Chem. Eng. J.*, **47**, 141-148, 1991.
- Naumann, E.B., "Reactions and Residence Time Distributions in Motionless Mixers", *Can. J. Chem. Eng.*, **60**, 136-140, 1982.
- Nigam, K.D.P., Nauman, E.B., "residence Time Distributions of Power Lay Fluid in motionless Mixers", *Can. J. Chem. Eng.*, **63**, 519-521, 1985.
- Nigam, K.D.P., Vasudeva, K., "Residence Time Distribution in Static Mixers", *Can. J. Chem. Eng.*, **58**, 543-544, 1980.
- Oberlehner, J., Cassagnau, P., Michel, A., "Local Residence Time Distribution in a Twin Screw Extruder", *Chem. Eng. Sci.*, **49**, 3897-3907, 1994.
- Ottino, J. M., Ranz, W., "A Lamellar Model for Analysis of Liquid-Liquid Mixing", *Chem. Eng. Sci.*, **34**, 877-890, 1979.
- Ottino, J.M., Ranz, W., "A Framework for Description of Mechanical Mixing", *AIChE J.*, 565-577, 1981.
- Ottino, J.M., "Description of Mixing with Diffusion and Reaction in Terms of the Concept of Material Surfaces", *J. Fluid Mech.*, **114**, 83-103, 1982.
- Ottino, J.M., "Mechanical Mixing Efficiency Parameter for Static Mixers", *AIChE J.*, **29**, 159-161, 1983.
- Ottino, J.M., "The Mixing of Fluids", *Scientific American*, **260**, 56-67, 1989a.
- Ottino, J.M., The Kinematics of Mixing: Stretching, Chaos, and Transport, Cambridge University Press, Cambridge, Great Britain, 1989b.

- Pahl, E.L., Mushchelknautz, E., "Static mixers and Their Applications", *Int. Chem. Eng.*, **22**, 197, 1982.
- Pinto, G., Tadmor, Z., *Polym. Eng. Sci.*, **10**, 279, 1970.
- Prasad, A.K., Adrain, R.J., Landreth, C.C., Offutt, P.W., "Effect of Resolution on the Speed and Accuracy of Particle Image Velocity Interrogation", *exp. Fluids.*, **13**, 105-116, 1992.
- Pustelnik, P., "Investigation of Residence Time Distribution in Kenics Static Mixers", *Chem. Eng. Process.*, **102**, 147-154, 1986.
- Ranz, W., "Applications of a Stretch Model to Mixing, Diffusion and Reaction in Laminar and Turbulent Flows", *AIChE J.*, **25**, 41-47, 1979.
- Rauwendaal, C., Polymer Extrusion, Hanser Publish., 1986.
- Rauwendaal, C., "Analysis and Experimental Evaluation of Twin Screw Extruders", Polym. Eng. Sci., **21**, 1092, 1981.
- Rauwendaal, C., "Which Twin Screw Extruder is for You?", *Plastics Formulating and Compounding*, November/December, 1995.
- Sastrohartono, T., Esseghir, M., Kwon, T. H., Sernas, V., "Numerical and Experimental Studies of the Flow in the Nip Region of a Partially Intermeshing Co-rotating Twin-Screw Extruder", *Polym. Eng. Sci.*, **30**, 1382-1398, 1990.
- Shah, N.F., Kale, D.D., "Pressure Drop of Non-Newtonian Fluids in Static Mixers", *Chem. Eng. Sci.*, **46**, 2159-2161, 1991.
- Spencer, R.S., Wiley, R.M., "The Mixing of Very Viscous Liquids", *J. Colloid. Sci.*, **6**, 133-145, 1951.
- Swanborough, A., "Compounding and Colouring", *British Plastic and Rubber*, 4-6, June 1994.

- Tadmor, Z., Gogos, C.G., Principles of Polymer Processing, New York, Wiley Interscience, 1979.
- Todd, D.B., *Polym. Eng. Sci.*, 15, 437, 1975.
- Todd, D.B., "Drag and Pressure Flow in Twin Screw Extruders", *Technical Papers, ANTEC*, 168, 1989.
- Tung, T.T., Low Reynolds Number Entrance Flows: A Study of a Motionless Mixer, Ph.D. Thesis, University of Massachusetts, 1976.
- Tung, T.T., Laurence, R.L., "A Co-ordinate Frame for Helical Flows", *Polymer Eng. Sci.*, 15, 401-405, 1975.
- Wang, C.Y., "On The Low Reynolds Flow in a Helical Pipe", *J. Fluid Mech.*, 108, 185-194, 1981.
- Zerafati, S.; Bigio, D.; "Flow and Mixing Analysis of Highly Viscous Fluids in a Wavy Wall Channel", *SPE ANTEC Tech. Papers*, 125-129, 1995.
- Zwietering, Th. N., "The Degree of Mixing in Continuous Flow Systems", *Chem. Eng. Sci.*, 2, 1-15, 1959.